

# **Simulation of growth and self-assembly of complex molecules on surfaces**

vorgelegt von

Master of Advanced Study

**Nicola Maria Kleppmann**

aus München

Von der Fakultät II - Mathematik und Naturwissenschaften

Technische Universität Berlin

zur Erlangung des akademischen Grades

Doktor der Naturwissenschaften

Dr. rer. nat.

genehmigte Dissertation

Promotionsausschuss:

Vorsitzender: Prof. Dr. Michael Lehmann

Gutachterin: Prof. Dr. Sabine H. L. Klapp

Gutachter: Prof. Dr. Andreas Heuer

Tag der wissenschaftlichen Aussprache: 01.09.2015

Berlin 2015



# Declaration of Authorship

I, Nicola Maria Kleppmann, declare that this thesis titled, ‘Simulation of growth and self-assembly of complex molecules on surfaces’ and the work presented in it are my own. I confirm that:

- This work was done wholly or mainly while in candidature for a research degree at this University.
- Where any part of this thesis has previously been submitted for a degree or any other qualification at this University or any other institution, this has been clearly stated.
- Where I have consulted the published work of others, this is always clearly attributed.
- Where I have quoted from the work of others, the source is always given. With the exception of such quotations, this thesis is entirely my own work.
- I have acknowledged all main sources of help.
- Where the thesis is based on work done by myself jointly with others, I have made clear exactly what was done by others and what I have contributed myself.

Signed:

Date:



*To my partner Sebastian and my family, who always believe in me.*



## *Acknowledgements*

First and foremost, I want to thank my supervisor Sabine Klapp for giving me the opportunity to work on the field of structure formation and collective ordering during self-assembly and growth of complex molecules, and for supporting me throughout my work. Through her constant support and invaluable input she made this work possible, has contributed to forming me as a physicist and scientist, and has made the last three years inspiring and successful. Also, I would like to thank Andreas Heuer for taking the time to grade this work, but also for fruitful and interesting discussions in the last year.

Next, I would like to thank our collaborators S. Bommel, C. Weber, H. Spranger, P. Schaefer, J. Novák, S. V. Roth, F. Schreiber and S. Kowarik for our very successful collaboration on the multilayer growth of C<sub>60</sub>. In particular, I would like to thank S. Bommel and S. Kowarik for our close collaboration, which has widened my awareness of molecules in the context of their features compared to atoms and colloids, and has given me many fundamental insights into the growth of complex molecules in general.

My thanks also go to the Collaborative Research Centre SFB 951 of the German Research Foundation DFG, which focuses on hybrid inorganic-organic systems. Besides funding my research, all members of the SFB 951 created an inspiring atmosphere to work in and significantly influenced my research. Specifically, my work has profited greatly from discussions with A. Zykov, S. Kowarik, M. Sparenberg, S. Blumstengel and F. Henneberger concerning the details of experiments, as well as K. Palczynski, J. Dzubiella and T. Heinemann concerning theoretical considerations.

Further, I am very grateful to the members of the group ‘Computer simulations and Theory of Complex Fluids’ of Sabine Klapp, which formed my academic ‘family’ for the last three years. In particular Robert, Christopher, Helge and Rodrigo have helped me with enlightening discussions.

Outside Berlin, my work has additionally benefited from constructive discussions with M. Klopotek, M. Öttel and F. Schreiber from the Eberhard Karls Universität Tübingen.

## Zusammenfassung

In Hybridmaterialien werden organische Moleküle und anorganische Substrate kombiniert, um durch die Symbiose der hohen Ladungsträgerdichte der organischen Moleküle mit der kristallinen Perfektion des anorganischen Substrats optimale Dünnfilm-Halbleiter zu erschaffen. Jedoch hängt der Wirkungsgrad solcher Halbleiter von der internen Struktur ab, die durch die Moleküle ausgebildet wird und durch Wachstumsbedingungen sowie Molekül- und Substrateigenschaften manipuliert werden kann. Die treibenden Prozesse im molekularen Dünnfilmwachstum sind bisher nur sehr wenig verstanden.

Das sphärische Molekül C<sub>60</sub> bildet unseren ersten Schwerpunkt. Das Wachstum von vielen Lagen von C<sub>60</sub> wird mittels dynamischer Monte-Carlo (DMC) Simulationen untersucht und mit zeitaufgelösten Röntgenstreu-Messungen des Multilagenwachstums verglichen [Bommel *et al.*, Nat. Comm. **5**, 5388 (2014)]. In dieser Zusammenarbeit mit dem Experiment bestimmen wir einen selbstkonsistenten Satz Energieparameter, mit dem wir die Nukleation und das Multilagenwachstum von C<sub>60</sub> für verschiedene Temperaturen und Aufdampfraten quantitativ richtig voraussagen können. Untersuchungen der simulierten Einzelteilchentrajektorien geben uns Einblicke in die Unterschiede und Ähnlichkeiten zwischen dem Wachstum des Moleküls C<sub>60</sub>, Wachstum von Atomen und Wachstum von Kolloiden. Das Molekül hat eine atomähnliche Stufenkantenbarriere, die sich von kolloidalen Stufenkantenbarrieren unterscheidet. Jedoch finden wir für C<sub>60</sub> viel glatteres Wachstum als für vergleichbare atomare Systeme, welches durch die Korrelation von Einzelteilchentrajektorien mit Einzelteilchenprozessen untersucht wird. Dies kann auf den Einfluss der kürzeren Teilchen-Teilchen Wechselwirkung zurückgeführt werden.

Basierend auf diesen Studien erweitern wir unser System, um anisotrope Moleküle auf strukturierten Substraten zu untersuchen. Wir entwickeln ein neues Modell, das die kondensierte Phase unseres repräsentativen Hybridsystems darstellt: das organische Molekül para-Sexiphenyl (6P) und die elektrostatisch strukturierte Zinkoxid-(10-10)-Facette. Innerhalb dieses Modells werden Wechselwirkungen zwischen Molekülen sowie zwischen Molekül und Substrat durch ihre stärksten elektrostatischen und nicht-elektrostatischen (sterische und van-der-Waals-) Wechselwirkungen dargestellt. Dieser Ansatz, bei denen jedes Molekül 3D-Rotationsfreiheitsgrade hat, jedoch die laterale Molekülposition auf einem 2D-Gitter fixiert ist, wird mit Equilibrium-Monte-Carlo Simulationen überprüft. Die Simulation erlaubt es das Orientierungsverhalten in einem kondensierten Zustand an einer Oberfläche zu untersuchen. Wir reproduzieren verschiedene experimentell beobachtete Eigenschaften, wie die Ausrichtung einzelner Moleküle mit dem elektrostatischen Streifenmuster des Substrats, die Bildung einer stehenden nematischen Phase mit Fischgrätenanordnung der molekularen Quadrupolmomente, und die Bildung einer liegenden nematischen Phase. Darauf aufbauend simulieren wir Wachstum, bei dem Moleküle zusätzlich zwischen Gitterplätzen diffundieren können. Für niedrige Aufdampfraten finden wir den experimentell beobachteten Übergang von einer liegenden Phase zu einer stehenden nematischen Phase, welcher das Equilibrium-Ordnungsverhalten der entsprechenden Teilchendichten reflektiert. Jedoch ändert sich das Ordnungsverhalten für hohe Aufdampfraten, wo der Wettbewerb zwischen unterschiedlich schnellen Prozessen und unterschiedlich starken Wechselwirkungen ein kompliziertes Orientierungsverhalten hervorruft. In manchen Wachstumsbedingungen verschwindet die Adsorptionsorientierung der Teilchen nach kurzen Zeiten, tritt jedoch für lange Zeiten wieder auf. Außerdem streben nicht alle Observablen monoton ihrem Equilibriumswert entgegen, die Orientierung weist nichtmonotonen Verhalten auf.

Unsere Studien liefern grundlegendes Verständnis der molekularen Wachstumsprozesse in Systemen, die zwischen Atomen und Kolloiden liegen. Diese Systeme haben ein kompliziertes Selbstordnungs- und Wachstumsverhalten, sowohl hinsichtlich der Oberflächenstruktur, als auch hinsichtlich der internen Orientierung.

## Abstract

Hybrid systems consisting of organic molecules on inorganic semiconductor surfaces have large charge carrier densities and tunable resonance energies, making them ideal candidates for semiconductor devices. However, the efficiency of such devices depends on the self-organised nanoscale structure formed by the adsorbed molecules, which depends, in turn, on the complex interplay of growth conditions with the molecular and substrate properties. Understanding elementary nanoscopic processes in molecular film growth is in its infancy.

First, we focus on the spherical molecule C<sub>60</sub>, using large-scale dynamic Monte-Carlo (DMC) simulations. We investigate C<sub>60</sub> nucleation and multilayer growth in collaboration with an experimental group that performs real-time *in situ* specular and diffuse x-ray scattering [Bommel *et al.*, Nat. Comm. **5**, 5388 (2014)]. We determine for the first time in a molecular system, a self-consistent set of energy barriers that describes the nucleation and multilayer growth of C<sub>60</sub> for different temperatures and adsorption rates in quantitative agreement with experiments. Analysing the particle-resolved dynamics, we find that the lateral diffusion is similar to colloidal systems, but characterised by an atom-like step-edge barrier. Comparing C<sub>60</sub> growth with an atom-like system, we find significant differences between the evolution of the surface morphology of C<sub>60</sub> and atoms, as well as between the single-particle dynamics on the respective growing material landscapes. By comparing the average travelling distance of particles after a given time with their current neighbourhood, we can identify the influence of the different time scales that compete during growth and can pinpoint the differences between the atomic systems, C<sub>60</sub>, and colloidal systems.

Next, we focus on anisotropic molecules on structured substrates. Here we propose a novel, coarse-grained model representing the condensed phases of a representative hybrid system, that is, para-Sexiphenyl (6P) at zinc-oxide (ZnO), specifically the electrostatically structured ZnO(10-10) facet. In our model, inter-molecular and molecule-substrate interactions are approximated through their most significant electrostatic and non-electrostatic (steric and van-der-Waals) interactions. To validate our approach, we perform equilibrium Monte Carlo simulations, where the lateral positions are fixed to a 2D lattice while the rotational degrees of freedom are continuous. We use these simulations to investigate orientational ordering in the condensed state. Here we reproduce various experimentally observed features such as the alignment of individual molecules with the line charges on the surface, the formation of a standing uniaxial phase with a herringbone structure, as well as the formation of a lying nematic phase. These studies form the basis for DMC simulations of sub-monolayer growth in which molecules can additionally move between lattice sites. We find an orientational transition from lying nematic to standing nematic order for low adsorption rates, as expected from experimental studies of self-assembled monolayers. This transition corresponds to the change from the low-density lying nematic phase to the high density standing nematic phase previously found for equilibrium. However, for high adsorption rate, the competition between the different process rates and interaction strengths yields complex orientational behaviour, such as the formation of a re-entrant biaxial phase and non-monotonous behaviour of observables as a function of adsorption rates.

Our studies provide fundamental understanding of molecular growth processes in systems which lie between atoms and colloids, and have complex self-assembly and growth behaviour with regards to both the morphology and the orientation.



# Contents

<b>Declaration of Authorship</b>	iii
<b>Acknowledgements</b>	vii
<b>Abstract</b>	ix
<b>Contents</b>	xi
<b>Abbreviations</b>	xv
<b>I Growth and self-assembly of complex molecules</b>	1
<b>1 Introduction</b>	3
1.1 Materials and devices . . . . .	4
1.2 Theoretical consideration: systems between Atomic and Colloidal length-scales . . . . .	8
1.2.1 Typical length-scales . . . . .	8
1.2.2 Influence on interactions . . . . .	9
1.2.3 COMs between atomic and colloidal length-scales . . . . .	11
1.3 Experimental status quo . . . . .	12
1.3.1 Static surface structure, molecular ordering and morphology . . . . .	12
1.3.2 Time resolved growth measurements . . . . .	13
1.3.3 Measurements of single-particle dynamics . . . . .	14
1.4 Theoretical modelling approaches . . . . .	14
1.5 Scope of the thesis . . . . .	17
<b>2 Simulation approach: Dynamic Monte-Carlo (DMC) simulations</b>	18
2.1 Motivation of DMC simulations . . . . .	18
2.2 Detailed balance . . . . .	19
2.3 The underlying master-equation . . . . .	20
2.4 Constant-time-step simulations (RSM) . . . . .	22
2.5 Event-driven simulations (KMC) . . . . .	23
2.5.1 Algorithm principle . . . . .	24
2.5.2 Time step lengths and waiting time distributions . . . . .	25
2.6 Equivalence of system evolution . . . . .	27
2.6.1 Analytic calculation of equivalence . . . . .	28
2.6.2 Numerical equivalence . . . . .	30
2.7 Hybrid approaches . . . . .	31
2.7.1 Continuous time null-event algorithms . . . . .	31
2.7.2 Composition and Rejection (CR) algorithms . . . . .	32

<b>3</b>	<b>Background to coarse-graining</b>	<b>33</b>
3.1	Time-scale separation and rate description . . . . .	33
3.1.1	Similarities and differences between the different derivations . . . . .	35
3.1.2	Derivation of Kramer's rate . . . . .	36
3.1.3	Derivation from Transition state theory . . . . .	39
3.2	Markov process . . . . .	43
3.3	Diffusion on a lattice . . . . .	44
3.3.1	Random walk on a 2D lattice . . . . .	44
3.3.2	Diffusion rates on a 2D lattice . . . . .	45
3.3.3	Deriving the diffusion coefficient . . . . .	46
<b>II</b>	<b>Isotropic particles: C<sub>60</sub></b>	<b>47</b>
<b>4</b>	<b>Introducing the isotropic particle C<sub>60</sub></b>	<b>49</b>
<b>5</b>	<b>Experimental and theoretical understanding of C<sub>60</sub> growth</b>	<b>53</b>
5.1	Experimental set-up and measurements . . . . .	53
5.1.1	Specular scattering . . . . .	54
5.1.2	In-plane scattering . . . . .	55
5.2	Coarse-graining for isotropic particles . . . . .	56
5.3	Algorithm specifics . . . . .	60
<b>6</b>	<b>Observables for C<sub>60</sub> growth</b>	<b>62</b>
6.1	Observables that allow comparison to experiment . . . . .	62
6.2	Target quantities to study differences between atomic and C <sub>60</sub> growth . . . . .	63
<b>7</b>	<b>Results for C<sub>60</sub> growth</b>	<b>66</b>
7.1	Collaboration with experiments . . . . .	66
7.1.1	First insight into multilayer growth . . . . .	66
7.1.2	Comments on the parametrisation . . . . .	68
7.1.3	Different temperatures and adsorption rates . . . . .	70
7.2	C <sub>60</sub> between atomic and colloidal length-scales . . . . .	72
7.2.1	Comparison to colloidal systems . . . . .	72
7.2.2	Comparison to atomic systems . . . . .	74
7.3	Particle dynamics and substrate morphology . . . . .	80
7.3.1	Local Dynamics . . . . .	80
7.3.2	Coupling of local dynamics to evolving surface . . . . .	83
<b>8</b>	<b>Conclusion C<sub>60</sub></b>	<b>85</b>

<b>III Anisotropic particles on structured substrates</b>	<b>87</b>
<b>9 Introducing anisotropic molecules on structured substrates</b>	<b>89</b>
<b>10 Model specifics for 6P on ZnO</b>	<b>94</b>
10.1 Coarse-graining for COMs on structured substrates . . . . .	94
10.2 Splitting the Hamiltonian . . . . .	95
10.3 Molecule-molecule interactions . . . . .	96
10.3.1 Non-electrostatic interactions: Gay-Berne (GB) potential . . . . .	97
10.3.2 The multipole moments of 6P molecules . . . . .	98
10.3.3 Electrostatic molecule-molecule interactions . . . . .	99
10.4 Molecule-substrate interactions . . . . .	101
10.4.1 Non-electrostatic interactions . . . . .	102
10.4.2 Electrostatic molecule-substrate interaction . . . . .	103
10.4.3 Parametrisation of the quadrupole-field interaction . . . . .	106
10.5 Equilibrium collective ordering using MC simulations . . . . .	108
10.6 Growth simulations for anisotropic molecules . . . . .	109
<b>11 Characterising the collective ordering</b>	<b>112</b>
11.1 Measures of evaluation for equilibrium . . . . .	112
11.1.1 Nematic and biaxial order parameter . . . . .	112
11.1.2 Angular distributions . . . . .	113
11.2 Additional measures to characterise growth . . . . .	113
11.2.1 Measures for coverage: Particle density and surface fraction . . . . .	113
11.2.2 Orientation-dependent particle densities . . . . .	115
11.2.3 Configuration-dependent cluster information . . . . .	116
<b>12 Collective ordering of anisotropic molecules</b>	<b>117</b>
12.1 Equilibrium . . . . .	117
12.1.1 Impact of molecule-molecule interactions on a quadratic lattice . . . . .	117
12.1.2 Tetragonal lattice . . . . .	121
12.1.3 Impact of the electrostatic substrate pattern . . . . .	123
12.2 Growth . . . . .	125
12.2.1 Surface coverage . . . . .	126
12.2.2 Orientational ordering . . . . .	128
12.2.3 Robustness to adsorption configuration . . . . .	132
12.2.4 Particle clustering during growth . . . . .	133
<b>13 Conclusion for the collective ordering of anisotropic molecules</b>	<b>135</b>
<b>IV General conclusion and Outlook</b>	<b>137</b>
<b>14 Overall conclusion and further directions of research</b>	<b>139</b>
14.1 Overall conclusion . . . . .	139
14.2 Further directions of research . . . . .	141

<b>Appendices</b>	<b>147</b>
<b>A Full equivalence of RSM and KMC time scales</b>	<b>147</b>
A.1 One process occurs and one is possible . . . . .	147
A.2 One process takes place, two are possible . . . . .	148
A.3 Two processes take place, two are possible . . . . .	149
A.4 Two processes take place, $n$ are possible . . . . .	150
A.5 Mathematical induction for $a$ processes taking place for $n$ possible processes . .	152
<b>B Algorithm details for C60 growth</b>	<b>157</b>
B.1 Particle relaxation on a hexagonal lattice . . . . .	157
B.2 Periodic boundary conditions . . . . .	157
B.3 Binary tree data structures . . . . .	159
<b>C The Hoshen-Kopelman cluster algorithm</b>	<b>162</b>
<b>D Multipole expansion up to the hexadecapole moment</b>	<b>164</b>
D.1 Continuous charge distribution . . . . .	164
D.2 Discrete charge distribution . . . . .	168
<b>E Multipole moments of 6P</b>	<b>169</b>
<b>F Quadrupole-field interaction for 6P on ZnO(10-10)</b>	<b>171</b>
<b>G Non-monotonous growth behaviour</b>	<b>174</b>
G.1 Experimental indicators for non-monotonous behaviour . . . . .	174
G.2 Simulations indicating a non-monotonous island density . . . . .	175
<b>Bibliography</b>	<b>179</b>

# Abbreviations

<b>6P</b>	para-Sexiphenyl (molecule name)
<b>C<sub>60</sub></b>	Buckminster Fullerene (molecule name)
<b>CR</b>	Composition and Rejection
<b>COM</b>	Conjugated Organic Molecule
<b>DFT</b>	Density Functional Theory
<b>DMC</b>	Dynamic Monte Carlo
<b>GB</b>	Gay-Berne
<b>MC</b>	Monte Carlo
<b>MD</b>	Molecular Dynamics
<b>HOMO</b>	Highest Occupied Molecular Orbital
<b>KMC</b>	Kinetic Monte Carlo
<b>LED</b>	Light Emitting Diode
<b>LJ</b>	integrated Lennard-Jones
<b>LUMO</b>	Lowest Unoccupied Molecular Orbital
<b>MMC</b>	Metropolis Monte Carlo
<b>MSD</b>	Mean Squared Displacement
<b>OTFT</b>	Organic Thin Film Transistor (also abbreviated as OFET)
<b>OLED</b>	Organic Light Emitting Diode
<b>OMBE</b>	Organic Molecular Beam Epitaxy
<b>OPV</b>	Organic Photo-Voltaics
<b>QQ</b>	Quadrupole-Quadrupole
<b>QS</b>	Quadrupole-Substrate
<b>RSM</b>	Random Selection Method
<b>TST</b>	Transition State Theory



## **Part I**

# **Growth and self-assembly of complex molecules**



# Chapter 1

## Introduction

While inorganic semiconductor devices used to form the technological frontier, their crystalline structure makes it difficult to finely tune their properties. In most cases, their tunability relies on doping, which is limited by crystal stability [5, 6] and defect formation [7, 8]. Here, organic and hybrid inorganic-organic semiconductor devices form a promising field for current and future technological advances [9–13]. Opening the field of semiconductors to include conjugated organic molecules (COMs) allows us to benefit from the broad, nearly infinite, spectrum of molecules that can be synthesised [14]. Devices made from COMs commonly only

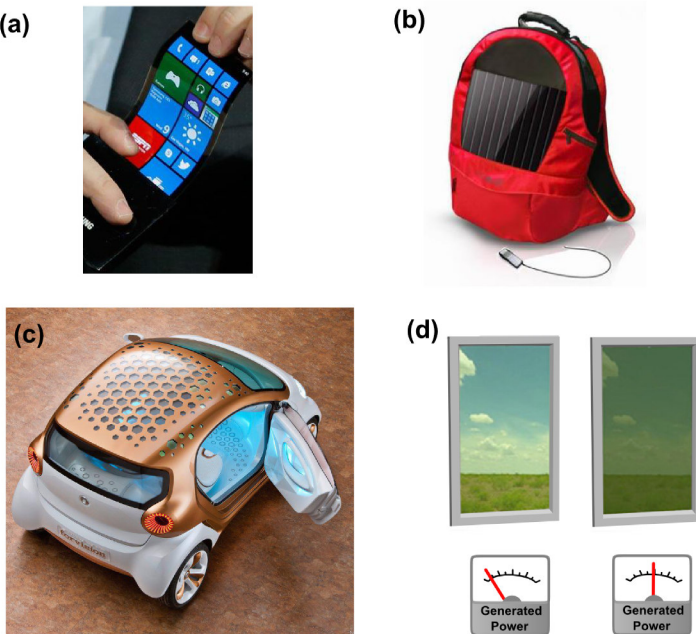


FIGURE 1.1: Examples of devices that exploit the advantages of organic semiconductors. Part (a) shows a flexible thin-film organic light-emitting diode (OLED) display that will not break if dropped (adapted from [1]), (b) shows a flexible lightweight solar cell integrated into a bag to charge devices on the move [2], (c) shows a car that uses lightweight transparent solar cells in the roof to cover a part of the car’s energy requirement. Furthermore, the car contains transparent white OLEDs in the ceiling (adapted from [3]). Part (d) shows transparent solar cells that have a tunable opacity and use the light adsorbed in the opaque state to generate power (adapted from [4]).

require thin films of material, making the devices lightweight. Additionally, the films of COMs do not have to be perfectly ordered. This makes the production cheaper. However the lack of perfect crystalline order also makes the production of flexible devices possible and allows the use of amorphous substrates such as glass. Furthermore, the order (and disorder) of the COMs can be manipulated by external fields. Careful material choice and construction allows us to manipulate the physical features of a device, such as transparency, conductivity and even morphology. I show a selection of devices that exploit these advantages in Fig. 1.1, and discuss some aspects in more detail in Sec. 1.1.

In this thesis we aim to support the creation and optimisation of such devices from a theoretical viewpoint. In order to understand the creation of the devices (and therefore predict procedures to optimise their performance), we create theoretical models of COMs and their interactions. These models are created such that we can study experimentally accessible length- and time-scales, focusing on structure formation during growth and self-assembly. In the modelling, we focus on materials that are promising concerning their application in devices. However before elaborating the scope of this thesis, I would like to present more background information on motivational aspects. In this introduction, I would first like to introduce the molecular systems and devices of relevance to the reader. Then I will introduce the fundamental physical aspects of the field of nano-molecules, where physics of both atomic and colloidal systems play a role. Next I will present the current *status quo* in experiment and theory, before finally outlining the scope of the thesis.

## 1.1 Materials and devices

**COMs.** The class of organic molecules that are of interest for semiconductor devices are so-called conjugated organic molecules (COMs).

A COM contains two or more atoms, with overlapping electronic p-orbitals. These overlapping orbitals form hybridised  $\pi$ -orbitals with delocalised electrons, which do not belong to a single atom or bond, but are delocalised across the whole group of atoms involved in the hybridisation. Conjugation typically occurs in atomic rings with alternating double and single bonds, such as aromatic rings. Through the delocalised electrons, the  $\pi$ -orbitals can easily respond to excitation and interact with the orbitals of other molecules and substrate materials. As a first estimate, the excitation's of COMs can be compared to the excitation of a guitar string: A longer guitar string has an excitation with a longer wave length. In analogy, a molecule with more conjugated bonds is excited by photons with a longer wave length (empirically described through the Woodward-Fieser rules [15, 16]<sup>1</sup>). Thus, each molecule has its own excitation spectrum, which depends on the composition and configuration of the molecule [17] as well as its neighbourhood [18, 19].

Figure 1.2 depicts examples of COMs that are commonly used in devices. It is taken from the review article of Hlawacek and Teichert [14]. The depicted examples include molecules with a fully 3D structure (e.g. Alq<sub>3</sub>), approximately 2D molecules (e.g. H<sub>2</sub>P), approximately 1D molecules (e.g. 6P) and molecules that can be approximated as zero-dimensional objects (C<sub>60</sub>).

---

<sup>1</sup>Note that COMs are significantly smaller than the wave-length of the light that they adsorb. The Woodward-Fieser rules are based on the fact that electro-magnetic oscillations with smaller frequencies are better suited to excite larger systems of delocalised electrons.

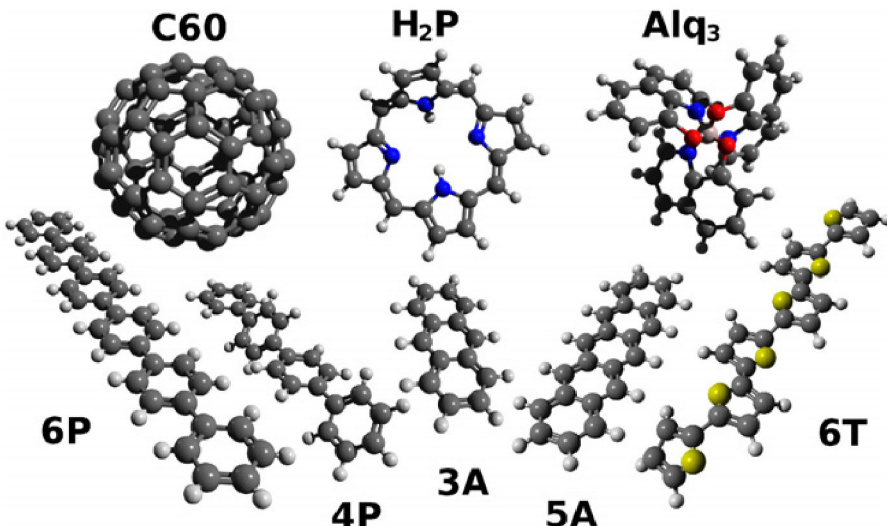


FIGURE 1.2: Select COMs used in semiconductor devices. This image contains depictions of Sexiphenyl (6P), Buckminster Fullerene (C<sub>60</sub>), Quaterphenyl (4P), Porphyrin (H<sub>2</sub>P), Anthracene (3A), Pentacene (5A), Tris(8-hydroxyquinoline)aluminium (Alq<sub>3</sub>), and Sexithiophene (6T). Black atoms represent carbon atoms, white represents hydrogen, yellow represents sulphur, red represents oxygen, blue represents nitrogen and pink represents aluminium. This figure is taken from Ref. [14].

Interactions of one COM with other COMs or any other substance alters the energetics [20–22] and therefore the excitation spectrum. As a result, we can choose and manipulate the energetics of our device through careful choice of materials, as well as the grown or self-assembled configuration of the molecules. If an inconvenient configuration is assembled, devices will be inefficient, even if the best-suited molecules are chosen [23]. Similarly, other features of device functionality, such as electron transport and charge carrier mobility, depend on the configuration of the molecules[14, 24] (see Fig. 1.3). Desired configurations of COMs include ultra-thin crystalline films [25], islands and crystallites [26], and nanowires [27], in which the molecules may lie or stand [28].

The COMs studied in this thesis are chosen around opto-electronic applications. Thus, I will briefly discuss two opto-electronic systems, OLEDs and organic photo-voltaics (OPVs), and show why the molecular self-assembly and growth studied in my thesis are significant for the efficiency of these devices.

**Organic light-emitting diodes (OLEDs).** Currently OLEDs are primarily used in displays. When compared to the common liquid crystal displays (LCDs), OLEDs have many advantages, e.g.

- the displays are thinner,
- the response time is significantly shorter and
- the contrast is better.

The main disadvantage of OLEDs currently is their reduced life-time, as organic molecules and their structures are vulnerable when exposed to heat or high energy.

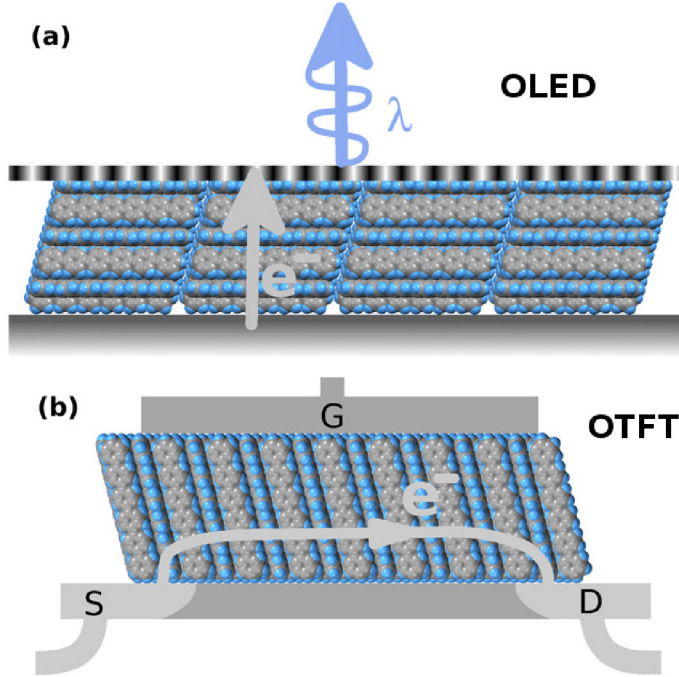


FIGURE 1.3: Sketch of the optimal configuration of 6P molecules in different devices. (a) In an OLED alignment of the long molecular axes within the plane described through the thin film is optimal. (b) In an OTFT the long axes are perpendicular to the thin film. This figure is adapted from Ref. [14].

Typically, OLEDs consist of a COM-based emitter layer, sandwiched between metal or metal-oxide electrodes [29]. The COMs of the emitter-layer are chosen specifically for their emission spectrum, where the wide variety of COMs allows the construction of virtually any colour of OLED [30, 31]. As a single COM is sufficient to generate OLED-photons, OLEDs do not require a mono-crystalline structure (while inorganic LEDs do). This means that OLEDs can be used in flexible thin-film devices [32], but also means that they require less perfection in the production [29], making them cheaper. However, it also means that they are normally not as efficient.

As device performance approaches the theoretical limit, research needs to expand from materials to their orientation and morphology to further increase performance [33]. For OLEDs a horizontal molecular orientation (sketched in Fig. 1.3) enhances both the charge transport and the light emission along the short molecular axis [33]. This enhancement is mediated through the overlap of the  $\pi$ -orbitals of neighbouring layers, which allows charges to flow through the overlapping orbitals, while the transition dipole moments that lead to light emission are aligned with the long axis of the molecules. As dipoles radiate most strongly perpendicular to the dipole moment, the light emission of OLEDs is maximised through a horizontal orientation of the COMs within the emitter layer [34].

Commonly, the COM-layer of OLEDs is slowly grown in vacuum, in order to enable the molecules to form ordered structures. The resulting structure can be manipulated by changing temperature, adsorption rate, substrate, etc. . However, the underlying physics during growth and self-assembly is little understood. In part III of this thesis, I contribute to the theoretical understanding and prediction of the collective ordering, by studying the collective ordering of the anisotropic COM 6P during self-assembly and growth.

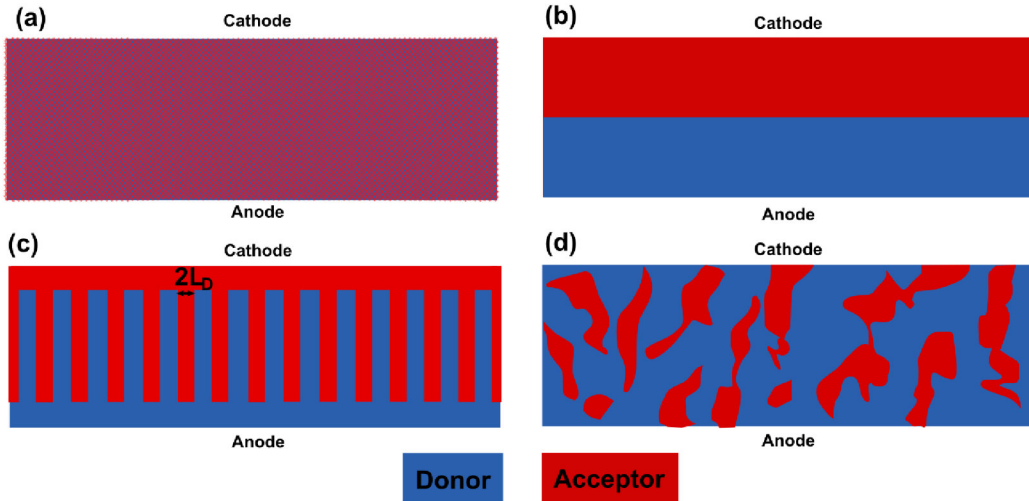


FIGURE 1.4: Cross-section through different bulk hetero-junction configurations. (a) is a homogeneous mixture of donor and acceptor, (b) is a two-block-configuration, (c) has comb-like interlinked domains and (d) has randomly distributed domains. This image is adapted from Scharber *et al.* [35]

**Organic Photo-voltaics (OPVs).** Organic photo-voltaics usually use the advantages of COMs to create flexible thin film solar cells that can be made transparent or colour-tunable. Thin films of COMs are sufficient to adsorb most of the light intensity because of their high opacity. Currently, however, OPVs struggle with low efficiency [36] and short lifetimes [37]. The low efficiency arises from two challenges [35]: first, excitons need to dissociate into electron-hole pairs, and second, the electron-hole pairs need to be extracted from the COM-matrix before they recombine. Using two materials with different charge affinities helps split excitons at their interfaces [36]. The resulting structures are called bulk hetero-junction organic solar cells.

The two components of bulk hetero-junctions are called donor and acceptor molecules. In many systems, Buckminster Fullerenes ( $C_{60}$  molecules) and their derivatives are used as acceptor molecules because of their high electron affinity [35, 36, 38]. I mention this specific material system here, because I will later use  $C_{60}$  as a sample system in my studies of COM growth in part II of this thesis.

The charge extraction is greatly increased if the donor-acceptor interface is within the diffusion length of the exciton, as the interface aids the charge separation in the system [35]. However, charge- (and exciton-) transport are optimal within domains of one material. So the optimal configuration of the bulk hetero-junction is a compromise between large connected areas and large contact surfaces between the two types of COMs. Examples of possible configurations are depicted in Fig. 1.4. Sub-figure 1.4 (a) depicts a fine mixture, which has large contact surfaces but small connected area. In contrast, the bi-layer depicted in Fig. 1.4 (b) ensures high charge transport but has a small contact surface. The interlinked combs depicted in Fig. 1.4 (c) are the optimal configuration [39], however most bulk hetero-junctions have a configuration somewhat like Fig. 1.4 (d). The interrupted domains in Fig. 1.4 (d) make charge transport difficult, reducing the device efficiency.

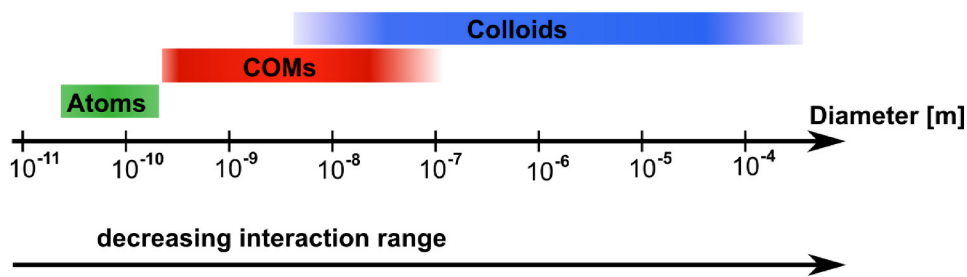


FIGURE 1.5: Typical diameter of different material systems: atoms [43, 44], COMs [45–47] and colloids [48].

These considerations, as well as recent experimental results, have shown that the details of the morphology [38, 40, 41] and orientation [38, 42] of the COMs in solar cells have a significant influence on the device efficiency. Here, theoretical understanding of the morphology during growth, as well as the underlying energetics and principles, may be the missing link for competitive device efficiency.

## 1.2 Theoretical consideration: systems between Atomic and Colloidal length-scales

### 1.2.1 Typical length-scales

From a theoretical viewpoint, COMs fill the interesting intermediate length-scale between the very well studied atomic [43] and colloidal length-scales [48]. Figure 1.5 sketches different typical length-scales to give a first impression.

For completeness, I list typical ranges:

- **Atoms.** The van-der-Waals radius of main-group elements ranges from  $1.1 \cdot 10^{-10}$  m (Hydrogen) to  $3.43 \cdot 10^{-10}$  m (Caesium) [43]. Note that typical covalent single bond diameters can be as small as  $6.4 \cdot 10^{-11}$  m (Hydrogen) [44].
- **COMs.** The next larger length-scale is bridged by COMs, where small molecules such as single aromatic rings have a van-der-Waals radius of  $4.65 \cdot 10^{-10}$  m [45]. If pure carbon structures with conjugated orbitals, such as carbon-nano-tubes, are seen as COMs, then COMs can be up to  $\mathcal{O}(10^{-5}$  m) long [46]. Otherwise the radius of gyration of large polymer chains is a reasonable upper limit, which yields a approximate diameter of up to  $\mathcal{O}(5 \cdot 10^{-7}$  m) [47].
- **Colloids.** Colloids are commonly expected to have diameters in the range of  $\mathcal{O}(10^{-9}$  m) to  $\mathcal{O}(10^{-4}$  m) [48]. There is some overlap between COMs and colloids. Especially in systems of particles larger than  $\mathcal{O}(10^{-8}$  m), COMs may be modelled as colloidal particles if the physics studied is less device oriented than fundamental (see, e.g. the chapter on modelling star polymers as ultra-soft colloidal particles in ‘Progress in Colloid and Polymer Science 115’ [49]).

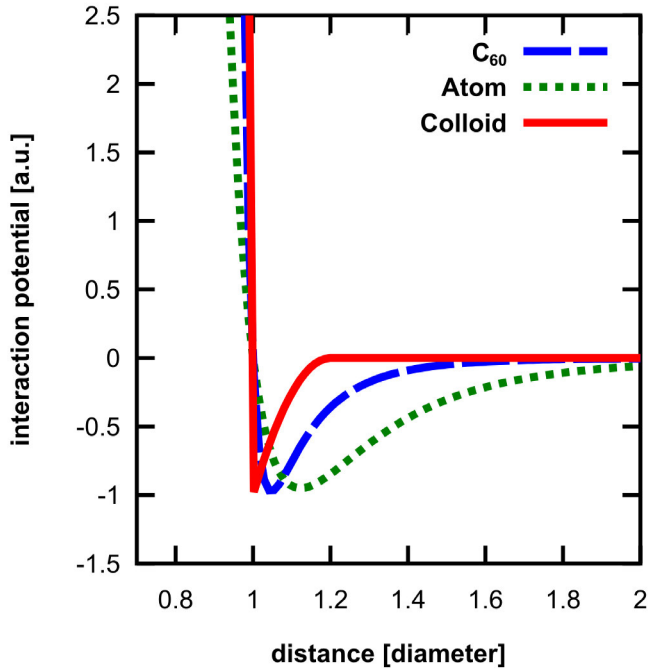


FIGURE 1.6: Pair interaction potentials for atoms [50], C<sub>60</sub> molecules [51] and colloids [52, 53]. The colloidal pair interaction results from solvent depletion, where the solvent diameter is 20% of the colloid diameter. All interactions are normalised to a potential depth of 1 and a repulsion range of 1 particle diameter.

### 1.2.2 Influence on interactions

The differences in size (shown in Fig. 1.5) have an influence on the range of non-electrostatic interactions shown in Fig. 1.6. Note that all interactions are scaled to the same well depth and the particle diameter, since this is the length-scale that they are significant for. The absolute value of potential minimum of C<sub>60</sub> is  $V^{C_{60}}|_{\min} = V(1 \text{ nm}) \approx 0.28 \text{ eV}$  [51, 54], while the potential minimum of carbon is  $V^C|_{\min} = V(0.39 \text{ nm}) \approx 0.003 \text{ eV}$  [51]. Absolute values for colloidal systems cannot generally be given, because they depend crucially on the colloidal and solvent particles and particle densities used.

In Fig. 1.6, I use the molecule C<sub>60</sub> as a prototypical COM. The molecule C<sub>60</sub> is spherical, stable and quite well understood, which makes it a unique prototype for direct comparison to spherical colloids, as well as atoms. However, similar considerations are possible for other COMs.

The three pair-interaction potentials depicted in Fig. 1.6 are standard models for particle-particle interactions and are commonly used in theoretical descriptions of the respective material systems.

**Atomic interaction.** The non-electrostatic interaction between two atoms is mediated through van-der-Waals attraction as well as Pauli-repulsion. These are commonly modelled through a 12,6-Lennard-Jones potential [50]

$$V^{\text{Atom}}(r) = 4\epsilon^{\text{Atom}} \left[ \left( \frac{\sigma^{\text{Atom}}}{r} \right)^{12} - \left( \frac{\sigma^{\text{Atom}}}{r} \right)^6 \right], \quad (1.1)$$

where the potential well depth  $\epsilon^{\text{Atom}}$  and the Lennard-Jones radius  $\sigma^{\text{Atom}}$  are material-specific. The radius  $\sigma^{\text{Atom}}$  defines the distance at which

$$V^{\text{Atom}}(\sigma^{\text{Atom}}) = 0. \quad (1.2)$$

**Molecular interaction.** The non-electrostatic interaction between two  $C_{60}$  molecules is modelled through the Girifalco potential [51]. In this model, Girifalco describes each  $C_{60}$  molecule as a sphere with a uniform surface density of carbon atoms [51]. The Lennard-Jones potential Eq. (1.1) of these uniformly distributed atoms is then integrated over the surfaces of two  $C_{60}$  molecules to determine their interaction. Based on this expression, the following potential can be used to describe  $C_{60}$ - $C_{60}$ -interaction (see Ref. [54] and references therein)<sup>2</sup>

$$V^{C_{60}}(r) = \frac{\epsilon^{C_{60}}}{34} \left[ 9 \left( \frac{1.047\sigma^{C_{60}}}{r} \right)^{43} - 43 \left( \frac{1.047\sigma^{C_{60}}}{r} \right)^9 \right]. \quad (1.3)$$

Here, accordingly  $\epsilon^{C_{60}}$  is related to the potential well depth and  $\sigma^{C_{60}}$  is the radius. As Fig. 1.6 shows, the attractive interaction of two  $C_{60}$ -molecules is noticeably shorter than the attractive interaction of two atoms (relative to their radius).

**Colloidal interaction.** Finally, as particle size further increases, most colloidal particles (with a diameter  $\geq \mathcal{O}(10^{-7} \text{ m})$ ) have very short-range attractive van-der-Waals interactions (when compared with their diameter) and are commonly modelled exclusively through their hard core. However, colloidal particles are commonly studied in a solvent. For colloidal particles in solvent, the solvent particles cause an additional attractive force: The area between two colloidal particles is depleted of solvent particles (for purely geometrical reasons). This depletion causes an osmotic pressure that leads to an effective attraction of the colloidal particles. From the geometry of the system, an expression for the depletion interaction with hard-core repulsion was derived by Asakura and Oosawa [52, 53], discussed in detail in the book of Lekkerkerker and Tuiner [60].

$$V^{\text{colloid}}(r) = \begin{cases} \infty & \text{if } r < \sigma^{\text{colloid}} \\ -P \frac{4\pi}{3} \left[ 1 - \frac{3}{4} \frac{r}{R_d} + \frac{1}{16} \left( \frac{r}{R_d} \right)^3 \right] & \text{if } \sigma^{\text{colloid}} \leq r \leq 2R_d \\ 0 & \text{otherwise} \end{cases} \quad (1.4)$$

<sup>2</sup>The potential given in Eq. (1.3) is an approximate form given to aid intuition, as the full potential derived by Girifalco has a less intuitive form that includes more summands, as well as poles for  $r \neq 0$  [51]. Our approximate form is widely used and correctly reflects the shorter interaction range of the full Girifalco potential [54–57]. However, other approximate forms exist [58, 59] and the details of the form are known to have very little influence on the phase behaviour as long as they are sufficiently short-ranged [57, 58].

In this expression  $R_d = \sigma^{\text{colloid}}/2 + \sigma^{\text{solvent}}/2$  is the depletion radius,  $\sigma^{\text{colloid}}$  is the colloidal diameter,  $\sigma^{\text{solvent}}$  is the solvent diameter and  $P$  is the pressure. Typically, the solvent particles are significantly smaller than the colloidal particles, i.e.  $\sigma^{\text{colloid}} \gg \sigma^{\text{solvent}}$  [61]. To illustrate an upper limit of the depletion attraction range, we use  $\sigma^{\text{solvent}} = 0.2 \cdot \sigma^{\text{colloid}}$  in Fig. 1.6.

Note that the range of systems still considered as colloidal depends somewhat on the author. Most authors speak of colloidal systems when their application is a system of solid or liquid particles of diameters  $\geq \mathcal{O}(10^{-7} \text{ m})$  in a liquid solvent. However, some authors also consider particles of the size of C<sub>60</sub> as a colloidal length-scale, which is then often called nano-colloidal.

### 1.2.3 COMs between atomic and colloidal length-scales

We expect a significant influence of interactions on phase-behaviour, self-assembly and growth of COMs. This expectation is based on other system types, where we know that the interaction between different types of building blocks are fundamental in understanding both the equilibrium phases [62] and structures, as well as the non-equilibrium behaviour [63].

For our prototypical system C<sub>60</sub>, literature reports a phase behaviour that reflects both aspects of atomic, and colloidal systems.

Liquid phases are associated with the long-ranged attraction of atomic systems [64] and not all colloidal systems have liquid phases. So far no stable equilibrium liquid phase for C<sub>60</sub> has been found experimentally [65]. Theoretical predictions disagree concerning the existence of a liquid phase [58, 65, 66], however they agree on the fact that if it exists, then it can only exist in a very narrow temperature range [54]. Instead of a liquid phase, C<sub>60</sub> is known to form a gel-phase [67]. These are commonly associated with systems with short-range attraction such as the depletion interactions of colloidal systems [64, 68].

In contrast to larger colloidal systems, C<sub>60</sub> does not require a solvent to display significant phase behaviour [67] and can be grown into solid structures even in ultra-high vacuum [69]. The solvent-free non-electrostatic interactions between C<sub>60</sub> molecules make it very atom-like. Its phase diagram is not dependent on any other materials (i.e. the solvent particles), as is commonly the case for colloidal systems [70].

As a further interesting atom-like detail, the hybridised orbitals of C<sub>60</sub> form hollow molecular orbitals that resemble atomic orbitals [71].

Some of these features, such as the atom-like orbits, are specific to C<sub>60</sub>. However, the majority of the observations for C<sub>60</sub>, such as the influence of the short interaction range in absence of solvent particles, are also expected to influence the behaviour of other COMs. Furthermore, the interesting equilibrium phase immediately poses the question how the interactions influence non-equilibrium behaviour such as growth. And how do they compete with other and longer-range interactions such as electrostatic interactions? These questions form the fundamental theoretical basis for our research and will arise throughout the thesis.

## 1.3 Experimental status quo

One common procedure to generate and study molecular configurations in thin films uses organic molecular beam epitaxy (OMBE) [72]. This is a procedure in which molecules are deposited on a substrate at a fairly small deposition rate (small enough for them to diffuse once on the surface) in ultra-high vacuum. The resulting films are usually smooth, highly ordered thin films, which leads to a better performance [73]. Though particles have time relax to some degree, the structures generated through OMBe or other deposition procedures are (non-equilibrium) grown structures [74]. Therefore it is crucial for us to understand both growth processes and equilibrium configurations on a microscopic (molecular) level.

In experiments, different approaches are required to gain insight into surface morphology and molecular ordering on different time and length-scales. The following underlying principle holds true: the smaller the time and length-scales are, the harder measurement is. In this section, I introduce different experimental approaches for different regimes.

### 1.3.1 Static surface structure, molecular ordering and morphology

Measurements of relaxed structures are ideal to get a first insight into a system. Note the choice of the word ‘relaxed’. The structures that I refer to here are commonly grown using some non-equilibrium approach such as OMBe [28, 75], and then relaxed until the surface no longer changes. This can result in different structures despite the same relaxation conditions (i.e. relaxed at the same temperature, layer coverage, pressure, etc.). If two structures are grown in two different conditions, but relaxed in the same condition, they can be markedly different [28]. The difference indicates that probably at least one of the structures is not equilibrated, but caught in kinetic arrest. Thus I will call structures that were grown and then relaxed until they no longer changed ‘relaxed’ unless there are clear indications for true equilibration.

As a rough categorisation, all morphology measurement approaches either directly measure or scan the real-space surface or scatter light or particles of some energy and therefore measure the reciprocal space of the surface.

**Real-space measurements.** Needle-based real-space measurements such as atomic-force-microscopy [28, 76, 77] and scanning-electron-microscopy [22, 78] measure a direct representation of the surface area that was scanned. These real-space measurement approaches can also be used to gain insight into the surface morphology on a larger scale [28, 77], such as the study of cluster sizes, shapes and the orientational ordering within such clusters [79]. As the surface of most systems does not change much in the relaxed state, slow high resolution measurements can resolve the surface on a single-molecule level [80] and the orientation of individual molecules [22, 81].

**Reciprocal-space measurements.** These include X-ray scattering [82–84] and electron scattering [85]. Essentially, the different scattering methods are used because they are sensitive to different length-scales. Thus, X-ray scattering is used to determine the macroscopic morphology such as the cluster density, but is especially well suited to extract information on several material layers such as the layer filling fraction [75, 84] and multilayer molecular order [86]. On the other hand, low energy electron diffraction is sensitive only to the topmost molecules. It is used to study both the periodicity and defects in the periodicity of surface structures (for example molecular ordering, step-edges, and islands) [85].

All reciprocal space imaging techniques contain information that is averaged over the entire illuminated area of the probe, such as the average crystal ordering, the average crystallinity, or the average layer filling fraction. In order to extract more detailed information such as an island size distribution from reciprocal measurements, assumptions have to be made (e.g. about the island morphology and ordering).

Commonly reciprocal and real-space methods are combined — often with theory — in order to make more complete statements on the morphology and order on and in relaxed surfaces [84].

### 1.3.2 Time resolved growth measurements

The majority of real-space surface methods interfere with particle adsorption on the surface, by casting a ‘shadow’ on the surface and through particles adsorbing to the tip of the microscope. While real-space atomic-force image sequences of growth exist, they are commonly measured by interrupting the growth and extracting the substrate from the growth chamber for each measurement [87]. Thus, each image in such a sequence displays a surface structure that is relaxed to some extent. This structure may differ considerably from the growth structure, as is known e.g. for material combinations that dewet, such as copper on silicate [88], or organic molecules on silicon [89].

The most reliable real-time in-situ measurement approaches are non-invasive approaches, without relaxation phases. These conditions are primarily satisfied by reciprocal space measurements (electron diffraction [90] and X-ray scattering [82, 83]). These approaches only give us average information about the surface and the morphology and they have a restricted time resolution  $\mathcal{O}(10^{-1}\text{ s})$  [91]. For example, in X-ray scattering, the time resolution is restricted through the luminosity of the source as well as the scattering intensity of the surface. Low surface coverages lead to a low scattering intensity, so the scattered signal needs to be integrated for a long time to obtain reasonable statistics on the measurement. Challenges such as weak signal intensities mean that even in scattering approaches, time resolved measurements of the initial stages of sub-monolayer growth are difficult to obtain [74, 75].

Here, the combination of experiment and simulation promise insight into the real-time real-space surface during growth, as well as insight into experimentally hard to access time scales.

### 1.3.3 Measurements of single-particle dynamics

Similarly, measurements of single-particle dynamics on a surface are experimentally very difficult to gain and are a promising field for the collaboration of experiment and theory. So far no experiment is capable of resolving single-particle dynamics for a COM adsorbed to some substrate at room temperature. The reason lies in the time scales involved: at room temperature single molecules move too quickly for them to be resolved by the minute-time-frame of atomic-force measurements [92] and are challenging for other microscopic measurements such as scanning tunnelling microscopy [91, 93].

If the motion of single adsorbed particles is slowed down, single-particle trajectories can be traced with real-space imaging. Particle motion can be slowed down by increasing the size of the particle, for example by considering colloidal particles instead of molecular particles [94]. Slowing down can also be achieved by cooling down the particle [95], or choosing materials with slow dynamics [96] or large domains [22, 81]. These approaches give some insight into the underlying behaviour, however they are still far from the temperatures and materials required for device manufacturing.

For reciprocal measurement techniques the scattering intensity of a single molecule is so small that it is hard to detect. Accordingly, reciprocal-space approaches need to use high luminosities, that excite or even destroy the molecule [74, 97, 98]. Reciprocal-space approaches can be used to obtain snapshots of individual molecular configurations (potentially with variable time delay to a first, weaker pulse that triggers a reaction)[97] but no full molecular trajectories.

Thus, the single-particle dynamics of most COMs at room temperature can currently only be studied in theoretical approaches.

## 1.4 Theoretical modelling approaches

From a theoretical point of view, there is a variety of approaches that can be taken to understand and predict self-assembly and growth of COMs. They differ in the length- and time-scales that they are best adapted for, as well as the accuracy with which they treat a system (see Fig. 1.7).

**Density functional theory (DFT).** On the level of a single molecule or a few crystal unit cells, DFT is commonly used to determine interaction and excitation energies at the level of molecular orbitals [100]. In DFT, the position-dependent electron density is determined by solving an approximation of the Schrödinger equation. Using the electron density, the system can be relaxed into its minimal-energy configuration under any given constraint. Using the orbital information as well as the energies and minimal configurations, various observables of the studied system can be extracted. Here, I list examples from literature that are specific to one of my sample systems, the molecule 6P (see Fig. 1.2). Similar calculations can be found for a broad variety of COMs.

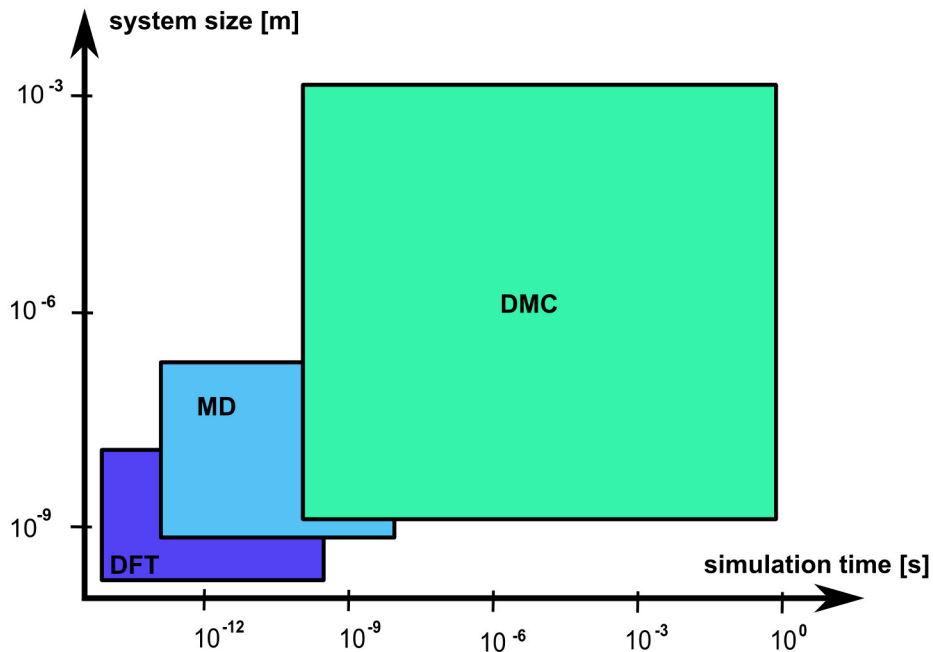


FIGURE 1.7: Sketched length and time scales for different modelling approaches: density functional theory (DFT), atomistic molecular dynamics (MD) and Dynamic Monte-Carlo (DMC). This image is based on an image by Kratzer [99].

In systems with one or several COMs, DFT is often used to determine the highest occupied molecular orbital (HOMO) and lowest unoccupied molecular orbitals (LUMO) [101] and their energetics. Additionally, DFT is used to determine energetics at a single-molecule level such as binding energies, diffusion energy barriers and rotation energy barriers [100]. As COMs deform when diffusing across a material edge, DFT can also be used to relax the COM at each intermediate position and determine the energy change associated with the conformational change [102]. However, it is a challenge to treat more than a few molecules [19] and surface unit cells using DFT [100], and the accessible times are very small [103].

**Molecular dynamics (MD) simulations.** The next length-scale is commonly treated using MD, mostly atomic resolved MD. In this simulation approach, all atoms of each molecule are treated explicitly and their interaction is treated using classical force fields. Our example-system 6P has been modelled both in a bulk crystal [104, 105] and in the context of organic-organic hetero-surfaces [22, 106]. Furthermore, the self-assembly of 6P molecules in simulated annealing, including all the phases that the system traverses, were treated using atomistic MD [105]. Atomistic MD is commonly limited to several 10s or 100s of COMs. Additionally, the majority of atomistic MD simulations can cover not much more than nanoseconds [105, 107].

Atomically resolved MD can serve as input for coarse-graining molecular interactions [108]. These can be used to develop models for coarse-grained MD [109] and MC simulations [110]. For non-equilibrium studies of coarse-grained systems, dynamic MC methods present an efficient approach to calculating the real-space surface.

**Dynamic Monte-Carlo (DMC) simulations.** DMC simulations give access to the large length and time scales without loosing the information of position and, if required, orientation of each molecule at each point in time [73]. Note that I denote all rate-based MC simulations as ‘DMC’, where Kinetic Monte-Carlo (KMC) is one specific DMC algorithm (various notations exist in the literature). All DMC simulations are based on rates of physical processes, while standard MC simulations are based on probabilities of configurations occurring in configuration space. The details and implications of this difference will be discussed in Chap. 2. Here, it is important to know that DMC simulations describe a time evolution rather than an ensemble average.

The majority of systems studied using DMC simulations involve the growth of atomic structures [111–113]. Here, elaborate models have been developed that include various subtle phenomena during growth, such as direction-resolved step-edge diffusion [114, 115], concerted gliding [116, 117] or even shearing of islands [117].

Only in the recent past have DMC approaches also been applied to COMs. As the atomic simulations are easily expanded to systems of spherical COMs, several studies focus on the spherical molecule C<sub>60</sub>. Previous to our studies, these simulations were restricted to sub-monolayer growth of C<sub>60</sub> [69, 118].

In our studies of C<sub>60</sub> growth, we have shown that DMC simulations with coarse-grained models of COMs give access to large time- (minutes) and length-scales (micrometres) of real-space growth. For the first time in literature, we have found a full set of parameters that describe multilayer growth of C<sub>60</sub> for different temperatures and adsorption rates [119]. Using these simulations, we are able to understand the details of experimentally observed growth, obtain real-time evolution of the surface morphology and study the similarities and differences between atomic systems [120], C<sub>60</sub>, and colloidal systems. Our studies scale both single-molecule trajectories, and the growth of many layers, studying the details of the particle-morphology interplay. Unravelling the details of competing time scales, we are able to fundamentally understand multilayer growth of C<sub>60</sub> on a broad set of length and time scales, and to predict experimental results.

Unlike the approximately isotropic COM C<sub>60</sub>, the majority of COMs are anisotropic. For these material systems, collective orientational ordering during growth provides a major challenge. Few approaches for growth simulations of anisotropic COMs exist in literature. For some questions, the anisotropy of molecules can simply be neglected [121, 122]. In other systems, the molecules are modelled by strings that occupy multiple lattice sites on a square lattice [73, 123, 124]. Studies that consider continuous rotational degrees of freedom, mostly restrict them to 2D [123, 125]. However, it is established that the orientational degrees of freedom influence the mobility [100, 126] and that systems such as 6P on Zn(10-10) show complex orientational ordering [28, 79, 100]. No simulation approach exists so far in the literature, that gives insight into the full 3D orientational ordering of anisotropic COMs during growth. Besides the lack of DMC algorithms that can handle continuous 3D rotational degrees of freedom, there also is a lack of suitable coarse-grained models of our representative material system [6P on Zn(10-10)].

In order to face this challenge, a novel simulation approach had to be developed, that allows DMC simulations with continuous 3D rotational degrees of freedom. Furthermore, results from experimental [28, 79, 100] and theoretical studies [100, 105, 106] were used to find an

empirical model for our representative material system 6P on ZnO(10-10). The model includes a number of features that are generic for COMs, making the understanding obtained from it fundamental for the growth of a broad variety of material systems [127].

Using this model, we explain the collective orientational ordering of COMs both in equilibrium and during growth and find growth behaviour of monolayers that is long-debated in the experimental community [128, 129]. Combining the insight from both isotropic and anisotropic COM growth, we provide new understanding on the field of molecular growth. We gain insight into the growth behaviour between atoms and colloids, understand collective ordering of large systems and further the methods in the field of growth simulations.

## 1.5 Scope of the thesis

In order to cover all of the content listed above, the thesis is split into four parts. Part I gives the general background to the growth of complex molecules. This includes an overview over materials, applications, and methods in Chap. 1. Then Chap. 2 discusses DMC methods and different algorithms, while Chap. 3 discusses all the theoretical background needed.

Part II treats the growth of isotropic COMs and specifically the multilayer growth of C<sub>60</sub>. Specifically, Chap. 4 introduces the molecule and the current understanding of C<sub>60</sub> growth, while Chap. 5 contains a brief description of the experiment, as well as a discussion of modelling details that are specific to C<sub>60</sub> growth. The theoretical observables are discussed in Chap. 6, before the results are discussed in Chap. 7. In particular Sec. 7.1 discusses the first minimal parameter set that allows the simulation of multilayer growth found in literature, and Secs. 7.2–7.2.2 discuss similarities and differences of C<sub>60</sub> and atomic/colloidal systems in detail. Part II closes with Chap. 8, which summarises the results obtained for isotropic particles in order to expand our studies to anisotropic particles in part III.

Part III deals with anisotropic COMs, and also focuses on structured substrates. Hybrid systems consisting of an inorganic substrate with a growing layer of anisotropic COM molecules are introduced in Chap. 9. Here, the theoretical background has two new aspects that require a detailed discussion: the adaptation of DMC methods to continuous 3D rotational degrees of freedom and the introduction of an empirical model for our representative material system 6P on ZnO(10-10) (see Chap. 10). A new set of observables that includes the characterisation of collective ordering is introduced in Chap. 11, before Chap. 12 discusses the collective ordering both in equilibrium and during growth. The new empirical model reproduces the experimentally observed collective ordering both in equilibrium (see Sec. 12.1.1), but also has interesting new behaviour during growth (see Sec. 12.2), which are summarised in Chap. 13.

As conclusion, part IV gives an overall summary if growth and collective ordering of complex molecules on patterned substrates and mentions some potential further paths of research in this field (see Chap. 14).

## Chapter 2

# Simulation approach: Dynamic Monte-Carlo (DMC) simulations

As previously mentioned in Sect. 1.4, I use the term ‘Dynamic MC’ (DMC) to describe all rate-based MC simulations. I specify the terminology here, because a broad variety of terminology exists in literature and sometimes the same words are used to mean different things.

### 2.1 Motivation of DMC simulations

Conventional (not-dynamic) MC approaches are based on probabilities and are constructed to sample the configuration space of a given ensemble. For now we consider only the canonical ensemble (where particle number, volume and temperature are constant) and the conventional MC algorithm we discuss is the Metropolis MC (MMC) algorithm [130]. Here, changes to the current configuration are proposed (e.g. delete a particle at a random place and add a particle at another). The changes are then accepted (or rejected) with a probability determined from the Boltzmann distribution for energies between the two configurations  $p^{\text{MC}} = \max\{1, \exp(-(E_{\text{final}} - E_{\text{initial}})/kT)\}$ . Thus, MMC simulations sample configuration space. Through the Boltzmann weighting, the sampling primarily scans configurations that form the major contributions to the partition sum of the ensemble, i.e. MMC simulations form importance-weighted sampling of configuration space and the importance is measured through the relative probability of the configuration arising [130]. Note that MMC and related algorithms contain purely thermodynamic, no dynamic information [131]. They lack dynamic information in their transition probabilities because these are determined by comparing the free energy of initial and final configuration and do not contain any information on the path between these configurations.

Following the idea of Battaile and Srolovitz, DMC simulations can be seen as an expansion of MMC methods [132]. For kinetic phenomena, each change to the system must be associated to a rate with which this specific change occurs. For example, a particle moving from one place to another is associated to a diffusion rate. For this rate description, separation of time scales is commonly assumed, i.e. fast processes must take place on far shorter time scales, as they occur many times between events of slower processes [99]. In the example of a moving

particle, the time scales that are commonly separated are slow time scale of motion between potential valleys and the fast time scale of the particle motion within one valley. For more details on the separation of time scales, see Sec. 3.1.

If each algorithm iteration corresponds to a finite time and particle motion is restricted to physical processes, then a diffusing particle can only move a finite distance (or angle) in one algorithm iteration because of causality. They cannot reappear at an arbitrary position, contrary to particles in most MMC approaches. In the separation of time scales, each diffusion process is linked to a diffusion rate  $r^{\text{diff}}$ . The rate is connected to the probability  $p^{\text{diff}} = \Delta t r^{\text{diff}}$  for the diffusion process occurring after the time  $\Delta t$ . This rate contains information on the obstacles along the transition path between site of origin and site of destination; for example, it may contain the height of the energy barrier as a parameter. Using transition rates that are based on dynamical models of the physical phenomenon, the construction of DMC simulations allows us to use MC methods to simulate a plausible time-evolution of the system [133].

Commonly, transition rates are constructed in such a way that they fulfil local equilibrium conditions. For example, the transition rate from the microscopic state  $\sigma_a$  to the microscopic state  $\sigma_b$  is commonly expressed through an Arrhenius-type rate

$$r_{a \rightarrow b} \propto e^{-\frac{(E_a - E_{\text{saddle}})}{kT}}. \quad (2.1)$$

Here,  $T$  is the system temperature,  $k$  is the Boltzmann constant,  $E_a$  is the energy of state  $\sigma_a$ , and  $E_{\text{saddle}}$  is the energy at the saddle-point separating the states  $\sigma_a$  and  $\sigma_b$ . The above transition rate can fulfil local equilibrium conditions, i.e. detailed balance (see Sec. 2.2). Furthermore, Sec. 3.1 derives the transition rates for diffusion processes and discusses their implications in detail. If all rates in a DMC simulation fulfil local equilibrium, then the simulation approaches global equilibrium (i.e. the Boltzmann distribution) given enough time [134]. Such a simulation can be used to determine equilibrium ensemble properties. Additionally, such DMC simulations can render time-resolved system information in an equilibrated system, such as the dynamics of individual molecules [126], which are not accessible in MMC simulations without dynamic information.

However, most DMC simulations include processes that break local and global equilibrium. These processes are included in order to study a system outside equilibrium. In surface growth, such a process is particle adsorption: More particles adsorb than desorb. Once we include a net particle adsorption, there is a particle current that contradicts the equilibrium condition of no net currents in the system and breaks local and global equilibrium [134]. For the limit of no adsorption, the simulation goes back to an equilibrium simulation because particle adsorption is the only rate that breaks equilibrium.

We discuss the equilibrium condition ‘detailed balance’ in Sec. 2.2, before introducing a generalised description of a system evolution in Sec. 2.3.

## 2.2 Detailed balance

Detailed balance is a strict equilibrium requirement to the system and is commonly used as a condition for the equilibration of MMC and DMC simulations. It requires the transition

between every pair of states  $a$  and  $b$  to cancel out, i.e. there is no net probability flow from any state to any other state. Expressed in terms of the occupation of state  $a$   $\pi_a$  and the transition probability  $p_{a \rightarrow b}$ , detailed balance takes the form

$$\pi_a p_{a \rightarrow b} = \pi_b p_{b \rightarrow a}. \quad (2.2)$$

Using Eq. (2.1), we can examine the conditions for detailed balance for MC simulations of surface growth.

$$\frac{p_{a \rightarrow b}}{p_{b \rightarrow a}} = \frac{e^{-\frac{(E_a - E_{\text{saddle}})}{kT}}}{e^{-\frac{(E_b - E_{\text{saddle}})}{kT}}} = \frac{e^{-\frac{(E_a)}{kT}}}{e^{-\frac{(E_b)}{kT}}} = \text{const.} \quad (2.3)$$

If there is no particle adsorption, the ratio of any two transition rates in the system is constant. If the energy barriers are finite, then the ratio of state occupations will adapt to the ratio of transition rates and fulfil detailed balance. Correspondingly, the diffusion processes of particles on the surface can be expressed as a reaction network that fulfils detailed balance once it has relaxed and no influence of the initial condition remains. Detailed balance is a sufficient, though not necessary, condition for equilibrium [135].

Note that particle adsorption cannot fulfil detailed balance, because there is a net current of particles from the surrounding gas phase to the surface. Then the particle currents cannot cancel out. The net particle current to the surface clearly breaks equilibrium.

Systems that fulfil detailed balance automatically fulfil global balance (where all probability currents to and from a state are summed up and their sums need to be balanced), while the reverse is not always true [136, 137]. Hence, global balance is a necessary but not sufficient condition for detailed balance, because features such as internal circular currents fulfil global but not detailed balance. In DMC simulations, commonly processes such as particle adsorption are included, which break detailed balance. Such a the system is described through the evolution of the probabilities for which states  $\sigma$  occur. The description assumes the form of a master-equation [131], where the equilibrium solution that fulfils detailed balance is a specific steady state solution of the master-equation.

## 2.3 The underlying master-equation

Dynamic MC simulations describe the state of a system in a purely stochastic, non-deterministic manner. If all processes fulfil detailed balance, DMC simulations yield equilibrium results that correspond to the results of MMC simulations. However, DMC simulations usually include processes that break detailed balance, such as the adsorption of particles during surface growth.

In surface growth, it is assumed that in the free energy landscape particles vibrate around minima that are separated by large energy barriers [131]. ‘Large’ here assumes that the stochastic jumps across these energy barriers are associated with time scales that are much larger than the vibrational times of the molecules, i.e. the molecules lose all memory of their previous trajectory, and the system has attained quasi-equilibrium.<sup>1</sup> As a result of this description, each microscopic state  $\sigma$  depends only on spatial and time coordinates and does not contain any information on momentum.

---

<sup>1</sup>In other words, the system is in equilibrium within the length-scale of the potential well.

For the current consideration, we assume a system in which the state  $\sigma_i$  corresponds to an occupation of the lattice site  $i$ , and  $\sigma$  is a vector containing the states of all lattice sites. The assumption that only lattice sites are accessible is commonly used in growth simulations. Such growth simulations model spherically-symmetric particles confined to lattice sites that self-assemble without overhangs or defects [138–140]. Commonly, these assumptions are suited for growth of atomic systems [117, 141]. We study such a system in our analysis of C<sub>60</sub> growth in Part II of this thesis. Note that descriptions in which the state also contains information on particle orientation or other information can be constructed in an analogous manner, as will become apparent for the collective ordering of anisotropic particle that we study in Part III.

If  $\sigma$  contains the states of all lattice sites  $i$ , then  $\sigma$  is observed with a probability density function (PDF)  $P(\sigma)$  [131]. The temporal evolution of this PDF is then described by the probability of any different state  $\sigma'$  changing to the state  $\sigma$ , as well as the probability of the state  $\sigma$  changing to any different state  $\sigma'$ . Expressed in terms of a master-equation, this expression becomes [131, 133].

$$\frac{dP(\sigma)}{dt} = \sum_{\sigma', \sigma' \neq \sigma} G(\sigma' \rightarrow \sigma) P(\sigma') - \sum_{\sigma', \sigma' \neq \sigma} G(\sigma \rightarrow \sigma') P(\sigma), \quad (2.4)$$

where  $G(\sigma' \rightarrow \sigma)$  denotes the element of the transition matrix describing transition from state  $\sigma'$  to state  $\sigma$  [131]. The system (physical) time is given as  $t$ .

If each state  $n_i$  corresponds to the occupation of site  $i$ , then we can rewrite the master-equation to a difference-differential equation [131]

$$\frac{d}{dt} n_i = \sum_j r_{ij}^+(\mathbf{n}) - \sum_j r_{ij}^-(\mathbf{n}), \quad (2.5)$$

where  $\mathbf{n}$  is the vector counting site occupation.

This difference-differential equation contains all processes  $j$  that lead to the addition or deletion of a particle at site  $i$ . Then  $r_{ij}^+$  is the transition probability of process  $j$  that leads to the addition of a particle at site  $i$  and  $r_{ij}^-$  is the transition probability of process  $j$  that leads to the deletion of a particle at site  $i$ . Note that in DMC literature, the transition probability is the same as the process rate [131]. Furthermore, the adsorption processes are among the elements of  $r_{ij}^+$  and that Eq. (2.5) describes the full evolution during surface growth (under the given approximations).

While the master-equation, Eq. (2.4), is deterministic, the high number of dimensions in the system renders an analytic solution impossible in all but the most minimal systems [131]. Here, DMC simulations become important since they find a numerical solution to Eq. (2.5) [131] efficiently. In principle, DMC simulations render exact solutions to the master-equation systems [114, 142], since they account for all included stochastic processes correctly. Any error in the configurational ‘solution’ stems either from excluding relevant processes from the simulation, or from a faulty basic assumption of all processes being truly Markovian. Algorithm-wise, there are two approaches to DMC simulations. In one approach the system is propagated by a constant time step  $\Delta t/n$  every iteration, where  $n$  is the number of currently possible processes (Constant-time-step simulation). In the other the system and clock are updated only after an event truly happens (Event-driven approach). These two approaches

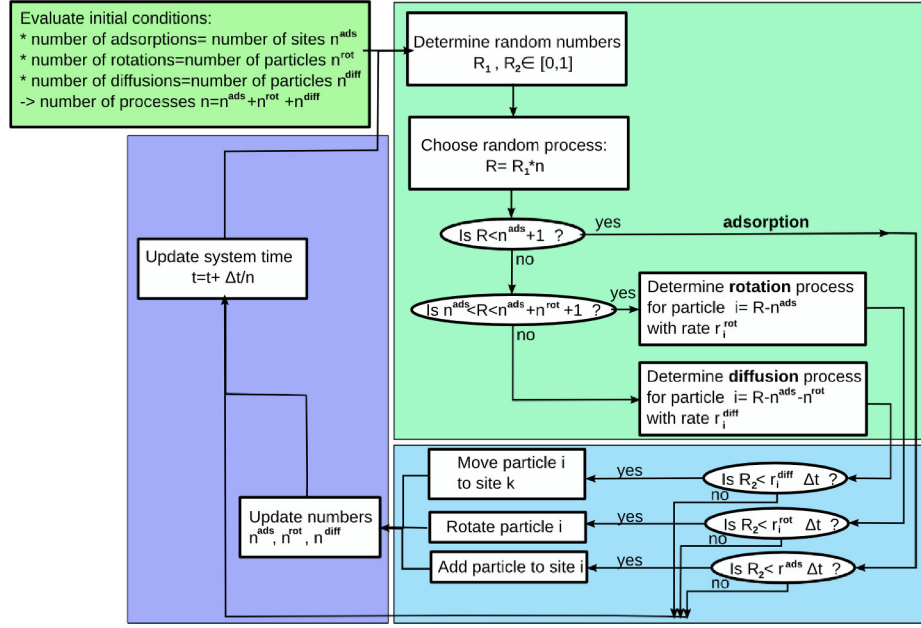


FIGURE 2.1: Fundamental decision sequence for a constant-time-step DMC simulation of surface growth. This is one possible basic form of an algorithm structure, note that more refined algorithms exist in literature [133, 143, 144].

form the basis for the majority of algorithms used in literature. In this thesis, we use an event-driven algorithm introduced in Sec. 2.5, as well as a hybrid form introduced in Sec. 2.7.2. However, in order to understand and verify the hybrid algorithms discussed in Sec. 2.7, we first introduce the constant-time-step algorithm in Sec. 2.4 and compare it to the event-driven algorithm in Sec. 2.6.

## 2.4 Constant-time-step simulations (RSM)

The constant-time-step DMC simulations have an algorithm quite close to the equilibrium-MMC algorithms, as was discussed in Sec. 2.1 [131, 132, 145]. However, in a general formulation, the constant-time-step DMC simulations can include non-equilibrium processes such as adsorption. As in constant-time-step DMC simulations, an attempted process is selected randomly. I will refer to constant-time-step DMC simulations as the Random Selection Method (RSM). However, not all RSM algorithms use constant time steps, we discuss some variants in Sec. 2.7.

In Fig. 2.1 we present an example of a decision sequence in the algorithm for surface growth simulated using the RSM. The fundamental processes available in this example are adsorption, rotational diffusion (called rotation) and translational diffusion (called diffusion). In each iteration, one process is attempted, accepted or rejected according to the relative size of the process rate, and then the system clock is updated. Thus, the first random number  $R_1$  is used to choose the attempted process type (adsorption, rotation or diffusion), as well as the site/particle of the attempted process. One or several additional random numbers may be used if the process type is ‘rotation’ or ‘diffusion’, in order to determine the diffusion direction

or the rotation angle <sup>2</sup>. Then the energetics of the system are used to determine a process rate (for details on the process rates, see Sec. 3.1). Another random number  $R_2$  is used to determine whether the process takes place or not: If  $R_2 \leq p_i$ , where  $p_i = r_i \Delta t$  is the process probability, then the process takes place and the according changes are implemented in the system configuration. Finally, the system clock is ‘ticked’ forward by a constant time step  $\Delta t/n$ , where  $n$  denotes the number of processes that are currently possible in the system. Using this construction, every process is attempted once on average in every time interval  $\Delta t$ . Once the clock is ‘ticked’ forward, the next iteration starts.

In summary, the noteworthy features are

- the random, uniformly-weighted selection of a process,
- the stochastic acceptance of the process, proportional to the process rate, and
- the constant time steps with which the system time progresses at every iteration.

The RSM is especially well suited for the simulation of large systems for short times [146], or for systems with a broad spectrum of different rates [131]. A broad spectrum of different rates occurs, e.g. if particles have continuous rotational degrees of freedom and anisotropic interactions. In this case each particle ‘feels’ its own landscape that will differ from the energetic landscapes of all other particles. Thus, each particle will have unique rotation and diffusion rates. It is advantageous to use a simulation method where only the rate of each currently relevant process is calculated ‘on-the-fly’ in each iteration.

A major disadvantage is given through the rejection of processes: In order to simulate the time evolution of a system,  $\Delta t$  needs to be small enough that  $r_i^{\text{ads}} \Delta t \leq 1$ ,  $r_i^{\text{diff}} \Delta t \leq 1$ , and  $r_i^{\text{rot}} \Delta t \leq 1$  at all times. Especially in systems with large spans of values for the rates, this condition can lead to the rejection of the vast majority of processes, making the simulation extremely inefficient [132]. In such systems, approaches more efficient are those that constantly monitor the entire system and only iterate if an event truly occurs — Event-driven DMC simulations are precisely such.

## 2.5 Event-driven simulations (KMC)

Event-driven DMC simulations are referred to under a broad selection of terms. The term ‘Kinetic Monte-Carlo’ (KMC) is commonly used to denote event-driven DMC simulations, though it is sometimes used to denote RSM simulations (as mentioned in Sec. 2.4). Other terms used for KMC simulations include the ‘rejection-free’ or ‘event-based’ algorithm [134], ‘N-fold Way’ [99, 132], ‘Gillespie’ algorithm [142, 147] and the ‘Bortz-Kalos-Lebowitz’ (BKL)[148] algorithm.

All of these names refer to an algorithm that follows the same fundamental idea: If the algorithm only performs a MC iteration when processes truly occur, then any rejected proposed moves are spared from computation time [131]. This kind of approach requires a decision structure, as depicted in Fig. 2.2 for the example of surface growth.

---

<sup>2</sup>A random number is never ‘re-used’ to prevent unnecessary auto correlations in the simulation

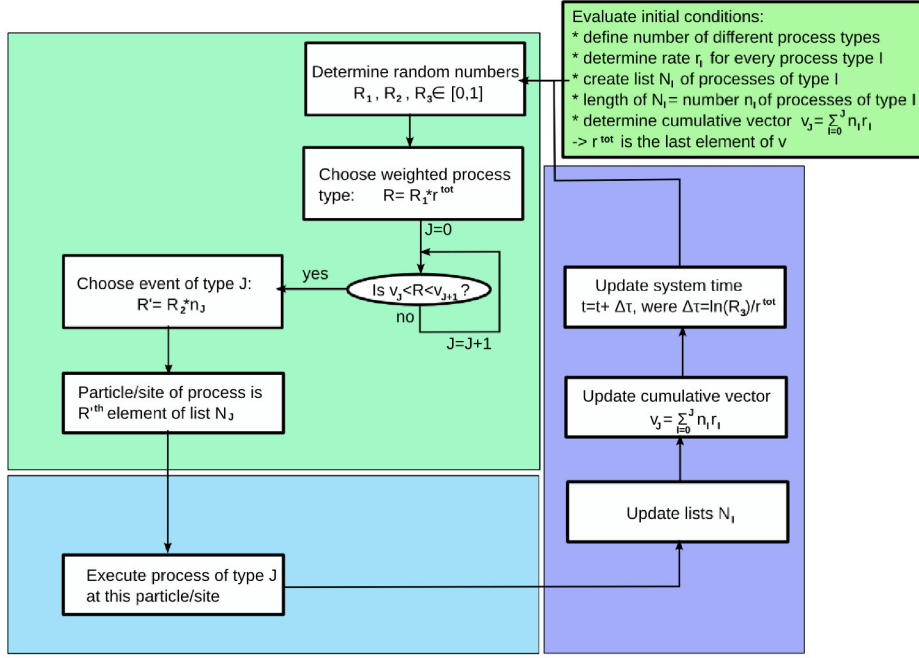


FIGURE 2.2: Fundamental decision sequence for a kinetic Monte-Carlo (KMC) simulation of surface growth. This is one possibility for the basic form of an algorithm structure, note that clever choice of data structures can accelerate the simulation considerably (see App. B for an example of a convenient data structure).

This section is based on personal experience, as well as several Review papers and book chapters. I would like to refer primarily to the book chapter by Voter [114].

### 2.5.1 Algorithm principle

Contrary to the RSM, a KMC algorithm always requires the complete set of process rates  $r_i$  for all processes  $i$  that are allowed to take place in the system at the current configuration. From this complete set a random process is selected and executed in one MC-iteration. However, the system is commonly coarse-grained such that only a finite number of process types  $I$  occur, i.e. the number of process types is smaller than the number of processes. See Chap. 3 for details on coarse-graining. Then it is sufficient to know the rates of each process type as well as the number of possible processes of this type  $n_I$  at the current system configuration. Every time a process takes place, the system configuration changes, and, therefore, the  $n_I$  change. Note that, here, process types might be the following: translational diffusion without lateral neighbouring particles, translational diffusion with one lateral neighbouring particle, translational diffusion with two lateral neighbouring particles, etc. In other words, the need to distinguish between a considerable number of differing process types is typical for KMC simulations.

Each iteration, one process type is drawn from the list of process types with a probability proportional to the rate  $r_I$  and number of this type of possible processes  $n_I$ . Then one process is randomly drawn from this list of processes of the selected process type. This two-step approach yields the same result as listing each single process  $i$  with its rate  $r_i$  in one long list and drawing one single process with a relative probability that is proportional to  $r_i$ . Either way, processes with higher rates likely are more selected than processes with lower rates.

As a higher rate corresponds to a more frequent occurrence, this selection procedure is most likely to select the ‘first process’ (i.e. the process that occurs most frequently and is therefore most likely to occur next). The chosen process is then executed and the lists of process types updated accordingly. Finally, the system time is propagated by a stochastic time step  $\Delta\tau$ <sup>3</sup> that is scaled with the overall escape rate of the system  $r^{\text{tot}}$ , which is the sum over all process rates that are possible in the system.

$$\Delta\tau = \frac{\ln(R_3)}{r^{\text{tot}}}, \quad r^{\text{tot}} = \sum_{i=0}^{n_i} r_i \quad (2.6)$$

where  $R_3 \in [0, 1]$  is a random number and  $n_i$  is the number of possible processes. This choice of time step length is motivated and discussed in detail in Sec. 2.5.2.

In summary, the most noteworthy features for the steps of a single iteration are the following

- Processes are selected with a probability proportional to their rate,
- the chosen process is always accepted, and, after executing it,
- the system time is propagated by a stochastic time step.

As mentioned above, KMC simulations do not reject processes, which makes it very efficient in systems that have both very frequent and very rare processes [132]. However, it is hard to implement a KMC algorithm efficiently for continuous degrees of freedom, as will be relevant for the continuous rotational degrees of freedom treated in part III of this thesis (specifically Sec. 10.6).

### 2.5.2 Time step lengths and waiting time distributions

The choice of step-length presented in Eq. (2.6) for a KMC simulation may seem slightly unintuitive. So, I present here a motivation for this choice based on the work of Fichthorn and Weinberg [133]. Section 2.6 shows that a KMC simulation using a time step length as in Eq. (2.6) fulfils the same average time evolution as a corresponding simulation using RSM. ‘Average’ here means an average over the coarse of many independent runs of the simulations.

We assume that we can describe the average escape rate of the system from its current configuration to the next state through the rate  $r^{\text{tot}}$ . The system finally escapes from its current configuration with the probability  $p_{\text{esc}}(\Delta t) = r^{\text{tot}}\Delta t$  in a time interval of length  $\Delta t$ . The complementary probability of the configuration surviving during this time interval is  $p_{\text{survive}}(\Delta t) = 1 - r^{\text{tot}}\Delta t$ . Thus, the probability of the configuration surviving for  $N$  steps of length  $\Delta t$  is

$$p_{\text{survive}}(N\Delta t) = (1 - r^{\text{tot}}\Delta t)^N. \quad (2.7)$$

In order to determine the limit  $\lim_{\Delta t \rightarrow 0}$ , we express  $N$  as  $N = t/\Delta t$ . Then

$$p_{\text{survive}}(t) = \lim_{\Delta t \rightarrow 0} (1 - r^{\text{tot}}\Delta t)^{\frac{t}{\Delta t}} = e^{-r^{\text{tot}}t}. \quad (2.8)$$

---

<sup>3</sup>Stochastic because the exact moment of *when* an event first occurs is random, as well. Specifically, each process is a Poisson process in time.

After some time  $t\ell$ , the integrated probability density of the system escaping,  $p_{\text{WTD}}(t)$ , must be equal to the  $1 - p_{\text{survive}}(t\ell)$ . Note that the probability density  $p_{\text{WTD}}(t)$  is also called the ‘waiting time distribution’ (WTD).

$$\int_0^{t\ell} p_{\text{WTD}}(t) dt = 1 - p_{\text{survive}}(t\ell) \quad (2.9)$$

Using Eq. (2.8), we find the WTD

$$p_{\text{WTD}}(t) = r^{\text{tot}} e^{-r^{\text{tot}} t}, \quad (2.10)$$

Then the mean residence time is defined through the average waiting time

$$\langle \tau \rangle = \int_0^\infty t p_{\text{WTD}}(t) dt = \int_0^\infty t r^{\text{tot}} e^{-r^{\text{tot}} t} dt = \frac{1}{r^{\text{tot}}}. \quad (2.11)$$

In KMC simulations, we draw the time step length from the WTD given in Eq. (2.10), i.e.  $p_{\text{WTD,KMC}}(t) = p_{\text{WTD}}(t)$ . Correspondingly, we arrive at the algorithm for time-steps defined in Eq. (2.6).

In RSM simulations, the precise derivation of the WTD requires a little more detailed treatment of the number of steps  $N$ , as  $N$  only assumes integer values. Correspondingly, the correct connection between  $N$  and  $t$  is  $N = \lfloor t/\Delta t \rfloor$ . Here  $\lfloor x \rfloor$  denotes a floor function, i.e. all values are rounded down to the next lowest integer. In order to handle this floor function, we rewrite it in terms of the Heaviside function  $\Theta(x)$ , using <sup>4</sup>

$$\lfloor x \rfloor = \sum_{i=1}^{\infty} \Theta(x - i). \quad (2.12)$$

Combining Eq. (2.7) with Eq. (2.12) and  $N = \lfloor t/\Delta t \rfloor$ , we can follow the derivation given in Eq. (2.9) to find an accurate expression for the WTD in RSM simulations

$$\begin{aligned} p_{\text{WTD,RSM}}(t) &= -\frac{1}{\Delta t} \log(1 - r^{\text{tot}} \Delta t) \cdot (1 - r^{\text{tot}} \Delta t)^{\lfloor t/\Delta t \rfloor} \frac{d \lfloor t/\Delta t \rfloor}{dt} \\ &= -\frac{1}{\Delta t} \log(1 - r^{\text{tot}} \Delta t) \cdot (1 - r^{\text{tot}} \Delta t)^{\sum_{i=1}^{\infty} \Theta(t/\Delta t - i)} \sum_{i=1}^{\infty} \delta(t/\Delta t - i). \end{aligned} \quad (2.13)$$

For small values of  $\Delta t$  (i.e. large values of  $x = t/\Delta t$ ), we can study the behaviour of the floor function to find the limit of the entire system.

$$\begin{aligned} \frac{\lfloor x \rfloor}{\lfloor x \rfloor + 1} &\leq \frac{\lfloor x \rfloor}{x} \leq \frac{\lfloor x \rfloor}{\lfloor x \rfloor} = 1 \\ \lim_{x \rightarrow \infty} \frac{\lfloor x \rfloor}{\lfloor x \rfloor + 1} &= 1 \\ \rightarrow \lim_{x \rightarrow \infty} \frac{\lfloor x \rfloor}{x} &= 1. \end{aligned} \quad (2.14)$$

We find that for large values of  $x$ , the floor function behaves like the function itself, i.e.  $\lim_{x \rightarrow \infty} \lfloor x \rfloor = \lim_{x \rightarrow \infty} x$ . Correspondingly, we expect that  $\lim_{\Delta t \rightarrow 0} \frac{d \lfloor t/\Delta t \rfloor}{dt} = 1$ . Applying these

---

<sup>4</sup>Thank you to Robert Gernert for helping me find this expression.

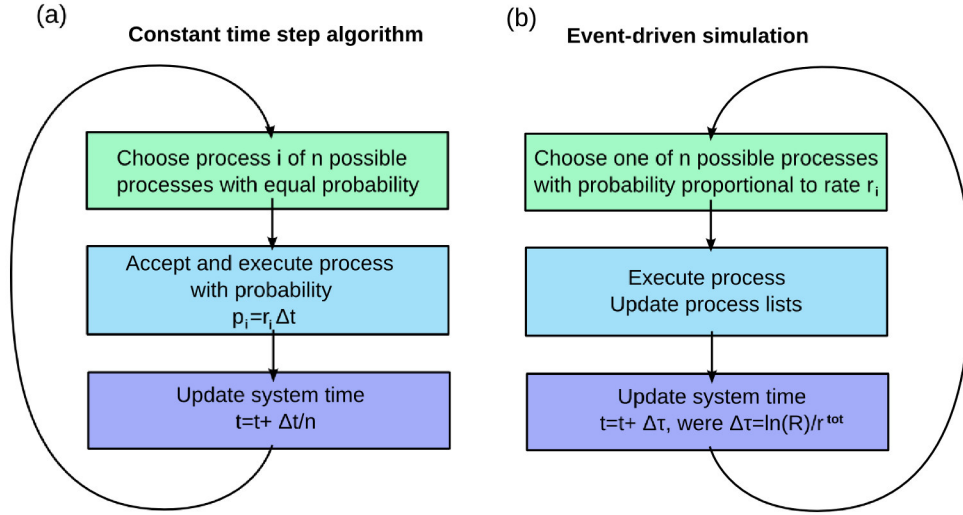


FIGURE 2.3: Sketched most fundamental iteration sequence for a constant-time-step Dynamic Monte-Carlo (DMC) algorithm in (a), as well as an event-driven DMC algorithm in (b). More detailed decision structures are depicted Fig. 2.1 for (a) and in Fig. 2.2 for (b).

findings to Eq. (2.13), we conclude that the WTD is the same in KMC and RSM simulations in the limit of small  $\Delta t$

$$\lim_{\Delta t \rightarrow 0} p_{\text{WTD},\text{RSM}}(t) = r^{\text{tot}} e^{-r^{\text{tot}} t} \quad (2.15)$$

$$= p_{\text{WTD},\text{KMC}}(t). \quad (2.16)$$

## 2.6 Equivalence of system evolution

Considering the similarities and differences between the WTDs given in Eq. (2.10) and (2.16), we are interested in the time evolution for a series of processes. Furthermore, we no longer want to automatically assume that the escape rate of the complete system is the sum of all contributing process rates. Here, I present my own proof for the equivalence of the time evolution in the two algorithms, without making these assumptions. The full, detailed calculation can be found in App. A —this section contains only the most central steps of the calculation.

Note that various sources in literature defend that RSM and KMC simulations are nothing more than procedural reordering of each other [132]. It has been shown in literature that the probability of a process being picked in the KMC simulation is the same as the probability of a process being picked and accepted in RSM simulations [131]. I would like to refer to the review paper of Chatterjee and Vlachos for details on the derivation of the equivalence between the process sequences [131]. Both algorithms assume that no two events occur absolutely simultaneously, though the time intervals between them may get very small.<sup>5</sup>

<sup>5</sup>The assumption comes from the underlying assumption of processes being Poisson processes in time.

### 2.6.1 Analytic calculation of equivalence

**System time in dynamic RSM simulations.** As previously discussed in Sec. 2.4, a RSM simulation advances the system time by a constant time step  $\Delta t/n$  every iteration. In each iteration a process with rate  $r_i$  is chosen uniformly among others, it is accepted with the probability  $p_i = r_i \Delta t$ , and finally the system time progresses by  $\Delta t/n$ .

In a system with two possible processes, i.e. for  $n = 2$ , the probability  $P$  of exactly one process occurring after exactly  $N - 1$  event-less iterations is described by

$$\begin{aligned} P(N) &= \left(\frac{1}{2}\right)^N \sum_{l=0}^{N-1} (1-p_1)^i (1-p_2)^{N-1-l} \binom{N-1}{l} (p_1 + p_2) \\ &= \left(\frac{1}{2}\right)^{N+1} (2-p_1-p_2)^{N-1} (p_1 + p_2). \end{aligned} \quad (2.17)$$

Based on this expression, we can determine the probability for exactly two processes to occur within  $N$  time steps. After the first process takes place, all probabilities in the system may change — new processes may become allowed and old processes may no longer be allowed. Without loss of generality, we assume that all processes — allowed or forbidden — are included in our description. However, forbidden processes are assigned the probability  $p^{\text{impossible}} = 0$ . In order to account for possible changes in the probabilities, we introduce a second index  $j$  that denotes how many processes have already taken place. In other words, each process (possible or impossible) is described through the probability  $p_{i,j}$ , and our previous notation is short-hand for  $p_i = p_{i,0}$  in situations in which  $j$  is constant. The time between two processes only is considered.

In a calculation with two processes, the processes initially have the probabilities  $p_{i,0}$ . Once the first process has occurred, the probabilities change to  $p_{i,1}$ . Using this notation, the probability for two events taking place given that the second event takes place after exactly  $N - 1$  iterations is

$$\begin{aligned} P_2(N) &= \left(\frac{1}{2}\right)^N \sum_{l=0}^{N-2} (2-p_{1,0}-p_{2,0})^l (p_{1,0}+p_{2,0}) (2-p_{1,1}-p_{2,1})^{N-2-l} (p_{1,1}+p_{2,1}) \\ &= \left(\frac{1}{2}\right)^N \sum_{l=0}^{N-2} (2-p_0^{\text{tot}})^l p_0^{\text{tot}} (2-p_1^{\text{tot}})^{N-2-l} p_1^{\text{tot}} \\ &= \left(\frac{1}{2}\right)^N \frac{(2-p_1^{\text{tot}})^{N-1} - (2-p_0^{\text{tot}})^{N-1}}{p_0^{\text{tot}} - p_1^{\text{tot}}} p_0^{\text{tot}} p_1^{\text{tot}}. \end{aligned} \quad (2.18)$$

Here  $p_0^{\text{tot}} = \sum_{i=0}^n p_{i,0} = \Delta t \sum_{i=0}^n r_{i,0}$  and  $p_1^{\text{tot}} = \sum_{i=0}^n p_{i,1}$ . The generalisation of Eq. (2.18) to a system with  $n \neq 2$  possible processes is

$$P_2(N) = \left(\frac{1}{n}\right)^N \frac{(n-p_1^{\text{tot}})^{N-1} - (n-p_0^{\text{tot}})^{N-1}}{p_0^{\text{tot}} - p_1^{\text{tot}}} p_0^{\text{tot}} p_1^{\text{tot}}. \quad (2.19)$$

Using the probability derived in Eq. (2.19), the average time two processes take is given as

$$\begin{aligned}
\langle t \rangle_2 &= \sum_{N=2}^{\infty} \frac{\Delta t}{n} N P_2(N) \\
&= \sum_{N=2}^{\infty} \frac{\Delta t}{n} N \left(\frac{1}{n}\right)^N \frac{(n-p_1^{\text{tot}})^{N-1} - (n-p_0^{\text{tot}})^{N-1}}{p_0^{\text{tot}} - p_1^{\text{tot}}} p_0^{\text{tot}} p_1^{\text{tot}} \\
&= \frac{\Delta t}{n} \frac{p_0^{\text{tot}} p_1^{\text{tot}}}{(p_0^{\text{tot}} - p_1^{\text{tot}})} \left[ \frac{1}{(n-p_1^{\text{tot}})} \sum_{N=0}^{\infty} N \left(\frac{(n-p_1^{\text{tot}})}{n}\right)^N \right. \\
&\quad \left. - \frac{1}{(n-p_0^{\text{tot}})} \sum_{N=0}^{\infty} N \left(\frac{(n-p_0^{\text{tot}})}{n}\right)^N \right] \\
&= \frac{\Delta t}{n} \frac{p_0^{\text{tot}} p_1^{\text{tot}}}{(p_0^{\text{tot}} - p_1^{\text{tot}})} \left[ \frac{n}{(p_1^{\text{tot}})^2} - \frac{n}{(p_0^{\text{tot}})^2} \right] \\
&= \Delta t \left( \frac{1}{p_0^{\text{tot}}} + \frac{1}{p_1^{\text{tot}}} \right) \\
&= \sum_{j=0}^1 \frac{1}{\sum_{i=0}^n r_{i,j}}.
\end{aligned}$$

This expression can be used as the basis for mathematical induction in order to show that the average time a dynamic RSM simulation needs for  $a$  processes to take place is

$$\langle t \rangle_a = \sum_{j=0}^{a-1} \frac{1}{\sum_{i=0}^n r_{i,j}}. \quad (2.20)$$

Note that though the full derivation (including the full mathematical induction) is an interesting way to spend some time with combinatorics, it is not very instructional at this point of the thesis. Therefore, I would like to refer any reader who is interested in the entire, thorough and rigorous calculation, including the entire mathematical induction, to App. A.

**System time in KMC simulations.** In KMC simulations, during each iteration the system time progresses by a time-step that fulfils  $\langle \Delta \tau \rangle = 1 / \sum_{i=0}^N r_i$  (see Eq. (2.6) in Sec. 2.5). Then a process is chosen with a relative probability that is proportional to its rate and is executed with a probability  $p_i = 1$ .

The average time it takes the system for two processes to take place is the sum of the average time for process one and the average time for process two. Therefore, the average time an  $N$ -process system takes for two processes is determined easily as

$$\langle \tau \rangle_2 = \sum_{j=0}^1 \frac{1}{\sum_{i=0}^n r_{i,j}} \quad (2.21)$$

Correspondingly, the average system time after  $a$  processes is

$$\langle \tau \rangle_a = \sum_{j=0}^{a-1} \frac{1}{\sum_{i=0}^n r_{i,j}}. \quad (2.22)$$

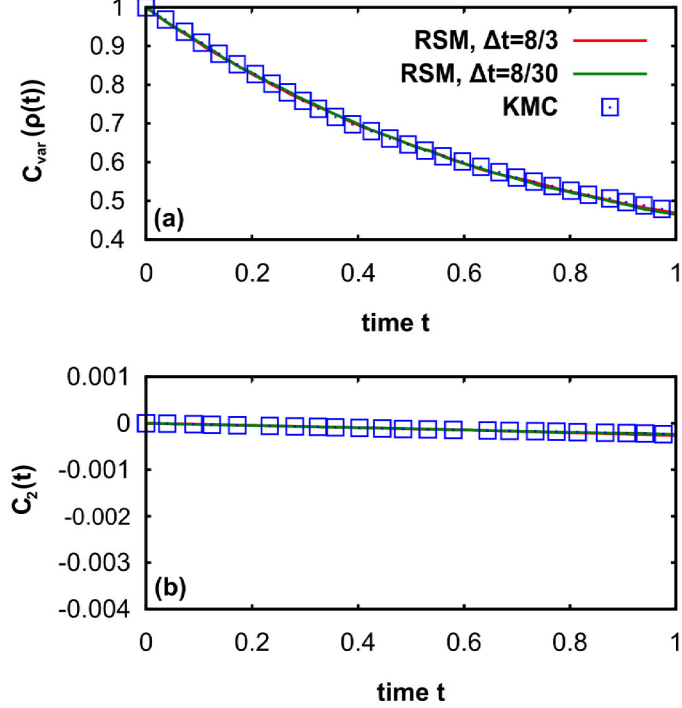


FIGURE 2.4: Comparison of numerical results obtained from RSM and KMC simulations for non-interacting particles diffusing on a tilted 1D plane. Part (a) contains the normalised occupation variance  $C_{\text{var}}$  [see Eq. (2.23)], while part (b) depicts the two-particle correlation function  $C_2$  [see Eq. (2.24)]. The results were obtained for  $r_{\text{right}} = 3/8$ ,  $r_{\text{left}} = 1/8$ , in accordance to the work of Riuz Bartlett *et al.* [149]. In part (a) we set  $n_{\text{lattice}} = 10000$  and  $n_{\text{particles}} = 10000$ , while in part (b)  $n_{\text{lattice}} = 2000$  and  $n_{\text{particles}} = 2000$  for reasons of computational time. In both parts the particles are all initially localised at one site and their positions relax with time. Note that the choice of axes in part (b) allow direct comparison to Fig. 4 in Ref. [149].

This expression is identical to the expression derived for the dynamic RSM simulation in Eq. (2.20).

### 2.6.2 Numerical equivalence

In order to study the equivalence of time scales numerically, we introduce a toy system. This system consists of a linear lattice with  $n_{\text{lattice}}$  lattice sites that are occupied by  $n_{\text{particles}}$  particles. In every iteration, every particle can diffuse to the right with a rate  $r_{\text{right}}$  and to the left with a rate  $r_{\text{left}}$ . Every diffusion step encompasses the transition from one lattice site to the next, under the consideration of periodic boundary conditions. Note that the particles in the toy system do not interact. Initially, all particles are localised at one lattice site. As time progresses, they diffuse on the lattice and spread evenly.

This toy system is based on a publication by Riuz Bartlett *et al.* [149], who claim that RSM and KMC simulations give fundamentally different results. However, comparing algorithms (see Sec. 2.4 for details on our algorithm), as well as our waiting time distributions (see Sec. 2.5.2 for a discussion of waiting time distributions), we find considerable discrepancies between their system and our system. After our studies on system equivalence in Sec. 2.6.1, we believe that our algorithms are equivalent, and thus cast some doubt on the methods and results of Riuz Bartlett *et al.* [149].

The equivalence of RSM and KMC algorithms is reflected in observables of the system, some of which are plotted in Fig. 2.4. In order to compare the relaxation times, we study the normalised occupation variance

$$C_{\text{var}}(t) = \frac{\langle \rho_i(t)^2 \rangle_i - \langle \rho_i \rangle_i^2}{\langle \rho_i(0)^2 \rangle_i - \langle \rho_i \rangle_i^2} \quad (2.23)$$

in Fig. 2.4 (a). Here,  $\rho_i(t)$  denotes the number of particles on a site  $i$  at time  $t$ , and  $\langle \dots \rangle_i$  denotes both the average over all sites. The particle number is conserved, so  $\langle \rho_i(t) \rangle_i = \langle \rho_i(0) \rangle_i = \langle \rho_i \rangle_i$ . Further, all particles are initially localised at one site, but their positions relax with time, so  $C_{\text{var}}(t) \neq C_{\text{var}}(0)$  if  $t \neq 0$ .

As a second observable we study the two-particle correlation function introduced by Riuz Bartlett *et al.* [149], which we depict in Fig. 2.4 (b).

$$C_2(t) = \langle (x_j(t) - \bar{x}(t))(x_k(t) - \bar{x}(t)) \rangle_{j,k: j \neq k}. \quad (2.24)$$

The particle positions are denoted as  $x_j(t)$  and  $x_k(t)$ , while  $\bar{x}(t)$  denotes the average particle position at time  $t$ . The average particle position moves because  $r_{\text{right}} \neq r_{\text{left}}$ , i.e. there is a drift current.

Both observables depicted in Fig. 2.4 show a very high agreement of RSM and KMC algorithms. We expect the largest deviations to occur for very small times, because the time step discretisation of RSM algorithms is likely to cause errors on small time scales. Hence, we study  $t \leq 1$  in Fig. 2.4. For the given rate parametrisation, these times correspond to less than one process per particle. Even on these small time scales, the graphs agree to beyond recognition. Furthermore, the agreement does not depend on the time-step length chosen in the RSM simulation, as long as the time step length fulfils  $\Delta t \leq 1 / \max(r_{\text{right}}, r_{\text{left}})$ .

We conclude that our algorithms yield identical system evolution and time-scales, and that we choose the algorithm according to its efficiency for any given problem.

## 2.7 Hybrid approaches

Section 2.4 discusses how RSM algorithms are more efficient if processes cannot easily be sorted into process types, but are inefficient if both very slow and very fast processes are present in the system. Hybrid algorithms that combine concepts of RSM and KMC algorithms can combine some advantages of both algorithm approaches. We will here discuss a class of algorithms is also called null-event algorithms [131], where not all attempted processes are accepted. These algorithms require resorting and slight variations of the steps in Sec. 2.4, however the simulation results are not influenced by the details of the algorithm.

### 2.7.1 Continuous time null-event algorithms

The first approach that makes a RSM simulation more like KMC algorithms is introduced by Fichthorn *et al.* [133]. The algorithm is called ‘Continuous time’ algorithm. This algorithm

randomly selects processes and accepts/rejects them according to the criteria discussed in Sec. 2.4. However, unlike the random selection method, the system time is updated as

$$t = t - \ln(R_3)\Delta t/n, \quad (2.25)$$

where  $R_3$  is a random number. This time increment has the same form as the time increment in KMC simulations, given in Eq. (2.6). While this is technically not more efficient than RSM simulations, it gives access to very precise time-resolved information even for very small times.

### 2.7.2 Composition and Rejection (CR) algorithms

Composition and Rejection (CR) algorithms expand from continuous time null-event algorithms to make them more efficient [143, 144]. They sort processes into groups with similar maximal rates and define a ‘propensity’ for each group that corresponds to the maximal process rate within this group. In our simulations, rates are described through an attempt frequency  $\nu$  and an acceptance rate  $p^{\text{acc}}$ , e.g. for a diffusion process the rate is  $r_i^{\text{diff}} = \nu^{\text{diff}} p_i^{\text{acc}, \text{diff}}$ . In a CR algorithm, we sort all diffusion processes into one process group. As we assume  $p_i^{\text{acc}, \text{diff}} \leq 1$ , the propensity of this group is  $\nu^{\text{diff}}$ . Exploiting these propensities (that do not need elaborate calculations), we can use a null-event algorithm that somewhat resembles the KMC algorithm discussed above. In each iteration the following steps take place

- Processes are selected with a probability proportional to their propensity,
- the chosen process is accepted with a probability  $p_i^{\text{acc}} = r_i/\nu$  or rejected with a probability  $p_i^{\text{rej}} = 1 - p_i^{\text{acc}}$ ,
- the system time is propagated by a stochastic time step  $\Delta\tilde{\tau}$ .

The stochastic time step in CR algorithms is based on the KMC time step given in Eq. (2.6), however it now contains the propensities instead of the rates. In a system with adsorption, diffusion and rotation, the stochastic time step has the form

$$\Delta\tilde{\tau} = -\ln(R_3) \frac{1}{n^{\text{diff}} \cdot \nu^{\text{diff}} + n^{\text{rot}} \cdot \nu^{\text{rot}} + n^{\text{ads}} \cdot \nu^{\text{ads}}}. \quad (2.26)$$

The CR algorithm is just a resorting of the RSM algorithm discussed in Sec. 2.4 under consideration of the time step length given in Eq. (2.25).

## Chapter 3

# Background to coarse-graining

Surface growth of molecular systems can be studied on different length-scales, as previously mentioned in Chap. 1.4. In our studies, we are interested in large time scales (up to 1000s of seconds) and large system-sizes (e.g.  $1\mu\text{m} \times 1\mu\text{m}$ ). These length- and time-scales are not accessible if all the details of trajectory information and the full interactions on a electronic level are taken into account because their computational cost is prohibitive. Instead, we require coarse-grained models in which we neglect events on shorter time- and smaller length-scales, as well as details of the interactions that are not essential for the considered questions. However, it is not always obvious which elements can be neglected and which requirements a coarse-grained model needs to meet.

In this chapter, the time-scale separation time scale separation which is fundamental for DMC simulations is discussed (see Sec. 2.1). Next, Sec. 3.2 comments on the Markov chain assumption in which the evolution of a system is assumed to consist of jump-like and adsorption events, where each event only depends on the current system configuration. This assumption is technically not a coarse-graining approach, but it is closely linked to the time-scale separation. The coarse-graining of both time- and length-scales allows us to describe particle diffusion through rate based transitions of particles between lattice sites. Section 3.3 treats some general properties of rate-based particle diffusion on a lattice. Material-specific details for the spherical particle  $\text{C}_{60}$  will be discussed in detail in Sec. 5.2. Similarly, details of the anisotropic particle 6P will be treated in Chap. 10.

### 3.1 Time-scale separation and rate description

Time-scale separation can be applied to a system in which there are both fast and slow processes. In other words, the separation occurs when the fast process occurs many times during the waiting period between events of the slow process [99]. If a system displays two clearly separated time scales it is often sufficient to study one of the time scales without explicitly modelling the other; these systems are also called ‘infrequent-event systems’. In growth scenarios, the short time scale is usually close to the time scale of particle oscillations within potential wells, while the large time scale is the time between diffusion events [114] between these potential wells. Instead of following the trajectory of the particle through every

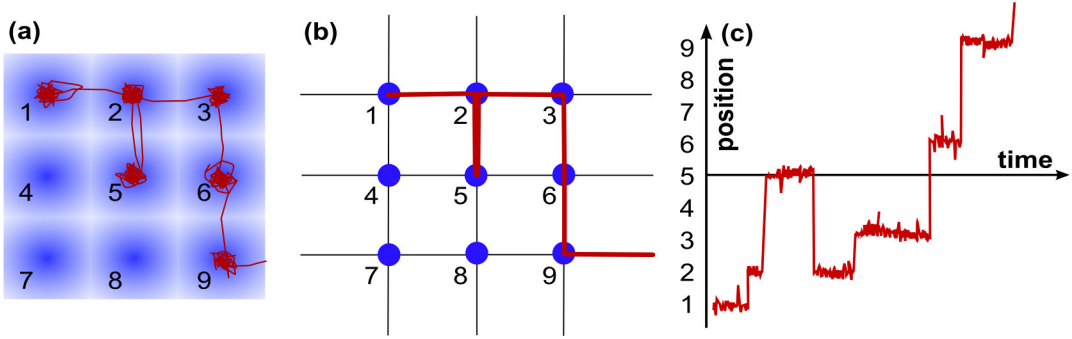


FIGURE 3.1: Sketch of a single particle trajectory and its coarse-grained mapping onto a lattice. Part (a) shows the diffusive trajectory of a single Brownian particle on a surface (red), where the surface is presented as a lattice of potential wells (blue). Here, the potential well depth is sketched through the intensity of blue, i.e. a deep potential is represented through an intense blue. The centres of the potential wells are enumerated through numbers between 1 and 9, and are represented through lattice points in part (b). The black lines connecting the lattice points in (b) represent the trajectories between lattice sites that require overcoming the smallest energy barrier, i.e. the black lines connecting lattice points go through saddle points in the potential landscape. The red line in part (b) represents a coarse-graining of the red trajectory in part (a). Part (c) depicts the time evolution of the system between the potential wells, where the y-axis lists the various wells depicted in parts (a) and (b).

vibration in a potential well (as MD simulations commonly do), we coarse-grain time and follow only the transitions between potential wells. This coarse-graining is sketched in Fig. 3.1. Figure 3.1 (a) shows the trajectory of a particle in a potential landscape. If the temperature is small enough, a particle will spend much more time moving within the potential well than transitioning between wells [see Fig. 3.1 (c)]. Furthermore, most transitions between potential wells follow trajectories that cross the energetic saddle point between potential wells, so the highest energy that the particle has to overcome is the saddle-point energy. For infrequent-event systems with diffusion via saddle-points, the diffusion depicted in Fig. 3.1 (a) can be modelled as random transitions between lattice sites, as depicted in Fig. 3.1 (b).

In DMC simulations, the fundamental approach describes processes through transition rates between lattice sites and neglects the details of the trajectories (see Sec. 2.1). This distinguishes DMC approaches from approaches that are based on solving the equations of motion, such as MD simulations. This ‘coarse-graining’ of time is the main factor that makes DMC simulations faster than MD simulations. However, detailed information on small time scales is lost, such as the particle trajectories during movement within a potential well. Most DMC simulations describe the dynamics of the system through coarse-grained transition rates between lattice sites.

Few DMC studies based on rates without a lattice assumption exist, but most of these are restricted to one dimension [150], as computing rates on a 2D substrate without lattice is a substantial challenge that requires the knowledge of the energetic saddle point between potential wells [151]. This decreases the speed of the algorithm considerably. Therefore most algorithms couple the coarse-graining of time with a coarse-graining of space (or configuration space for processes such as rotation).

The rates used in DMC simulations (see Sec. 2.1) are usually Arrhenius-type rates

$$r_{a \rightarrow b} \propto e^{-\frac{(E_{\text{saddle}} - E_a)}{kT}}, \quad (3.1)$$

which depend exponentially on an energy barrier height, the difference between the potential-well depth  $E_a$  at the origin a and the saddle-point energy  $E_{\text{saddle}}$  ( $k$  is the Boltzmann temperature and  $T$  the temperature). The energies and states required for this definition are sketched in Fig. 3.2. For lattice-based simulations in which each lattice point corresponds to a potential well, the position of the saddle point is well known and, for isotropic particles, the full set of possible saddle point energies can be determined in advance.

If the potential landscape is more finely discretised, the potential between particle origin a and particle destination b may be monotonous. Then the saddle-point corresponds to the destination energy  $E_b$ . Heinsalu *et al.* [152] show that rate-based diffusion on a discretised lattice reproduces the results of the continuous Fokker-Planck equation for lattices with at least one lattice site per potential minimum. Thus, we expect the exact discretisation to have little or no influence on our results as long as it resolves every potential minimum. If we should interested in behaviour on time scales smaller than the escape time from a potential well, then a finer discretisation would be necessary.

Different derivations of Arrhenius-type rates exist in literature, derived for different systems but similar in form. The derivations all yield the same exponent, but different prefactors. The pre-factors result from different approximations made during the derivation. I will briefly sketch and discuss two derivations here: Kramer's rate and the Transition-State-Theory rate.

### 3.1.1 Similarities and differences between the different derivations

This discussion of Kramer's rate and the Transition-State-Theory rate is based on the discussion by Pollak [153]. Both rates are an exponential function of the energy barrier height  $\Delta E/kT$ . The differences lie in the pre-factors and in their derivation.

Kramer's rate is derived using the single-particle over-damped Smoluchowski equation (see Sec. 3.1.2 and Ref. [154]). In other words, Kramer's rate is an escape rate over a potential barrier in the over-damped limit, assuming a high friction  $\gamma$ . Here, the image is a particle that immediately loses all information about its previous velocity, only follows thermal fluctuations and escapes the potential well when fluctuations are large enough. Accordingly, the prefactor is dominated by the friction  $\nu_{0,\text{Kramers}} = \sqrt{(\partial_x)^2 E(x_a) |(\partial_x)^2 E(x_{\text{saddle}})|}/(2\pi\gamma)$ . This approximation holds very well for systems in a solvent, e.g. colloidal particles, especially if the fluid is microscopically viscous.

The rate derived using Transition-State-Theory is based on the decomposition of the potential landscape into harmonic modes. The image behind this derivation is the following: Particles oscillate within a potential-well, where thermal energy perturbs the oscillations. The information from the previous trajectory may be contained in the entropy; however, the difference in entropy between minimum and saddle-point is mostly assumed to be constant. Correspondingly, the information of the previous trajectory is assumed to be lost during the oscillations. This limit in which the motion is dominated by oscillations is a low-friction limit, i.e. the rate derived from Transition-State-Theory differs markedly from the rate derived from Kramer's

rate under a high-friction assumption. The prefactor for the oscillatory approximation contains all vibrational modes  $\nu_0 = \prod_{j=1}^N \nu_j / \prod_{j=1}^{N-1} \nu_j t$ , and the description holds especially well for systems with very low friction, such as atomic or molecular growth without solvent. Note that in molecular systems internal oscillations are also an indiscernible part of the make-up of phase-space. Hence, the prefactor needs to be treated with special care.

Reducing the dimensionality of the rate-prefactor from transition state theory to  $N = 1$ , we find  $\nu_0 = \nu_1$ , where  $\nu_1$  is the oscillation frequency of the dominant harmonic oscillation for a particle close to the potential minimum. This prefactor does not contain any information on the saddle point, nor does it contain the friction constant  $\gamma$ , so it is clearly different from the prefactor obtained for Kramer's rate.

### 3.1.2 Derivation of Kramer's rate

This subsection follows the book ‘The Fokker-Planck Equation’ by Risken [154], Chap. 5.10.

By using the Fokker-Planck equation it is possible to determine escape rates of particles in a potential well across the saddle point.

#### The Fokker-Planck equation

We start the derivation with the master equation Eq. (2.4) in Sec. 2.3. Performing a Taylor expansion of this evolution equation around position  $x$ , as well as time  $t$ , and truncating the series at second order of  $x$ , we obtain a partial differential equation called the ‘Fokker-Planck equation’. This Fokker-Planck equation in one dimension is

$$\partial_t P(x, t) = -\partial_x D^{(1)}(x, t)P(x, t) + (\partial_x)^2 D^{(2)}(x, t)P(x, t). \quad (3.2)$$

This equation is called the ‘Smoluchowski-equation’ if  $x$  describes a true particle position. If  $x$  is identified as a particle position, then  $D^{(1)}$  is the drift coefficient of the particle and  $D^{(2)}$  is the diffusion coefficient. The Smoluchowski equation determines the time evolution of the probability density  $P(x, t)$ , which is the probability of finding the particle at position  $x$  at time  $t$ .

Assume an over-damped Brownian particle, i.e. a particle where the motion is dominated by thermal fluctuations, as well as where the surroundings create enough friction for the particle to lose all information about its previous trajectory instantaneously. If this particle is placed in a potential  $E(x)$ , which manifests a force  $F(x)$  on the particle, the coefficients  $D^{(1)}$  and  $D^{(2)}$  can be identified as

$$D^{(1)} = \frac{F(x)}{\gamma} = -\frac{\partial_x E(x)}{\gamma}, \text{ and} \quad D^{(2)} = \frac{kT}{\gamma}. \quad (3.3)$$

Note that this identification of  $D^{(2)}$  makes the particle a Brownian particle. The fact that both  $D^{(1)}$  and  $D^{(2)}$  are independent of the particle velocity reflects the assumption of an over-damped particle (i.e. the friction  $\gamma$  causes the particle to lose the information about its momentum on a much smaller time scale than the waiting time). This choice of coefficients also makes Eq. (3.2) independent of the particle velocity.

The over-damped Smoluchowski equation implies continuity, i.e. it implies that no particles are generated or lost in the system:

$$\partial_t P(x, t) = -\partial_x S(x, t), \quad (3.4)$$

where  $S(x, t)$  is the probability current.

### Equilibrium solution

The equilibrium solution requires that the probabilities are constant  $\partial_t P(x, t) = \partial_x S(x, t) = 0$  and there is no current, i.e.  $S = 0$ . Then Eq. (3.2) becomes

$$\partial_x P_{\text{eq}}(x) = \frac{-\partial_x E(x)}{kT} P_{\text{eq}}(x), \quad (3.5)$$

and the solution is the Boltzmann distribution

$$P_{\text{eq}}(x) = N e^{-E(x)/kT}, \quad (3.6)$$

with the normalisation constant  $N$ .

### Variation around the equilibrium solution

In order to consider small deviations to the equilibrium solution, we vary the constant  $N \rightarrow N + c(x)$  and find

$$c(x) = -\frac{S}{D^{(2)}} \int_{x_a}^x e^{E(x')/kT} dx' = -\frac{S}{D^{(2)}} I(x). \quad (3.7)$$

This solution allows us to determine the probability density for small changes to the equilibrium,

$$P_{\text{eq},2}(x) = \left( N - \frac{S}{D^{(2)}} I(x) \right) e^{-E(x)/kT}. \quad (3.8)$$

Exploiting that  $\partial_x S(x, t) \approx 0$  in this small variation to the equilibrium solution, we can take the spatial derivative of Eq. (3.8), and use it to express the probability current as

$$S e^{E(x)/kT} = -D^{(2)} \partial_x \left( e^{E(x)/kT} P(x) \right). \quad (3.9)$$

### Kramer's escape rate

In order to determine the diffusion rate, we consider a single potential valley, as depicted in Fig. 3.2. Assume a particle in the potential valley  $a$  at time  $t = 0$ . In order to escape the potential valley, it has to cross the saddle point, which is denoted as ‘saddle’. We assume that the potential barrier  $\Delta E = E_{\text{saddle}} - E_a$  is large relative to  $D^{(2)}\gamma$ , i.e. we assume that the probability of finding the particle in the valley changes very slowly. Within the valley, the particles are assumed to occupy positions close to the potential minimum, i.e. positions within the interval  $[x_1, x_2]$  with  $x_1 < x_a < x_2 < x_{\text{saddle}}$ .

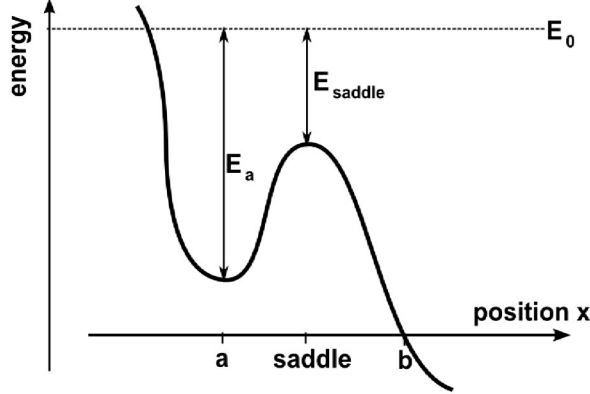


FIGURE 3.2: Sketched energy landscape with a potential valley ‘a’ and a saddle point ‘saddle’ in the potential energy landscape. The dashed line represents the reference-energy  $E_0$ .

Furthermore, we assume that the particle can never return once it has crossed the point ‘b’, i.e. that a particle vanishes at point ‘b’, and that  $P_{\text{eq},2}(b) = 0^1$ . Then we determine the constant  $N$  using Eq. (3.8).

$$N = \frac{S_{\text{eq},2} I(b)}{D^{(2)}}, \quad (3.10)$$

We combine this expression with Eq. (3.8) to determine the probability density

$$P_{\text{eq},2}(x) = N e^{-E(x)/kT} \left( 1 - \frac{I(x)}{I(b)} \right). \quad (3.11)$$

Note that for values of  $x$  close to  $x_a$ , we find  $I(x) \ll I(b)$ . We then set  $I(x)/I(b) \approx 0$  in Eq. (3.11), thus reproducing the stationary solution  $P_{\text{eq}}$  of Eq. (3.6).

Further, assuming that particle positions are close to the minimum of the potential valley, we find particles in the valley with a probability

$$P_I = \int_{x_1}^{x_2} P_{\text{eq},2}(x) dx \approx \int_{x_1}^{x_2} P_{\text{eq}}(x) dx = \int_{x_1}^{x_2} N e^{-E(x)/kT} dx. \quad (3.12)$$

We define the escape rate from the potential valley  $r$  using the probability of being in the minimum, Eq. (3.12), as well as the probability current, Eq. (3.10).

$$\frac{1}{r_{\text{Kramers}}} = \frac{P_I}{S_{\text{eq},2}} = \frac{1}{D^{(2)}} \int_{x_1}^{x_2} e^{-E(x)/kT} dx \int_{x_a}^b e^{E(x')/kT} dx'. \quad (3.13)$$

We now set  $x_2 = x_{\text{saddle}}$  and expand the potential  $E(x)$  around the turning points  $x_a$  and  $x_{\text{saddle}}$  to the second order using a Taylor expansion.

$$E(x) \approx E(x_a) + \frac{(x - x_a)^2}{2} (\partial_x)^2 E(x_a) \quad (3.14)$$

$$E(x) \approx E(x_{\text{saddle}}) + \frac{(x - x_{\text{saddle}})^2}{2} (\partial_x)^2 E(x_{\text{saddle}}) \quad (3.15)$$

(3.16)

<sup>1</sup>The point ‘b’ is often called the ‘point of no return’.

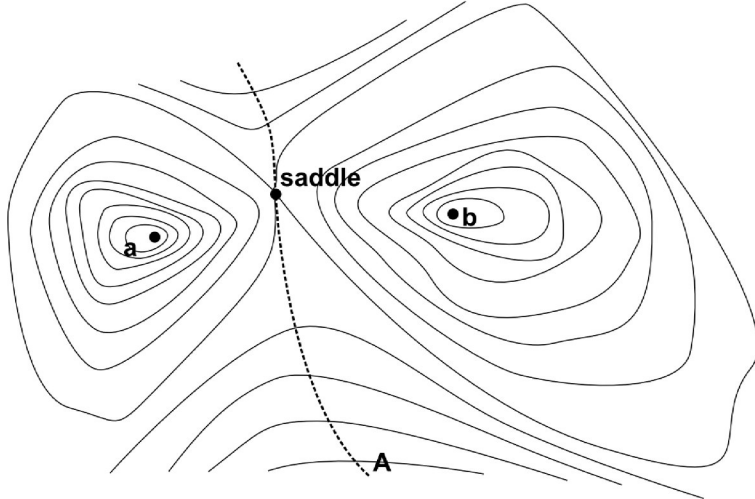


FIGURE 3.3: Topological map of a fictitious potential landscape with two valleys ‘a’ and ‘b’, an intermediate saddle point ‘saddle’ and a plane separating ‘a’ and ‘b’. The plane is denoted as  $A$  and is depicted as a dashed line. Note that ‘saddle’ is an element of the plane  $A$ .

The resulting rate is known as Kramer’s rate

$$r_{\text{Kramers}} = \frac{D^{(2)} \sqrt{(\partial_x)^2 E(x_a) |(\partial_x)^2 E(x_{\text{saddle}})|}}{2\pi k T} e^{-(E(x_{\text{saddle}}) - E(x_a))/kT}. \quad (3.17)$$

### 3.1.3 Derivation from Transition state theory

This section is primarily based on the work of Vineyard [155]. However, other derivations and descriptions exist, e.g. the derivations for quantum-mechanical systems in Refs. [156, 157]. For a more detailed version of the derivation presented here, the reader is directed to the derivation based on detailed balance by Hänggi *et al.* [158].

The original derivation was an iterative process, where I would like to point out the work of Herzfeld [159], along with the work by Eyring and Polanyi that is commonly seen as the original source of the derivation [160, 161].

#### Setting up a diffusion rate

Following the assumptions made in Eq. (3.13) for Kramer’s rate, we express the transition rate as the ratio of the transition current,  $S$ , and the probability of finding a particle in the potential well ‘a’,  $P_a$ ,

$$r_{\text{TST}} = \frac{S}{P_a}. \quad (3.18)$$

The potential landscape studied here is that defined through  $n$  particles in a crystal, as depicted in Fig. 3.3. This potential landscape depends on  $N = 3n$  configurational degrees of freedom, which will later become interesting when the energies are decomposed in eigenmodes. The system is close to equilibrium when it is close to the potential well ‘a’. Hence, we can determine the probability of the configuration being at position  $x_1, \dots, x_N$  close to the potential minimum from the Boltzmann distribution

$$\rho(x_1, \dots, x_N) = \rho_0 e^{-E(x_1, \dots, x_N)/kT}, \quad (3.19)$$

where  $\rho_0$  is a normalisation constant. Note that the particle mass  $m$  is scaled into  $\mathbf{q}$  as  $\mathbf{q} = \mathbf{q}'/\sqrt{m}$ . Accordingly, we can determine the probability of finding the system in the potential well as equal to the probability integrated over all  $N$  configurational degrees of freedom of the potential well,

$$P_a = \int_a \rho_0 e^{-E(x_1, \dots, x_N)/kT} d^N x. \quad (3.20)$$

In order to study the current  $S$ , we introduce the surface  $A$  separating the potential wells ‘a’ and ‘b’. The surface  $A$  goes through the saddle point ‘saddle’, and contains all points  $Y_i \in A$ . We then describe the current through sections of the area  $A$  around each point  $Y$ , where each element is represented by a vector  $d\mathbf{A}$  orthogonal to the surface. Then we can describe the probability of finding particles at  $Y$  with a velocity  $\mathbf{P} = \partial_t \mathbf{q}$  within the range  $d^N P = dP_1 \dots dP_N$  as [155]

$$\rho(Y_1, \dots, Y_N, \mathbf{P}) d^N = P \rho_1 e^{-E(Y_1, \dots, Y_N)/kT} e^{-P^2/2kT} d^N P, \quad (3.21)$$

where the new normalising constant  $\rho_1$  is

$$\rho_1 = \rho_0 \left( \frac{1}{\sqrt{2\pi kT}} \right)^N, \quad (3.22)$$

and where  $N$  is the number of dimensions in the configuration space. Note that the renormalisation is based on the integral

$$\int_{-\infty}^{\infty} e^{-P_i^2/(2kT)} dP_i = \sqrt{2\pi kT}. \quad (3.23)$$

In order to find the current  $dS$  per surface unit  $d\mathbf{A}$ , we integrate over the velocities  $\mathbf{P}$  and the probability  $\rho(Y_1, \dots, Y_N, \mathbf{P})$ :

$$d^N S = d\mathbf{A} \left( \int \mathbf{P} \rho(Y_1, \dots, Y_N, \mathbf{P}) d^N P \right). \quad (3.24)$$

In order to integrate this expression, we assume that we have a positive current through all  $d\mathbf{A}$  for all velocities  $\mathbf{P}$ , i.e.

$$d\mathbf{A} \cdot \mathbf{P} > 0. \quad (3.25)$$

The surface  $A$  is not clearly defined yet, except for the conditions that it goes through the saddle point and separates ‘a’ from ‘b’. We exploit the condition given in Eq. (3.25) to specify the surface  $A$ . It is chosen such that only one  $dA_i \neq 0$ , where  $i$  fulfils the condition that  $P_i \neq 0$ . Without loss of generality, we choose  $P_1 dA_1 \neq 0$ . Then we can use Eq. (3.22) to rewrite Eq. (3.24) as

$$\begin{aligned} d^N S &= d\mathbf{A} \left( \int \mathbf{P} \rho_0 \left( \frac{1}{\sqrt{2\pi kT}} \right)^N e^{-E(Y_1, \dots, Y_N)/kT} e^{-P^2/2kT} d^N P \right) \\ &= \rho_0 \left( \frac{1}{\sqrt{2\pi kT}} \right)^N e^{-E(Y_1, \dots, Y_N)/kT} dA_1 \left[ \int_0^\infty P_1 e^{-P_1^2/(2kT)} dP_1 \times \prod_{j=2}^N \int_{-\infty}^\infty e^{-P_j^2/(2kT)} dP_j \right] \\ &= \rho_0 \sqrt{\frac{kT}{2\pi}} e^{-E(Y_1, \dots, Y_N)/kT} dA_1. \end{aligned} \quad (3.26)$$

Through our choice of surface, we can state that  $dA = |\mathbf{d}\mathbf{A}| = dA_1$ . Hence, we can determine the total current by integrating Eq. (3.26) over the surface  $A$ .

$$S = \int_A dS = \rho_0 \sqrt{\frac{kT}{2\pi}} \int_A e^{-E(Y_1, \dots, Y_N)/kT} dA \quad (3.27)$$

Now we finally have the expressions required to the transition rate  $r_{\text{TST}}$ . We combine Eq. (3.18) with Eq. (3.20) and Eq. (3.27) to find

$$r_{\text{TST}} = \sqrt{\frac{kT}{2\pi}} \frac{\int_A e^{-E(Y_1, \dots, Y_N)/kT} dA}{\int_a e^{-E(x_1, \dots, x_N)/kT} dx^N}. \quad (3.28)$$

### Approximating the potential landscape

Now we have an expression that focuses around two areas: the plane  $A$  that passes through the saddle point in the potential landscape as well as the potential valley ‘a’. We can then expand the potential around these points, so the expansion around the minimum ‘a’ is

$$\begin{aligned} E|_{x_1 \approx x_{1,a}, x_2 \approx x_{2,a}, \dots} &= E(x_{1,a}, x_{2,a}, \dots) + \\ &\sum_{j,k=1}^N \frac{\partial_{x_j} \partial_{x_k} E(x_{1,a}, x_{2,a}, \dots)(x_j - x_{j,a})(x_k - x_{k,a})}{2} + \dots, \end{aligned} \quad (3.29)$$

where  $\partial_{x_j} \partial_{x_k} E(x_{1,a}, x_{2,a}, \dots)$  denotes the potential  $E$  derived by  $x_j$  and  $x_k$  at the point  $(x_{1,a}, x_{2,a}, \dots)$ . We terminate the expansion after the second order in an harmonic approximation. The first order of the expansion vanishes because we expand around the minimum.

The basis  $(x_{1,a}, x_{2,a}, \dots)$  can be transformed using a orthogonal transformation into a new basis  $(x'_{1,a}, x'_{2,a}, \dots)$ , where  $\partial_{x'_j} \partial_{x'_k} E(x'_{1,a}, x'_{2,a}, \dots)$  is diagonal [162] (discussed in detail by Lanczos [163]). Then the potential is approximated as

$$E|_{x_1 \approx x_{1,a}, x_2 \approx x_{2,a}, \dots} = E(x_{1,a}, x_{2,a}, \dots) + \sum_{j=1}^N \frac{(\partial_{x'_j})^2 E(x'_{1,a}, x'_{2,a}, \dots)(x'_{j,a})^2}{2} + \dots, \quad (3.30)$$

where  $x'_{j,a} = x'_j(x_{1,a}, x_{2,a}, \dots)$ . In the theory of small vibrations [164] we express the second derivative of the potential through small vibrations with the angular frequency  $\omega_i = 2\pi\nu_i$ , where  $\nu_i$  is a re-scaled ordinary frequency. Then we can express the potential close to ‘a’ as

$$E|_{x_1 \approx x_{1,a}, x_2 \approx x_{2,a}, \dots} \approx E(x_{1,a}, x_{2,a}, \dots) + \sum_{j=1}^N \frac{(2\pi\nu_j)^2 (q_j)^2}{2}, \quad (3.31)$$

where we describe the second derivative of the potential through vibrations around the point ‘a’:  $E_{j,2} = m\omega_j^2/2$ . In Eq. (3.31),  $q_j$  denotes the coordinates with respect to  $x_{j,a}$ . Note that the vibrations here correspond to eigenmodes of the particle in this potential.

A similar eigenmode expansion is made for the potential close to the saddle point contained in the surface  $A$ .

$$E|_{x_1 \approx x_{1,s}, x_2 \approx x_{2,s}, \dots} \approx E(x_{1,s}, x_{2,s}, \dots) + \sum_{j=1}^N \frac{(2\pi\nu_j t)^2 (q_j t)^2}{2} \quad (3.32)$$

Here,  $\nu_j t$  denote the re-scaled ordinary frequencies around the saddle point while  $q_j t$  describe the coordinates with respect to  $x_{j,s}$ . As the surface  $A$  is  $(N-1)$ -dimensional, we can set  $q_N t = 0$  without loss of generality. In a kinetic interpretation, this reduced dimensionality can be seen as an unstable oscillation that decays, because it follows the negative curvature of the potential<sup>2</sup>. All  $N - 1$  other oscillations follow the positive curvature and hence are stable. Correspondingly, there are  $N - 1$  stable oscillations at the saddle point, while the  $N^{\text{th}}$  eigenmode is unstable, and, therefore, does not contribute. As a result, the sum in the second order terms of the saddle point potential includes only  $N - 1$  eigenmodes in Eq. (3.32), instead of  $N$  in Eq. (3.31).

Including Eq. (3.32) and (3.31) into the rate given in Eq. (3.28), we can now explicitly integrate over the coordinates

$$\begin{aligned} r_{\text{TST}} &= \frac{\sqrt{\frac{kT}{2\pi}} e^{-E(x_{\text{saddle}})/kT} \prod_{j=1}^{N-1} \int_{q_j} e^{-(2\pi\nu_j t)^2 (q_j t)^2/kT} dq_j t}{e^{-E(x_a)/kT} \prod_{j=1}^N \int_{q_j} e^{-(2\pi\nu_j t)^2 (q_j t)^2/kT} dq_j t} \\ &= \left( \frac{\prod_{j=1}^N \nu_j}{\prod_{j=1}^{N-1} \nu_j t} \right) e^{-\left( E(x_{\text{saddle}}) - E(x_a) \right)/kT}. \end{aligned} \quad (3.33)$$

$$(3.34)$$

Note that the final expression, Eq. (3.34), uses the prefactor  $\nu_0 = \prod_{j=1}^N \nu_j / \prod_{j=1}^{N-1} \nu_j t$ , which is the ratio of eigenmode contributions at the potential minimum and saddle point [153].

### Rephrasing the attempt frequency

In the form presented in Eq. (3.33), the rate already contains the Arrhenius factor with the energy barrier  $\Delta E = E(x_{\text{saddle}}) - E(x_a)$  known from Kramer's rate given in Eq. (3.17). The main difference from other descriptions the rate prefactor, also called the 'attempt frequency'. In order to derive the form that we use in our simulations, I will modify the prefactor on the basis of both Vineyard's [155] and Hänggi's work [158].

In order to find the rate, we expanded the energy landscape in terms of a set of vibrational modes around the minimum and the saddle point in Eq. (3.32) and (3.31), respectively. We can now perform a harmonic approximation on the configurational partition functions at the points 'a' and 'saddle'. Note that we consider a configurational partition function<sup>3</sup> that is

<sup>2</sup>In the  $N$ -dimensional saddle point,  $N-1$  second derivatives are positive, denoting a parabolic potential in which harmonic oscillations are stable. However, the  $(\partial_{x^N})^2 E(x_{1,s}, x_{2,s}, \dots) < 0$ , denoting an unstable direction. Any particle motion away from the saddle point move the particle onto a negative gradient of the potential, pushing the particle away from the saddle point. Oscillations in this direction cannot be stable.

<sup>3</sup>The momenta are treated as a constant contribution that cancels out, as we are considering a small deviation from equilibrium [see Eq. (3.20)].

constrained to the surface  $A$  at ‘saddle’ [158]

$$Z_a \approx \prod_{j=1}^N \left( \frac{kT}{h\nu_j} \right) e^{-E(a)/kT}, \text{ and} \quad (3.35)$$

$$Z_{\text{saddle}} \approx \prod_{j=1}^{N-1} \left( \frac{kT}{h\nu_j'} \right) e^{-E(\text{saddle})/kT}, \quad (3.36)$$

where  $Z_a$  and  $Z_{\text{saddle}}$  are the (constrained) configurational partition functions at the minimum and the saddle point, respectively. Note that the expansion of the partition functions in terms of their eigenmodes is a quadratic approximation in accordance with the eigenmode-series in Eq. (3.33). Including Eq. (3.35) and (3.36) in the rate, we find [158, 161]

$$r_{\text{TST}} = \left( \frac{kT}{h} \right) \frac{Z_{\text{saddle}}}{Z_a} = \left( \frac{kT}{h} \right) e^{\Delta S/k} e^{-\Delta E/kT}, \quad (3.37)$$

where  $\Delta S = S(x_{\text{saddle}}) - S(x_a)$  is the change in entropy between the potential valley and the saddle point. This difference is usually treated as constant and temperature-independent. For COMs that have a lot of internal degrees of freedom, this is not generally the case [165]. However, for our two COMs C<sub>60</sub> and 6P,  $\Delta S(T) = \text{const.}$  is a good approximation.

The nearly spherical molecule C<sub>60</sub> does not have a lot of internal degrees of freedom, which allows us to assume that  $\Delta S(T)$  is constant and atom-like (discussed in more detail in Sec. 5.2). This assumption is supported through the very good agreement of our parameters with literature values (see Sec. 7.1.2). This agreement also strongly supports this approximation, because our parameter set was fitted to experimentally determined observables (which include entropic effects), while the literature values were determined from DFT and analytic calculations (which do not include entropic effects).

The second material, 6P, has a lot of internal degrees of freedom. However, recent MD simulations have shown that the attempt frequency is not temperature-dependent for a wide span of temperatures [106]. Hence,  $\Delta S$  can be assumed as temperature-independent for 6P, however the value needs to be determined using an Arrhenius-plot of the molecular diffusion constants determined from extensive MD simulations [106]. Based on this analysis of the entropy-influence, all diffusion rates used in the rest of this thesis will be based on the expressions given in Eq. (3.37) with an interpretation using the equivalent form of this rate, given in Eq. (3.34). The prefactor will always be assumed as a constant, reflecting the temperature independence of  $\Delta S$  for our material systems.

## 3.2 Markov process

The rates derived from Transition-State-Theory, as well as Kramer’s rate both are based on the concept of particles losing the memory of their previous trajectory upon entering the potential well. This means that every diffusion step of a particle is independent of the particle’s previous trajectory; every diffusion step depends exclusively on the current configuration. Such a diffusion process is called a ‘Markov process’.

In other words, the probability of a configuration only depends on the previous configuration, i.e.

$$P(\sigma_{t_m} | \sigma_{t_0} \sigma_{t_1} \dots \sigma_{t_{m-1}}) = P(\sigma_{t_m} | \sigma_{t_{m-1}}), \quad (3.38)$$

or, if expressed in terms of the transition probabilities  $G(\sigma_{t_{m-1}} \rightarrow \sigma_{t_m})$  between the configurational states  $\sigma_{t_{m-1}}$  and  $\sigma_{t_m}$ :

$$P(\sigma_{t_m}) = G(\sigma_{t_{m-1}} \rightarrow \sigma_{t_m}) P(\sigma_{t_{m-1}}). \quad (3.39)$$

A succession of Markov processes is called a ‘Markov chain’, where the probability of the final configuration  $P(\sigma_{t_m})$  can be described through a chain of transition probabilities,

$$P(\sigma_{t_m}) = G(\sigma_{t_{m-1}} \rightarrow \sigma_{t_m}) \dots G(\sigma_{t_2} \rightarrow \sigma_{t_3}) G(\sigma_{t_1} \rightarrow \sigma_{t_2}) P(\sigma_{t_1}). \quad (3.40)$$

If the processes constituting the Markov chain are diffusion processes, the diffusion motion is called a ‘random walk’, where the term ‘random’ alludes to the stochastic Markovian property of the motion.

Note that the assumption that processes can be described through Markov processes is the underlying principle on which the master equation Eq. (2.5) is based. As all DMC simulations are based on the master equation (as discussed in Sec. 2.3). In this way, the Markov assumption is fundamentally important for the simulation of surface growth using DMC methods.

If a network of states that is connected through a reaction network fulfils detailed balance (discussed in Sec. 2.2) then corresponding Markov chain also fulfils detailed balance [166].

### 3.3 Diffusion on a lattice

In Sec. 3.1 we derive two different expressions for diffusion rates for the transition between potential. For a particle diffusing on a crystalline substrate, these potential wells correspond to lattice sites<sup>4</sup>. A single particle that diffuses with a constant diffusion rate

$$r = \nu_0 e^{-\Delta E/kT} \quad (3.41)$$

from site to site, allows us to relate the energy barrier  $\Delta E$  and the attempt frequency  $\nu_0$  to a diffusion coefficient  $D$ .

#### 3.3.1 Random walk on a 2D lattice

For a random walk on a 2D lattice (assuming the length  $a$  for each step  $j$ ), a single step can be described as motion in the complex plane with the displacement  $a e^{i\theta_j}$  such that one particle travels a displacement

$$x = \sum_{j=1}^N a e^{i\theta_j} \quad (3.42)$$

---

<sup>4</sup>Strictly speaking this particle is a ‘test particle’, because its motion is assumed to not influence the potential landscape that it is diffusing in.

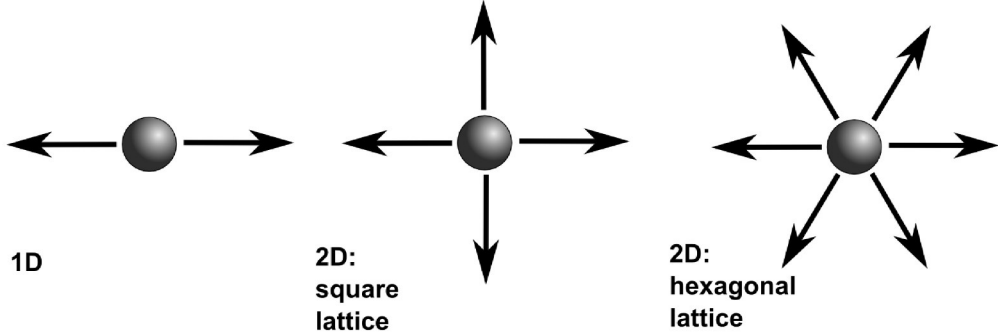


FIGURE 3.4: Sketched diffusion paths for a particle in a 1D system, a particle on a 2D lattice with a square lattice configuration and a particle on a 2D lattice with a hexagonal lattice configuration. The number of possible diffusion paths is 2, 4 and 6 respectively.

in  $N$  steps. This description is independent of the lattice geometry, as  $\theta_j$  can take any value to suit the lattice geometry. Furthermore, the ratio of particle diameter to lattice constant  $a$  has no influence on this consideration.

The particle displacement  $x$  has the absolute square

$$|x|^2 = a^2 \sum_{j=1}^N e^{i\theta_j} \sum_{m=1}^N e^{-i\theta_m} \quad (3.43)$$

$$= a^2 \sum_{j=1}^N \sum_{m=1}^N e^{i(\theta_j - \theta_m)} \quad (3.44)$$

$$= a^2 N + a^2 \sum_{j,m=1; j \neq m}^N e^{i(\theta_j - \theta_m)}. \quad (3.45)$$

Assuming that the directions of steps cancel out because opposite steps are equally likely, we find the mean square displacement (MSD)

$$\Delta x(t)^2 = \langle |x|^2 \rangle = a^2 N + a^2 \left\langle \sum_{j,m=1; j \neq m}^N e^{i(\theta_j - \theta_m)} \right\rangle \quad (3.46)$$

$$= a^2 N, \quad (3.47)$$

The MSD corresponds to the variance of the position. In random walks, the average position in an ensemble does not change, i.e.  $\langle \Delta z \rangle = 0$ .

### 3.3.2 Diffusion rates on a 2D lattice

The MSD is related to the diffusion rates via the number of steps  $N$ , as a particle can take  $N = t/\Delta t$  steps on the lattice in time  $t$ . For diffusion on corrugated surfaces, the mean residence time  $\tau$  quantifies the average time that the particle takes to escape from a lattice site. Note that this is not equivalent to the time it takes for one specific escape process because there may be several processes that allow the particle to escape from one lattice site. If the escape via a single escape route takes  $\tau_l = 1/r^D$ , then the mean residence time can be assumed to scale with the number of escape routes  $N_r$ , i.e.  $\tau = 1/(N_r r^D)$ . On a square 2D lattice,

there are four equally probable escape routes (see Fig. 3.4), so

$$\tau = \frac{\tau'}{4} = \frac{1}{4r^D} = \frac{1}{4\nu_0^D \exp(-\Delta E/kT)}. \quad (3.48)$$

We assume that the time the particle needs to actually execute one escape process is much smaller than  $\tau'$ , i.e. the processes themselves are quasi-instantaneous and the majority of  $\tau'$  is waiting time. Thus we can approximate the diffusion as a series of subsequent, independent, instantaneous escape processes. We model this chain of processes with a random walk model by setting  $\Delta t = \tau$ . Incorporating this into our expression for the mean-squared displacement, we arrive at

$$\Delta x(t)^2 = a^2 t \cdot 4\nu_0^D \exp(-\Delta E/kT). \quad (3.49)$$

Note that the MSD depends linearly on time, which reflects the free diffusion of the particle. If the MSD scales slower (faster) than linearly with  $t^*$ , the particle motion is called sub-diffusive (super-diffusive) [167].

### 3.3.3 Deriving the diffusion coefficient

To determine the diffusion coefficient  $D$ , we use the following definition for free diffusion [61]

$$\Delta x(t)^2 = 2nDt, \quad (3.50)$$

which reflects the linear time dependence of free diffusion, as found Eq. (3.49). The prefactor 2 accounts for forwards and backwards motion (see Fig. 3.4), while  $n$  denotes the number of spatial dimensions that are included in the particle trajectories. Here  $n = 2$ .

$$\Delta x(t)^2 = 4Dt = a^2 t \cdot 4\nu_0^D \exp(-\Delta E/kT), \quad (3.51)$$

which gives us an analytic expression for the diffusion coefficient  $D$

$$D = a^2 \nu_0^D \exp(-\Delta E/kT). \quad (3.52)$$

This expression holds only if all diffusion processes have the same diffusion rate. In general, however, particles interact with other particles, the substrate, step-edges and defects. These interactions have an influence on the energy barriers. Correspondingly, more care needs to be taken during modelling, and the modelling needs to be tailored to the material system. In order to study specific effects, we use the insight gathered in this and the last chapter and now progress to refining the description for isotropic particles. Specifically, the next part of the thesis will centre around the nearly spherical nano-molecule C<sub>60</sub>.

## Part II

Isotropic particles: C<sub>60</sub>



## Chapter 4

# Introducing the isotropic particle $C_{60}$

Fullerenes are spherical all-carbon molecules, with a high internal symmetry. Different numbers of carbon atoms may be used to form approximately spherical hollow all-carbon molecules, such as 60, 70, 72, 74, or 76 carbon atoms [169]. The fullerene  $C_{60}$  (with 60 carbon atoms) is especially stable and is closest to spherical in shape (see Fig. 4.1(a)). The spherical shell

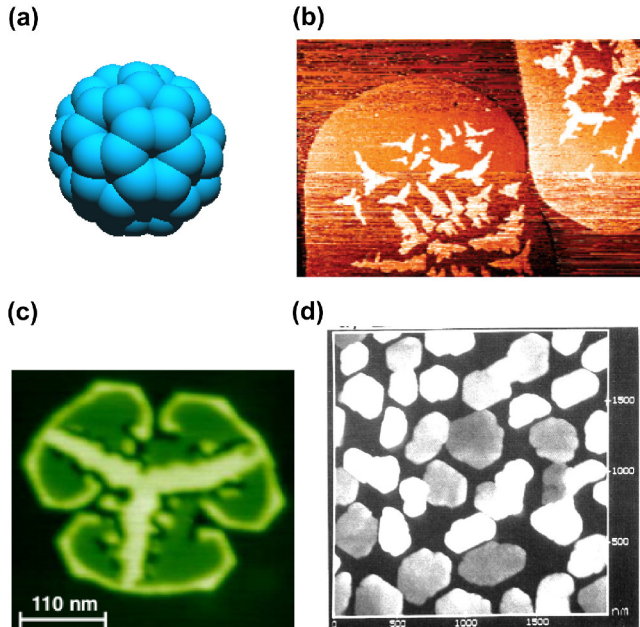


FIGURE 4.1: Snapshots from  $C_{60}$  growth. Part (a) depicts the molecule itself, while parts (b)–(d) show atomic force/scanning tunnelling microscopic measurements of growth structures on different substrates, taken from various publications. The first experimental image, part (b), is adapted from the work of Liu *et al.* [69] and depicts fractal islands of  $C_{60}$  deposited on rounded islands of  $C_{60}$  deposited on graphite. The  $C_{60}$  coverage in this image is less than 2 monolayers, and the width of the image is  $1.5\ \mu\text{m}$ . Part (c) depicts a single dewetted  $C_{60}$  island on  $\text{CaF}_2$  for a coverage of less than two monolayers [118]. Finally, part (d) depicts an approximately 80 nm (i.e. of the order of  $\mathcal{O}(100)$  monolayers) thick film of  $C_{60}$  on mica and is adapted from the work of Busmann *et al.* [168].

formed by the carbon atoms has a diameter of  $\approx 7 \text{ \AA}$  [170], which results in a molecule with a van-der-Waals diameter of  $\approx 1 \text{ nm}$  [51, 54]. This van-der-Waals radius determines the crystal lattice, where the molecular centres of mass are approximately 1 nm apart [171]. The carbon shell of  $C_{60}$  displays delocalised orbitals similar to aromatic molecules. As  $C_{60}$  is not aromatic according to conventional rules, this aromatic character may be referred to as ‘spherical aromaticity’ [172].

$C_{60}$  naturally occurs in minerals such as Shungite [173], and is even formed in outer space [174], making it one of the largest compounds that is currently known to exist outside the earth atmosphere [175]. However, the natural occurrences do not yield high concentrations of  $C_{60}$ , hence the molecules are normally produced using techniques such as an electric arc between two carbon electrodes that are placed in inert surroundings [176].

**Interest in  $C_{60}$ .** Among the widely spread applications of  $C_{60}$  in engineering [177, 178] and medicine [179–181], I will here highlight its application in opto-electronics, such as OPVs [182, 183] and OLEDs [184]. The large conjugated orbitals of  $C_{60}$  result in low-lying excited states, which give  $C_{60}$  a high electron affinity and make it an ideal acceptor material in solar cells [185]. In order to optimise this functionality, a broad variety of different derivatives of  $C_{60}$  have been synthesised [186], mostly involving small molecular end groups attached to one of the carbon atoms. As discussed in Sec. 1.1, understanding the growth morphology is a prerequisite for design and optimisation of devices such as solar cells because device efficiency depends on the interface configuration of molecules.

In addition to these applications,  $C_{60}$  is also of fundamental interest. Its size and shape makes it a unique sample system to study the transferability of knowledge from atomic and colloidal systems to the COM-length-scale. Various aspects of this feature were previously discussed in Sec. 1.2. Therefore I will only briefly summarise here: The relative range of the pair attractive interaction between two  $C_{60}$  molecules [51, 54] is shorter than between two atoms [50], but longer than between two colloidal particles [52, 53, 60]. Accordingly,  $C_{60}$  is expected to have a very small or no liquid phase [54, 58, 65, 66] but it is expected to form a gel-phase [67] which is commonly associated with short-ranged interactions. Here, we are primarily interested in the influence of short interaction range on the growth behaviour of  $C_{60}$ .

**Growth experiments.** Real-space experimental approaches to understand the growth of COMs such as  $C_{60}$  include scanning-electron [69, 78], electron [85, 187] and atomic-force microscopy [28, 76, 118, 168]. Examples of such studies are depicted in Fig. 4.1 (b)-(d), which show atomic-force and scanning tunnelling images of a  $C_{60}$  surface during growth. The common procedure for such imaging involves shutting down the source, waiting until most of the non-adsorbed molecules are extracted from the growth chamber, extracting the substrate from the growth chamber, transferring it to the measurement chamber, setting up the measurement devices and finally measuring the surface. This procedure takes approximately half an hour [188], giving the molecules on the substrate sufficient time to relax from their growth configuration. The resulting configuration is likely to be a steady-state configuration, somewhere between the growth configuration and the equilibrium configuration (see Sec. 1.3). The assumption that the structures relax is strongly supported by the experiments performed in our collaboration with S. Bommel *et al.* [119], where  $C_{60}$  on mica clearly dewets after the end of

growth. The dewetting is further supported by studies of C<sub>60</sub> on CaF<sub>2</sub>, where the structure is dominated by dewetting [118] (see Fig. 4.1 (c)).

Scattering measurements such as Raman [189] and X-ray scattering [83] avoid dewetting effects because they are simultaneous and do not require the transport of the substrate to a measurement chamber. Hence, the simulations are compared with real-time *in situ* X-ray scattering measurements in the collaboration with S. Bommel *et al.* [119]. The experimental setup combines specular growth oscillations [75, 190] with diffuse scattering [191–193] (see Fig. 4.2 for an overview). This approach allows a real time-observation of both average in-plane and out-of-plane morphology. It was successfully used in several studies of COM growth in order to extract real-time information without interfering with growth or observing dewetting effects [75, 194]. The experimental setup and the information gained from the experiment are introduced in Sec. 5.1. However, as I only performed the theoretical side of the studies, I would like to refer readers to our collaborative publication [119] as well as additional publications of the group of S. Kowarik for details on the experiment (see Refs. [195–197]).

**Theoretical understanding of C<sub>60</sub>.** On a theoretical level, C<sub>60</sub> and its growth properties have been studied on different length-scales using various approaches. I previously discussed some of these in Chap. 1.4, so I will summarise the most relevant approaches here. Analytic descriptions on the single molecule level give insight into the pair-interaction potential [51, 54], as well as the interaction potential of a single C<sub>60</sub> molecule adsorbed to a C<sub>60</sub> (111) surface [198]. On a more coarse-grained level, MD simulations have been employed to study the potential landscape and single-particle trajectories of a C<sub>60</sub> molecule on Pentacene [199], as well as studying the step-edge barrier that a C<sub>60</sub> molecule has to overcome to move off an island in C<sub>60</sub> (111) multilayer growth [102]. On the level of several C<sub>60</sub> molecules, DMC studies of growth exist, such as the growth of C<sub>60</sub> islands on a single layer of C<sub>60</sub> on graphite [69] as well as C<sub>60</sub> dewetting on CaF<sub>2</sub> [118]. However, prior to our work, no parametrisation for the full multilayer growth of any COM existed, each study gave insight into only a subset of system properties.

In this thesis a minimal coarse-grained description for multilayer growth of C<sub>60</sub> is developed. This description gives insight into the real-space evolution of the surface and its morphology during growth, which are not accessible in experiments. The parametrisation of our minimal model enables quantitative prediction of growth, but it also gives insight into the similarities and differences of C<sub>60</sub> growth compared with colloidal and atomic growth (see Sec. 1.2 for more background). Further, single-particle dynamics can be studied and correlated to the morphology. Single-particle dynamics and morphology are used to pinpoint the influence of energetic differences between atomic and COM systems. The study of the rotationally symmetric prototypical system C<sub>60</sub> gives first insights into the fundamental principles governing COM growth, which are discussed in the current part of the thesis, Part II.

This fundamental understanding will be expanded to describe anisotropic molecules and structured substrates in Part III of the thesis.

**Structuring of the following sections.** This part of the thesis is structured as followed: Chap. 5 introduces the experiment (in Sec. 5.1), theoretical background (in Sec. 5.2) and algorithm specifics for C<sub>60</sub> growth (in Sec. 5.3). Next, Chap. 6 introduces the observables, before

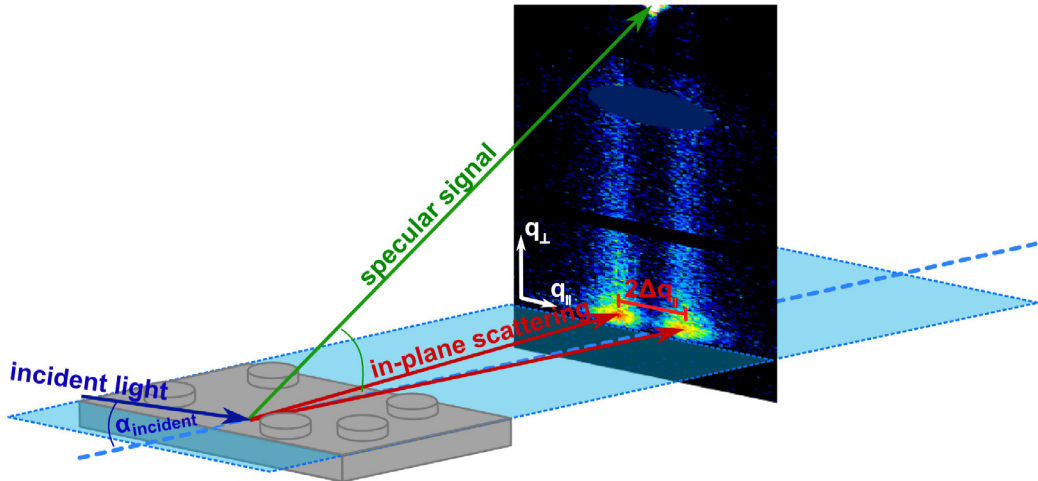


FIGURE 4.2: Sketched experimental measurement process. The incident X-ray beam is depicted in blue. In the measurement, the specular scattering signal and the in-plane scattering signal are measured simultaneously as a function of time. Correspondingly, the scattering image on the right hand side contains information vertical to the substrate plane (parallel to  $q_{\perp}$ ) and parallel to the substrate plane (parallel to  $q_{\parallel}$ ). The scattering image used in this sketch is a measurement snapshot from  $C_{60}$  growth, courtesy of S. Bommel.

Chap. 7 discusses the results obtained for the simulation of  $C_{60}$  multilayer growth. Here, special focus is placed on the theoretical understanding and prediction of experimental results (in Sec. 7.1), and on the similarities and differences between  $C_{60}$ , atomic, and colloidal growth (in Sec. 7.2). Finally, Chap. 8 gives a concluding overview over the different aspects of  $C_{60}$  multilayer growth.

## Chapter 5

# Experimental and theoretical understanding of C<sub>60</sub> growth

Our simulations of C<sub>60</sub> growth were performed using a coarse-grained KMC algorithm, and some of the questions we consider are based on our close collaboration with X-ray scattering measurements. Here, I will give a short overview over the experiments performed by S. Bommel, C. Weber, H. Spranger, P. Schäfer, J. Novak, S. V. Roth, F. Schreiber, and S. Kowarik [119] in Sec. 5.1, before discussing details of the system modelling in Sec. 5.2, as well as some aspects of the employed algorithm in Sec. 5.3.

### 5.1 Experimental set-up and measurements

This section is based on Refs. [119] and [75]. Note that we did not perform any experiments ourselves. However, we were in close collaboration with the experiments, especially concerning the interpretation of the experimental data. So, I will briefly discuss the most fundamental aspects of the experimental setup and conclusions drawn from the measurement here.

In the experiment, multilayer growth of C<sub>60</sub> was performed on mica and studied in real time. Mica has a suitable lattice constant  $a_{\text{mica}} \approx 0.5 \text{ nm}$ [200] for C<sub>60</sub> to grow in strain-free layer-by-layer growth [171], which is also called Frank-van der Merwe growth [201–203]. The well-defined layer-by-layer growth makes mica the ideal substrate to study C<sub>60</sub> homoepitaxy, as the substrate influence is minimal.

As previously discussed in Sec. 1.3.2 and also briefly in Sec. 4, X-ray scattering measurements are ideal to study time resolved growth, while other methods such as scanning microscopic approaches require repeated interruptions of the growth process, and, hence, relaxation of the growth structures. In the context of C<sub>60</sub> on mica, it may even be the only time-resolved measurement technique applicable in our collaboration, as we find that the system dewets on a time scale of approx. 10 minutes, and charging effects in the mica substrate make electron measurements such as low energy electron microscopy impossible [119].

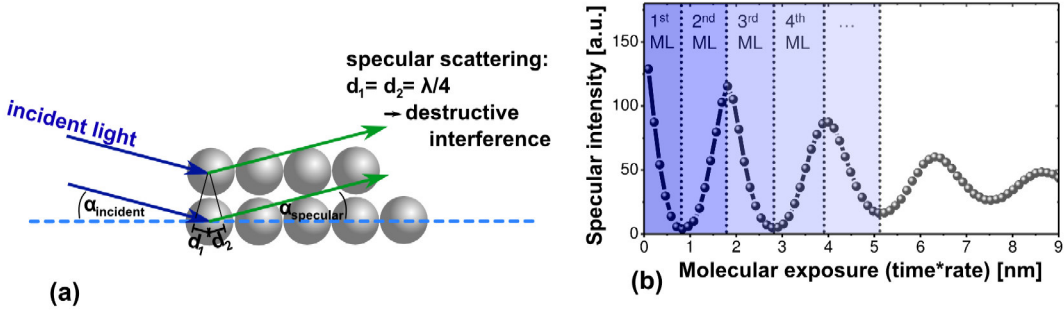


FIGURE 5.1: The principle concept of specular scattering. Part (a) contains a sketch of the principle behind specular scattering. The specular signal is measured under an angle  $\alpha_{\text{specular}} = \alpha_{\text{incident}}$ . The incident angle is the anti-Bragg angle that corresponds to the anti-Bragg point (discussed in Sec. 5.1.1). Correspondingly, every second layer interferes constructively. Part (b) depicts a measurement of the specular intensity as a function of time during multilayer growth of  $C_{60}$  (courtesy of S. Bommel). The alternating destructive and constructive interference of  $C_{60}$  layers leads to an oscillation of the intensity as a function of the number of layers. Note that this data set was measured for the temperature  $T = 60^\circ \text{C}$ , an adsorption rate of  $f = 0.1 \text{ ML/min}$  and an incidence angle of  $\alpha_{\text{incident}} = 1.65^\circ$ .

During the growth procedure, the X-ray signal of specular and in-plane scattering, sketched in Fig. 4.2 are measured simultaneously as a function of time. These contain average in-plane and out-of-plane information during growth.

### 5.1.1 Specular scattering

The specular scattering intensity is measured at the so-called anti-Bragg point. Here, a layer of adsorbed  $C_{60}$  molecules scatters with a phase shift of  $\pi$  compared to the previous layer, which results in destructive interference [depicted in Fig. 5.1 (a)]. However, every second layer scatters with a phase shift of  $2\pi$ , resulting in constructive interference. So, while the scattering signal of the second monolayer interferes destructively with the signal of the first monolayer, the signal of the third monolayer will interfere constructively with the signal of the first monolayer, and so forth. In order to achieve this interference pattern, the anti-Bragg point is situated at half the out-of-plane distance of the Bragg point. At the Bragg point, the scattering signal of all layers interferes constructively. The Bragg point has the coordinates  $q_{\perp, \text{Bragg}}$  and  $q_{\parallel, \text{Bragg}} = 0 \text{ \AA}$ . Correspondingly, the anti-Bragg point has the coordinates  $q_{\perp, \text{anti-Bragg}} = 1/2 q_{\perp, \text{Bragg}}$  and  $q_{\parallel, \text{anti-Bragg}} = q_{\parallel, \text{Bragg}} = 0 \text{ \AA}$ . During growth, as monolayer upon monolayer is filled, the alternating constructive and destructive interference causes the intensity of the signal at the anti-Bragg point to oscillate, depicted in Fig. 5.1 (b). For  $C_{60}$  on mica, the intensity-modulation is up to 90%, indicating nearly perfect layer-by-layer growth [119].

For layer-by-layer growth, the periodicity of the intensity modulation makes it possible to extract the times required to fill the first monolayer, the second monolayer, etc. Note that the time-axis is re-scaled with the effective net adsorption rate  $f = f_{\text{adsorb}} - f_{\text{desorb}}$  in Fig. 5.1 (b). This allows us to express time in terms of molecular exposure. The molecular exposure is equal to  $f t c k$ , where  $c = 0.81 \text{ nm}$  is the out-of-plane lattice constant and  $k$  is a sticking coefficient. The sticking coefficient is extracted from experiment. It is exactly one for the first monolayer and slightly larger than one for subsequent layers [119]. Correspondingly, the first monolayer is filled for a molecular exposure of  $0.81 \text{ nm}$ . We exploit the fact that the light scattered from

two successive layers has a phase shift of  $\pi$  at the anti-Bragg point. The scattering intensity at the anti-Bragg point then is

$$I_{\text{anti-Bragg}}(t) = \left| A_{\text{sub}} e^{i\varphi_{\text{sub}}} + f(q_{\perp, \text{anti-Bragg}}) \sum_n \Theta_n(t) e^{in\pi} \right|^2 \quad (5.1)$$

where  $A_{\text{sub}}$  is the scattering amplitude of mica,  $\varphi_{\text{sub}}$  is the scattering phase of mica,  $f(q_{\perp})$  is the molecular form factor of  $C_{60}$  and  $\Theta_n(t)$  is the layer coverage of the  $n^{\text{th}}$  layer at time  $t$ . An iterative procedure is used to extract the layer coverage from data of the form depicted in Fig. 5.1 (b) using Eq. (5.1). The coverages are extracted using an analytic growth model for the coverages [204] that were derived and discussed by Trofimov *et al.* [205, 206]. Other rate equation descriptions exist [207] and have been compared [208]. The Trofimov model is found to quantitatively describe the X-ray reflectivity during the growth of organic molecules [208].

Note that the scattering amplitudes and phases of  $C_{60}$  and mica interfere such that the scattering intensity reaches nearly zero. This is a serendipitous coincidence that has no consequences for the growth behaviour, but gives us a very nice curve for the intensity oscillations. The fit parameters found by S. Bommel *et al.* in the scope of our collaboration are

$$f(q_{\perp}) = 0.92A_{\text{mica}} \text{ and } \varphi_{\text{sub}} = 170^\circ.$$

### 5.1.2 In-plane scattering

The in-plane scattering signal results from the interference of light that is diffusely scattered from structures on the substrate, as depicted in Fig. 5.2. It reflects different in-plane length-scales in the system during growth, such as the particle diameter and the cluster density. The length-scale resolved in this experiment corresponds directly to the average island distance at time  $t$  [209, 210]

$$\bar{D}(t) \approx \frac{2\pi}{\Delta q_{\parallel}(t)}. \quad (5.2)$$

This observation is supported by the excellent overlap of the in-plane scattering intensity distribution with the Fourier transform of atomic-force structures for thick  $C_{60}$  films on mica [119]. The Fourier transform allows us to identify the two symmetric in-plane intensity peaks since the scattering signal associated with the average island distance.

Assuming a hexagonal island arrangement with an island distance  $\bar{D}(t)$ , i.e. one island per surface  $\sqrt{3}/2\bar{D}(t)^2$ , the island density can be derived directly from the in-plane scattering data as

$$N(t) = \frac{2}{\sqrt{3}} \frac{1}{\bar{D}(t)^2}. \quad (5.3)$$

For further details on the experimental observables as well as technical details of the measurement, I would like to refer the reader to our joint publication [119] and S. Bommel's PhD thesis [197]. My work concerns the simulation, interpretation and the prediction of the experiment, as well as fundamental understanding that can be derived thereof.

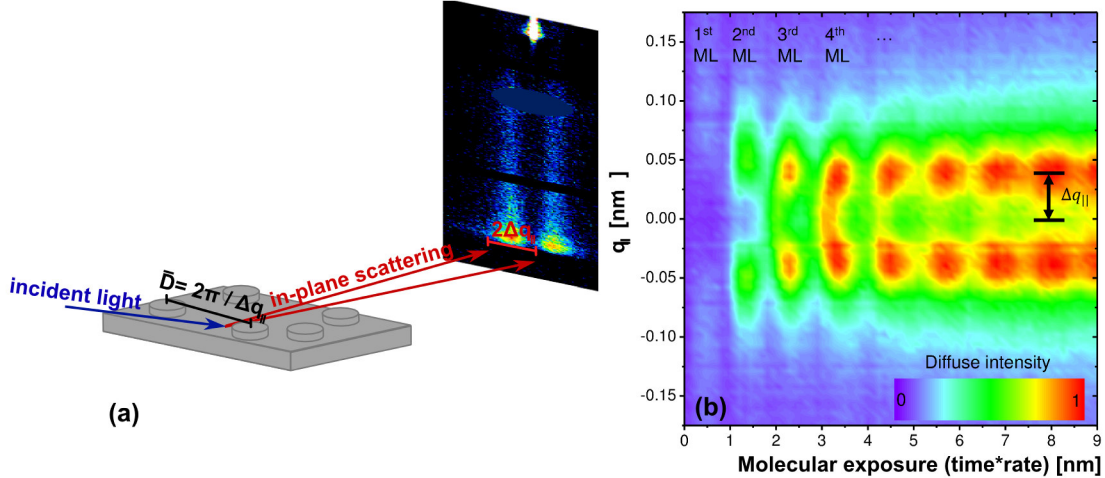


FIGURE 5.2: In-plane X-ray scattering. Part (a) depicts a sketch of the set-up, where the scattering image corresponds to the image depicted in Fig. 4.2. The in-plane scattering signal reflects the lateral length-scales of the signal. Studying small angles, i.e. finely resolving  $q_{\text{parallel}}$ , gives information on the larger lateral length-scales. The distance  $2\Delta q_{\text{parallel}}$  between the two symmetric intensity peaks are related to the average island distance  $\bar{D} \approx 2\pi/\Delta q_{\text{parallel}}$ . During growth these two peaks oscillate both in intensity and position while islands nucleate and coalesce (see Part (b)). The position of the intensity maximum depends on the specific monolayer observed. This image is courtesy of S. Bommel, and was measured for multilayer growth of  $C_{60}$  under the conditions listed for Fig. 5.1.

## 5.2 Coarse-graining for isotropic particles

In order to simulate multilayer growth of  $C_{60}$  on a system, we use a rate description as introduced in Chap. 3. In this description the most significant processes during surface growth are described through rates, neglecting the previous system trajectory. Following the rate description given in Eq. (3.37), we describe all diffusion processes on the surface as

$$r_{\text{diff}} = \left( \frac{2kT}{h} \right) e^{-\Delta E/kT}. \quad (5.4)$$

The pre-factor is chosen in accordance to models used in literature (see Refs. [138, 139, 211]).

The most significant diffusion processes for a spherical particles are depicted in Fig. 5.3: free diffusion on the surface (green), interaction with neighbouring particles (blue) and step-edge crossing (purple). Note that rotational diffusion is neglected. This assumption is based on the observation that at the range of temperatures considered,  $C_{60}$  rotates freely in linear confinement [212] and in its bulk crystal [213]. Further studies have shown that even at lower temperatures the rotational degrees of freedom of  $C_{60}$  can be neglected for centre-of-mass distances larger than 9.5 Å [199]. Based on these studies we neglect the rotational degrees of freedom of  $C_{60}$  and study only translational diffusion using Eq. (5.4). Neglecting internal degrees of freedom effectively results in an atom-like modelling of  $C_{60}$ . Only the exact parametrisation of the energy barrier  $\Delta E$  distinguishes it from atomic systems. We determine  $\Delta E$  in accordance to the experiment discussed above. However, in order to simulate systems large enough and length-scales broad enough to resolve  $\Delta E$ , we implement several approximations that I will discuss in the following paragraphs.

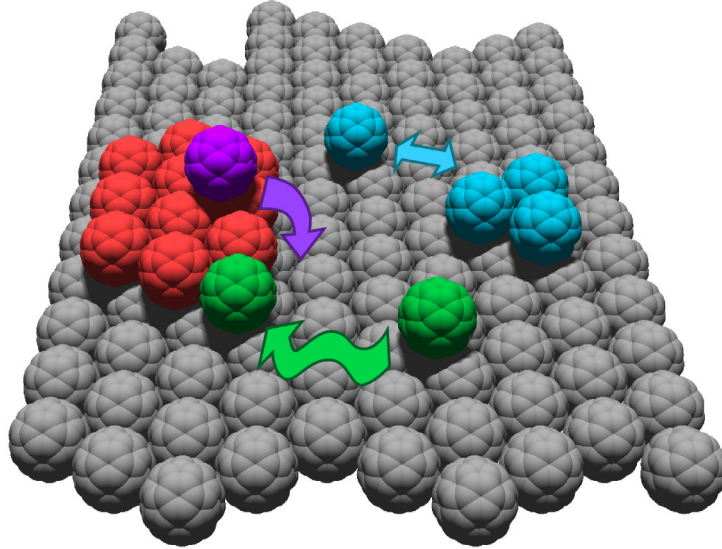


FIGURE 5.3: Sketched diffusion processes that occur most frequently during multilayer growth of  $C_{60}$ : Free diffusion of a single particle on the surface (green), detachment of a particle from a cluster of particles (blue) and step-edge crossing of a particle (purple). The particles forming the island that the purple particle is diffusing down from are drawn in red.

**Homoepitaxy on a lattice.** As discussed at the beginning of Sec. 5.1,  $C_{60}$  forms strain-free hexagonal layers on mica [171]. The strain-free growth is indicated by a high quality crystallinity because, in contrast, strain creates deviations of particle positions that destroy the crystallinity. The high crystallinity of  $C_{60}$  is proven by scattering measurements of our experimental collaborators. Rotating the X-ray source shows very narrow and clear peaks in the in-plane scattering intensity every  $60^\circ$ . These clear peaks indicate negligible deviations from perfect crystalline growth [119].

Furthermore, in our growth scenario, the first monolayer of  $C_{60}$  on mica is filled more than 90% in the experiments before the next monolayer starts to form. Based on the lack of strain, the high coverage of the first  $C_{60}$  layer on the mica substrate, and on the high crystallinity of the growing structure, we make the following assumptions

- We can neglect the mica substrate and model  $C_{60}$  growth as  $C_{60}$  homoepitaxy from the second monolayer onward.
- We restrict  $C_{60}$  molecules to the lattice sites of the growing fcc(111) lattice.

Note that the bulk crystal of  $C_{60}$  molecules has a fcc lattice [214], so the hexagonal growth of  $C_{60}$  on mica follows the fcc(111) structure with an in-plane lattice constant of  $a \approx 1\text{ nm}$  [171]. This implies an ABCABC-stacking of hexagonal layers, neglecting interstitial sites (see Figs. 5.4 and 5.5 for details). Correspondingly, we also neglect stacking faults and domain formation through interstitial sites. Considering the lattice depicted in Fig. 5.4, domain formation would arise if some islands on sites marked with red crosses, while other islands nucleate on sites marked with blue boxes. Neglecting domain formation is supported by the strong minima in the experimentally observed island density that occur when islands merge to form a closed filled layer (see e.g. Fig. 7.2 in Chap. 7). If significant domain formation were present, then the islands would not be able to merge and the island density would vary much less.

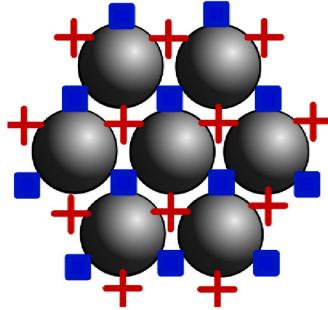


FIGURE 5.4: Sketched fcc(111) crystal facet. The sites of potential minima on this facet are marked through red crosses and blue boxes. Note that only one subset of these sites — either all red crosses or all blue boxes — can be occupied simultaneously because of steric repulsion. Without loss of generality, assume that the red crosses are the sites that correspond to the bulk crystal (i.e. they fulfil ABC-stacking, see Fig. 5.5). Then, the blue boxes mark the so-called ‘interstitial sites’.

Defect-free growth is further motivated through the high crystallinity with the clean and narrow scattering peaks every  $60^\circ$ . However, in general, domain boundaries, stacking faults and other defects cannot be excluded completely in the experiments.

While DMC simulations without a lattice of positions are possible [150, 151], they require finding all energetic saddle points in any given configuration, making them extremely costly (discussed in Sec. 3.1). Therefore, they are not well suited for our time- and length-scales (see Sec. 5.1).

**Solid-on-solid assumption.** The solid-on-solid assumption is a common implicit assumption in modelling approaches, such as the rate descriptions used to fit experimental data (see Refs. [205, 206]) and the majority of DMC simulations. In this approximation, we assume that particles do not form overhangs or defects, i.e. that every lattice site supporting a particle is filled. On a hexagonal lattice, this means that the three sites below each particle are filled. Figure 5.5 shows that each particle touches exactly three particles in the lower layer. These three particles form the support of the particle above them. If a particle lands on a not fully-supported lattice site, it will relax until it reaches a fully supported lattice site. As  $C_{60}$  grows in a layer-by-layer fashion where layers fill nearly completely under our experimental conditions (see Fig. 5.1 and Chap. 7), the assumption of solid-on-solid growth is a small approximation to the system; however, it needs to be treated with care in rough growth regimes.

**Splitting the potential.** Using the assumptions discussed in the last paragraph, we model diffusion through the motion of the top-most particles between two lattice sites on a  $C_{60}$  substrate. Reflecting this assumption, we will split the energy barrier  $\Delta E$  into three parts: First, the energy barrier that a single particle on a closed  $C_{60}$  layer must overcome to move from one site to its neighbouring site,  $E_D$ . Second, the additional interaction due to neighbouring particles,  $E_{\text{neighbours}}$  is included. Lastly, we included an additional interaction reflecting the layer the site of origin and the site of destination are in,  $E_{\text{layer}}$

$$\Delta E = E_D + E_{\text{neighbours}} + E_{\text{layer}}. \quad (5.5)$$

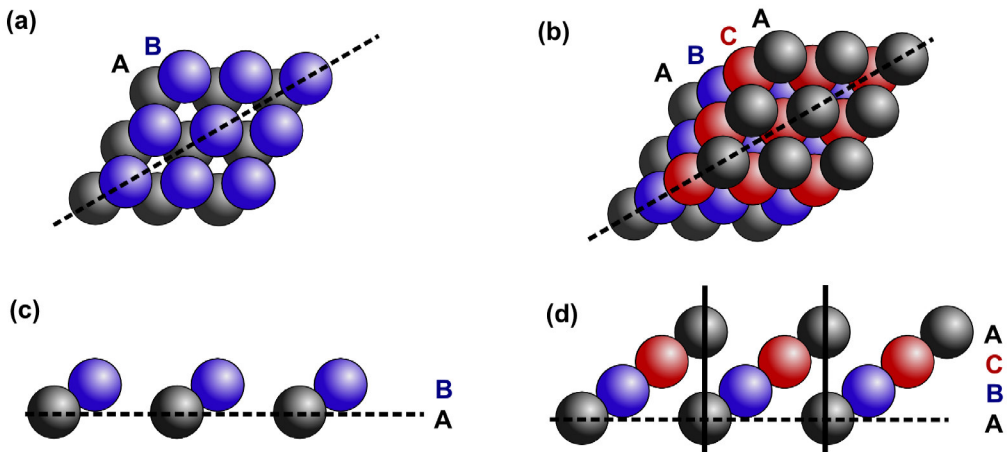


FIGURE 5.5: Sketched ABC-stacking of an fcc(111) crystal. Parts (a) and (b) show the surface from a top view, while parts (c) and (d) depict a cross-section along the dashed line included in parts (a) and (b).

Every lattice site has the same value of  $E_D$ ; however, the values of  $E_{\text{neighbours}}$  and  $E_{\text{layer}}$  depend on the local neighbourhood. We make further approximations in their description, listed below.

**Free diffusion energy  $E_D$ .** The free diffusion energy barrier  $E_D$  describes the energy barrier that a particle has to overcome to diffuse from one fcc(111) lattice site to another site on an otherwise empty  $C_{60}$  layer. Note that the fcc(111) facet also displays interstitial sites, as depicted in Fig. 5.4. Through our lattice assumption, the free diffusion barrier gives us an effective barrier for the diffusion between two sites of the bulk crystal and neglects the interstitial sites.

**Neighbour interaction potential  $E_{\text{neighbours}}$ .** We take only the closest neighbours into account, due to the short interaction range of  $C_{60}$  [51, 54]. If we assume that each of these increases the potential well depth by a constant contribution  $E_n$ , we can use the Clarke-Vvedensky bond-counting approach [215, 216]

$$E_{\text{neighbours}}(i) = n_i E_n. \quad (5.6)$$

Here, every lateral neighbour to a particle  $i$  contributes a constant energy  $E_n$  to the energy barrier. The number of lateral neighbours to the particle  $i$  is reflected through the integer  $n_i$ . Note that other pre-factors to the neighbour binding energy have been suggested in literature [111, 114]. These increase the diffusion rate of particles along island edges. As a consequence, the islands become more compact. In our  $C_{60}$  system, however, the islands are quite compact from the very onset of the growth. Therefore, the details of the pre-factor do not significantly influence the results at the parameters considered.

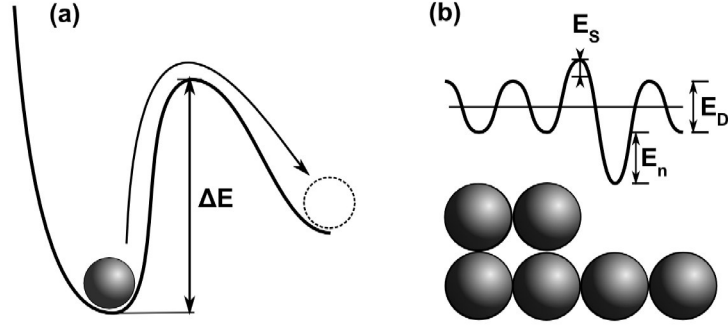


FIGURE 5.6: Sketch of the energy-barrier contributions that a particle must overcome before escaping from its potential well: Part (a) depicts the well, Part (b) illustrates the free diffusion barrier  $E_D$ , the neighbour interaction contribution  $E_n$ , and the step-edge barrier  $E_S$  in a 1D potential landscape sketch.

**Step-edge barrier  $E_{\text{layer}}$ .** The step-edge barrier is an effective barrier that a particle has to overcome when traversing a step-edge. It is also called the ‘Ehrlich-Schwoebel-barrier’ [217, 218]. This effective energy contribution is a reflection of the fact that the particle traverses a site with very low coordination number at a step-edge. Assuming a short-ranged interaction, the step-edge barrier is the only factor of the material that influences the dynamics of layering during growth. Since it contributes whenever a particle crosses a step, the Boolean  $s_{i,j}$  expresses if the particle  $i$  crosses a step on its way to its destination  $j$  ( $s_{i,j} = 1$ ) or not ( $s_{i,j} = 0$ ).

$$E_{\text{layer}}(i, j) = s_{i,j} E_S \quad \rightarrow \quad \Delta E(i, j) = E_D + n_i E_n + s_{i,j} E_S \quad (5.7)$$

The resulting description of the energy landscape is depicted in Fig. 5.6. In our work, we fit the three energy barrier contributions  $E_D$ ,  $E_n$ , and  $E_S$  to the experiment. The fit values, their influence on the observables, their comparison to literature, and their error bars are discussed in detail in Secs. 6.1 and 7.1.2.

### 5.3 Algorithm specifics

The assumptions made in the model are directly translated into the algorithm. As I am not interested in the algorithm details too much, I will briefly mention the assumptions here, but I refer the reader to the App. B for more details and useful data structures.

- **KMC algorithm (see Sec. 2.5).** With the new nomenclature listed above, it is easy to list all possible process types. On a hexagonal lattice, there is in-plane diffusion with  $n_i \in \{0, \dots, 6\}$ , interlayer diffusion with  $n_i \in \{0, \dots, 6\}$ , and particle adsorption. Correspondingly, there are 15 easily distinguishable process types. This makes a KMC algorithm ideal: It is easy to identify the process types and their rates, and efficient lists of all processes can be created.

- **(2+1)-dimensionality.** A (2+1)-dimensional simulation can be implemented under the assumption of solid-on-solid growth for spherically symmetric molecules [131, 138]. Essentially, ‘2+1’ means that the three-dimensional morphology formed through particles on the substrate is represented through a two-dimensional lattice. Each lattice position corresponds to the horizontal position on the substrate, while the third dimension is reflected through the height of particles stacked above this lattice site. Note that for a hexagonal fcc(111) lattice these ‘particle towers’ are not vertical. In order to avoid an un-physical directional bias through this assumption, we implement particle relaxation. In order to use a (2+1)-dimensional simulation, defect- and overhang-free growth needs to be assumed.
- **Particle relaxation.** On a hexagonal lattice every particle is supported through three sites. In the (2+1)-dimensional simulation we ensure this assumption by relaxing any particle that diffuses to a site that is not fully supported. A particle can relax to any of the 6 neighbour sites accessible from the current site of the particle. The relaxation probability to a given neighbour site is proportional to the rate of a diffusion process in this direction. For example: If a particle relaxes from a site with 2 lateral neighbours, it is more likely to relax away from the neighbours than onto the neighbours. This is because the latter would require crossing a step-edge which has the energetic penalty  $E_S$ .
- **Periodic boundary conditions.** We assume periodic boundary conditions in order to avoid the effect of substrate boundaries. Note that this assumption can cause difficulties if the substrate is small enough for particles to traverse across the entire substrate before they are immobilised and, ultimately, embedded through other adsorbed particles. However, during growth, the substrate size is less crucial than it is in equilibrium studies, where phase transitions are known to scale with the system size. This conundrum is known as ‘finite size scaling’ [219].
- **Neighbouring sites.** In order to describe the system in terms of arrays<sup>1</sup>, we need to translate the hexagonal symmetry of the fcc(111) facet onto the quadratic structure of a tensor. Correspondingly, we define the neighbouring sites to a site  $(x, y)$  through  $\{(x+1, y), (x+1, y+1), (x, y+1), (x-1, y), (x-1, y-1), (x, y-1)\}$  under consideration of the periodic boundary conditions (see App. B).

---

<sup>1</sup>The data format commonly used in algorithms.

# Chapter 6

## Observables for C<sub>60</sub> growth

In order to compare the real-space simulated surface growth with the reciprocal-space measurements during growth, the first task is to identify information and length-scales accessible to both surface-growth approaches. Once we have identified these features, we can use further observables to characterise the particle-resolved growth and morphological evolution in C<sub>60</sub> and atomic systems.

### 6.1 Observables that allow comparison to experiment

The X-ray scattering gives information about the thin film through in-plane and specular (out-of-plane) scattering. Using these the coverage  $\Theta_n(t)$  of the layer  $n$ , the corresponding specular scattering intensity  $I_{\text{anti-Bragg}}(t)$ , and the average island density  $N(t)$  as a function of the time  $t$  can be extracted. The corresponding measurement approaches and extraction procedures are briefly discussed in Sec. 7.1. Note that these observables depend on the system temperature  $T$ , as well as the adsorption rate  $f$ . In the simulations, these units are easy to extract from the real-space data that is available.

The coverage  $\Theta_n(t)$  is determined from the fraction of lattice sites that are occupied in layer  $n$ . Expressed in terms of the solid-on-solid approximation discussed in Sec. 5.2, this corresponds to the number of sites with a height larger than  $h_i \geq n \cdot h$ , where  $h = 0.816 \text{ \AA}$  is the unit cell height of C<sub>60</sub>. Then the coverage is

$$\Theta_n(t) = \frac{n_{(h_n \geq n \cdot h)}^{\text{sites}}(t)}{n_{(h_n \geq 0)}^{\text{sites}}(t)}, \quad (6.1)$$

where  $n_{(h_i \geq n \cdot h)}^{\text{sites}}(t)$  is the fraction of sites  $i$  that are occupied with more than  $n$  particles, while  $N_{(h_n \geq 0)}(t)$  denotes the number of sites available on the substrate.

Using the coverage  $\Theta_n(t)$  obtained from simulations in Eq. (5.1), we can derive the specular scattering intensity  $I_{\text{anti-Bragg}}(t)$  that is observed in experiments. The scattering amplitudes and relative phases needed for this calculation are derived from experiment by S. Bommel [119]. Note that the specular scattering intensity does not contain more information, however it is more directly comparable to the experiment. In addition, this comparison requires fewer

assumptions. Both the coverage and the specular scattering intensity render out-of-plane information. In order to determine the in-plane island density  $N(t)$  on our substrate, we use a Hoshen-Kopelman cluster algorithm [220], a standard procedure for systems lattice systems. A rough overview over the algorithm is given in App. C. The experimental  $N(t)$  is measured using in-plane scattering techniques; hence, we use a in-plane cluster algorithm. Extensive comparison between experiment and simulation has shown us that the in-plane island density  $N_n(t)$  of the layer  $n$  is connected to the measured island density  $N(t)$  via

$$N(t) = \max\{N_1(t), N_2(t), \dots, N_{\text{max layer}}(t)\}. \quad (6.2)$$

In order to express the island density in the physical units needed for comparison, we note that C<sub>60</sub> has a hexagonal lattice with an in-plane particle distance of 1.0 nm [176]. Correspondingly, the surface of one unit cell is 0.866 nm<sup>2</sup>.

The out-of-plane growth behaviour reflected by  $\Theta_n(t)$  and  $I_{\text{anti-Bragg}}(t)$ , as well as the in-plane information reflected by  $N(t)$  can be directly compared to the experiment. We use these to fit the three degrees of freedom given in our simulations; the free diffusion energy barrier  $E_D$ , the neighbour interaction energy  $E_n$ , and the step-edge barrier  $E_S$  are determined through the experiment. The sensitivity of the fit, along with the values and their significance are discussed in Sec. 7.1.2.

In order to understand the details of the growth behaviour and compare C<sub>60</sub> growth to atomic growth, we introduce further observables that characterise growth morphology and single-particle dynamics in more detail.

## 6.2 Target quantities to study differences between atomic and C<sub>60</sub> growth

The focal point of our comparison is the interplay between the time-dependent surface morphology on the one hand, and the particle-resolved dynamics on the other hand.

To characterise the surface morphology, we calculate the height-height correlation function  $G(d, t)$  defined as

$$G(d, t) = \left\langle \frac{\sum_i^M \sum_j^M (h(\mathbf{x}_i, t) - \bar{h})(h(\mathbf{x}_j, t) - \bar{h})}{N(d)} \right\rangle, \quad (6.3)$$

where  $M$  is the number of points on the surface, and  $d = |\mathbf{x}_i - \mathbf{x}_j|$  is the distance between two points on the surface,  $i$  and  $j$ . These points are characterised by their position vectors  $\mathbf{x}_i$ ,  $\mathbf{x}_j$  and their heights  $h(\mathbf{x}_i)$ ,  $h(\mathbf{x}_j)$ . In Eq. (6.3), the function  $G(d, t)$  is determined by averaging over the  $N(d)$  pairs of points on the surface, which have a distance  $d$ , followed by an average over realisations (denoted as  $\langle \dots \rangle$ ), while  $\bar{h}$  is the average height of the surface.

The height-height correlation function ( $G(d, t)$ ) has successfully been used to characterise a variety of systems, both in experimental studies (e.g. using scanning tunnelling microscopy [221]) and in simulations [222]. The definition (6.3) implies two particularly interesting special cases regarding the values of the distance  $d$ . The first one corresponds to  $d = 0$  (and thus  $i = j$ ). In this case,  $G(0, t)$  can be interpreted as the variance of the surface height,

$$G(0, t) = \left\langle \frac{\sum_i (h(\mathbf{x}_i, t) - \bar{h})(h(\mathbf{x}_i, t) - \bar{h})}{N(0)} \right\rangle. \quad (6.4)$$

The variance clearly is sensitive to deviations from the average surface height  $\bar{h}$ , which is why it is commonly interpreted as the roughness. The second special case is that the points  $i, j$  are nearest neighbours ( $i, j \in n$ , which is equivalent to  $|\mathbf{x}_i - \mathbf{x}_j| = a$ ). We find a measure for the mean squared step height,

$$G(1, t) = \left\langle \frac{\sum_{i,j \in n} (h(\mathbf{x}_i, t) - \bar{h})(h(\mathbf{x}_j, t) - \bar{h})}{N(1)} \right\rangle, \quad (6.5)$$

which correlates the heights of neighbouring sites. Therefore,  $G(1, t)$  is the correlation function that is most sensitive to local variations; hence, it is often called the ‘local roughness’ or ‘mean square step height’ [223].

Characteristic of the present growth process is the formation of islands. As soon as these are present, the surface can also be characterised through scalar morphological descriptors such as the fractal dimension  $D$  [224]. The latter is determined through the scaling behaviour of island surface  $A$  with the radius of gyration  $x_{\text{gyr}}$

$$A \propto x_{\text{gyr}}^D, \quad (6.6)$$

where  $x_{\text{gyr}}^D$  is defined as

$$x_{\text{gyr}} = \sqrt{\frac{1}{N_{\text{island}}} \sum_{i \in \text{island}} (\mathbf{x}_i - \bar{\mathbf{x}}_{\text{island}})^2}. \quad (6.7)$$

In Eq. (6.7),  $N_{\text{island}}$  is the number of particles in the island, and  $\bar{\mathbf{x}}_{\text{island}}$  is the centre-of-mass position of the island, i.e.

$$\bar{\mathbf{x}}_{\text{island}} = \frac{1}{N_{\text{island}}} \sum_{i \in \text{island}} \mathbf{x}_i. \quad (6.8)$$

The island is defined using a cluster algorithm (Hoshen-Kopelman algorithm, see [220] and App. C) to identify all particles within one island.

The fractal dimension  $D$  describes how branched structures are: The closer to two the fractal dimension of a 2D island is, the less dendritic is its morphology. Because the island size increases in discrete steps, the scaling behaviour of  $A$  [see Eq. (6.6)] breaks down for small islands.

So far we have focused on system-averaged quantities. To understand the dynamics on a particle level, we analyse the MSD of particles as a function of time introduced in Sec. 3.3.

$$\Delta x(t^*)^2 = \langle |\mathbf{x}(t^*) - \mathbf{x}(0)|^2 \rangle_t, \quad (6.9)$$

where  $\mathbf{x}(t^*)$  is the position of the particle at the time  $t^*$  after its arrival on the substrate, and  $\langle \dots \rangle_t$  is the average over all realisations for particles that arrive at time  $t$ .

In order to extract an MSD from the particle dynamics that the morphology of the substrate, only particles are considered that arrive on the surface at time  $t$  after surface growth begins when averaging over realisations (e.g. after the growth of 0.5ML). Note that the MSD of freely diffusing particles is expected to scale linearly with time [see Eq. (3.49)], while interactions with other particles is expected to influence the temporal behaviour.

To interpret our MSD results, we look at the processes occurring at time  $t^*$ . The processes considered are free diffusion, diffusion away from sites with neighbouring particles, diffusion across step-edges and also immobilisation. Immobilised particles are embedded and stay put for the rest of the simulation. We define  $N(p, t^*)$  as the fraction of particles that perform a specific process of type  $p$  at time  $t^*$ .

# Chapter 7

## Results for C<sub>60</sub> growth

Using the theoretical and experimental techniques developed in Chap. 5, we have the tools to understand, predict and supplement the measurements made in the experiments. In this chapter, we develop a strategy to parametrise our simulation from experimental data in Sec. 7.1. However, we also gain insight into the underlying principles of C<sub>60</sub> growth. We compare it to colloidal and atomic growth scenarios. Section 7.2 focuses on the comparison between C<sub>60</sub>, atoms and colloids. This section studies C<sub>60</sub> growth the macroscopic length-scale that is accessible in experiment, before Sec. 7.3 treats the microscopic length-scale of single-particle diffusion that is nearly impossible to access in experiments at room temperature.

### 7.1 Collaboration with experiments

First it is significant to gain some insight into the growth behaviour itself, before we focus on the parametrisation of our model. Using this parametrisation, the simulation needs to consistently reproduce/predict experimental results for different temperatures and adsorption rates.

#### 7.1.1 First insight into multilayer growth

C<sub>60</sub> multilayer growth occurs in a layer-by-layer fashion, as was discussed from the experimental side in Sec. 5.1. An exemplary real-space surface evolution for C<sub>60</sub> layer-by-layer growth is given in Fig. 7.1, depicting three distinguishable phases that appear during the growth of one layer. Initially, as more and more molecules are deposited on the 2<sup>nd</sup>, these molecules aggregate and islands nucleate. The so-called ‘nucleation regime’ is characterised by an increasing number of islands. As time progresses, the islands broaden, forming a regime called ‘lateral island growth’, where the number of islands and their positions stay constant, but the islands themselves grow within the plane. Finally, once the islands have grown large enough to touch, the islands merge by filling their gaps until a nearly closed layer is formed for the next layer to nucleate on. During layer-by-layer growth, this sequence of events repeats iteratively except for small deviations, resulting in a periodicity in the island number.

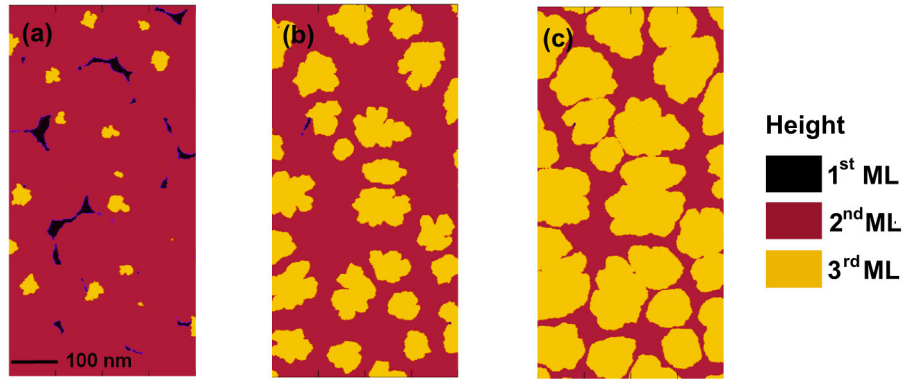


FIGURE 7.1: Snapshots of simulated  $C_{60}$  multilayer growth at different stages of monolayer-growth. The three snapshots show the nucleation of the 3<sup>rd</sup> monolayer in part (a), the lateral growth of islands in part (b), and the merging of islands in part (c). The data plotted is taken from multilayer growth simulations of  $C_{60}$  for  $T = 60^\circ\text{C}$  and  $f = 0.1 \text{ML/min}$ .

The periodicity in the number of islands is reflected in the island density  $N(t)$ , that is determined using Eq. (5.3) for the experiment and Eq. (6.2) for the simulation. The resulting island density for  $C_{60}$  multilayer growth is depicted in Fig. 7.2 (a). During nucleation the island density increases, during lateral growth it stays approximately constant, and during merging it decreases again in both experiment and simulations. Note that the first layer of the experiment is not included in our simulations because in the experiment  $C_{60}$  is grown on mica, as discussed in Sec. 5.1. The absence of the mica substrate in the simulations also accounts for the deviations at the beginning of the second  $C_{60}$  monolayer, i.e. for molecular exposures<sup>1</sup> between 1 and 1.3. However, later layers clearly display the layer-by-layer growth in the system.

As one layer fills during layer-by-layer growth, the coverage of one layer  $\Theta_{n-1}(t)$  nearly reaches 1 before the next layer begins to be covered with  $\Theta_n(t) \neq 0$ . This form of coverage evolution is reflected in depicted in Fig. 7.2 (c), where the coverage of each layer nearly perfectly meets 1 before the next layer nucleates. As discussed in the context of Eq. (5.1), the coverage of the different layers can also be expressed in terms of the specular scattering intensity, which is depicted in Fig. 7.2 (b). The necessary parameters for this calculation are derived from experiment. The specular scattering intensity oscillates with the periodicity of two monolayers, i.e. it is maximal when the 0<sup>th</sup>, 2<sup>nd</sup>, ... monolayer is filled, and it is minimal when the 1<sup>rst</sup>, 3<sup>rd</sup>, ... monolayer is filled. The decrease in the heights of the intensity maxima is an indicator of the roughening of the growth. The roughening reflects the deviation from layer-by-layer growth, when layers no longer close perfectly before the next layer nucleates.

There is clearly excellent agreement between the experimental and simulated data regarding the island density and anti-Bragg growth oscillations in Fig. 7.2 (a) and (b). The minima and the maxima in the island density, as well as the trend of decreasing density for the different layers (increase of island size) are clearly reproduced. The apparent increase of the island density in the fifth layer, which deviates slightly from the true island density, indicates the limits of our data analysis. The analysis of the simulation given in Eq (6.2) only takes the islands in a single, currently growing layer into account. However due to the roughening

<sup>1</sup>The concept of molecular exposure is defined in Sec. 5.1.1.

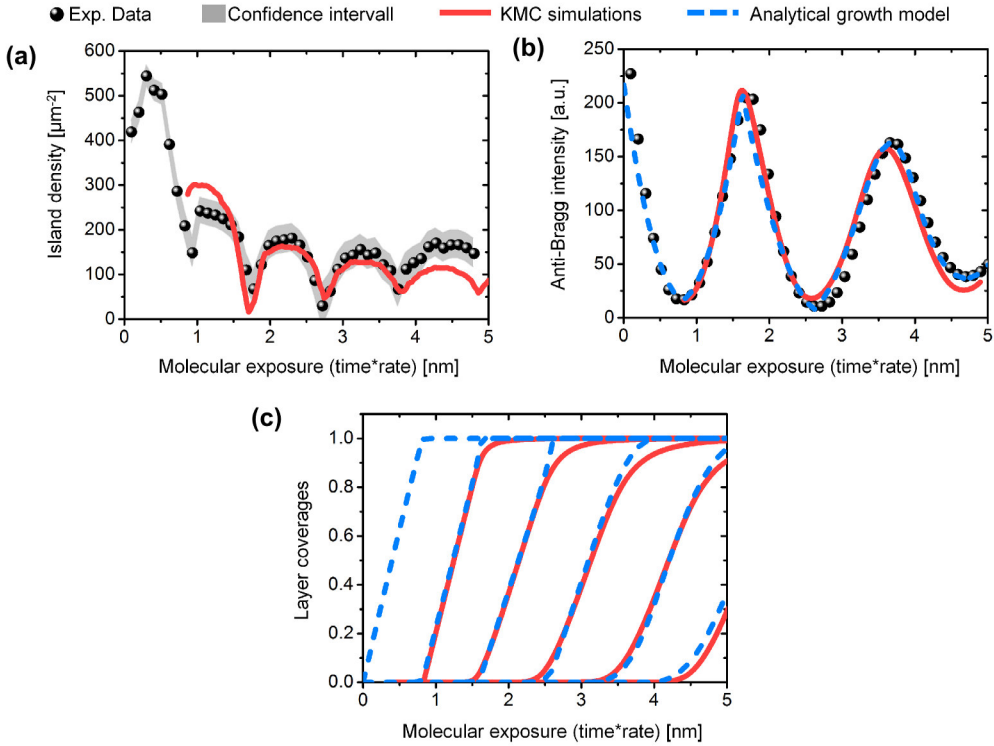


FIGURE 7.2: Experimental and simulated measures of surface morphology. (a) Island density, (b) specular scattering intensity, and (c) layer coverages are shown as a function of the molecular exposure for a  $C_{60}$  film grown at  $T = 40^\circ\text{C}$  and  $f = 0.1 \text{ ML/min}$ . Parts (b) and (c) include data from an analytic growth model. The KMC simulations have been performed from the second layer onward. The confidence interval in (a) is calculated from the experimental uncertainties.

of the film all islands in the simultaneously growing 4<sup>th</sup> and the 5<sup>th</sup> layer contribute to the diffuse scattering at that stage. This cannot be taken into account in the simulation, as the contributions from the two layers cannot be distinguished clearly. The vertical layer filling and roughening are also highly consistent, as can be seen from the agreement between experimental and simulated evolution of anti-Bragg intensity in Fig. 7.2 (b). In order to prove consistency of our analysis, we also determined the anti-Bragg intensity using the coverages derived from an analytic growth model discussed in Sec. 5.1.1 called the Trofimov model. The coverages derived from the Trofimov model agree with the simulated coverages, shown in Fig. 7.2 (c).

### 7.1.2 Comments on the parametrisation

**Parameter set.** Using the observables discussed in Sec. 6.1, we are able to adjust the energy barrier contributions  $E_D$ ,  $E_n$ , and  $E_S$  until both the simulated specular scattering intensities and island densities fit the experiment. We find

$$E_D = 0.54 \text{ eV}, E_n = 0.13 \text{ eV}, \text{ and } E_S = 0.11 \text{ eV}. \quad (7.1)$$

Note that, to date, there is no organic compound for which even the ‘minimal’ set of the three parameters (diffusion barrier, lateral binding energy, and Ehrlich-Schwoebel barrier) have been quantified simultaneously to describe multilayer molecular growth. Therefore, predictive simulations of the rate- and temperature-dependent morphology in molecular multilayer growth have so far been impossible, contrary to the situation for elemental atomic [117, 138–141] and colloidal systems [94]. Our parameter set is the first set in literature, with which it is possible to achieve quantitative agreement with the experimental data, enabling us to predict how thin-film morphology depends on the adsorption-rate, the temperature and the film thickness.

Before discussing the temperature- and rate-dependant results in detail in Sec. 7.1.1 and 7.1.3, I will delve into the details of the fit procedure, as well as the significance of the parameter values listed in Eq. (7.1).

**Fit procedure.** To adjust the parameters  $E_D$ ,  $E_n$ , and  $E_S$  that appear in the energy barrier ( $\Delta E(i, j) = E_D + n_i E_n + s_{i,j} E_S$ ) [see Eq. (5.7)], we start from initial values suggested in the literature [69, 102, 118]. We then optimise the parameter set to match, as accurately as possible, the experimental data for the island density and the filling fraction at  $T = 40^\circ \text{C}$  and  $f = 0.1 \text{ ML/min}$ . This is shown in Fig. 7.2. This experimental data-set has the best lateral and temporal resolution.

In performing such an optimisation, we should note that the influences of the different energy barrier contributions on our observables are strongly correlated. For example,  $E_D$  determines the free diffusion time and is therefore of prime importance for the calculated island density. The latter, however, is also influenced by  $E_n$ : If the neighbour energy is sufficiently small, island nuclei can dissociate, which effectively reduces the island density. Therefore the influence of  $E_D$  and  $E_n$  on the island is correlated. Another example occurs during step-edge crossing: The energy barrier of this process is given by  $E_S$ . However, the effective crossing rate is also influenced by the island morphology (which determines the probability of reaching a step), and thus, by  $E_n$ . Due to this mutual influence it is clear that optimisation of the energy parameters is rather challenging, one danger being that the resulting set may not be completely unique. We note, however, that the final parameter set selected in our study [see Eq. (7.1)] yields a satisfying match of the experimental data not only for the case  $T = 40^\circ \text{C}$  and  $f = 0.1 \text{ ML/min}$ , but also at the other temperatures and adsorption rates considered. This “robustness” strongly supports our predictions.

For the estimation of the error bars of the extracted energies their mutual correlation as well as the experimental confidence interval were taken into account. It is perhaps notable even a small alteration of one of the energy contributions (changes of the order of 20 meV) results in significant changes of the calculated morphology, i.e. in a deviation from experimental results. The confidence interval of the experimental island density data shown in Fig. 7.2 is calculated from the experimental uncertainties of X-ray wavelength, sample-to-detector distance as well as the fit uncertainty of the double peak distance in the diffuse X-ray scattering experiments. When we take the experimental confidence interval of the island density and anti-Bragg intensity into account, the error bar of the diffusion barrier increases to 40 meV.

**Comparison to literature.** The energy parameters listed in Eq. (7.1) are of the same order of magnitude as other values [69, 118] reported in the literature, but differ in their

actual magnitude. In the following we briefly discuss to which end these discrepancies can be attributed to differences of energy barrier definitions and of simulation approaches.

We start by considering the energy barrier stemming from nearest-neighbour interactions. The corresponding value quoted in the KMC study of Körner *et al.* [118] is  $E_b^{\text{Körner}} = 0.271 \text{ eV}$ . This equals the depth of the pair interaction potential of two interacting  $C_{60}$  molecules, as derived by Girifalco [51]. However, particles in the simulation of Körner *et al.* need to overcome  $nE_b/2$  to move from a site with  $n$  neighbouring particles to a site with no neighbouring particles. Therefore the definition of  $E_b$  differs from our definition of  $E_n$ . To be precise, we compare  $E_b^{\text{Körner}}/2 = 0.1355 \text{ eV}$  with our value  $E_n = 0.13 \pm 0.02 \text{ eV}$ . Clearly, these are in very good agreement.

Next, we consider the free diffusion energy. Both Körner *et al.* [118] and Liu *et al.* [69] report a value  $E_{\text{D}, \text{Körner}} = 0.178 \text{ eV}$ ; however, they also use an attempt frequency of  $\nu = 2 \cdot 10^{11} \text{ Hz}$ . Moreover, both studies are based on a hexagonal lattice under consideration of interstitial sites. We neglect these sites, yielding a somewhat coarse-grained approach. We note that without the coarse-grained approach it would not be possible to simulate such a large system for minutes to hours of experimental (real-)time. A particle overcomes two times the barrier  $E_{\text{D}, \text{Körner}} = 0.178 \text{ eV}$  in one diffusion step on our coarse-grained lattice. In addition there are three options to diffuse from the interstitial site<sup>2</sup>. Only one option leads to our coarse-grained destination site, an additional geometric factor of  $1/3$  needs to be included in the diffusion rate.

There is a difference in the attempt frequency  $\nu$  that we must take into account, as well. We finally gain the following estimate of a coarse-grained free diffusion barrier from the values reported in [69, 118]

$$\begin{aligned} E_{\text{D}, \text{Körner}} &\approx -\ln\left(\frac{1.4 \cdot 10^{13} \text{ Hz}}{2 \cdot 10^{11} \text{ Hz}}\right) kT - \ln\left(\frac{1}{3}\right) kT \\ &\quad + 2 \cdot E_{\text{fD}, \text{Körner}} \\ &\approx 0.122 \text{ eV} + 0.032 \text{ eV} + 0.356 \text{ eV} \\ &\approx 0.51 \text{ eV}, \end{aligned} \tag{7.2}$$

which lies within the error margins of our value  $E_{\text{D}}$ . This estimate uses  $T = 60^\circ\text{C}$ .

Finally, our value of the Ehrlich-Schwoebel barrier  $E_S = 0.11 \pm 0.02 \text{ eV}$  is in very good agreement with values derived from density-functional theory calculations for step-edge barriers  $E_S^{\text{Goose}} \approx 0.104 \text{ eV}$  [102].

### 7.1.3 Different temperatures and adsorption rates

We compare the experimental lateral information (island density) and vertical information (anti-Bragg growth oscillations and layer coverages) for rates of  $f = 0.1 \text{ ML/min}$  and  $f = 1 \text{ ML/min}$  and temperatures of  $40^\circ\text{C}$ ,  $60^\circ\text{C}$ , and  $80^\circ\text{C}$ . The data for a temperature of  $T = 40^\circ\text{C}$  and rate of  $f = 0.1 \text{ ML/min}$  is shown in Fig. 7.2. We present in Fig. 7.3(a)-(c) an additional example for a temperature of  $T = 60^\circ\text{C}$  and a rate of  $f = 0.1 \text{ ML/min}$ . We find that

---

<sup>2</sup>The concept of interstitial sites is introduced and discussed in Sec. 5.2.

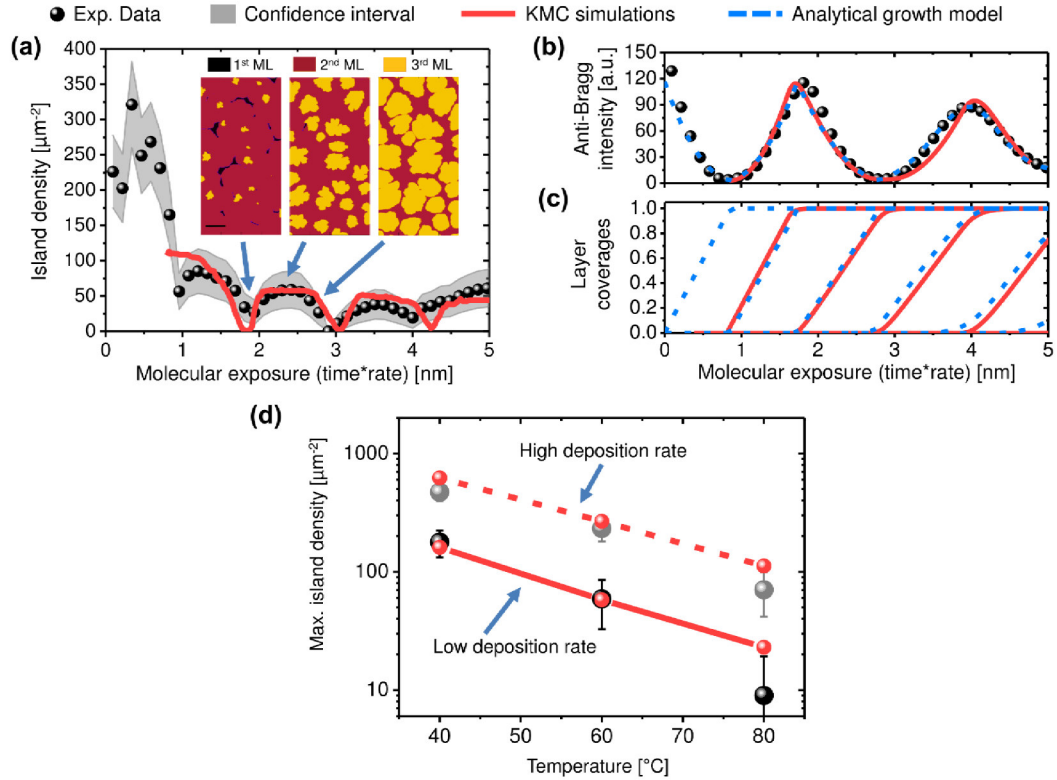
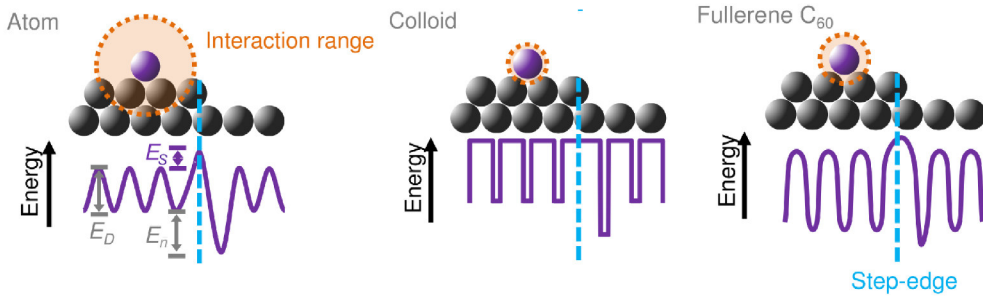


FIGURE 7.3: Experimental and simulated measures of the morphology for  $T = 60^{\circ}\text{C}$ . (a) Experimental and simulated island density (inset: 2D island growth regimes as simulated by KMC; scale bar: 100 nm), (b) anti-Bragg growth oscillations and (c) layer coverages for  $T = 60^{\circ}\text{C}$  and  $f = 0.1 \text{ ML/min min}$  as a function of molecular exposure. Part (d) compares the maximal island density for the third layer for both a low deposition rate of  $f = 0.1 \text{ ML/min}$  and a high deposition rate of  $f = 1 \text{ ML/min min}$  as a function of temperature, where the error bars calculated from the experimental uncertainties.

even beyond the specific experimental parameters chosen in Fig. 7.2, KMC simulations show a good agreement with the experimental findings for different temperatures and adsorption rates.

We find that the island density decreases (that is, the island size increases) with a higher substrate temperatures [Fig. 7.3(a)]. This corresponds to the results found in growth theories and experiment [119]. The specular intensity [Fig. 7.3(b)] for  $T = 60^{\circ}\text{C}$  also shows the distinct growth oscillations indicating layer-by-layer growth, as it did for  $T = 40^{\circ}\text{C}$  [Fig. 7.2(b)]. From fitting the anti-Bragg growth oscillations using the Trofimov model [205, 206] one can extract the layer coverage. The results support the simulated KMC layer coverages for  $T = 60^{\circ}\text{C}$  as can be seen in Fig. 7.2(c). The observed agreement between experiment and simulation holds for all studied rates ( $f = 0.1 \text{ ML/min}$  and  $f = 1 \text{ ML/min}$ ) and the full experimental temperature range of  $40^{\circ}\text{C} - 80^{\circ}\text{C}$ . This is seen in Fig. 7.2(d), where we compare the experimental and simulated values for the maximum island density in the third monolayer. In accordance with growth theories predicting a scaling of island density with deposition rate/diffusivity [225, 226], we find that the island density decreases for higher substrate temperature and lower deposition rate by an order of magnitude. Furthermore, KMC simulations correctly predict the change in island density by an order of magnitude when changing deposition rate and temperature. Notably, this comprehensive agreement of temperature-, rate- and time-dependent data was



**FIGURE 7.4:** Schematic illustration of energy landscape for atoms, colloids and the fullerene  $C_{60}$  near an island step-edge: The interaction range of the different materials clearly affects the character of step-edge barrier as one can distinguish between real and a diffusion-mediated pseudo-barrier [94].

achieved with a physical model of surface processes that contains only three parameters — the nanoscopic energy barriers for diffusion, nucleation and step-edge crossing (discussed in Sec. 7.1.2).

## 7.2 $C_{60}$ between atomic and colloidal length-scales

Conjugated organic molecules in general and  $C_{60}$  in specific lie between colloidal and atomic systems, concerning their length scale and the range of their interactions, as discussed in Sec. 1.2. Figure 7.4 illustrates the influence of the difference in interaction range on the effective potential landscape that particles experience. We find that the difference in interaction range is reflected in the values of  $E_D$ ,  $E_n$ , and  $E_S$  found in Sec. 7.1.2. Comparing these parameters to typical values found for colloidal [94, 227, 228] and atomic systems [111, 226, 229], we find that the step-edge barrier  $E_S$  is too large for a colloidal step-edge barrier. Instead resembles values found in atomic systems, which we will discuss in detail in Sec. 7.2.1. On the other hand we find that our ratio of  $E_n$  to  $E_D$  is much smaller than that found in corresponding atomic systems. This reflects the short interaction range of  $C_{60}$  (see Fig. 1.6). We will discuss this feature in detail in Sec. 7.2.2.

### 7.2.1 Comparison to colloidal systems

The attractive interaction between colloids is mediated through solvent particles, as discussed in Sec. 1.2.2. Hence, in colloidal systems, the strength of the neighbour binding energy  $E_n$ , as well as the diffusion constant (related to  $E_D$ ) can be tuned through the choice of the solvent. The only parameter that can realistically be compared is the step-edge barrier  $E_S$ . For  $C_{60}$ , the step-edge barrier depends on the coordination number on a slightly longer range than the direct contact (see Sec. 5.2).

Colloids have such a limited range of attraction, that they do not ‘sense’ any particles except for the ones they touch. Hence, for both diffusion in a plane and across a step-edge, colloids sense only two particles. Their short interaction range does not allow them to sense a change in coordination number at a step-edge. The energetic barrier at the step-edge effectively vanishes.

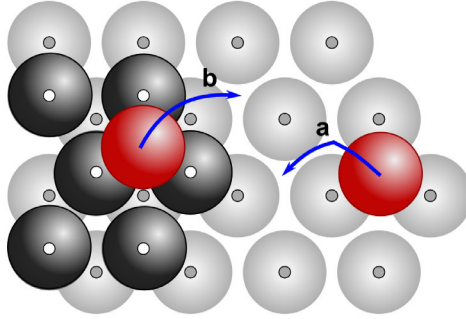


FIGURE 7.5: Sketch of diffusion paths. Diffusion paths during (a) in-plane and (b) step-edge crossing processes.

Instead, a purely diffusive Ehrlich-Schwoebel barrier arises due to geometric reasons: There is a lower diffusion probability along the longer path across the step-edge [94].

Atoms crossing an island edge ‘sense’ an energetic Ehrlich-Schwoebel barrier, in contrast. This is their long interaction range allows them to sense the missing longer-ranged bonds that arise at a step-edge. For  $C_{60}$  we can estimate an upper bound for a diffusive barrier based on the waiting time of a typical hopping process. Multiplying this time by a geometric factor (see reference [94]), which accounts for the longer path of a step-edge crossing, we obtain a diffusive pseudo-barrier of  $E_{S,\text{geo}} = \ln(F)kT < 50 \text{ meV}$ . This is markedly smaller than the value of  $E_S = 110 \text{ meV}$  obtained from the KMC simulations. The calculation that this observation is based on is illustrated below.

**Calculation of the geometric step-edge barrier.** The subsequent argumentation closely follows that given by Ganapathy *et al.* [94] for colloidal systems. We consider a  $C_{60}$  particle moving on a surface formed by other  $C_{60}$  particles. As a consequence of the short range of interactions the travelling particle tries to be in constant contact with two other particles. This effectively reduces local transport to one-dimensional (1D) motion along a straight path. The potential landscape along the path can be assumed to be constant. We note that the length of the 1D path between binding sites ( $d_{\text{island}}$ ) on an island is smaller than that of a path crossing the step-edge ( $d_{\text{step}}$ ), see Fig. 7.5 for an illustration of such paths. Therefore, the time it takes to do a step-edge jump can be up to a factor of

$$F = \frac{\langle t_{\text{step}} \rangle}{\langle t_{\text{island}} \rangle} = \left( \frac{d_{\text{step}}}{d_{\text{island}}} \right)^2 \quad (7.3)$$

longer, where  $\langle t \rangle = 1/r$  where  $r$  is the Arrhenius-type rate describing the surface processes [230] (see Chap. 3). Associated with this increase in diffusion time along the 1D potential is an increase of the probability to return to the original site [231]. As a consequence, the step-edge crossing probability decreases. This consideration leads to an effective, geometrical Ehrlich-Schwoebel barrier  $E_{S,\text{geo}}$  determined by

$$E_{S,\text{geo}} = \ln \left( \left( \frac{d_{\text{step}}}{d_{\text{island}}} \right)^2 \right) kT. \quad (7.4)$$

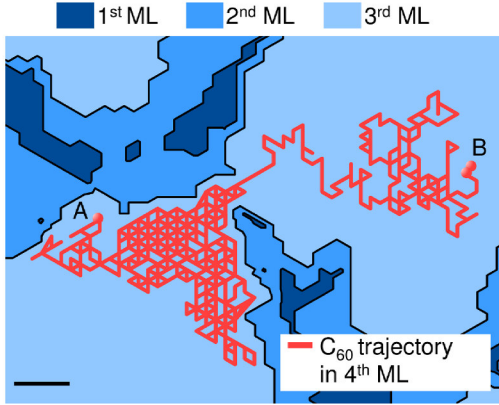


FIGURE 7.6: Trajectory of a single molecule in the 4<sup>th</sup> ML ( $T = 40^\circ\text{C}$  and  $f = 1 \text{ ML/min}$ ; scale bar: 5 nm). The influence of the Ehrlich-Schwoebel barrier can be clearly seen as a caging of the single  $C_{60}$ -molecule on the island. The letters A and B denote the adsorption of one molecule on the surface (A) and the formation of a dimer (B).

To quantify this geometry-induced energy contribution, we recall that our KMC simulations performed on a triangular lattice. This yields a value of 1.4 for the ratio  $d_{\text{step}}/d_{\text{island}}$ . This value is based on the considerations made in the supplemental material of Ganapathy *et al.* [94]. They found that, for a hexagonal lattice, the path-length crossing a step-edge (see path ‘b’ in Fig. 7.5) is 2.8 times as long as the path-length between two neighbouring potential minima (one of the two diffusion steps that path ‘a’ in Fig. 7.5 is composed of). Since our simulation is restricted to a triangular lattice, an in-plane diffusion process involves two nearest-neighbour steps. This results in the ratio  $d_{\text{step}}/d_{\text{island}} = d_b/d_a = 2.8a/2a = 1.4$ . Combining this result with Eq. (7.4) we conclude that the geometrical Ehrlich-Schwoebel barrier  $E_{S,\text{geo}}$  is less than 50 meV for a temperature equal or less than  $T = 80^\circ\text{C}$ . The value  $E_S = 110 \text{ meV}$  that we find is considerably larger, and leads to a larger confinement of the particles to their layer. This confinement becomes visible when studying single-particle trajectories as depicted in Fig. 7.6. We thus conclude that the Ehrlich-Schwoebel barrier in  $C_{60}$  surface growth is, at least partially, of energetic character, consistent with the intermediate range of the  $C_{60}$ -interactions.

### 7.2.2 Comparison to atomic systems

In order to compare the growth dynamics of  $C_{60}$  with atomic systems, we compare the energy barriers (and their ratios) associated with the different material systems (published in Ref. [120]). To this end we hold a general discussion about the fundamental differences in the energies in Sec. 7.2.2, and a detailed discussion of our two representative atomic systems Pt grown on Pt(111) and Ag grown on Ag(111) in Sec. 7.2.2. The observables that we study are defined in Sec. 6.2, and those we have observed at a single-particle level in Sec. 7.2.2 and on the level of the overall surface morphology in Sec. 7.2.2. Finally, the understanding of the differences between the materials is exploited in Sec. 7.3 to understand the interplay between single-particle dynamics and the evolution of the surface morphology for different material systems.

Note that all graphs in this section were determined for  $T = 40^\circ\text{C}$  and  $f = 0.1 \text{ ML/min}$ .

System	$E_D$	$E_n$	$E_S$	$E'_n$
$C_{60}$	0.54 eV	0.13 eV	0.11 eV	0.13 eV
Ag	0.067 – 0.12 eV	0.19 eV	0.28 – 0.3 eV	0.72 eV
Pt	0.26 eV	0.5 eV	0.08 eV	0.92 eV

TABLE 7.1: Energy parameters used for the KMC simulations of  $C_{60}$  [119] and two atomic systems Ag (Refs. [111, 232–237]) and Pt (Refs. [111, 238, 239]). The interaction energies  $E'_n$  are discussed in Sec. 7.2.2.

### Systems under investigation

For  $C_{60}$ , the energetic barrier stemming from the interactions with the nearest neighbours is relatively small; an effect which we explain through the fact that the attractive centre-of-mass interactions between two  $C_{60}$  molecules have a rather short range (as compared to atomic systems). The atomic and  $C_{60}$  pair-potentials are depicted in Fig. 1.6. As a consequence, the ratio between the energy barrier for in-plane diffusion  $E_D$ , on the one hand, and the total energy barrier for a particle to break from a dimer,  $E_n + E_D$ , on the other hand, is relatively large. Specifically, we find (see Tab. 7.1)

$$R(C_{60}) = \frac{E_D}{E_D + E_n} \approx 0.8. \quad (7.5)$$

This large magnitude of  $R$  is due to the size of  $C_{60}$  and the influence of its small interaction range on the energy parameters  $E_D$ ,  $E_n$  and  $E_S$  (see Sec. 1.2.3 and 7.1.2). We intend to isolate, within the realm of our KMC simulations, the role of neighbour interactions. Specifically, we look at its effect on the growth of atomic systems. Thus, we proceed as follows: The atom-like KMC simulations are performed with the same values of  $E_D$ ,  $E_S$  used in the  $C_{60}$  simulations. We also assume the same lattice configuration and experimental input parameters for the atom-like simulations. However, the values for the neighbour interaction  $E'_n$  of atomic systems are chosen such that the ratio  $R = E_D/(E_D + E'_n)$  fulfils the literature values of  $R \approx 0.37$  for Pt and  $R \approx 0.43$  for Ag. The values used in determining these ratios are listed in Tab. 7.1 and discussed in Sec. 7.2.2 below.

Analysing systems that are identical in all parameters except the ratio  $R$  allows us a direct comparison of single-particle dynamics in experiment and simulation. This is possible despite that the time- and length-scales of growth in atomic systems is small relative to  $C_{60}$ .

### Detailed discussion of the representative atomic systems

In this work we focus on two representative atomic systems: the growth of Pt on Pt(111), as well as the growth of Ag on Ag(111). Note that these material systems are grown using homoepitaxy, and they concern crystal growth on the 111-facet of an fcc lattice. These features also appear in our studies of  $C_{60}$ . The direct comparison to atomic systems considered in this work is made possible through the work of several other groups, in which the energy parameters listed in Tab. 7.1 were successfully employed to simulate atomic growth on a coarse-grained lattice such ours. The groups are listed in the table along with the parameters that are obtained from their work.

**Pt on Pt(111).** Hohage *et al.* [238] used a free diffusion energy of  $E_{D,Pt} = 0.26 \text{ eV}$  and a attempt frequency of  $\nu = 5 \cdot 10^{12} \text{ Hz}$  to simulate the growth of Pt on Pt(111). They employed a simulation grid that only contains sites that are occupied in a bulk crystal. This approach to lattice coarse-graining is equivalent to ours, which enables a comparison between diffusion energies. Specifically, we compare the energy  $E_{D,Pt}$  to the free diffusion energy  $E_D$  of  $C_{60}$ , where  $E_{D,Pt}$  is related to  $E_{D,Pt}$  [238] via the attempt frequency

$$E_{D,Pt} = 0.26 \text{ eV} - \ln\left(\frac{5 \cdot 10^{12} \text{ Hz}}{1.4 \cdot 10^{13} \text{ Hz}}\right) kT \approx 0.29 \text{ eV}. \quad (7.6)$$

Using neighbour interaction energies of Feibelman and Michely [239], who find  $E_{b,2} = 0.5 \text{ eV}$ , we obtain a ratio

$$R(\text{Pt}) = \frac{E_{D,Pt}}{E_{D,Pt} + E_{b,2}} \approx 0.37. \quad (7.7)$$

**Ag on Ag(111).** The values for free diffusion energy barriers for Ag/Ag(111) reported in the literature show a wider spread, presumably due to the tendency of Ag to oxidise and the influence of this impurity on measurements. Values quoted range from  $E_{D,Ag} = 0.1 \text{ eV}$  with  $\nu = 10^{11} \text{ Hz}$  [233] and  $E_{D,Ag} = 0.097 \text{ eV}$  with  $\nu = 2 \cdot 10^{11} \text{ Hz}$  [234], via the combination of  $E_{\text{free},Ag} \approx 0.067 \text{ eV}$  with  $\nu = 10^{12} \text{ Hz}$  [232, 235] to  $E_{D,Ag} = 0.1 \text{ eV}$  with  $\nu = 10^{13} \text{ Hz}$  [236] and the combination of  $E_{D,Ag} = 0.12 \text{ eV}$  with  $\nu = 10^{13} \text{ Hz}$  [237]. All of the quoted values have been used to study Ag on Ag(111) using KMC simulations on a coarse-grained lattice.

In view of this spread in values, we have considered an intermediate value for the diffusion energy-barrier, which was determined for pure Ag using MD and so-called ‘nudged-elastic band’ approaches<sup>3</sup>:

$$E_{D,Ag} = 0.067 \text{ eV} - \ln\left(\frac{10^{12} \text{ Hz}}{1.4 \cdot 10^{13} \text{ Hz}}\right) kT \approx 0.143 \text{ eV}. \quad (7.8)$$

Similarly the range of neighbour interaction energies ranges from  $E_n = 0.15 \text{ eV}$  to  $E_n = 0.24 \text{ eV}$  ([111] and references within), while most studies appear to agree on  $E_n \approx 0.19 \text{ eV}$ . Using these values we find:

$$R(\text{Ag}) = \frac{E_{D,Ag}}{E_{D,Ag} + E_n} \approx 0.43. \quad (7.9)$$

## Morphology and trajectories of Ag and $C_{60}$

As a first comparison of the material systems, we show in Fig. 7.7 two surface structures illustrating the morphology of  $C_{60}$  and the Ag system after the growth of 1.5 ML. All lengths are plotted in units of the lattice constant  $a$ . The depicted surfaces have distinctly different structures. Most prominently,  $C_{60}$  has well rounded islands while Ag forms dendritic, nearly fractal structures. This morphological difference reflects the fact that  $C_{60}$  has a noticeably higher ratio  $R$  than Ag [see Eq. (7.5)]; therefore, processes that break bonds to lateral neighbours are far more likely. As a consequence,  $C_{60}$  molecules can easily move to sites with high

<sup>3</sup> An approach that uses constrained optimisation combined with fictitious spring forces to locally sample the energetic landscape. This method is mostly used to find minimum energy paths and energetic saddle points.

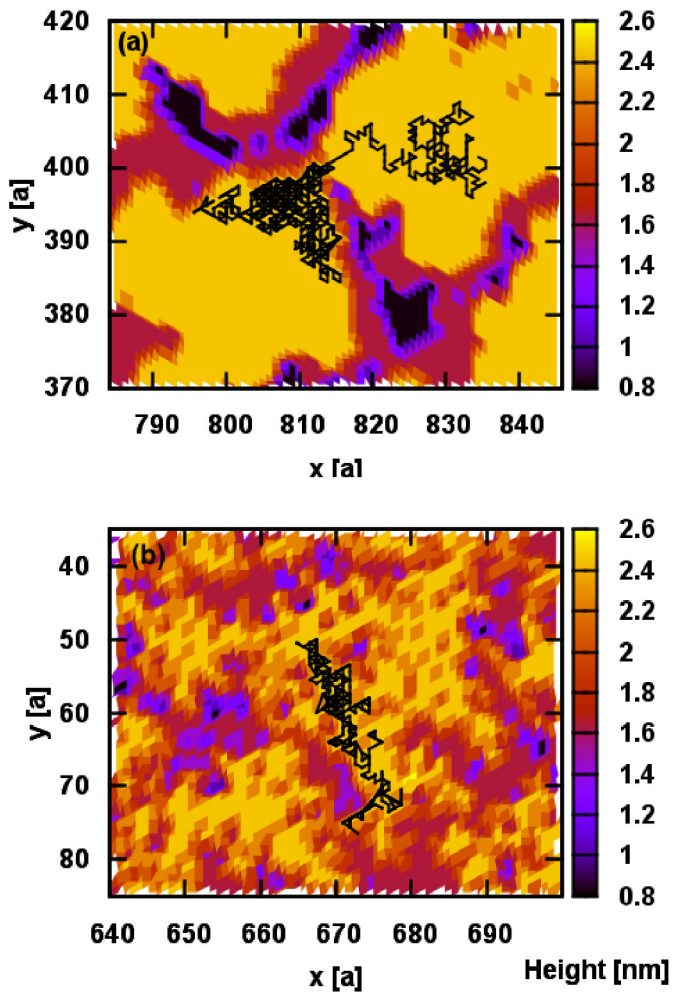


FIGURE 7.7: Height of surface structures after the growth of 1.5 ML for (a)  $C_{60}$  on  $C_{60}(111)$  and (b) Ag on Ag(111). The black lines depict trajectories of a particle which arrived on an island. Both systems are simulated on a triangular lattice with equal energy barriers  $E_D = 0.54\text{ eV}$  and  $E_S = 0.11\text{ eV}$ , but different neighbour binding energies  $E_n = 0.13\text{ eV}$  and  $E_n(\text{Ag}) = 0.72\text{ eV}$ , respectively. Note that part (a) depicts the same snapshot previously depicted in Fig. 7.6.

coordination numbers, which smooths out island edges. Ag is characterised by a much smaller ratio  $R$ . Therefore, once particles are bound to their neighbours these bonds are less likely to break. As a result one observes the formation of dendritic structures.

In Figs. 7.7 (a) and (b) we have plotted a single trajectory typical for a particle diffusing across the surface of an island after being deposited there. For both systems, we clearly see that motion across a step-edge is hindered. This leaves the particles to meander on the island surface, caged by the island edges. However, as Figs. 7.7 (a) and (b) clearly show, the different shapes of the islands influence the shape of the paths. In particular, the rounded islands of  $C_{60}$  lead to caging into a relatively small surface area within which the particles can diffuse (essentially) freely. On the other hand, the more fractal landscape of Ag allows for longer paths of free diffusion ('stretches'), that is, particles move along 'ridges' formed by island edges.

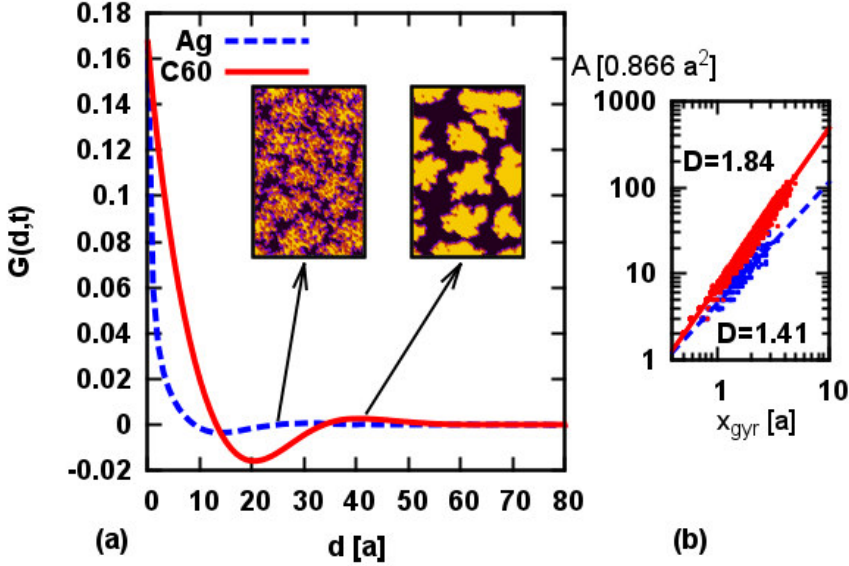


FIGURE 7.8: (a) Height-height correlation function  $G(d,t)$  as a function of the distance  $d$  after the growth of 0.5 ML ( $t \approx 22$  s) for  $C_{60}$  and Ag. The inset depicts a snapshot of size  $75a \times 125a$  of the surfaces. Part (b) shows the dependence of the average island size on the radius of gyration,  $x_{\text{gyr}}$ , in a double-logarithmic representation. Included are values for the resulting scaling exponents  $D$  [see Eq. (6.6)].

### Correlation functions of Ag and $C_{60}$

In the previous subsection (Sec. 7.2.2) we have seen that the single-particle dynamics depends crucially on the morphology of the surface. Thus it is important to understand the evolution of the surface morphology with time. To this end, we now discuss the behaviour of the spatio-temporal correlation functions introduced in Eqs. (6.3)–(6.5).

Figure 7.8 (a) depicts the height-height correlation function  $G(d,t)$ , which correlates the deviation from the average height  $\bar{h}$  at two points with distance  $d$  at time  $t$  [see Eq. (6.3)]. Specifically, we focus on the growth regime of the first monolayer ( $t \approx 22$  s). For the Ag system,  $G(d,t)$  decays rapidly to zero. The corresponding function for  $C_{60}$  reflects correlations ranging over much larger distances. These differences can be understood with the help of the surface snapshots shown in the inset of Fig. 7.8 (a). The  $C_{60}$  system displays clearly separated islands with well defined radii and distances. These features are mirrored by strong and long-ranged spatial correlations in the corresponding  $G(d,t)$ . In particular, the maximum at  $42$  Å corresponds to the average distance between neighbouring islands. The Ag system, however, is characterised by a far more dendritic island structure, which is reflected in the short range and smooth structure of  $G(d,t)$ .

The different island structures of  $C_{60}$  and Ag can be quantified by means of the fractal dimension  $D$ . We have determined this quantity via a scaling plot of the island area as function of the radius of gyration (see Fig. 7.8 (b) and Eq. (6.6), respectively). From this we find  $D \approx 1.84 \pm 0.01$  for  $C_{60}$  and  $D \approx 1.41 \pm 0.03$  for Ag. The much smaller values for Ag indicates the dendritic morphology of Ag islands. This confirms our interpretation that the small value of  $D^{\text{Ag}}$  is due to its strongly dendritic growth. Regarding  $C_{60}$ , we note that despite the rather large, ‘colloid-like’ value of the energy ratio  $R$ , our value of  $D$  is surprisingly large. It

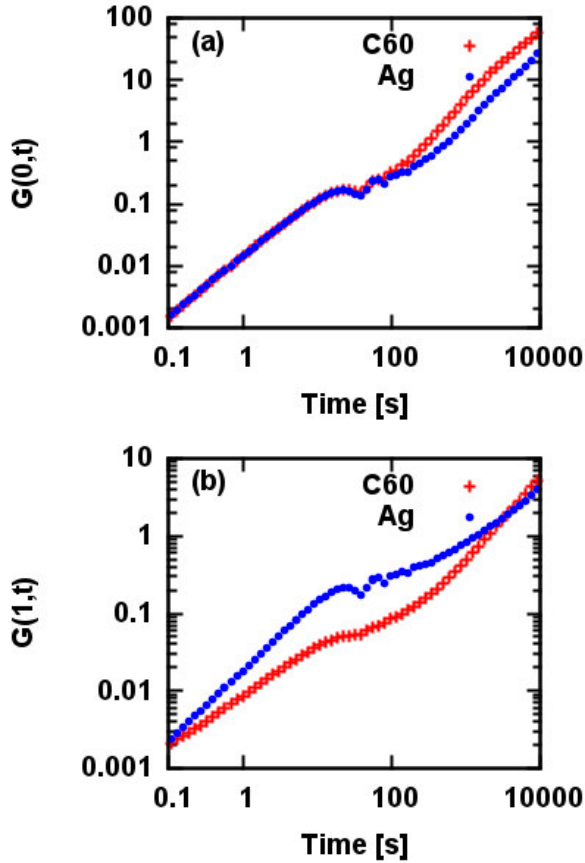


FIGURE 7.9: Height-height correlation functions  $G(d, t)$  of  $C_{60}$  and Ag as a function of time for two distances (a)  $d = 0 \text{ a}$ , (b)  $d = 1 \text{ a}$ .

deviates from the fractal dimension characteristically found for (uncharged) colloidal systems [240, 241]. Instead it lies within the range of values expected for atomic systems.

To further characterise the growth, we show in Fig. 7.9 the correlation functions  $G(0, t)$  and  $G(1, t)$  as a function of time. As mentioned in Sec. 6.2, the functions  $G(0, t)$  and  $G(1, t)$  measure the degree of overall and local roughness, respectively. In systems characterised by layer-by-layer growth the overall roughness initially grows. After approx. 20s, the overall roughness saturates at approximately 0.2 and oscillates around this value [140]. At later times, when layer-by-layer growth breaks down, roughening of the surface starts and  $G(0, t)$  increases again [242]. Indeed, it can increase even indefinitely if mounds or crystallites form on the surface (similar roughness evolution was found, e.g. by Šmilauer and Vvedensky [140]). In Fig. 7.9(a) we see that, for the growth of the first layers ( $t \lesssim 200\text{s}$ ),  $C_{60}$  and Ag grow with an identical roughness  $G(0, t)$ , indicating that the systems do not differ significantly in their inter-layer diffusion behaviour and follow similar growth modes. In the subsequent time range  $200\text{s} \lesssim t \lesssim 400\text{s}$ , Ag maintains a constant roughness with a value of about 0.2, while the roughness of  $C_{60}$  progressively increases. We interpret the behaviour of Ag as prolongation of layer-by-layer growth, which is characterised by approximately constant deviations of local from average surface height. Since the Ag system is simulated with the same Ehrlich-Schwoebel barrier as the  $C_{60}$  system, the observed deviation in the temporal behaviour of the roughness indicates a complex coupling of particle trajectories and surface morphology. Finally, for long times ( $t \gtrsim 1000\text{s}$ ), the roughness of Ag and  $C_{60}$  increases with the same exponent, though the

curves are shifted with respect to each other due to the different behaviour at intermediate times.

More pronounced differences are seen in the local roughness  $G(1, t)$ , plotted in Fig. 7.9 (b). This is expected, since  $G(1, t)$  is more sensitive to the differences in surface morphology seen in Figs. 7.7 and 7.8. One main feature of the  $C_{60}$  growth is the rounded island structure. This leads to a slower increase of the local roughness compared to the Ag system, where the islands are dendritic. On the other hand, the Ag system is characterised by a layer-by-layer-like growth at intermediate times. This is reflected by the longer plateau on the corresponding  $G(1, t)$  in the corresponding range of times. However, for long times the local roughness of  $C_{60}$  grows faster than for Ag, resulting in very similar values of  $G(1, t)$  at long times. This can be interpreted as an indication for similar morphologies in the two systems during the late stages of growth.

## 7.3 Particle dynamics and substrate morphology

So far, we have studied the evolution of the substrate morphology for different materials. However, we expect the differences in energies to also be reflected by the dynamics on the particle-resolved level. In this section, we focus on the particle-resolved dynamics and correlate it to the current surface morphology in order to establish the connection between the dynamics on a particle-resolved level and the dynamics of the surface morphology. Again, all data was simulated for  $T = 40^\circ\text{C}$  and  $f = 0.1 \text{ ML/min}$  for different material systems.

### 7.3.1 Local Dynamics

In order to understand the local dynamics, we study the MSD of  $C_{60}$  and our representative atomic systems, where the MSD is defined in Eq. (6.9). Figure 7.10 depicts the MSD after the growth of 0.5 ML, where we distinguish between particles that arrive between [Fig. 7.10 (a)] and on [Fig. 7.10 (b)] islands. All curves share the same general structure in that the MSD initially grows in time (with exponent approx. 1) and then saturates (indicating immobilisation). However, when comparing the curves for arrivals between and on islands, the two systems behave differently. Indeed, the diffusion behaviour of the Ag system is quite sensitive to the location of a particle's arrival, whereas that of  $C_{60}$  is not. We now relate these features to the morphology.

In the atomic system, the islands are fairly dendritic [see Fig. 7.7 (b)]. As a consequence, particles that arrive between the islands [Fig. 7.10 (a)] only travel short distances before they encounter the edge of an island. The majority of atomic particles either attaches for long time-spans or becomes immobilised completely, as further particles attach before they can detach themselves. This leads to an early onset of sub-diffusive behaviour (for  $t^* > 0.05 \text{ ms}$ ) and average travel distances of just a few nanometres before the particles are immobilised (see plateau in the MSD).

A quite different behaviour is seen for atomic particles that arrive on the islands [see Fig. 7.10 (b)]. These particles can diffuse across fairly large dendritic structures before encountering other particles. The step-edges hinder particles from leaving the island, but they do not slow down

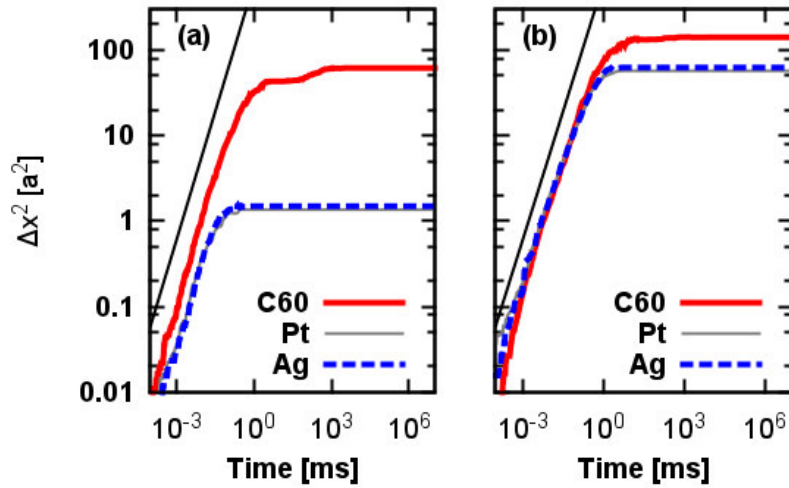


FIGURE 7.10: The MSD of particles that arrive (a) between islands or (b) on top of islands after the growth of 0.5 ML for different interaction energies  $E_n(C_{60}) = 0.13 \text{ eV}$ ,  $E_n(Ag) = 0.72 \text{ eV}$  and  $E_n(Pt) = 0.92 \text{ eV}$ . All systems are simulated on a triangular lattice with equal energy barriers  $E_D = 0.54 \text{ eV}$  and  $E_S = 0.11 \text{ eV}$ . The turquoise lines represent the MSD for free diffusion (linear time dependence).

their motion on the islands noticeably. Therefore, atomic particles on the islands can travel significantly further (as compared to the case discussed before) before they become immobilised and the MSD saturates.

The  $C_{60}$  system is characterised by a completely different island morphology [see Fig. 7.7 (a)]. As a consequence, molecules that arrive between islands can diffuse far further before encountering other molecules. This is simply because there is more free space. Moreover,  $C_{60}$  molecules can *detach* after encountering other molecules (as a result of the weaker binding). These effects lead to much larger travelled distances both between and on islands. Furthermore, the MSD curves for these two cases are similar.

An even better understanding of the systems emerges when we relate features of the MSDs to the fractions of particles performing different processes. This is done in Fig. 7.11, where we focus on particles arriving in between islands. Parts (a) and (c) show the corresponding MSDs, while parts (b) and (d) contain data for the fraction of particles involved in a specific process,  $N(p, t)$ . For both  $C_{60}$  and Ag systems it is clearly visible that the early stages of growth are dominated by freely diffusing particles ( $n = 0$ ). These form the main contribution to the MSD at small times. However, once particles begin to interact, distinct differences between  $C_{60}$  and Ag become apparent. During the growth of  $C_{60}$  there are many events where particles detach from one or two neighbouring particles (see curves in Fig. 7.11 (b) with  $n = 1, 2$ ). Such events are absent in the Ag system. We understand this difference as a consequence of the larger binding energy in the Ag system.

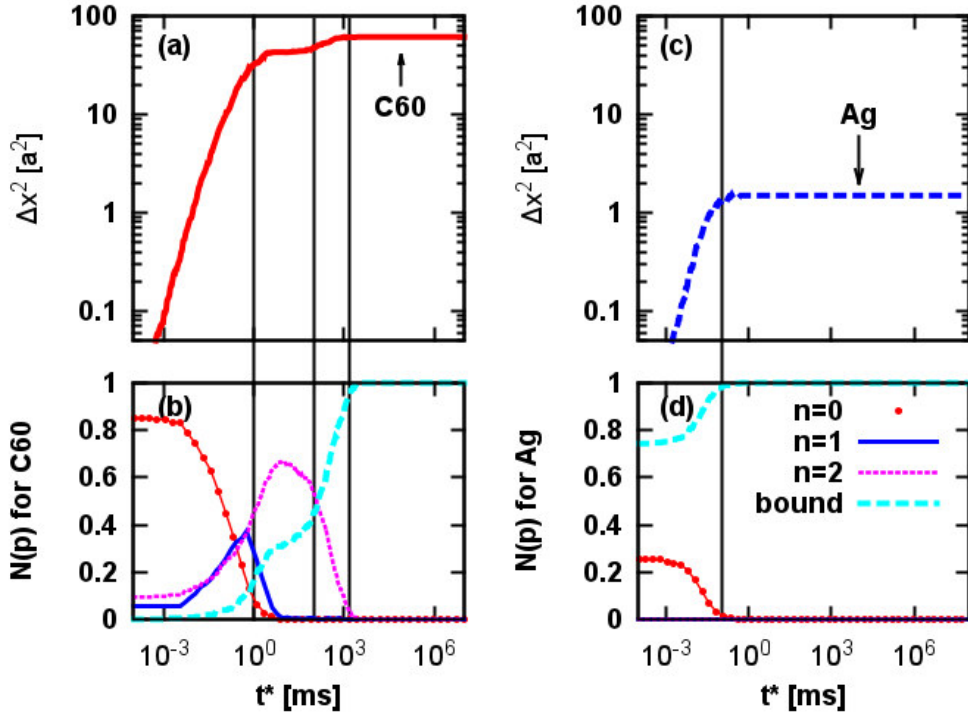


FIGURE 7.11: Part (a) and (c) show the MSD of the  $C_{60}$  and Ag systems already plotted in Fig. 7.10 (a) (i.e. diffusion in between islands), while (b) and (d) correlate these data to the time dependence of the fraction of particles doing a certain process. These processes can be free diffusion ( $n = 0$ ) and diffusing away from a site with  $n = 1$  or  $2$  neighbour particles. Also plotted are the fractions of particles that are immobilised (bound). All other processes are negligible.

**Free diffusion** For the initial free diffusion of particles arriving on the substrate, we can use the derivation discussed in Sec. 3.3 to derive a diffusion constant  $D(E_D = 0.54 \text{ eV})$ . Following the derivation of Sec. 3.3 for diffusion on a hexagonal lattice, we find that each lattice site has  $N = 6$  escape routes (see also Fig. 3.4). Correspondingly, we find the following expressions for the MSD

$$\Delta x(t^*)^2 = a^2 t^* \cdot 6\nu_0^D \exp(-\Delta E/kT) = 4Dt. \quad (7.10)$$

From this expression, we can determine an analytic expression for the diffusion constant

$$D = a^2 \cdot \frac{3}{2} \nu_0^D \exp(-E_D/kT) \approx 3.9 \cdot 10^{-14} \frac{\text{m}^2}{\text{s}}, \quad (7.11)$$

for  $T = 40^\circ \text{C}$  and  $a = 1 \text{ nm}$ . Fitting the MSD for  $C_{60}$  in Fig. 7.11 (a) on the interval  $0.0005 \text{ ms} \leq t^* \leq 0.1 \text{ ms}$ , we find the diffusion constant  $D = 3.6 \cdot 10^{-14} \text{ m}^2/\text{s}$ . Considering that a small fraction of the particles are already interacting with other particles in this time interval [see Fig. 7.11 (b)], we expect a slightly smaller  $D$  in the simulation. Following these considerations, we find a very good consistency between the expected and the simulated value of  $D$ .

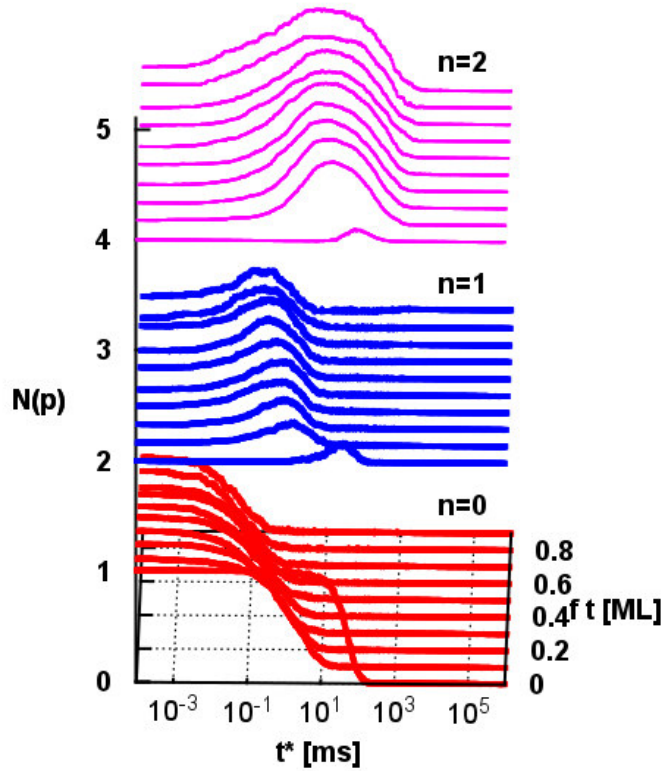


FIGURE 7.12: Number fraction of  $C_{60}$  molecules currently doing a certain process, as discussed in Fig. 7.11 (b), for particles arriving after  $f \cdot t = 0, 0.1, \dots, 0.9$  ML growth, considered at times  $t^*$  after their arrival. Only particles arriving between islands are considered. The red, blue and pink lines represent diffusion processes with 0, 1 and 2 neighbours respectively, where the blue curve is displaced by 2 in z direction and the pink by 4 to increase the overview. Processes with more neighbours occur rarely and are not plotted explicitly, bound particles are also not shown. Each curve in this graph is averaged over more than 500 independent runs.

### 7.3.2 Coupling of local dynamics to evolving surface

As the surface evolves we expect local neighbourhoods and therefore particle dynamics to change. In Fig. 7.12 we analyse how the most significance of the different diffusion processes change during the growth of a layer for different arrival times  $t$ . To this end, we resolve the single-particle motion in terms of the process types that we previously considered in Fig. 7.11 (b) and (d). However, while Fig. 7.11 (b) and (d) resolve the particle processes that arrive between islands at a coverage of 0.5 ML when particles arrive, we now study particles that arrive between the islands for different coverages  $f \cdot t$ . As previously discussed, the processes are studied at time  $t^*$  after arrival on the substrate.

The majority of molecules start out diffusion freely, independent of the substrate coverage. This observation is indicative for compact islands with few edge sites relative to neighbourless sites on the substrate.

On the empty substrate ( $f \cdot t = 0.0 \text{ ML}$ ), molecules initially diffuse freely without interacting with islands or edges, but are then bound fairly abruptly. Once particles meet other particles, they hardly move, as is indicated by the small peaks for the 1 and 2 neighbour processes. Instead, the particles are probably bound into the first island nuclei after the arrival of other particles.

At higher coverages, the majority of molecules also initially diffuse freely, but the time span of free diffusion decreases with increasing coverage. This can be explained in terms of the free path lengths between islands, which decrease as the coverage increases. However while the free diffusion time decreases, there is an increase in neighbour interaction processes, indicating that more particles attach to island edges but detach again. In total, particles stay mobile for a similar time span (approx. 100 ms), but the dominant process shifts from free diffusion to diffusion from neighbouring particles as the surface coverage increases.

In short, the local dynamics and the morphology are closely correlated during growth, and they influence each other during each stage in a non-trivial fashion.

## Chapter 8

# Conclusion C<sub>60</sub>

In conclusion, the experimental and theoretical study of C<sub>60</sub> multilayer growth presented in this part of the thesis yields, for the first time, a quantitative description of molecular thin film growth for the important case of C<sub>60</sub>, as an intermediate between atoms and colloids. In-situ specular X-ray reflectivity and diffuse scattering are powerful tools for non-invasive real-time studies of the morphological evolution during molecular growth. Furthermore, KMC simulations of C<sub>60</sub> multilayer growth can be constructed to access the experimental time- and length-scales required to study multilayer growth. In collaboration with S. Bommel *et al.* [119], we find observables that allow us to compare the experimental results to results from KMC simulations.

Using this comparison, we have been able to determine a consistent set of energy parameters determining the growth kinetics on the molecular level. This way we can quantitatively predict C<sub>60</sub> deposition at different temperatures and rates, including the evolution of island density and surface roughening with film thickness. Thus, our combined analysis provides a detailed understanding of C<sub>60</sub> in terms of molecular scale processes. Moreover, our study sheds new light on various dynamical aspects accompanying the growth. In particular, we show that the colloid-like, short-ranged character of C<sub>60</sub>-interactions leads to relatively long surface diffusion times before immobilisation occurs at existing islands. Nevertheless, the step-edge crossing barrier of C<sub>60</sub> differs from colloids [94] in that it is not a pseudo-step-edge barrier arising from lower diffusion probability at a step-edge, but a true energetic barrier as observed for atoms.

Comparing C<sub>60</sub> to atomic systems, we have discussed the single-particle and global dynamics accompanying the surface growth of the nano-molecular system C<sub>60</sub>. One main goal in this context was to understand the similarities and differences between nano-molecular and atomic growth. To this end, we have first identified energetic differences between the two system types. We then used the two system types to study both single-particle trajectories and the overall surface morphology.

We have found that there are indeed pronounced differences in the surface morphology during growth: The C<sub>60</sub> system displays compact islands with a rather large fractal dimension and significant spatial correlations between the islands. In contrast, the fractal dimension and range of ordering are far smaller in atomic systems. These differences in the global surface morphology during growth can be traced back to the differences in the energy barriers that single particles have to overcome. Moreover, we have shown that the differences in morphology

is intimately related to the single-particle dynamics. Atomic particles diffusing between islands can cover only small distances before they are immobilised, because the islands are fairly dendritic. On the other hand, particles in the  $C_{60}$  system can diffuse quite far, since the compact islands are separated through large, free surfaces.

The large diffusion distances are effectively enhanced by the fact that due to the small binding energies,  $C_{60}$  molecules can detach from island edges before they are immobilised. However, unlike colloidal systems [94],  $C_{60}$  has to overcome an energetic atom-like step-edge barrier for interlayer diffusion. This leads to a reduced mobility of both, molecules and atoms, between layers. The reduced mobility then leads to a roughening of the surface on large time-scales.

Further, we find a complex interplay of single-particle and global dynamics, whose characteristics reflect special molecular features of  $C_{60}$ , in particular the relatively small effective binding energy. Starting from our findings, one interesting question for further studies would be the connection between single-particle-trajectories and the long-time scaling behaviour derived from continuous rate-model descriptions.

Further, for a more detailed insight concerning the interplay of energy landscape and dynamics, it may be interesting to couple KMC simulations and MD simulations. Within such a study, configurations gained from KMC could be used to generate initial configurations for MD simulations. Conversely, MD simulations could be used calculate ‘on the fly’ the energy parameters required in the KMC simulations, thus taking into account the time-dependence of the energetics. Such an approach would yield important insight into all time-scales from up to  $\mathcal{O}(10^{-9})$ s towards  $\mathcal{O}(10^4)$ s.

Experimentally, real-time measurements of the overall surface morphology during the growth of organic molecules are possible through X-ray scattering [119] or low energy electron microscopy [85, 187]. In contrast, the dynamics of individual molecules is experimentally not (yet) accessible, as these phenomena take place on very small time-scales. Very recently, measurements of the particle-resolved dynamics of colloidal particles at room temperature have been performed [94]. However, in molecular systems, particle resolved dynamics under consideration of the local particle neighbourhood is only accessible at very low temperatures. An example are scanning tunnelling microscopy experiments to track the motion of individual molecules on a substrate and to determine waiting times [95]. Extending such investigations to higher temperatures may open the path to quantities such as the ones calculated in the present work.

Since  $C_{60}$  features aspects of both, atomic and colloidal systems, our findings will help to gain insight into island nucleation and surface growth processes for van-der-Waals bound molecules between the scales of atomic and colloidal systems. This quantitative, scale-bridging understanding enables predictive simulations and a rational choice of growth conditions, which, together with molecular design and synthesis, ultimately leads to optimised design of functional materials.

## **Part III**

# **Anisotropic particles on structured substrates**



## Chapter 9

# Introducing anisotropic molecules on structured substrates

So far, in Chap. 4-8, the fundamental growth properties of isotropic molecules on the nanometre length-scale were studied. However, C<sub>60</sub> is a unique model system because it is spherically symmetric. Nearly all molecules on the nanometre length-scale have an anisotropic shape and an anisotropic charge distribution. Furthermore, most growth setups involve structured substrates made of different materials.

In this part of the thesis, the fundamental understanding gained from the thorough study of C<sub>60</sub> growth is expanded to more general material systems. The considerations made here can be applied to a broad variety of material systems but we focus on hybrid organic-inorganic material systems, where the anisotropic COMs are grown on an inorganic substrate.

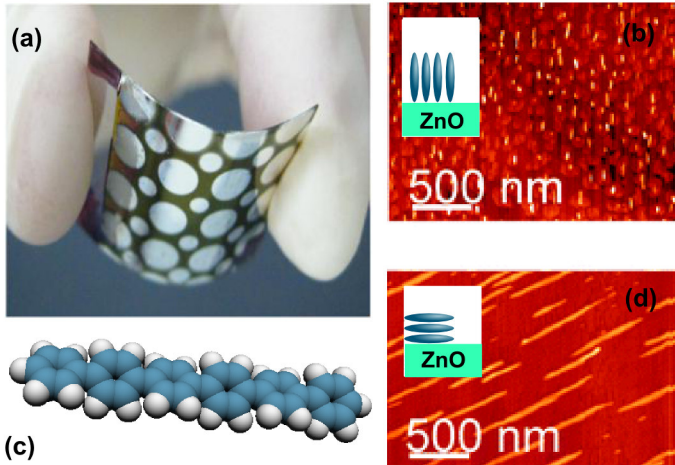


FIGURE 9.1: Insight into growth of anisotropic molecules on structured substrates. Part (a) depicts a flexible hybrid organic-inorganic solar cell using a conjugated polymer as the organic component and ZnO as inorganic component [243]. Parts (b) and (d) show atomic force microscopic images of the anisotropic COM 6P grown on ZnO(10-10) at  $T = 294\text{K}$  and  $373\text{ K}$  respectively. The images in parts (b) and (d) are adapted from the work of Blumstengel *et al.*[28]. Finally, part (c) contains a snapshot of a 6P molecule in vacuum, obtained from MD simulations [244].

**Hybrid devices** Hybrid structures made of conjugated organic molecules (COMs) adsorbed onto inorganic semiconductor substrates open a novel field of application in opto-electronics. On the one hand, the highly ordered crystalline and electronic structure of semiconductor surfaces leads to well-defined surface patterns. On the other hand, the anisotropic character of the COMs allows them to self-assemble into a variety of structures each characterised by different features in terms of functionality (charge transfer, optimisation of band-gaps, excitation transfer). Combining these materials thus leads to tunable hybrids whose characteristic properties, such as the work-function and charge carrier mobility, can be tailored by the choice molecules and substrates [183, 245, 246], as well as by the self-assembled structures formed by the adsorbed molecules [14, 247, 248]. This wide range of possibilities could not be achieved with an organic or inorganic component alone. An example of a hybrid organic-inorganic device is the flexible solar cell presented in Fig. 9.1 (a), where the use and assembly of ZnO nanowires make the solar cell flexible, and the choice and alignment of the organic molecules increases the solar cell efficiency.

In Sec. 1.1 the influence that orientational ordering of anisotropic COMs can have on the device functionality, and the importance of understanding and predicting the collective orientational ordering was discussed. This is now extended to include the influence of structured inorganic substrates.

A variety of different substrates are used as inorganic component in hybrid devices. These range from plain silicon[249], via simple two-element crystals such as SiO<sub>2</sub> [250] and ZnO [251] to complex crystalline materials such as gadolinium gallium garnet Gd<sub>3</sub>Ga<sub>3</sub>O<sub>12</sub> [252]. In order to gain the insight that applies to a field of materials instead of being very material-specific, we focus on two element crystals. Two different elements have different electron affinities. As the inorganic material is a semiconductor and hence does not have a wide-spread electron gas, the differences in electron affinity can lead to one element ‘stealing’ electrons from the other. Correspondingly, two-element inorganic semiconductors often have an interesting charge distribution that creates an electrostatic structure on the crystal surface. The generated electric field interacts with the charge distribution of the COMs, creating another level of complexity in our growth setting.

**Growth of anisotropic molecules** A comprehensive understanding of the complex interplay of molecular structure, substrate characteristics such as the structuring of the substrate, and experimental conditions, as well as the consequences for self-assembly and growth of the COMs has not yet been achieved [253]. In addition, most of the knowledge for inorganic semiconductors [254, 255] is not immediately transferable to organic semiconductors, because of the anisotropy of organic semiconductor molecules and the vast number of different molecules with different anisotropic physio-chemical properties [256]. Hence it is difficult to gain fundamental insight into the underlying phenomena and very little is known, especially for non-equilibrium conditions [253].

From a theoretical point of view, a major challenge in understanding self-assembled structures of hybrid systems is that these structures involve the *collective* (i.e. many-particle) behaviour occurring on length-scales beyond those achievable by traditional approaches such as electronic density functional theory (DFT). This calls for more coarse-grained computational approaches

where, to some extent, microscopic features are neglected in favour of relevant ‘ingredients’ for collective behaviour.

**Simulations using MC approaches** MC approaches towards complex hybrid organic-inorganic material systems are in their infancy. While for some problems it is sufficient to treat the COM as a point-like particle [121], it is well established that the mobility of molecules is influenced by the orientational degrees of freedom [126, 257].

Within the few existing DMC studies of anisotropic molecules at interfaces, the molecules’ orientations are typically strongly restricted; e.g. molecules are modelled by strings occupying multiple lattice sites [73, 123, 258], or the orientations are restricted to 2D-rotations [125] (note that the latter study also considers the influence of a structured substrate). Such restrictions are inappropriate for many material systems, where it is known from experiments that the molecules can explore the full, 3D space of orientations [28, 79, 82, 259]. An example of the three-dimensional orientational ordering of anisotropic COMs is given in Fig. 9.1(b) and (d), where the same materials were used and only the growth conditions differ between the two images. Clearly, the orientational ordering depends on the growth conditions, and closer study of the scans reveals that for one set of growth conditions the particles form clusters of standing particles [in Fig. 9.1(b)], while for a different set of growth conditions they form clusters of lying particles [in Fig. 9.1(d)].

While there are very few growth simulations that study organic-inorganic interfaces with anisotropic molecules, it is worth noting that our system has similarities to systems studied in the liquid crystal community. In the context of liquid crystals, a variety of models exist that are used to study the equilibrium collective ordering of rod-like particles. These are mostly based on lattice-models that are used to investigate phase behaviour, mostly using MC simulations. Prominent examples are the Zwanzig model (involving discretised translational motion and discretised rotations) [260–263] and the Lebwohl-Lasher model (particles fixed to lattice sites, continuous rotational motion) [264–266]. These models have been successfully used to study orientational ordering both in bulk [264] and in spatially confined systems [261–263, 265] including confinement to a 2D plane. The majority of these calculation is based on a coarse-grained modelling of the particles, where the details of the material are neglected and particles are treated as rigid rods.

**Example material system: 6P on ZnO(10-10)** In this spirit, we propose in the present study a classical, coarse-grained model as a representative hybrid system, that is, the conjugated organic molecule 6P [depicted in Fig. 9.1(c)] adsorbed onto zinc-oxide (ZnO), particularly the substrate facet ZnO(10-10). We choose this material system as a representative system because the components [104, 105, 247, 267, 268] and some aspects of their interactions [79, 100, 106] are well understood. Furthermore, this material combination is promising for opto-electronic applications [269–271]. The modelling principles and growth results obtained for this material system are transferable to other material systems and reflect more fundamental principles of orientational ordering during growth.

Experimentally, systems of 6P have been studied both in the three-dimensional (3D) bulk crystal phase [267] and in film-like geometries (see, e.g. Refs. [14, 247] and references therein).

As to the substrate, ZnO is known to have suitable energy characteristics for many opto-electronic applications [268] and it has been studied experimentally in combination with various COMs including 6P [28, 272]. Indeed, ZnO is already used in prototype hybrid devices [243, 273]. Here we are particularly interested in the ZnO(10-10) facet, since this is characterised by an alternating arrangements of positively charged Zn atoms and negatively charged O atoms. This leads to a stripe-like electrostatic surface field, which has already been found to have a strong impact on the shape and orientational structure of adsorbed islands of 6P [28]. Nevertheless, while many experimental studies of both, 6P and ZnO, exist, little is known about the details and, more importantly, the origin of the orientational ordering, both in equilibrium and during growth.

So far, most theoretical studies of 6P at surfaces are based on DFT. For example, Berkebile *et al.* have studied 6P on Cu(110) [274, 275]. They found that the periodicity of the 6P layer has a large influence on the energetics of the resulting hybrid system, as these depend e.g. on how the  $\pi$  orbitals of the adsorbed 6P molecules lie in relation to the hybridisation states that are available at the metal surface. This observation further supports the significance of the self-assembled structures for device functionality. Other DFT studies emphasise the influence of the molecule-substrate interactions, e.g. Braun and Hla found that 6P molecules adsorb with alternating twist of the  $\pi$  rings if physisorbed on Ag(111) [276]. Quite recently, della Sala *et al.* [100] studied the behaviour of an *individual* 6P molecule on a ZnO(10-10) surface. This study demonstrates that 6P adsorbs in a planar configuration and aligns with the positively charged rows of Zn atoms on the surface. Moreover, Goose *et al.* [102] and Hlawacek *et al.* [277] have considered the diffusion behaviour of 6P at step-edges.

For computational reasons DFT is still restricted to single molecules or very small clusters of molecules. Therefore various recent studies have attempted to investigate 6P-substrate systems by MD, where the molecules and substrates are modelled with atomic resolution, but the dynamics is determined by classical force fields. An example is the study by Potocar *et al.* who consider the transition from lying small clusters to the upright larger clusters of 6P molecules [107] at 6P crystalline surfaces. Recently, MD simulations of 6P bulk crystals [104] and organic-organic hetero-surfaces involving 6P [278] also have been performed.

**Structuring of the following sections.** In order to study large systems and growth of large numbers of 6P molecules, we implement a coarse-grained model of 6P at ZnO(10-10) suitable for DMC simulations with continuous, 3D orientations in Chap. 10. Within our model, inter-molecular interactions are modelled via a Gay-Berne (GB) potential (describing steric and van-der-Waals interactions) combined with the electrostatic potential between two linear quadrupoles (see Sec. 10.3). Similarly, the molecule-substrate interactions are described via a combination of an integrated Lennard-Jones (LJ) potential and the coupling between a linear quadrupole and the electric field stemming from line charges characterising ZnO(10-10) [100] (see Sec. 10.4). These interactions are parametrised using DFT calculations and experimental input.

To understand the interplay of the various contributions to the interaction Hamiltonian, we first perform equilibrium MC simulations that are introduced in Sec. 10.5, before performing growth simulations (introduced in Sec. 10.6). The collective ordering is characterised using observables that are defined in Chap. 11.

Chapter. 12 studies the collective ordering of 6P molecules on ZnO(10-10). This study is split into two parts: First, we study the collective ordering in equilibrium, where we pick apart the influence of the various interactions as well as the substrate configuration in Sec. 12.1. Here, we observe various experimentally found forms of ordering including a lying nematic phase and a standing nematic phase with internal Herringbone ordering. Then, we use the equilibrium phases as a basis to understand the collective ordering of 6P molecules during growth in Sec. 12.2. For low adsorption rates, we find behaviour close to the equilibrium phase behaviour. However for intermediate to high adsorption rates we find complex competition between the different time scales and interaction strengths, which lead to re-entrant growth and non-monotonous behaviour as a function of the adsorption rate.

Finally, all results for the collective ordering of 6P are summarised in Chap. 13.

# Chapter 10

## Model specifics for 6P on ZnO

In order to access the time and length-scales required for growth simulations and large-scale collective ordering phenomena, we require a coarse-grained model (as discussed in detail in Chap. 2 and 3). Unlike the spherical molecule C<sub>60</sub> (see Chap. 4-8), general COMs are anisotropic. This anisotropy cannot be neglected if the ordering behaviour is studied. However, no well established modelling approach for anisotropic molecules in DMC simulations exists so far, as we review in Sec. 9. So before studying the orientational ordering, we develop and parametrise a coarse-grained description of our materials.

Here, we use 6P on ZnO(10-10) as a representative sample system for anisotropic molecules on structured substrates. However, very similar considerations can be made to describe any COM on any topologically smooth surface with an electrostatic line structure. While the details of the model that we will develop in the following sections are specific to 6P on ZnO(10-10), the general approach as well as the resulting ordering (see Chap. 12) are generic to COMs on metal-oxide surfaces with alternating rows of metal and oxygen.

### 10.1 Coarse-graining for COMs on structured substrates

In order to find a coarse-grained description, we first focus on the molecule 6P as shown in Fig. 10.1. The molecule consists of six aromatic rings that form a chain [see Fig. 10.1(a)]. From experimental and DFT studies, we know that individual molecules adsorb on the surface in a planar configuration and a straight molecular backbone that forms the molecule's long axis [100]. Furthermore, in the bulk crystal and in vacuum the molecules also have a straight long axis [267] [see Fig. 10.1 (c) for an example of a molecule in vacuum]. From DFT studies of step-edge crossing we know that bending of the long axis of the molecule is associated with a significant energetic penalty [277] and that 6P may prefer to rotate and cross step-edges by twisting around its long axis instead of bending the long axis [102]. Based on these observations, we describe the molecules by a rigid long axis  $\mathbf{u}(\vartheta, \varphi)$  [see Fig. 10.1 (c)].

6P molecules on ZnO have interesting collective orientational ordering, where the growth conditions dominate the structure even after subsequent relaxation, as found in experimental

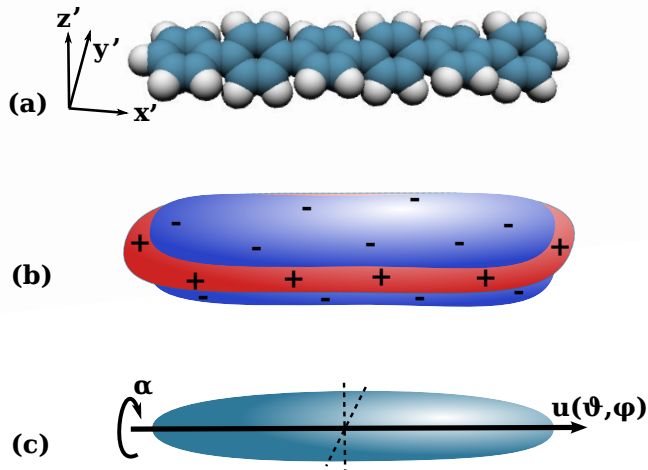


FIGURE 10.1: Three sketches of a 6P molecule with different degrees of sophistication: (a) atomistic model (twisted configuration) with the blue (white) parts representing C-(H-)atoms, using atomic coordinates obtained by Palczynski *et al.* [244], (b) roughly sketched charge distribution with negative  $\pi$ -orbitals above and below the molecule and positively charged H atoms around the edge, and (c) representation as an uniaxial ellipsoid. In part (a) we introduce the three eigendirections of the molecules, where  $x'$  is parallel to the longest axis of the molecule and  $z'$  parallel to the shortest. The uniaxial ellipsoid in (c) is characterised by the vector  $\mathbf{u}(\vartheta, \varphi)$ , which lies parallel to the eigendirection  $x'$  ( $\vartheta, \varphi$  are Euler angles in the space-fixed coordinate system). The ellipsoid is insensitive to rotation by the angle  $\alpha$  around the axis  $\mathbf{u}(\vartheta, \varphi)$ .

studies [268]. Correspondingly, we do not want to restrict the orientational degrees of freedom of the molecules. In our coarse-graining model, every molecule has continuous rotational degrees of freedom described by the three Euler angles  $\varphi, \vartheta, \alpha$ . However, in order to perform DMC simulations, we coarse-grain the translational diffusion into diffusion between lattice sites. We motivate the lattice-based model as follows: First, real ZnO(10-10) surfaces have a well-defined unit cell characterised by a charge pattern. From DFT calculations [100] and experiments [28, 100] it is known that this electrostatic pattern is so strong that, the molecule's  $y$ -coordinates are *essentially* fixed by the stripes. Second, restricting the lateral positions reduces computational effort. And third, as we discussed in Sec. 9, we know that lattice-based simulations are well suited to study the fundamentals of orientational ordering in systems of anisotropic particles.

## 10.2 Splitting the Hamiltonian

A system of anisotropic molecules on a patterned substrate is subject to a multitude of interactions, both between different molecules and between molecules and substrate. In the following we aim to construct a simplified, coarse-grained Hamiltonian  $H$ , which still takes into account the most significant interactions occurring in a system of 6P molecules on a ZnO(10-10) substrate. One main simplification is that we neglect the internal atomistic structure of a 6P molecule (and likewise that of the substrate). The molecule's atomistic structure, consisting

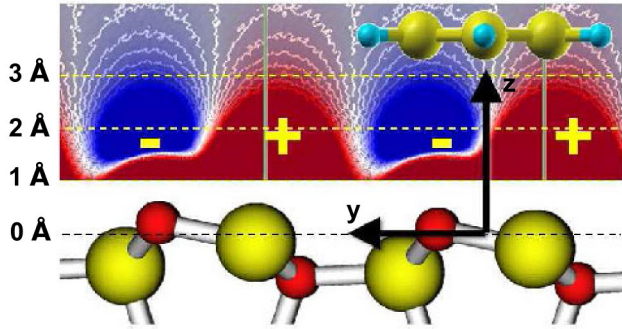


FIGURE 10.2: Charge distribution above the ZnO(10-10) facet. The surface is below where the  $y$ -direction is across the charge lines, the  $x$ -direction (into the image plane) is along the charge lines and the  $z$ -direction is orthogonal to the substrate plane. The red spheres in the substrate represent O-atoms, while the yellow larger spheres are Zn-atoms. Above the right hand side of the substrate a 2P molecule is shown at its optimal height above the substrate  $z_{\min} = 3.5 \text{ \AA}$ . This image is adapted from the DFT and experimental studies of della Sala *et al.* [100].

of C- and H-atoms, is sketched in Fig. 10.1(a). Here we rather represent each molecule as a rigid body, specifically, a uniaxial ellipsoid, as sketched in Fig. 10.1(c). However, despite this strong simplification we do take into account the fact that 6P has a complex charge distribution, which is indicated in Fig. 10.1(b). The interaction of the molecular charge distribution with the substrate charge distribution shown in Fig. 10.2 is also significant for the orientational ordering, hence it needs to be taken into consideration in the modelling of the system interactions. To proceed, we divide the (potential part of the) Hamiltonian into

$$H = H_{\text{mol-mol}} + H_{\text{mol-sub}}, \quad (10.1)$$

where the subscripts ‘mol’ and ‘sub’ refer to the molecule and substrate, respectively.

In the following sections we will discuss this Hamiltonian in detail and analyse the implicit assumptions made. Specifically, Sec. 10.3 discusses both the electrostatic and the non-electrostatic contributions to the molecule-molecule interactions  $H_{\text{mol-mol}}$ , while Sec. 10.4 introduces the corresponding electrostatic and non-electrostatic molecule-substrate interactions.

### 10.3 Molecule-molecule interactions

Like all COMs, 6P interacts both via non-electrostatic (van-der-Waals attraction and Pauli repulsion) and electrostatic interactions. The main contributions to these interactions are sketched in Fig. 10.1, which shows both the approximate morphology of a 6P molecule and the charge distribution of this molecule. In order to reflect these two aspects of interaction, we split the molecule-molecule interactions into a non-electrostatic and an electrostatic contribution. We introduce, discuss and parametrise these contributions below.

$d_w$	$l$ [nm]	$d$ [nm]	$\epsilon_0$ [eV p.p.]	$\epsilon_e/\epsilon_s$	$\mu$	$\nu$
0.6	2.79	0.335	0.07	1/12.5	2.0	1.0

TABLE 10.1: Parametrisation of the inter-molecular GB potential for 6P molecules based on the bead model and parameters for individual benzene rings suggested by Golubkov and Ren [279]. The abbreviation p.p. stands for ‘per particle’.

### 10.3.1 Non-electrostatic interactions: Gay-Berne (GB) potential

To model the non-electrostatic part of the molecule-molecule interaction, each molecule is represented by an uniaxial ellipsoid as illustrated in Fig. 10.1 (c). The geometry of the resulting coarse-grained 6P ‘molecules’ is characterised by the molecular length  $l$  and diameter  $d$ . These values (as well as those of the other GB parameters) are listed in Tab. 10.1. Moreover, the orientation corresponding to the uniaxial ‘molecule’ is defined by the vector

$$\mathbf{u}_i = (\sin \vartheta_i \cos \varphi_i, \sin \vartheta_i \sin \varphi_i, \cos \vartheta_i) \quad (10.2)$$

[see Fig. 10.1 (c)].

The role of the biaxiality [which is indeed present in true 6P molecules, see Fig. 10.1 (a)] will be discussed below. As molecules on the nanometre length-scale display an attractive (van-der-Waals) interaction as well as the repulsion of their cores, we use a generalisation of the LJ potential for anisotropic molecules, that is, the Gay-Berne (GB) potential [280, 281]. Specifically, we use the formulation suggested by Golubkov and Ren [279]. The resulting potential of two molecules with orientations  $\mathbf{u}_i$ ,  $\mathbf{u}_j$  and connection vector  $\mathbf{r}_{ij} = \mathbf{r}_i - \mathbf{r}_j$  is given by <sup>1</sup>

$$V_{\text{GB}}(\mathbf{u}_i, \mathbf{u}_j, \mathbf{r}_{ij}) = 4\epsilon(\mathbf{u}_i, \mathbf{u}_j, \mathbf{r}_{ij}) \cdot \left( \left[ \frac{\sigma_0 d_w}{r_{ij} - \sigma(\mathbf{u}_i, \mathbf{u}_j, \hat{\mathbf{r}}_{ij}) + d_w \sigma_0} \right]^{12} - \left[ \frac{\sigma_0 d_w}{r_{ij} - \sigma(\mathbf{u}_i, \mathbf{u}_j, \hat{\mathbf{r}}_{ij}) + d_w \sigma_0} \right]^6 \right). \quad (10.3)$$

The position of the potential minimum for molecules with parallel long axes is determined by  $\sigma_0$ , and  $d_w$  determines the softness of the molecules. The configuration-dependent well depth  $\epsilon(\mathbf{u}_i, \mathbf{u}_j, \mathbf{r}_{ij})$  allows for different well depths for different configurations of the molecules [281].

$$\epsilon(\hat{\mathbf{u}}_i, \hat{\mathbf{u}}_j, \hat{\mathbf{r}}_{ij}) = \epsilon_0 \epsilon(\hat{\mathbf{u}}_i, \hat{\mathbf{u}}_j)^\nu \epsilon'(\hat{\mathbf{u}}_i, \hat{\mathbf{u}}_j, \hat{\mathbf{r}}_{ij})^\mu, \quad (10.4)$$

with

$$\epsilon(\hat{\mathbf{u}}_i, \hat{\mathbf{u}}_j) = [1 - \chi^2(\hat{\mathbf{u}}_i \cdot \hat{\mathbf{u}}_j)^2]^{-1/2} \quad (10.5)$$

and

$$\epsilon'(\hat{\mathbf{u}}_i, \hat{\mathbf{u}}_j, \hat{\mathbf{r}}_{ij}) = [1 - \chi'/2(B_+ + B_-)]. \quad (10.6)$$

---

<sup>1</sup>Note that the GB potential [279] displays an artefact for strongly anisotropic molecules, which attract each other under conditions of high overlap. In order to circumvent this artefact we assign a large energy ‘penalty’ to configurations with  $\mathbf{r}_{ij} \leq 0.9\sigma(\mathbf{u}_i, \mathbf{u}_j, \mathbf{r}_{ij})$ .

Furthermore, the configuration-dependent contact distance  $\sigma(\mathbf{u}_i, \mathbf{u}_j, \hat{\mathbf{r}}_{ij})$  is [280, 281]

$$\sigma(\hat{\mathbf{u}}_i, \hat{\mathbf{u}}_j, \hat{\mathbf{r}}_{ij}) = \sigma_0 [1 - \chi/2(A_+ + A_-)]^{-1/2}. \quad (10.7)$$

The anisotropic parameters included are

$$\chi = \frac{l^2 - d^2}{l^2 + d^2} \quad \text{and} \quad A_{\pm} = \frac{((\hat{\mathbf{r}}_{ij} \cdot \hat{\mathbf{u}}_i) \pm (\hat{\mathbf{r}}_{ij} \cdot \hat{\mathbf{u}}_j))^2}{1 \pm \chi(\hat{\mathbf{u}}_i \cdot \hat{\mathbf{u}}_j)}, \quad (10.8)$$

$$\chi' = \frac{1 - (\epsilon_e/\epsilon_s)^{1/\mu}}{1 + (\epsilon_e/\epsilon_s)^{1/\mu}} \quad \text{and} \quad B_{\pm} = \frac{((\hat{\mathbf{r}}_{ij} \cdot \hat{\mathbf{u}}_i) \pm (\hat{\mathbf{r}}_{ij} \cdot \hat{\mathbf{u}}_j))^2}{1 \pm \chi'(\hat{\mathbf{u}}_i \cdot \hat{\mathbf{u}}_j)}. \quad (10.9)$$

To parametrise the GB potential in accordance with 6P we use the bead-chain model introduced in the work of Golubkov and Ren [279]. These authors started from the GB interaction potential of two benzene rings, which is known. In this spirit, we can model the interaction of two planar 6P molecules through the interaction of two planar chains of benzene rings (beads). As a further step of simplification, we parametrise the uniaxial interaction potential  $V_{\text{GB}}(\mathbf{u}_i, \mathbf{u}_j, \mathbf{r}_{ij})$  [see Eq. (10.3)] to match the potential gained from the interactions of the two benzene bead chains. Examples of both the bead-chain and the GB potential are shown in Fig. 10.3, where we focus on three relevant pair configurations.

### 10.3.2 The multipole moments of 6P molecules

To start with, we analyse the molecular charge distribution, which is sketched in Fig. 10.1(b), in terms of its multipole moments. To ensure that our model is robust we determine the moments for two different molecular configurations, a planar and a twisted molecule.

The basic configuration used in our modelling is the planar molecule, which was also used by della Sala *et al.* [100]. To define this configuration, we use the partial charges  $q_l$  and atomic positions  $\mathbf{r}_l$  (where  $l = 1, \dots, M$  with  $M$  being the total number of atoms in the molecule) gained from a planar 6P model constructed in MARVINSKETCH by ChemAxon [282]. The second molecular configuration that we study is a 6P molecule with twisted benzene rings. This configuration is the relevant one for a single 6P molecule in vacuum. The corresponding partial charges and atomistic coordinates were determined by Palczynski *et al.* [105, 244].

For reasons discussed later, the highest multipole moment considered is the hexadecapole. The explicit expressions for the constant charge  $q$ , the dipole moment  $p_\alpha$ , the quadrupole moment  $Q_{\alpha\beta}$ , the octupole moment  $O_{\alpha\beta\gamma}$  and the hexadecapole moment  $H_{\alpha\beta\gamma\eta}$  are derived and listed in App. D.

Our numerical values for the multipoles are given in Tab. E.1 in App. E. It is seen that the monopole ( $q$ ) and dipole moments ( $p_\alpha$ ) are essentially zero, whereas the quadrupole moment ( $Q_{\alpha\beta}$ ) is not. However, as we will see in Sec. 10.4.2, the quadrupole moment alone is not sufficient to correctly describe the molecule's orientation to the substrate. We note in passing that our quadrupole moment for the planar configuration is very close to that obtained in Ref. [100]. One also sees from Tab. E.1 in Appendix E that the octupole ( $O_{\alpha\beta\gamma}$ ) and the

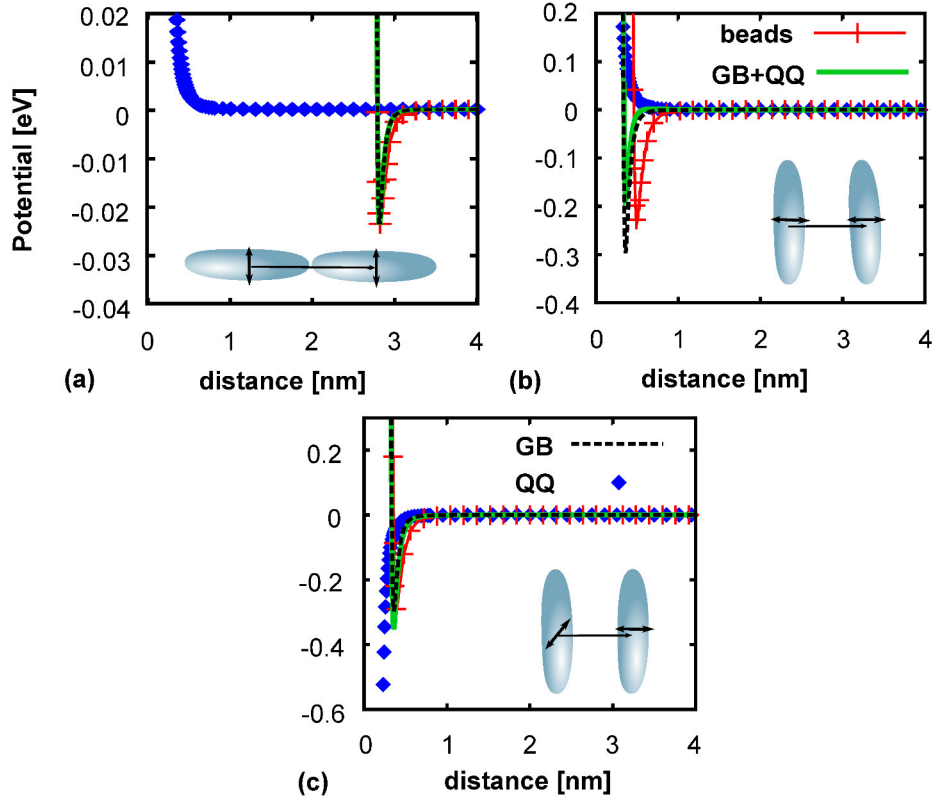


FIGURE 10.3: Parts (a)–(c) show the contributions to the molecule-molecule interaction energy for different pair configurations. Here, the legends in parts (b) and (c) apply to the corresponding graphs of all three parts. In the sketches at the bottom of each plot, the molecules are shown in the representation introduced in Fig. 10.1(c). The orientation of the additional linear quadrupole moment (see Sec. 10.3.3) is indicated through the double arrow at the centre of each molecule. Each part includes the potential between the molecules evaluated from the bead-chain parametrisation suggested by Golubkov and Ren [279] as a crosshatched (red) line labelled ‘beads’. The other three traced potentials are the GB potential (GB), the quadrupole-quadrupole interaction (QQ) and the sum of the two (GB+QQ).

Note the differences in the energy scales.

hexadecapole ( $H_{\alpha\beta\gamma\eta}$ ) are also non-zero. We will come back to this point in the discussion of the molecule-substrate interaction.

### 10.3.3 Electrostatic molecule-molecule interactions

To describe the electrostatic part of the molecule-molecule interaction we focus on the first non-vanishing multipole contribution, that is, the interaction stemming from the quadrupole moments ( $Q_{\alpha\beta}$ ). As seen from Tab. E.1 in Appendix D, one has  $Q_{xzx} \approx Q_{yyz} > 0$ ,  $Q_{zzz} \approx -2Q_{xzx}$  [in the eigensystem of the particle, see Fig. 10.1(a)] for both, the planar and the twisted configuration. It therefore seems justified to approximate the full quadrupole-tensor by that related to a *linear* quadrupole. The latter is equivalent to three charges of magnitude  $-q/2$ ,  $q$ , and  $-q/2$  that lie aligned, separated by equal distances  $D$ , on the  $z$  eigenaxis of the original molecule [see Fig. 10.1(a)]. The corresponding value of  $Q$  is  $Q = qD^2$ .

In the following we denote the direction of this linear quadrupole by the vector  $\mathbf{q}_i$ . Note that  $\mathbf{q}_i$  lies *perpendicular* to the symmetry axis  $\mathbf{u}_i$  of the uniaxial ellipsoid introduced in Sec. 10.3.1.

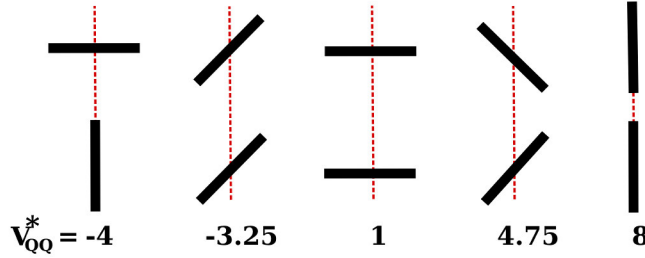


FIGURE 10.4: Interaction energy of two linear point quadrupoles for specific configurations.

In other words, the coarse-grained particle now becomes effectively biaxial. Consequently, the orientation of  $\mathbf{q}_i$  in the space-fixed coordinate system is characterised by the three (Euler) angles, that is,

$$\mathbf{q}_i(\alpha, \vartheta, \varphi) = \begin{pmatrix} \cos \alpha \cos \vartheta \cos \varphi + \sin \alpha \sin \varphi \\ \cos \alpha \cos \vartheta \sin \varphi - \sin \alpha \cos \varphi \\ -\cos \alpha \sin \vartheta \end{pmatrix}. \quad (10.10)$$

We are now in the position to write down the electrostatic interaction between two coarse-grained 6P molecules. In our model this is the interaction between two linear quadrupoles [283] given by

$$V_{QQ}(\mathbf{q}_i, \mathbf{q}_j, \mathbf{r}_{ij}) = \frac{3}{4} \frac{1}{4\pi\epsilon_0} \frac{Q^2}{r_{ij}^5} [1 - 5 \cos \beta_i^2 - 5 \cos \beta_j^2 - 15 \cos \beta_i^2 \cos \beta_j^2 + 2(\cos \gamma_{ij} - 5 \cos \beta_i \cos \beta_j)^2], \quad (10.11)$$

where  $r_{ij} = |\mathbf{r}_{ij}|$ ,  $\cos \beta_i = \mathbf{q}_i \cdot \hat{\mathbf{r}}_{ij}$  (with  $\hat{\mathbf{r}}_{ij} = \mathbf{r}_{ij}/r_{ij}$ ),  $\cos \beta_j = \mathbf{q}_j \cdot \hat{\mathbf{r}}_{ij}$  and  $\cos \gamma_{ij} = \mathbf{q}_i \cdot \mathbf{q}_j$ . The value of the quadrupole moment  $Q = Q_{zz'}$  is discussed in Tab. E.1 and App. D).

**The configuration dependence of quadrupole-quadrupole interactions.** We study here the dimensionless expression [compare with Eq. (10.11)]

$$V_{QQ}^*(\mathbf{q}_i, \mathbf{q}_j, \mathbf{r}_{ij}) = [1 - 5 \cos \beta_i^2 - 5 \cos \beta_j^2 - 15 \cos \beta_i^2 \cos \beta_j^2 + 2(\cos \gamma_{ij} - 5 \cos \beta_i \cos \beta_j)^2], \quad (10.12)$$

in order to compare the relative energies of different configurations. In Fig. 10.4 we show five relevant configurations together with the corresponding values of  $V_{QQ}^*$ . It is seen that the T-configuration has the smallest interaction energy, closely followed by a configuration in which both quadrupoles are parallel and form an angle of 45° with the connection vector. The interaction energy is maximal for parallel quadrupoles that are aligned with respect to their connection vector.

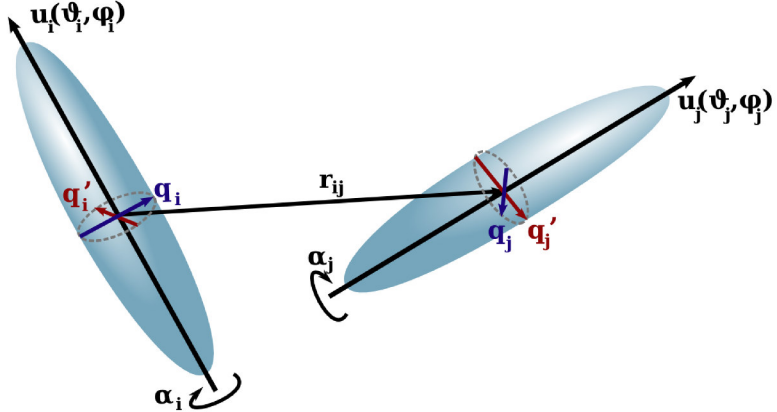


FIGURE 10.5: Exemplary configuration of two coarse-grained 6P molecules with the long axes  $\hat{\mathbf{u}}_i$  and  $\hat{\mathbf{u}}_j$  and the linear quadrupole moments oriented along  $\mathbf{q}_i$  and  $\mathbf{q}_j$ . The quadrupole moments  $\mathbf{q}'_i$  and  $\mathbf{q}'_j$  denote the quadrupole moments that mimic the electrostatic molecule-substrate interaction [see Eq. (10.20)].

**Hamiltonian of the full molecule-molecule interaction.** Taken altogether, the total Hamiltonian for the molecule-molecule interaction is given by

$$H_{\text{mol-mol}} = \sum_{i=1}^N \sum_{j \neq i} (V_{\text{GB}}(\hat{\mathbf{u}}_i, \hat{\mathbf{u}}_j, \mathbf{r}_{ij}) + V_{\text{QQ}}(\mathbf{q}_i, \mathbf{q}_j, \mathbf{r}_{ij})), \quad (10.13)$$

where  $V_{\text{GB}}$  and  $V_{\text{QQ}}$  are defined in Eqs. (10.3) and (10.11), respectively. An exemplary configuration of two coarse-grained 6P molecules is shown in Fig. 10.5. Furthermore, numerical results for the various types of molecule-molecule interactions as a function of the distance are plotted in Fig. 10.3. The lowest-energy configuration corresponds to parallel oriented ellipsoids with a T-like orientation of the quadrupole moments.

## 10.4 Molecule-substrate interactions

As previously discussed in Sec. 10.2, both the non-electrostatic and, more importantly, the electrostatic molecule-substrate interactions have a significant impact on the orientational ordering in the system. The alignment and position of a single 6P molecule on a ZnO(10-10) substrate was previously studied by della Sala *et al.* [100]. They found an approximate description of the electrostatic field generated by the substrate, as well as determining the exact optimal position of a 6P molecule on the substrate.

The ideal configuration for a 6P molecule above ZnO(10-10) is found to be above and aligned with the positively charged ZnO(10-10) (see Fig. 10.6). This observation is in agreement with our expectation regarding the molecular charge distribution (shown in Fig. 10.1(b)). The negative charge clouds above and below the molecular plane are attracted to the positively charged Zn-atoms. Correspondingly, we expect the electrostatic molecule-substrate interaction to position the molecules above the Zn-lines and to align them with the charge lines. On the other hand, the non-electrostatic contribution is expected to bind the molecule to the surface, determine the binding height and attract the molecule to lie flat on the substrate plane.

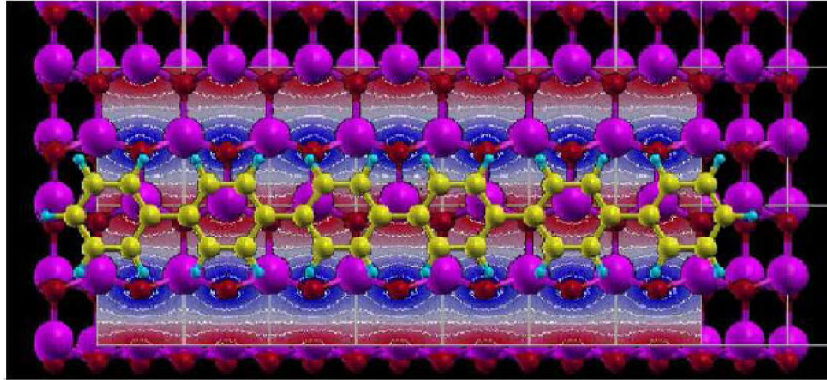


FIGURE 10.6: Alignment of a single 6P molecule on a ZnO(10-10) facet. The pink and red spheres of the substrate represent Zn and O, respectively, while the yellow and turquoise spheres represent the carbon and hydrogen atoms that the 6P molecule is composed of. Underneath the substrate there is a surface depicting the electro-negativity (blue) and -positivity (red) that arises through the higher electron affinity of O. For the energetically optimal configuration, the 6P molecule lies above the positively charged Zn-atoms and aligns with the charge lines. This image is adapted from the work of della Sala *et al.* [100].

#### 10.4.1 Non-electrostatic interactions

First, we consider the non-electrostatic part of the interaction between a molecule and the substrate in more detail. We assume that the substrate is a (smooth) plane located in the  $x$ - $y$ -plane (at  $z = 0$ ) of our system. In the literature (see, e.g. [284–286]) several expressions for the interaction between a GB-like particle and a planar substrate have been proposed and used for simulations of, e.g., GB bulk fluids in contact with a wall [287] or confined GB films [288]. Here we use a simpler expression which is motivated by two important results from DFT calculations [100]: First, the energetically most favourable distance between the molecule’s centre of mass and the surface is given by  $z_{\min} \approx 0.35$  nm, which corresponds approximately to the diameter  $d$  of our GB-particles (see Tab. 10.1). Second, at  $z_{\min} \approx 0.35$  nm the most favourable orientation is parallel to the surface, i.e., the (azimuthal) Euler angle  $\vartheta$  of the molecule [see Fig. 10.1(c)] is  $\pi/2$ .

In our simulations we realise this situation as follows. The  $z$ -position of each molecule is restricted to the range  $z_{\min} \leq z_i \leq z_{\min} - d/2 + l/2$ . The lower limit of this interval corresponds to a planar orientation ( $\vartheta = \pi/2$ ) while the upper limit corresponds to a molecule standing upright ( $\vartheta = 0$ ). Next, we introduce a potential which, at the same time, favours the distance  $z = z_{\min} \approx 0.35$  nm of the centre of mass and the planar orientation of the molecule’s long axis. To this end we use an integrated LJ potential [289] given by

$$V_{\text{LJ}}(\mathbf{u}_i) = \epsilon_s \left( \frac{2}{15} \left( \frac{\sigma_s}{z(\mathbf{u}_i)} \right)^9 - \left( \frac{\sigma_s}{z(\mathbf{u}_i)} \right)^3 \right). \quad (10.14)$$

Here,  $\sigma_s$  denotes a constant length (to be defined in accordance with  $z_{\min}$ , see below), and the function  $z(\mathbf{u}_i)$  is defined as

$$z(\mathbf{u}_i) = \sqrt{\left( \frac{d}{2} \right)^2 (\sin \vartheta)^2 + \left( \frac{l}{2} \right)^2 (\cos \vartheta)^2 + \left( z_{\min} - \frac{d}{2} \right)^2}. \quad (10.15)$$

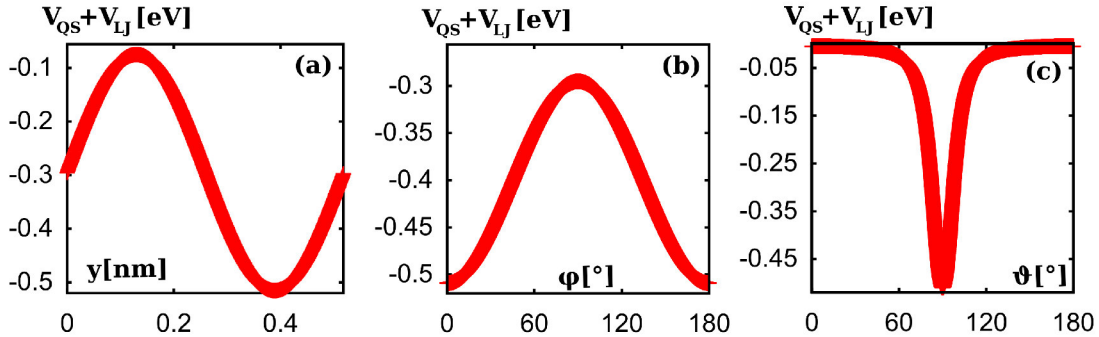


FIGURE 10.7: Interaction potential of a single 6P molecule with the ZnO(10-10) substrate according to Eq. (10.18) at  $z = z_{\min}$ . Part (a) shows the potential as a function of the  $y$ -coordinate. At  $y = 0.129$  nm the molecule lies above a negative charge (energetic maximum), while at  $y = 0.389$  nm it lies above a positive charge (energetic minimum). Parts (b) and (c) show the potential as a function of the angles  $\varphi$  and  $\vartheta$ .

By construction,  $z(\mathbf{u}_i) = z_{\min}$  for  $\vartheta = \pi/2$  while  $z(\mathbf{u}_i) = z_{\min} + (d - l)/2 \approx 1.57$  nm for  $\vartheta = 0$ , in accordance with the  $z$ -interval considered here.

To energetically favour the first case (consistent with the DFT calculations [100]) we adjust the constant  $\sigma_s$  in Eq. (10.14) accordingly. The minimum of the attractive well of the potential  $V(z)$  in Eq. (10.14) is located at  $z_0 = (2/5)^{1/6}\sigma_s$ . Setting  $z_0 = z_{\min}$  we find  $\sigma_s = 0.408$  nm. The potential depth,  $\epsilon_s$ , is not known and therefore an adjustable parameter. As an estimate we choose  $\epsilon_s = 0.28$  eV. In this way, the potential plotted in Fig. 10.7(c) has the same order of magnitude as the molecule-substrate interaction energies found by della Sala et al. [100] for 6P on ZnO(10-10).

#### 10.4.2 Electrostatic molecule-substrate interaction

We now turn to the construction of an effective molecule-substrate interaction mimicking the influence of electrostatics. We start from the molecular multipoles introduced in Eqs. (D.26)–(D.30) and discussed in Sec. 10.3.3. As we will see below, the quadrupole moment alone is not sufficient to correctly describe the molecule’s orientation to the substrate.

In order to evaluate the importance of various moments, we consider the corresponding interaction energies  $U_m(\mathbf{r})$  [with  $m$  referring to a specific multipole moment] in the presence of an external (substrate) field  $\tilde{\mathbf{E}}(\mathbf{r})$ . The corresponding expressions for a molecule with centre-of-mass position  $\mathbf{r}$  are given by Eqs. (D.22)–(D.25) in App. D.

**Electrostatic field of ZnO(10-10).** In the present study, the field  $\tilde{\mathbf{E}}(\mathbf{r})$  stems from the ZnO(10-10) substrate, which is characterised by a so-called ‘mixed’ termination: the substrate features alternating rows of Zn atoms and O atoms [28]. Since these have different effective charges, the ZnO(10-10) substrate effectively displays alternating, parallel rows of positive and negative charges. In the following we assume that these rows are oriented along the  $x$ -axis of the coordinate system (see Fig. 10.8). According to Ref. [100], the resulting electrostatic field

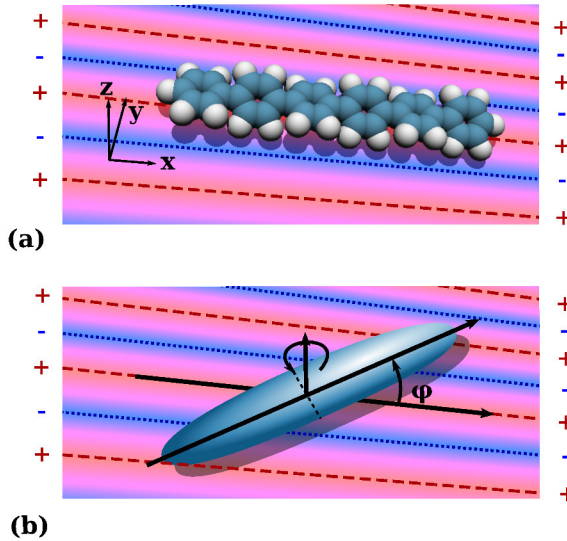


FIGURE 10.8: 6P molecule on the sketched ZnO(10-10) substrate (a) in its energetically most favoured configuration and (b) in a coarse-grained representation, which illustrates the rotation discussed in Fig. 10.10. The substrate is characterised by line charges with alternating sign, as indicated by the red (dashed) and blue (dotted) lines for the positive and negative charges, respectively. The angle  $\varphi$  describes the rotation with respect to the charge lines.

can be approximated as

$$\tilde{\mathbf{E}}(\mathbf{r}) = \begin{pmatrix} 0 \\ A \exp(-kz) \cos(ky) \\ -A \exp(-kz) \sin(ky) \end{pmatrix}, \quad (10.16)$$

where  $A \approx 97 \text{ eV}/(\text{nm e})$  is the field strength and  $k = 2\pi/0.519 \text{ nm}$  is the wave length of a substrate unit cell measured in  $y$ -direction (i.e., orthogonal to the charge lines on the substrate plane). The form of the field is shown in Fig. 10.9. With the field given in Eq. (10.16) we can evaluate the electrostatic energy contributions given in Eqs. (D.22)–(D.25) as functions of all molecular degrees of freedom, that is the position  $\mathbf{r}$ , and the angles  $\varphi$ ,  $\vartheta$  and  $\alpha$ . To investigate the importance of the multipoles, we choose  $\mathbf{r}$ ,  $\vartheta$  and  $\alpha$  according to an energetic minimum [100], that is,  $x = 0 \text{ nm}$ ,  $y = 0.519 \text{ nm} \cdot 3/4 = 0.389 \text{ nm}$ ,  $z = z_{\min}$ , and  $\alpha = 0$ ,  $\vartheta = \pi/2$  (in-plane configuration). Correspondingly, we are interested in the rotational energy  $E_{\text{electr}}(\varphi)$ , where  $\varphi$  is the in-plane angle relative to the  $x$ -direction.

**Rotational energy contributions of 6P on ZnO(10-10).** We determine the rotational energy for the different multipole moments  $E_{\text{electr}}(\varphi) = U_p(\varphi), U_Q(\varphi), U_O(\varphi), U_H(\varphi)$  individually. To this end we rotate every atomic position  $\mathbf{r}_l$  by  $\varphi$  around the centre of the molecule, evaluate the multipole moments via Eqs. (D.27)–(D.30) and finally determine the energy of the respective multipole in the field given in Eq. (10.16) using Eqs. (D.22)–(D.25). The resulting energy functions are shown in Fig. 10.10(a)–(d), respectively.

It is seen that the first (dipole) and the third (octupole) moment do not contribute at all to the in-plane rotational energy [see Figs. 10.10(a) and (c)]. The second (quadrupole) moment does

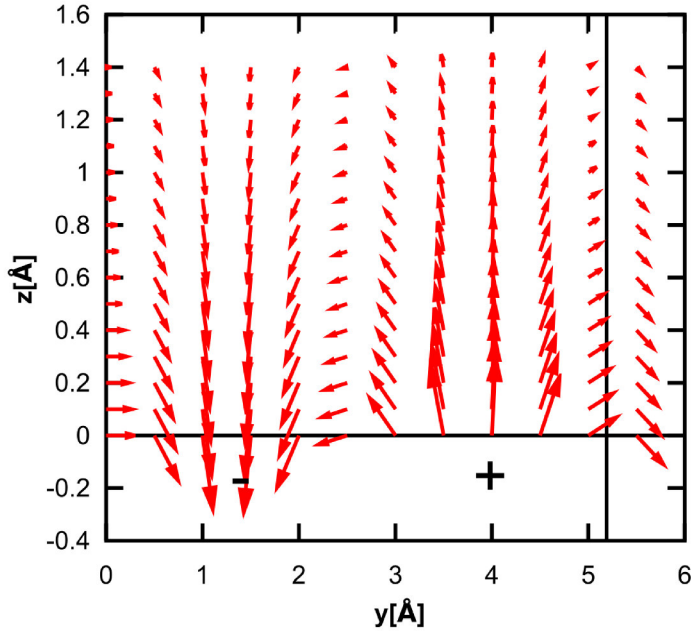


FIGURE 10.9: Approximate electrostatic field of ZnO(10-10) derived in Ref. [100]. We represent the electric field as a red vector-field, where the arrow orientation represents the field direction at the base of the arrow, while the arrow length represents the field amplitude. The horizontal black line marks the plane of the substrate, while the vertical black line marks the beginning of the unit cell introduced by della Sala *et al.* [100]. The '+' lies below the position of the Zn-atoms, while the '-' lies below the O-atoms.

contribute to the rotational energy, however, it contributes with an approximately constant value [see Fig. 10.10(b)]. The absence of a clear minimum means that the quadrupole does *not* favour the alignment of the molecule with the charge lines on the substrate. The first significant contribution to the molecular orientation arises through the interaction of the fourth (hexadecapole) moment with the substrate field [see Fig. 10.10(d)]. This rotational energy is minimal for a molecule that is aligned with the charge lines of the substrate for both, the planar and the twisted configuration (even though the actual values do depend on the configuration). We therefore conclude that the hexadecapole moment is responsible for the alignment observed by della Sala *et al.* [100].

**Model for electrostatic molecule-field interactions.** From a computational point of view, the treatment of the hexadecapole-field interaction for *many* molecules implies a very large effort. We therefore *mimic* the effect of this interaction by assigning to each molecule an additional, fictitious, quadrupole which is linear in character and is oriented *perpendicular* to the original one. We call this quadrupole  $\mathbf{q}'_i$ . The value of the corresponding moment is discussed in Sec. 10.4.3, while the electrostatic quadrupole-field interaction is discussed more detail in App. F.. The *effective* electrostatic part of the molecule-substrate interaction is then given by

$$V_{QS}(\mathbf{q}'_i, \mathbf{r}_i) = -\frac{1}{3} \times \sum_{\alpha\beta} \left( \sum_{\gamma\eta} R_{\alpha\gamma}(\mathbf{q}'_i) Q_{\gamma\eta} R_{\beta\eta}(\mathbf{q}'_i) \right) \frac{\partial \tilde{E}_\alpha}{\partial x_\beta} \Big|_{\mathbf{r}_i}. \quad (10.17)$$

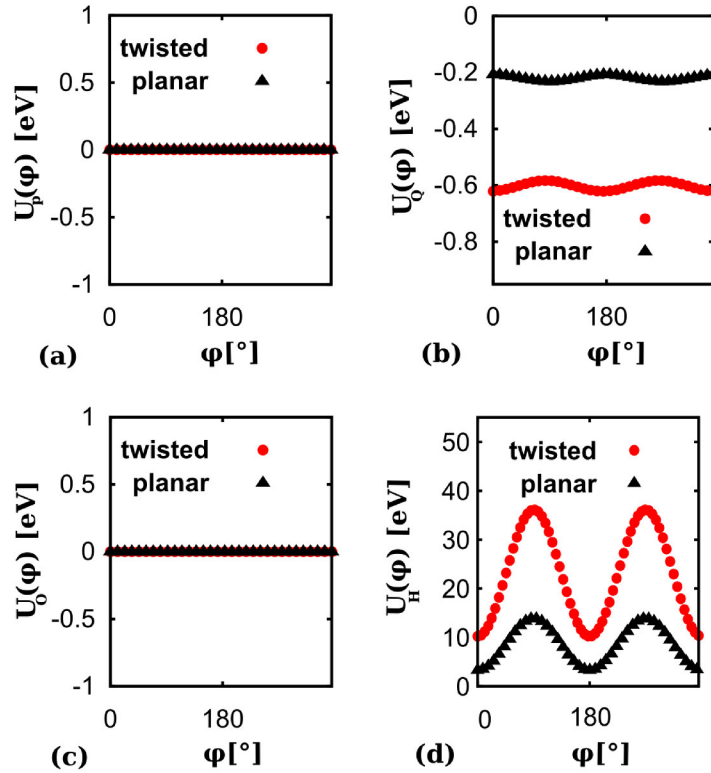


FIGURE 10.10: Contributions to the in-plane rotational energy from the molecular multipole moments in the electrostatic field of the ZnO(10-10) substrate [(a) dipole, (b) quadrupole, (c) octupole, (d) hexadecapole]. In all sub-figures,  $\varphi$  denotes the angle by which the molecule is rotated with respect to the charge lines. During this rotation the shortest axis of the molecule,  $z\ell$ , forms the axis of rotation and thus remains perpendicular to the substrate, which is equivalent to saying that  $z\ell$  lies parallel to  $z$  [see Fig. 10.8(b)]. The molecules considered are 6P in its planar configuration (planar) and a twisted configuration that the molecule assumes in vacuum (twisted) [105, 244].

Here  $Q_{\alpha\beta'}$  denotes the *effective* quadrupole tensor of the molecule in the molecule's eigensystem (see Sec. 10.4.3) and  $R = R(\varphi, \vartheta, \alpha)$  is a conventional rotation tensor in euclidean space involving the Euler angles  $(\varphi, \vartheta, \alpha)$ .

**Hamiltonian of the full molecule-substrate interaction.** Using Eq. (10.17) for the electrostatic molecule-substrate interaction  $V_{QS}(\mathbf{q}'_i, \mathbf{r}_i)$  and Eq. (10.14) for the non-electrostatic interaction  $V_{LJ}(\hat{\mathbf{u}}_i)$ , we obtain the total Hamiltonian for the molecule-substrate interaction,

$$H_{\text{mol-sub}} = \sum_{i=1}^N (V_{LJ}(\hat{\mathbf{u}}_i) + V_{QS}(\mathbf{q}'_i, \mathbf{r}_i)). \quad (10.18)$$

#### 10.4.3 Parametrisation of the quadrupole-field interaction

To adjust the magnitude of the fictitious linear quadrupole introduced in Eq. (10.17) we make use of the value for the rotational energy barrier  $\Delta E_r$  given in Ref. [100]. For a molecule which lies flat on the substrate and is rotated around the  $z$ -axis, the authors in Ref. [100] report a value of  $\Delta E_r = 220$  meV. In our case the corresponding barrier is given by

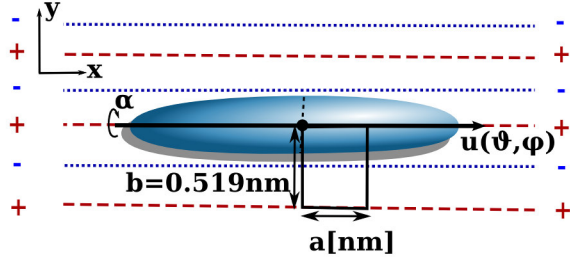


FIGURE 10.11: Sketched configuration of a molecule on the substrate lattice. The centre of mass sits at a position on the positive charge lines [see Fig. 10.8(a)]. Two positive (negative) charge lines have a distance  $b$ , while the lattice constant  $a$  in  $x$  direction is given by  $a = 0.329 \text{ nm}$  [290]. The molecule has continuous 3D rotational degrees of freedom described by the Euler angles  $\varphi$ ,  $\vartheta$  and  $\alpha$ .

$$\Delta E_r = \left( V_{QS}(\varphi = 0) - V_{QS}(\varphi = 90^\circ) \right)_{\vartheta=\pi/2, \alpha=0, y=0.389 \text{ nm}}, \quad (10.19)$$

where the electrostatic molecule-substrate interaction  $V_{QS}(\mathbf{q}'_i, \mathbf{r}_i)$  is defined in Eq. (10.17).

It turns out that we can reproduce the literature value for  $\Delta E_r$ , as well as the functional form of the molecule-substrate potential with respect to  $y$  and  $\varphi$ , by using a linear quadrupole  $\mathbf{q}'_i$  corresponding to a quadrupole tensor of the form

$$QI = \begin{pmatrix} -0.013 & 0 & 0 \\ 0 & 0.026 & 0 \\ 0 & 0 & -0.013 \end{pmatrix} \text{ e nm}^2. \quad (10.20)$$

The quadrupole element  $QI_{x/x'}$  describes the quadrupole strength parallel to the longest axis of the molecule and  $QI_{z/z'}$  is the quadrupole strength parallel to the shortest axis (see Fig. 10.1). The linear quadrupole  $\mathbf{q}'_i$  defined by Eq. (10.20) is orthogonal to both the long axis of the molecule  $\mathbf{u}_i$  and the orientation of the quadrupole direction  $\mathbf{q}_i$  used for the electrostatic molecule-molecule interaction [as is shown in Fig. 10.5]. The latter is oriented parallel to the  $z'$ -axis of the molecule (see Sec. 10.3.1). Therefore its orientation is not influenced if the molecule lies on the substrate and is rotated around its  $z'$ -axis by  $\varphi$ . This explains why the linear quadrupole  $\mathbf{q}_i$  cannot account for the orientation of the molecule within the plane.

The full molecular-substrate potential [see Eq. (10.18)] as function of  $y$ ,  $\vartheta$  and  $\varphi$  using the parametrisation given in Eq. (10.20) is plotted in Fig. 10.7. The translational energy ‘landscape’ shown in Fig. 10.7(a) agrees on a qualitative level with the corresponding landscape for 2P on ZnO(10-10) found by della Sala *et al.* [100] (this study does not include corresponding results for 6P). Moreover, qualitative and *quantitative* agreement is achieved for the rotational energy plotted in Fig. 10.7(b). In particular, the energy barrier height  $\Delta E_r \approx 220 \text{ meV}$  fully reproduces the value given in Ref. [100].

## 10.5 Equilibrium collective ordering using MC simulations

In order to obtain insight into the orientational ordering, we study equilibrium configurations with different interactions and different lattice configurations before performing growth simulations. I will discuss the assumptions and implications for equilibrium and growth simulations separately. The specifications discussed in this section apply only to the equilibrium simulations.

**Rotational degrees of freedom and lattice configurations.** Our equilibrium simulations are based on a two-dimensional lattice consisting of either square unit cells (lattice constant  $a$ ) or tetragonal unit cells characterised by lattice constants  $a \neq b$ . The tetragonal cell is inspired by the unit cell of the real ZnO(10-10) substrate where  $a = 0.329\text{ nm}$  and  $b = 0.519\text{ nm}$  [290]. A corresponding sketch is given in Fig. 10.11. For both lattice types, we set the number of particles per unit cell to one; moreover, this molecule's centre of mass is fixed in lateral directions. Specifically, we set  $x = n \cdot a$  and  $y = m \cdot b + 3b/4$ , where  $n, m$  are integers (recall that  $y = 3b/4 = 0.389\text{ nm}$  is the position of the energetic minimum in the  $y$ -direction, see Fig. 10.7). Thus, the main degrees of freedom are the three Euler angles  $\vartheta, \varphi, \alpha$  introduced in Fig. 10.1(c). Note that the rotational freedom of the particles implies that their centre of mass can have different distances from the surface, since  $z_i = z_i(\mathbf{u}_i)$  [see Eq. (10.15)]. As a consequence, our simulations allow for both lying and standing configurations.

**Equilibrium MC scheme.** The acceptance probability for each rotational movement of a molecule  $i$  (involving all three Euler angles) is given by the conventional Metropolis scheme, that is

$$p_i^R = \min \left\{ \exp \left( \frac{H_{\text{initial}}(i) - H_{\text{final}}(i)}{kT} \right), 1 \right\}, \quad (10.21)$$

where the Hamiltonians  $H$  for the initial and the final configuration are determined using Eq. (10.1), (10.13) and (10.18). For computational efficiency, we restrict the range of the molecule-molecule interaction to centre-of-mass distances  $r_{ij} < 1.2l = 3.25\text{ nm}$ . The temperature  $T$  is chosen as  $T = 300\text{ K}$  unless specified otherwise. In fact, the only system we have studied at temperatures below  $300\text{ K}$  are systems without molecule-molecule interaction, where frustration effects are absent per definition. At  $300\text{ K}$ , we have checked equilibration by testing different (randomly oriented) initial conditions and monitoring acceptance rates for rotational moves. These rotational moves have been carried out as follows:

The angles  $\alpha$  and  $\varphi$  are randomly selected from a normal distribution  $\in [0, 360^\circ]$ , while  $\vartheta$  is drawn from the distribution  $\arccos(1 - r)$ , with  $r$  being a random number chosen uniformly from the interval  $[0, 1]$ . Correspondingly,  $0^\circ \leq \vartheta \leq 90^\circ$ . Note that our model of 6P has a mirror symmetry with respect to each plane defined by two of its axes. Hence, the full configurational space is available using this choice of angles <sup>2</sup>.

---

<sup>2</sup>To verify the results for high densities, additional simulations were performed where the angular rotation was restricted to an interval that is small enough to guarantee an acceptance probability of  $\geq 30\%$ .

**Varying interactions and lattice configurations.** Our aim is to understand the role of the individual contributions to the Hamiltonian for the overall orientational ordering behaviour. To this end, we perform MC simulations for different subsets of the interactions determined in Eqs. (10.13) and (10.18).

First, for systems in which no molecule-substrate interactions are considered, we use square unit cells and vary the density by varying the lattice constant  $a$ . Second, for systems with electrostatic field, we fix the lattice constant in  $y$  direction to the distance of the substrate charge lines, i.e.,  $b = 0.519 \text{ nm}$ . To vary the density, we then vary only the lattice constant  $a$  in  $x$ -direction (see Fig. 10.11). Note that the molecule's length of  $l = 2.79 \text{ nm}$  (see Tab. 10.1) is much larger than  $b = 0.519 \text{ nm}$ . Thus, even for large values of  $a$ , the rotational motion of molecules in  $y$  direction is strongly restricted.

**Simulation details.** The entire simulation box consists of at least 1000 unit cells for the square lattice and up to 2000 unit cells for simulations on the tetragonal lattice, in order to maintain reasonable statistics despite the broken lateral symmetry. We employ periodic boundary conditions in the  $x$ - and  $y$ -directions. We initialise the lattice with randomly oriented molecules and then equilibrate the systems for at least  $10^5$  MC steps, followed by production runs over another  $10^5$  MC steps.

## 10.6 Growth simulations for anisotropic molecules

We use a CR algorithm (see Ref. [143], discussed in Sec. 2.7.2) to simulate the sub-monolayer growth of 6P. This is a null-event algorithm that was previously used for different biochemical models [143, 144]. Null-event algorithms are advantageous for growth simulations with continuous rotational degrees of freedom, as it does not require the computationally expensive calculation of a complete process rate catalogue after each process [131].

For our sub-monolayer growth, the substrate is coarse-grained as a 2D lattice. While we do not restrict rotational degrees of freedom, we coarse-grain translational diffusion such that the molecule's centre-of-mass can only move between adjacent lattice sites, i.e.

$$x = na \text{ and } y = mb, \quad (10.22)$$

where  $n$  and  $m$  have integer values and  $a = 0.319 \text{ nm}$  and  $b = 0.519 \text{ nm}$  are the lattice constants of ZnO(10-10) [290]. In this lattice-confined model, the processes that occur during surface growth are summarised in Fig. 10.12. They can be expressed in terms of three different process types: rotational diffusion, translational diffusion and adsorption of molecules, described through the rates  $r_i^{\text{rot}}$ ,  $r_i^{\text{diff}}$  and  $r_i^{\text{ads}}$ , respectively. Each process type is associated with a maximal frequency, the ‘attempt frequency’  $\nu$ , which we use as propensity (used in the algorithm [143], as discussed in Sec. 2.7.2). In each iteration, a process is selected with a probability proportional to its propensity and then accepted with a probability  $p^{\text{acc}} = r/\nu$  or rejected with a probability  $p^{\text{rej}} = 1 - p^{\text{acc}}$ . The average time step length that corresponds to one iteration is  $\Delta\tau = 1/(n^{\text{part}}(\nu^{\text{rot}} + \nu^{\text{diff}}) + n^{\text{latt}}\nu^{\text{ads}})$ , where  $n^{\text{part}}$  is the number of particles and  $n^{\text{latt}}$  the number of unoccupied lattice sites.

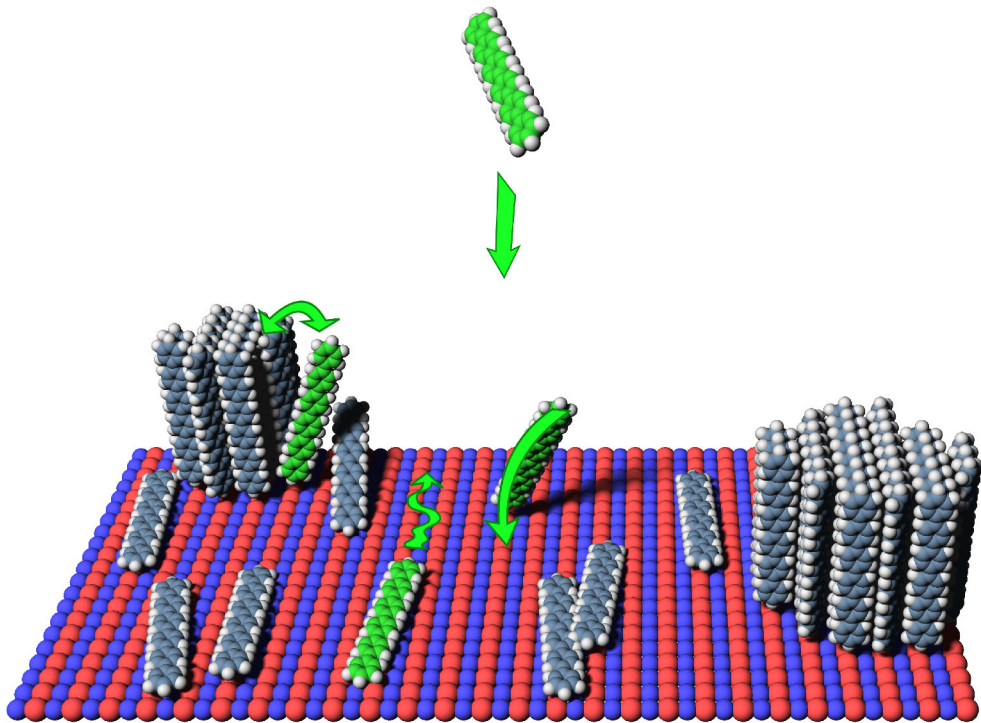


FIGURE 10.12: Sketched dominant diffusion processes that occur during sub-monolayer growth of 6P. Here the ‘active’ molecules are shown in bright green, the currently immobile molecules are shown in dull blue. The bright blue and bright red spheres of the substrate depict the O and Zn-atoms, respectively. The dominant processes shown are: translational diffusion, rotational diffusion and molecule adsorption. Both translational and rotational diffusion can occur with or without interacting with neighbouring molecules.

The rotational rate allows continuous rotational degrees of freedom. Using an equilibrium approximation, it can be expressed as

$$r_i^{\text{rot}} = \nu^{\text{rot}} \min \left\{ \exp \left( \frac{H^i(i) - H^f(i)}{kT} \right), 1 \right\}, \quad (10.23)$$

where  $H^i$  and  $H^f$  are the interaction Hamiltonians for the initial and final configuration, respectively. The lack of transitional information between the initial- and final configuration reflects the equilibrium approximation. This approximation reflects the assumption that rotational diffusion relaxes more quickly than translational diffusion. Rotational diffusion makes an individual molecule align with the charge lines of the ZnO(10-10) substrate through the effective interaction Hamiltonian  $H_{\text{eff}}^{\text{pot}}$ , which contains the molecule-molecule and molecule-substrate interactions. This rotational alignment is observed in experiment [28, 100]. To this end, we use the Hamiltonian defined in Eq. (10.1), parametrised according to Secs. 10.3 and 10.4.

The same Hamiltonian determines the translational diffusion rate between lattice sites is determined using a Kramer’s activated process rate. A diffusing particle has to overcome a constant diffusion barrier  $E_D$  determined by the substrate, as well as interaction with other

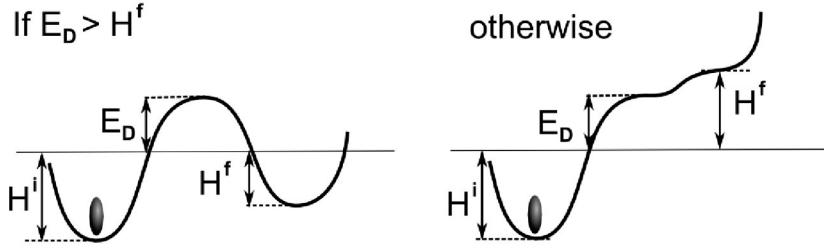


FIGURE 10.13: Sketched potential barrier that a molecule has to overcome for translational diffusion. This energy barrier includes molecule-molecule interactions at the initial site  $H_{m-m}^i$ , as well as the energy barrier  $E_D$  (left image) or the final molecule-molecule interactions  $H_{m-m}^f$  (right image). The corresponding rate equation is given in Eq. (10.24).

molecules at the initial  $H_{m-m}^i$ .

$$r_i^{\text{diff}} = \nu^{\text{diff}} \times \begin{cases} \min \left( \exp \left( \frac{H_{m-m}^i(i) - E_D}{kT} \right), 1 \right) \\ \quad \text{if } H_{m-m}(i) \leq E_D \\ \min \left( \exp \left( \frac{H_{m-m}^i(i) - H_{m-m}^f(i)}{kT} \right), 1 \right) \\ \quad \text{otherwise} \end{cases} \quad (10.24)$$

If the final site is blocked through repulsive interaction with other particles, i.e. if  $H_{m-m}^f(i) > E_D$ , then the second part of Eq. (10.24) becomes relevant (see Fig. 10.13). The diffusion energy barrier  $E_D$  can be modelled with a constant value because the lattice is coarse-grained and each lattice site is identical. This constant value can be derived from long-time simulations of atomically resolved molecules [106]. In principle,  $E_D$  is direction dependent, however we initially set  $E_D = 0$  eV for all directions of diffusion.

This expression for the diffusion rate is a generalisation of the bond counting approach discussed in Sec. 5.2. This is easily observed through coarse-graining  $H_{m-m}^i = -nE_n$  and  $H_{m-m}^f = -mE_n$ , where  $n, m$  are integers<sup>3</sup>, and step-edge crossing is forbidden, i.e.  $s_{i,j} = 0$ . Then we find that  $H_{m-m}^f(i) \leq E_D$  and we reproduce Eq. (5.7).

The final process is the adsorption of particles, expressed through the adsorption rate

$$r_i^{\text{ads}} = \nu^{\text{ads}} = f \cdot \nu^{\text{diff}}. \quad (10.25)$$

Note that we currently choose  $\nu^{\text{diff}} = \nu^{\text{rot}}$ . The attempt frequency  $\nu^{\text{diff}}$  can in general be extracted from long-term MD simulations in a fairly straight-forward fashion [106], while the rotation attempt frequency  $\nu^{\text{rot}}$  is not obviously accessible. Hence, we use dimensionless units and express the system time  $t$  in terms of  $[t] = 1/\nu^{\text{diff}}$ . In order to perform detailed quantitative simulations, further studies concerning the parametrisation of the rotational diffusion are required.

In general, particles can adsorb with different orientations. Here we choose a vertical adsorption orientation of particles unless specified otherwise. This assumption is tested and discussed in Sec. 12.2.3.

<sup>3</sup>The negative sign reflects that  $H_{m-m}^i$  is negative if the interaction is attractive, while  $E_n$  is positive by definition.

# Chapter 11

## Characterising the collective ordering

For anisotropic molecules, we are especially interested in the collective ordering both in equilibrium and during growth. Hence, we need to expand the evaluation approaches discussed in Sec. 6 to include new measures that characterise the alignment, as well as correcting the previously discussed observables such as the island density (treated in Sec. 6 and App. C) to anisotropic molecules. First, we introduce measures that are suitable to characterise the density-dependent collective ordering in equilibrium, before discussing observables used to characterise growth.

### 11.1 Measures of evaluation for equilibrium

#### 11.1.1 Nematic and biaxial order parameter

In order to analyse the orientational ordering of the system, we use the conventional, trace-less second-rank tensor defined in Ref. [291, 292],

$$A_{\alpha\beta} = \frac{1}{N} \sum_{i=1}^N \left\langle \mathbf{u}_{i,\alpha} \cdot \mathbf{u}_{i,\beta} - \frac{1}{3} \delta_{\alpha\beta} \text{Tr}(\mathbf{u}_i \otimes \mathbf{u}_i) \right\rangle, \quad (11.1)$$

where  $\otimes$  stands for a dyad product,  $\text{Tr}$  is the trace and  $\langle \dots \rangle$  denotes an average over an ensemble of configurations.

To determine the overall degree of (nematic) order, we consider the eigenvalues and eigenvectors of the tensor  $A_{\alpha\beta}$ . In a system with perfect uniaxial order, the set of eigenvalues is of the form  $\{\mu_k\} = \{-1/3, -1/3, 2/3\}$ . The eigenvector associated to the eigenvalue  $\mu_1$  with the largest absolute value (i.e.  $|\mu_1| \geq |\mu_k|$  for all  $k$ ) [293–296] is the director of the system. Further, the largest absolute eigenvalue of  $A_{\alpha\beta}$  is also directly proportional to the conventional Maier-Saupe order-parameter  $S = 3\mu/2$  [292, 297]. For a perfectly uniaxial system it follows that  $S = 1$ . In our system, large values of  $S$  typically occur at large densities, where the molecules form a standing uniaxially ordered phase.

Another important situation occurs when the molecules' orientations are restricted to (arbitrary) directions within the plane, say, the  $x$ - $z$ -plane. Then the eigenvalues of  $A_{\alpha\beta}$  are of the form  $\{\mu_k\} = \{1/6, 1/6, -1/3\}$ , yielding  $S = -1/2$  [292, 298–300]. Here, we observe such negative values of  $S$  on tetragonal lattices. Finally,  $S = 0$  represents a completely disordered system.

Using the other two eigenvalues  $\mu_2$  and  $\mu_3$ , we can determine a biaxiality parameter  $B = |\mu_2 - \mu_3| / |\mu_1|$ , which quantifies the difference in alignment between the two eigenvectors that are not the principle axis [293, 296]. The biaxiality parameter assumes values in the range of  $0 \leq B \leq 1$ . If  $S \geq 0$ , then a large value of  $B$  corresponds to a high biaxiality. However the highest biaxiality corresponds to  $S = -1/2$  and  $B = 0$ .

### 11.1.2 Angular distributions

In order to further characterise the orientation of the molecules, we determine various angular distributions involving the Euler angles  $\varphi_i$ ,  $\vartheta_i$  and  $\alpha_i$ . Specifically we define the probability that a particle has an angle  $\beta = \varphi$ ,  $\alpha$ , or  $\beta = \varphi + \alpha$  as

$$P(\beta) = \left\langle \frac{n_{[\beta-\Delta\beta/2, \beta+\Delta\beta/2]}}{N \cdot \Delta\beta} \right\rangle, \quad (11.2)$$

where  $n_{[\beta-\Delta\beta/2, \beta+\Delta\beta/2]}$  is the number of particles in a tolerance interval chosen as  $\Delta\beta = 6^\circ$ . In the absence of orientational ordering these distributions are constant. Also note that  $\alpha, \varphi, \alpha+\varphi$  take values between 0 and  $180^\circ$ . To describe the distribution of the azimuthal angle  $\vartheta$  we consider the quantity  $P(\cos \vartheta)$  defined in accordance with Eq. (11.2), but with  $\Delta\beta = 0.02$ . The advantage of considering  $P(\cos \vartheta)$  rather than  $P(\vartheta)$  is that  $P(\cos \vartheta)$  is constant in an isotropic phase, contrary to  $P(\vartheta)$ .

Additionally, we study the height distribution function  $P(z)$ . The height distribution function is defined in analogy to the angular distribution function  $P(\beta)$  [see Eq. (11.2)], where the height interval used is  $\Delta z = 0.02$  nm. Note, however, that in our system  $P(z)$  and  $P(\cos \vartheta)$  are intimately related through Eq. (10.15).

## 11.2 Additional measures to characterise growth

### 11.2.1 Measures for coverage: Particle density and surface fraction

During growth the coverage of the substrate changes. For anisotropic molecules there are two different ways that coverage can be determined: the coverage can be the number of molecules per number of unit cells (or surface), or the fraction of the surface that the molecules cover. We call the first measure ‘particle density’, while the second is called ‘surface fraction’.

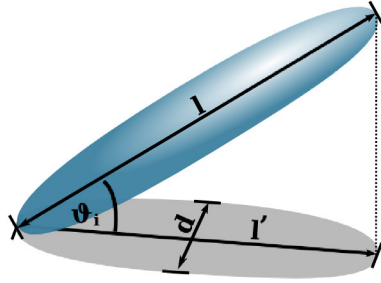


FIGURE 11.1: Molecular ‘shadow’ used in order determine the covered surface fraction of the substrate. Each molecule is projected onto the substrate plane using the tilt angle  $\vartheta_i$ . Correspondingly, the projected molecular length  $l'$  depends on  $\vartheta_i$  [as given in Eq. (11.5)] and assumes values between the molecular diameter  $d$  and the molecular length  $l$ .

**Particle density.** The particle density is directly determined from the number of particles  $n^{\text{part}}$  per number of unit cells  $x_{\max} \cdot y_{\max}$

$$\rho^{\text{part}} = \frac{n^{\text{part}}}{x_{\max} \cdot y_{\max}}. \quad (11.3)$$

It can either be expressed in terms of the number of molecules per unit cell ( $1/A$  or  $A^{-1}$ ) or, by scaling with the unit cell surface  $A = a \cdot b = 0.17 \text{ nm}^2$ , it can be expressed as a surface density expressed in  $1/\text{nm}^2$ .

As the adsorption is determined through the number of unoccupied lattice sites  $n^{\text{latt}}$  [confer Eq. (10.25)], we can also determine the particle density analytically as

$$\rho^{\text{part}} = 1 - e^{-\nu^{\text{ads}} t}. \quad (11.4)$$

This observation is easily derived from Poisson statistics and is a logical consequence of the model used. Hence, the information contained is somewhat trivial. In order to obtain non-trivial information about the coverage, which includes information on molecular orientation, we define a measure for the fraction of the substrate surface that is covered through the molecules.

**Surface fraction.** The surface fraction reflects the fact that a lying molecule covers a larger surface than a standing molecule. In our uniaxial ellipsoidal molecule-model, we determine the surface that a molecule covers as the molecule’s ‘shadow’, as illustrated in Fig. 11.1. Reflecting the uniaxial model morphology, the shadow of a molecule  $i$  primarily depends on the projection of the molecule with its tilt angle  $\vartheta_i$  [301]<sup>1</sup>

$$l'(i) = \sqrt{d^2 + (l^2 - d^2) \sin(\vartheta_i)^2}. \quad (11.5)$$

Then the surface of the shadow is an ellipse with the surface

$$A_{\text{shadow}}(i) = \frac{\pi d l'(i)}{4}. \quad (11.6)$$

<sup>1</sup>The original expression also depends on  $\varphi_i$  because it treats a fixed lab system. We rotate the lab-system with  $\varphi_i$ , so we can set  $\cos \varphi_i = 1$ .

Using this definition of the surface coverage, we can determine the surface fraction as

$$\rho^{\text{surf}} = \frac{\sum_i A_{\text{shadow}}(i)}{x_{\max} y_{\max} A}. \quad (11.7)$$

Here, the maximal surface fraction that the definition allows is 4.30. However, the model cannot assume this value, because it requires all molecules to lie parallel to the substrate plane. As the long molecular axis is several unit cells long, steric exclusion will force molecules out of this planar configuration as the particle density approaches one. A more realistic estimate is given if every lattice site is occupied however all molecules are standing. The surface fraction assumes a value of 0.52. The numerical maximum will however lie above this value, as even for maximal particle density the molecules will not stand perfectly upright.

### 11.2.2 Orientation-dependent particle densities

In order to determine the orientational behaviour in more detail, we use orientationally dependent versions of the particle density defined in Eq. (11.3). Here, we distinguish between standing ( $|\vartheta_i| \leq 0.25\pi$ ) and lying ( $\vartheta_i > 0.25\pi$  or  $\vartheta_i < -0.25\pi$ ) molecules.

**Absolute particle densities.** The absolute particle density for standing molecules simply is the ratio of the number of standing molecules to the overall number of lattice sites. It is defined in a similar fashion to Eq. (11.3) as

$$\rho^P|_{\text{standing}} = \frac{n^P|_{\text{standing}}}{x_{\max} \cdot y_{\max}}. \quad (11.8)$$

Correspondingly, an absolute particle density can be defined along the same principle.

**Relative particle densities.** In order to see the impact of the orientational ordering, it is also interesting to study what fraction of the adsorbed molecules is standing. This is more easily visualised using relative particle densities

$$\tilde{\rho}^P|_{\text{standing}} = \frac{n^P|_{\text{standing}}}{n^P}. \quad (11.9)$$

Again, the relative particle density of lying molecules can be defined along the same principle. We can, however, correspondingly define it as

$$\tilde{\rho}^P|_{\text{lying}} = 1 - \tilde{\rho}^P|_{\text{standing}}. \quad (11.10)$$

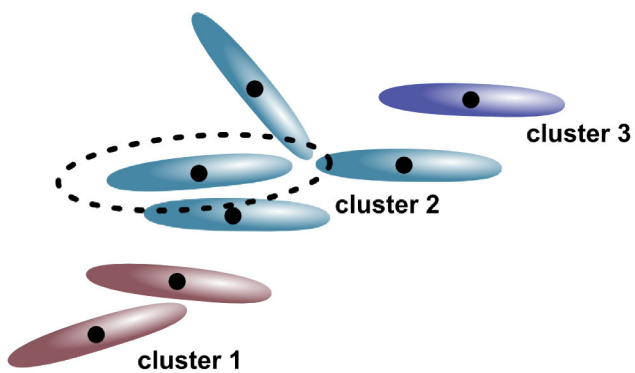


FIGURE 11.2: Visualisation of a cluster algorithm implemented for anisotropic molecules. Here, the molecular neighbourhood is defined through the contact distance of the molecular surfaces rather than the distance of their centres of mass, which are depicted as big black dots. Molecules can have a large centre-of-mass-distance and can still belong to the same cluster, as depicted in cluster 2, while other molecules may have a smaller centre-of-mass distance yet not be part of the same cluster.

### 11.2.3 Configuration-dependent cluster information

In principle, we can determine clusters as previously discussed in Sec. 6.1 and App. C. For anisotropic molecules, however, the molecule-molecule configurations need to be taken into consideration as an additional factor. If it is not considered, molecules with centres of mass far apart are not identified as part of the same cluster, even if their relative configurations make their surfaces touch (see Fig. 11.2 for a representative example).

In order to correctly account for the anisotropic form of the molecules, our cluster algorithm scans a very large neighbourhood for potentially touching molecules. Two molecules are identified as part of the same cluster if their contact distance [defined in Eq. (10.7)] is smaller than 0.2 nm (see Fig. 11.2). Otherwise, the cluster algorithm for anisotropic molecules follow the same principles and the same methodology.

Note that the cluster algorithm also allows us to identify clusters of only standing molecules, by eliminating molecules that do not fulfil  $|\vartheta_i| \leq 0.25\pi$  before identifying clusters.

# Chapter 12

## Collective ordering of anisotropic molecules

The coarse-grained model for COMs on structured surface that we introduced in Sec. 10.1 involves a complex set of different interactions. Furthermore, there are different possible choices for the substrate lattice, as discussed in Sec. 10.5. Hence, we initially perform equilibrium studies of the collective ordering of 6P molecules on ZnO(10-10) under the influence of different subsets of interactions in Sec. 12.1. These give us insight into the driving mechanisms behind different forms of ordering phenomena that is indispensable in order to understand the ordering behaviour during growth, which we study in Sec. 12.2.

### 12.1 Equilibrium

The equilibrium studies are intended to verify our coarse-grained model introduced in Sec. 10.1, as well as understanding the influence of the different contributions to the interaction Hamiltonian (see Sec. 10.2). Here, we perform equilibrium MC simulations (introduced in Sec. 10.5) for molecules that have no translational degrees of freedom and are confined to lattice sites, however they are given full 3D rotational degrees of freedom. The translation is restricted here in order to dis-tangle the influences of rotational and translational diffusion under the various interaction contributions. Later we perform growth simulations (in Sec. 12.2), where molecules are given additional translational degrees of freedom and the full interaction potential is considered.

#### 12.1.1 Impact of molecule-molecule interactions on a quadratic lattice

In this section, we study the orientational ordering of molecules on a quadratic lattice without a substrate pattern, before studying the tetragonal lattice in Sec. 12.1.2. The  $z$ -coordinates of the centres of mass are restricted to the interval  $[z_{\min}, z_{\min} - d/2 + l/2]$  where  $l/2$  is half of one molecule's length and  $d/2$  is half of one molecule's diameter. Thus, the angular coordinate  $\vartheta_i$  of each molecules can assume all possible values. Figure 12.1 (a) shows the order parameter  $S$  as a function of the lattice constant  $a$  in a system of molecules that interact exclusively through

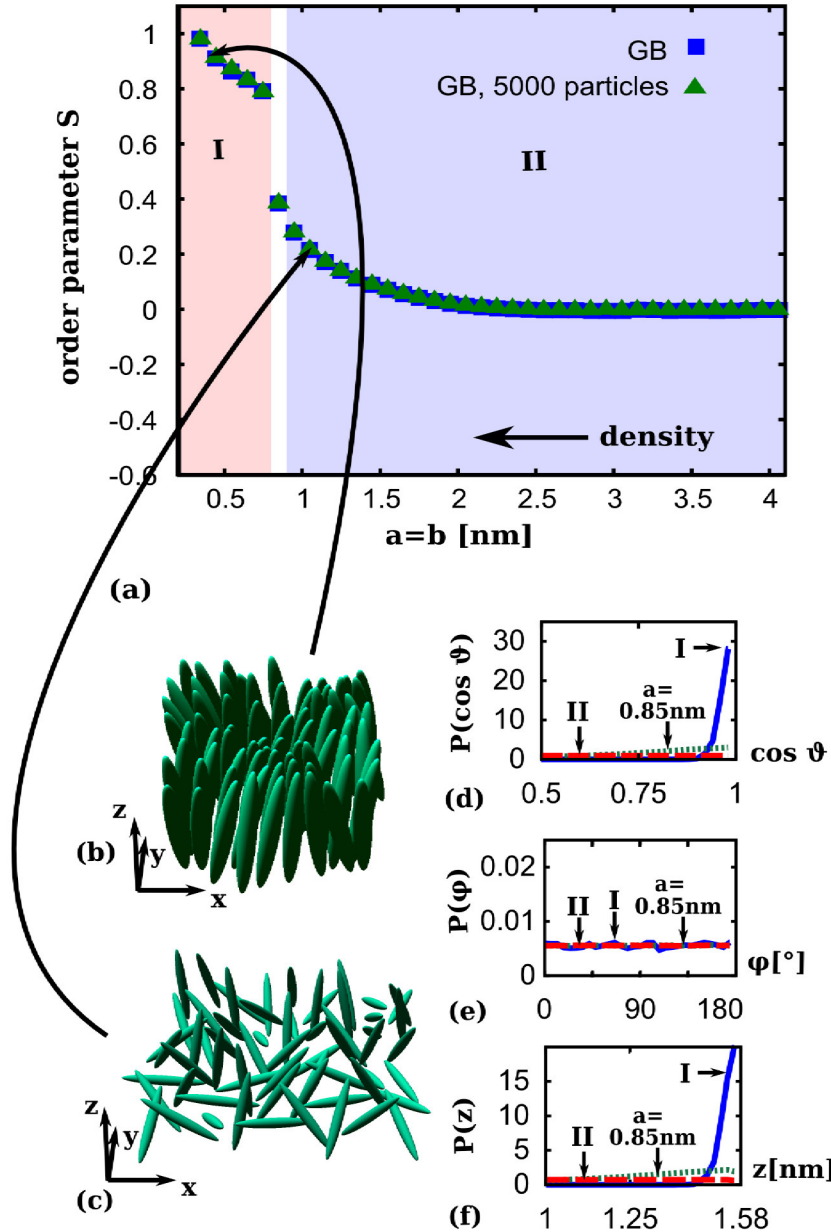


FIGURE 12.1: Ordering behaviour of molecules interacting exclusively through GB interactions (with axis ratio 1:8.3, corresponding to 6P). The  $x$  and  $y$  positions of the centres of mass are positioned on a square lattice with lattice constant  $a = b$ . Part (a) displays the nematic order parameter for different values of  $a$  in a systems with 1000 (blue squares) and 5000 particles (green triangles), respectively. The two observed orientational states are denoted by roman numbers: I stands for standing (upright) uniaxial order, II stands for 3D (isotropic) disorder. Parts (b)–(c) show snapshots of a subset of the molecules at  $a = 0.4$  nm (state I) and  $a = 1.0$  nm (state II), respectively. The two states are further characterised in parts (d)–(f), in which we present the angular distributions for  $\cos \vartheta$  and  $\varphi$  at  $a = 0.4$  nm (state I) and  $a = 4.0$  nm (state II), as well as the height distribution  $P(z)$ . Parts (d)–(f) also contain the angular distributions for a lattice constant  $a = 0.85$  nm, which corresponds to the last point of phase II before the transition to phase I.

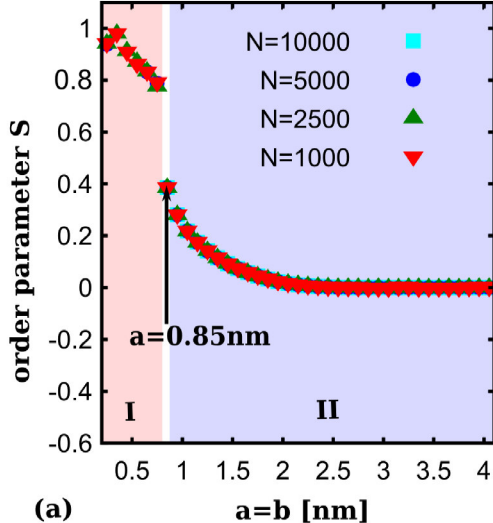


FIGURE 12.2: Nematic order parameter for molecules interacting exclusively through GB interactions in a system with 1000 (red inverted triangles), 2500 (green triangles), 5000 (dark blue dots) and 10000 molecules (light blue squares). The molecules have an axis ratio 1:8.3, corresponding to 6P. The  $x$  and  $y$  positions of the centres of mass are positioned on a square lattice with lattice constant  $a = b$ .

GB interactions. As the lattice constant increases, the density of the molecules decreases. The order parameter  $S(a)$  in Fig. 12.1 (a) has two different regions depending on  $a$ . In the first region (state I), where the lattice constant is small, the ordering parameter  $S$  takes large positive values, indicating uniaxial ordering. The director of this ordering points along the  $z$ -direction, i.e. the molecules stand upright, as illustrated by the snapshot in Fig. 12.1 (b) and by the peak of the distribution function  $P(\cos \vartheta)$  at  $\cos \vartheta = 1$  in Fig. 12.1 (d) (introduced in Sec. 11.1.2). As expected, the corresponding distribution  $P(\varphi)$  in Fig. 12.1 (e) is essentially flat. This uniaxial upright ordering is indeed expected in view of the fact that the lattice constant is significantly smaller than the molecule's length. We also note that uniaxial ordering is a generic feature of dense systems of elongated particles, even when the interactions are purely repulsive [302].

Increasing the lattice constant  $a$  towards larger values, a second region appears, where  $S$  takes initially small, yet non-zero values and eventually approaches zero upon further increase of  $a$ . In this region (II), the molecules have full rotational freedom as reflected by the snapshot in Fig. 12.1 (c) and by the nearly flat distributions of  $\cos \vartheta$  and  $\varphi$  in Fig. 12.1 (d), (e). These features correspond to a 3D disordered phase. Note that at lattice constants within region II, but close to the transition to region I (e.g. at  $a = 0.85$  nm), the values of  $S$  become relatively large ( $S \approx 0.4$ ). We find that these values are uninfluenced through system size [see Fig. 12.1 (a) and Fig. 12.2]. Test simulations for lower temperatures show that the value of  $S$  before the transition decreases to  $S \approx 0.05$ . At 300K and  $a = 0.85$  nm, the system displays a slight collective (i.e. system-averaged) ordering in  $\vartheta$  and no collective ordering in  $\varphi$ , as is depicted in Fig. 12.1 (d) and (e). Thus, we find a finite degree of collective ordering in the ‘isotropic’ phase very close to the boundary to phase I.

Finally, in Fig. 12.1 (f), we show the distribution  $P(z)$ . Phase II is characterised by a homogeneous distribution of  $z$ -values within the accessible interval. In contrast, we find a clear peak

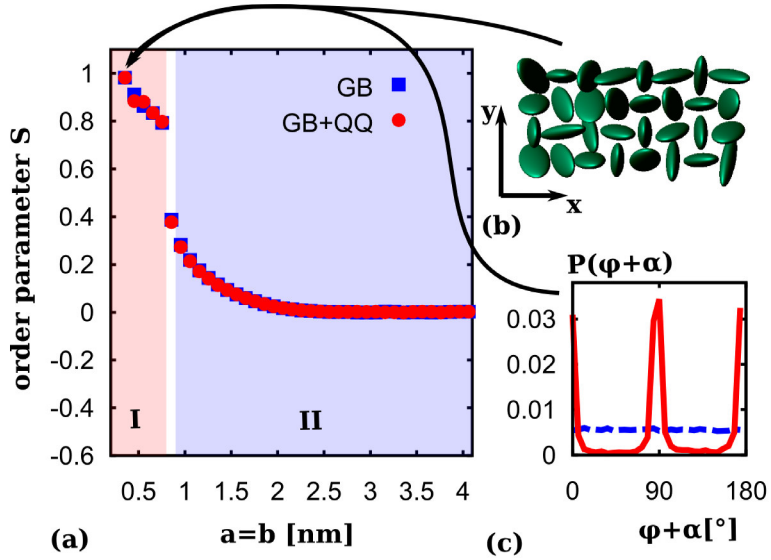


FIGURE 12.3: Ordering behaviour induced by the full molecule-molecule interactions on a square lattice. In part (a), red dots indicate the values of  $S$  for GB plus quadrupolar (QQ) interactions; the corresponding values for a pure GB system are included as a reference (blue squares). The snapshot in part (b) pertains to  $a = 0.4$  nm, where the molecules display a standing uniaxial order of their long axes combined with a T-shaped ordering of their quadrupoles. To better visualise this T-shaped configuration, the particles are shown flattened along their  $z\ell$ -axis. Part (c) shows the corresponding distribution  $P(\varphi + \alpha)$  for pure GB (blue dashed) and GB plus quadrupolar interactions (red). For standing molecules ( $\vartheta_i = 0$ ), the angle  $\varphi + \alpha$  denotes the rotation of the molecule around its long ( $x\ell$ )-axis.

at  $z \approx 1.57$  nm for phase I. This peak corresponds to an upright ordering, as is discussed in the text under Eq. (10.15).

We now consider the impact of the additional electrostatic interactions induced by the quadrupole moments  $\mathbf{q}_i$  oriented perpendicular to the molecule's long axis  $\mathbf{u}_i$  (see Fig. 10.5). Corresponding results for  $S$  as function of  $a$  are plotted in Fig. 12.3 (a), where we have included the data from Fig. 12.1 (a) for the pure GB system as a reference.

The quadrupolar interactions (QQ) do not significantly change the magnitude of  $S$ , indicating that the general phase behaviour remains unchanged. We note in this context that the definition of  $S$  involves the directions  $\mathbf{u}_i$  alone. However, one marked difference occurs in the local structure within the upright uniaxially ordered phase: In the system with quadrupolar interactions, neighbouring molecules tend to order into T-shaped configurations with respect to the directions of their quadrupole moments, see Fig. 12.3 (b). In the T-shaped ordering, the  $y\ell$ -axes of two molecules enclose a  $90^\circ$  angle, so the two  $y\ell$ -axes form a T-like alignment. This T-like ordering is also reflected by the angular distribution function  $P(\varphi + \alpha)$  plotted in Fig. 12.3 (c). It is seen that the distribution function  $P(\varphi + \alpha)$  has two pronounced (and equally high) peaks at  $\pi/2$  and  $\pi$ , indicating that these are the favoured orientations of the molecular axis  $z\ell$ . The resulting structure resembles that in the “herringbone phase”, which has been observed in real 6P systems [104, 267]. In these real systems, the angle between neighbouring molecules is typically less than  $90^\circ$  [303]. In our system, the angle of about  $90^\circ$  between the quadrupoles of neighbouring molecules reflects the fact that the T-configuration of two linear quadrupoles has the lowest pair energy and is compatible with the square lattice (see Appendix F). In the sense that the square lattice structure *stabilises* the T-like alignment

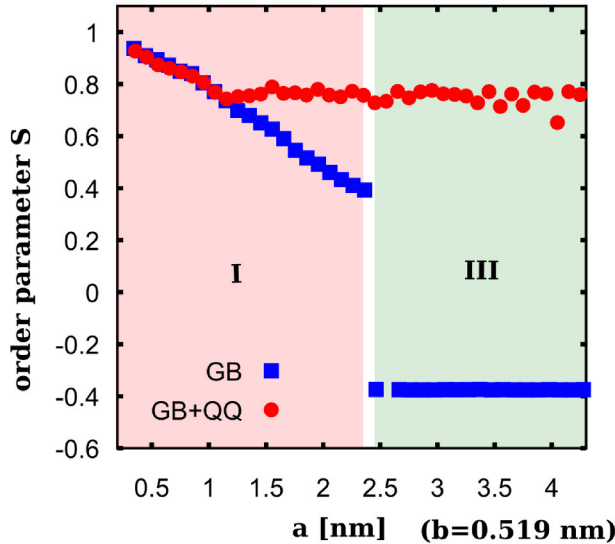


FIGURE 12.4: Nematic order parameter of 6P molecules interacting through GB (blue squares) as well as full molecule-molecule interactions (red dots) on a tetragonal lattice with varying lattice constant  $a$ . The different ordering states are denoted through roman numerals: I upright uniaxial order, III disorder within the  $x$ - $z$ -plane. These states are further analysed in Fig. 12.5.

of the quadrupoles. If the positions of molecules were allowed to freely vary, we would rather expect a herringbone orientational structure.

### 12.1.2 Tetragonal lattice

We now turn to the ordering behaviour on a tetragonal lattice. Tetragonal unit cells are characteristic of real ZnO(10-10) surfaces with substrate pattern, as shown in Sec. 10.5. In the present subsection, we investigate the impact of the tetragonal lattice for (full) molecule-molecule interactions alone, before discussing the full set of interactions in Sec. 12.1.3. Recall that on the tetragonal lattice, we vary the density by varying solely the lattice constant  $a$ , while the second lattice constant is kept fixed at  $b = 0.519 \text{ nm}$ . Figure 12.4 shows the order parameter  $S$  as a function of  $a$ , where we have included data for both, systems with GB plus quadrupole interactions and pure GB systems. Corresponding snapshots and orientational distribution functions are shown in Fig. 12.5.

Comparing the order parameter  $S(a)$  for the tetragonal lattice (in Fig. 12.4) with the quadratic lattice in Fig. 12.3, we see that the lattice type has indeed a profound impact on the overall behaviour. This holds particularly for larger values of  $a$ , where, moreover, pronounced differences between the GB system with quadrupolar interactions and the pure GB fluid occur.

Both the pure GB and the fully interacting system (GB+QQ) on the tetragonal lattice display an upright uniaxial phase (I) for small lattice constants  $a$  (e.g.  $a = 0.2 \text{ nm}$ ), as in the case of the square lattice. Also, the quadrupole interactions induce a preference of T-like configurations for neighbouring particles, as illustrated by the snapshot in Fig. 12.5 (a) and the angular distribution  $P(\alpha + \varphi)$  in Fig. 12.5 (f). This herringbone-like ordering is most pronounced at  $a \approx 0.519 \text{ nm}$ , where the lattice is approximately quadratic.

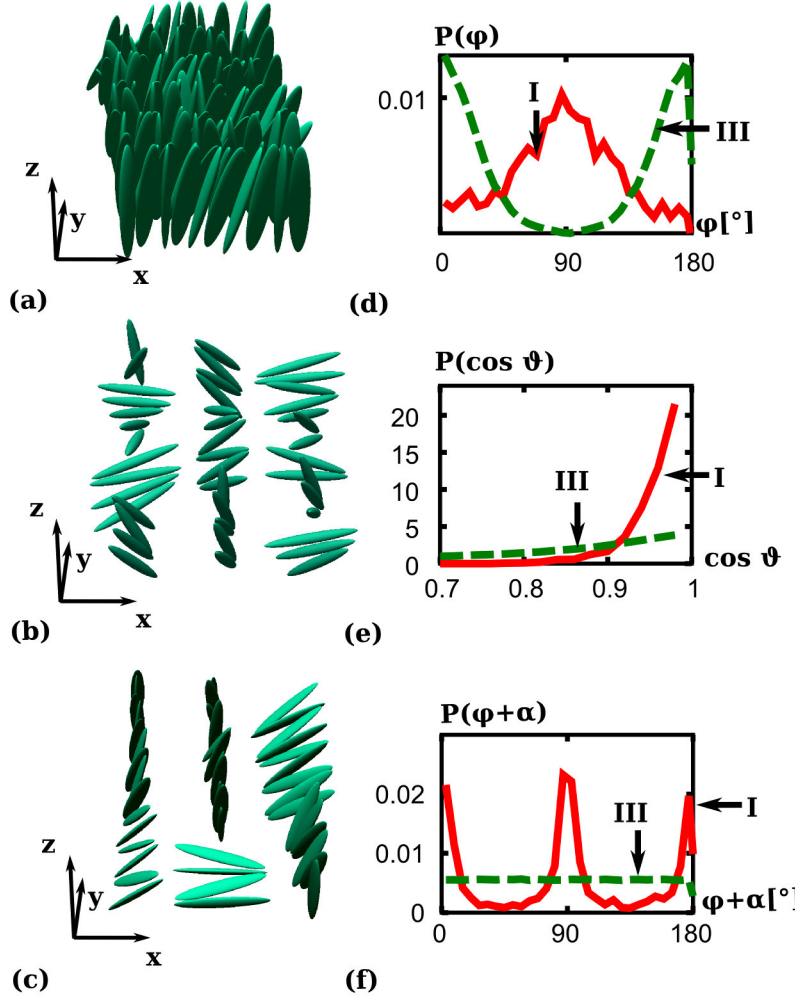


FIGURE 12.5: Orientational states of 6P molecules with different molecule-molecule (but no molecule-substrate) interactions. Parts (a) and (b) contain typical snapshots in region I ( $a = 0.4 \text{ nm}$ , GB+QQ) and III ( $a = 2.5 \text{ nm}$ , GB only), respectively. Corresponding angular distributions are plotted in parts (d)–(f). For additional insight, part (c) contains a snapshot for GB+QQ interacting molecules at lower density ( $a = 2.5 \text{ nm}$ ).

Upon increasing  $a$ , the order parameter first decreases for both type of systems. However, beyond a lattice constant of  $a \approx 1.2 \text{ nm}$  dramatic differences between the interaction models (and between the lattice types) occur. For molecules without electrostatic interactions (pure GB), the (upright) uniaxial order first remains up to  $a \approx 2.4 \text{ nm}$ . Crossing this value, the tetragonal unit cell induces a transition into a globally disordered state (III). Specifically, the overall order parameter  $S \approx -0.4$  is indicative for molecules restricted orientationally to a plane, as was previously discussed in Sec. 11.1. In the present case, this plane is the  $x$ - $z$  plane [see snapshot in Fig. 12.5 (b), as well as the angular distributions  $P(\phi)$  and  $P(\cos \vartheta)$  in Fig. 12.5 (e) and (f), respectively]. We interpret the restriction to the  $x$ - $z$  plane from the fact that, in our simulations, the lattice constant in the  $y$ -direction is fixed to a rather small value ( $b = 0.519 \text{ nm}$ ). This restriction precludes the molecules to fully explore the orientational space (or even align) in  $y$ -direction. However, despite the overall disorder in the  $x$ - $z$  plane, one observes finite domains characterised by local alignment, as expected in a strongly coupled system.

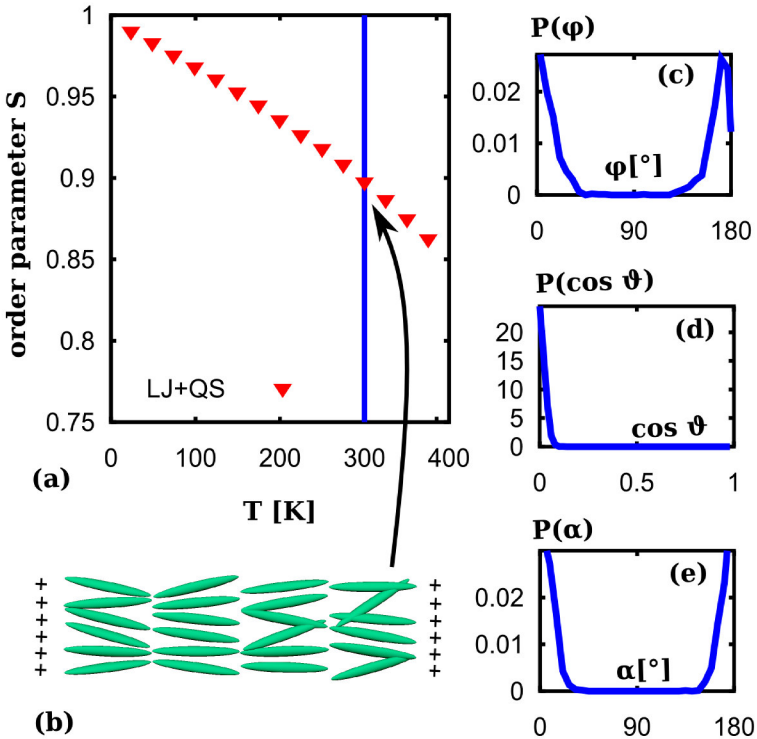


FIGURE 12.6: Ordering of a system of non-interacting molecules subject to the full substrate potential [see Eq. (10.18)]. Part (a) depicts the nematic order parameter  $S$  as function of temperature. Part (b) contains a snapshot of a subset of the molecules at 300K, represented through the vertical line in part (a), while parts (c)–(e) contain corresponding angular distributions.

Including now the quadrupolar inter-molecular interactions, the system behaves in a completely different way (see the data labelled ‘GB+QQ’ in Fig. 12.4): It does not leave the upright uniaxial phase even for very large values of  $a$  [see snapshot in Fig. 12.5 (c)]. At first sight, this uniaxial ordering seems surprising due the fact that a low density is considered and the pure GB system eventually forms a disordered state. To understand the impact of the quadrupolar interactions in this regime we recall two points. First, the nearest-neighbour distance in  $y$ -direction (i.e., the lattice constant) is small ( $b = 0.519$  nm) even at low densities due to our way to vary the density. Thus, the quadrupoles ‘feel’ each other even at large values of  $a$ . Second, each (point) quadrupole sits in a molecules centre-of-mass. By forming an upright uniaxial phase, the molecules can thus reduce their electrostatic energy, while keeping still some orientational freedom (note that for standing molecules, fluctuations of the angle  $\vartheta$  induce only small changes of the height, and thus, of the interacting energy, contrary to the situation for lying molecules). Moreover, within this standing uniaxial order, the quadrupole-quadrupole interactions induce a T-like ordering, which is visualised in Fig. 12.5 (c).

### 12.1.3 Impact of the electrostatic substrate pattern

So far, we have been focusing on the role of the various molecule-molecule interactions on the overall ordering behaviour, while the substrate has been considered just as a confining medium. This seems appropriate if one considers, e.g. 6P at an oxygen-terminated ZnO(000-1) surface.

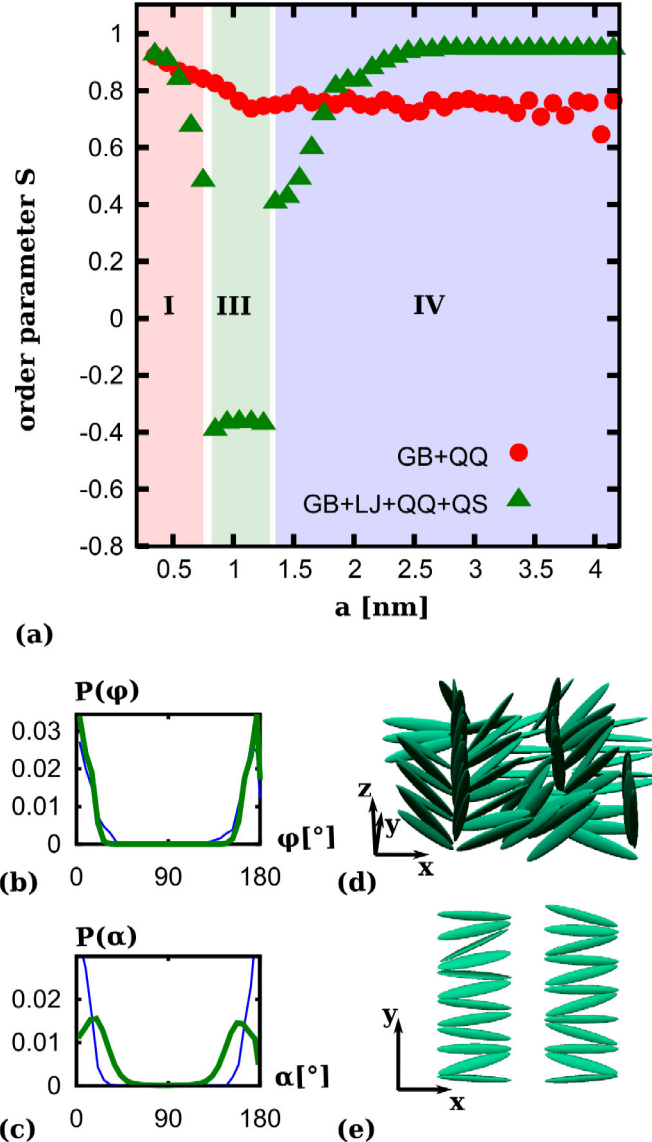


FIGURE 12.7: (a) Nematic order parameter of the fully interacting system including all types of molecule-molecule and molecule-substrate interactions. The different ordering states are denoted through roman numerals: I upright uniaxial order, III disorder within the  $x$ - $z$ -plane, and IV planar uniaxial order in the  $x$ - $y$ -plane. As a reference, we have included data for the system without molecule-substrate interaction (see Fig. 12.4). Parts (b) and (c) present the distributions for the angles  $\varphi$  and  $\alpha$ , respectively, at  $a = 4.0$  nm. The thick green lines in parts (b)–(c) represent the angular distributions for the system including all types of interactions, while the thin blue lines represent a system with only molecule-substrate interaction [see Figs. 12.6 (c) and (e)]. Parts (d) and (e) show snapshots at  $a = 1.0$  nm (phase III) and  $a = 4.0$  nm (phase IV).

We now discuss the impact of the electrostatic field generated by a ZnO(10-10) surface. Based on our considerations in Sec. 10.4.2, where we constructed the corresponding molecule-substrate potential [see Eq. (10.18)], we expect an individual molecule to lie flat on the substrate and to align with the line charges, if the temperature is sufficiently low. To determine the degree of substrate-induced ordering at the temperature studied here ( $T = 300K$ ), we consider in Fig. 12.6 (a) the order parameter  $S$  of a system of *non-interacting* molecules as function of  $T$ . It is seen that the substrate alone induces a very large degree of single-particle ordering ( $S \approx 0.9$ ) even at room temperature. Upon cooling the system,  $S$  further increases as one would expect. We recall in this context that, within our model, the ordering is mediated through the interaction of the substrate field with the fictitious quadrupole moment  $\mathbf{q}'_i$ , which lies parallel to the molecular  $y'$  axes. Thus, for perfect substrate-induced order, all  $\mathbf{q}'_i$  lie parallel to the  $y$ -axis of the coordinate system. Figures 12.6 (b)-(e) show a snapshot of the (decoupled) many-particle system and corresponding angular distribution functions, respectively, at  $T = 300K$ .

In Fig. 12.7 (a) we present the order parameter  $S$  of a system with the same strength of molecule-substrate interaction, but full (GB plus quadrupolar) molecule-molecule interactions, as function of  $a$  (tetragonal lattice). We find that the substrate-induced ordering ‘survives’ only at very large  $a$ , that is, at very low densities, whereas the high-density behaviour is dominated by molecule-molecule interactions. Specifically, for  $a \lesssim 0.6$  nm we recover the upright-uniaxial phase (I) with herringbone-like order of the molecular quadrupoles  $\mathbf{q}_i$ . In the range  $0.7 \text{ nm} \lesssim a \lesssim 1.3$  nm, the system displays a state resembling state III discussed before [see Fig. 12.5 (b)], that is, the majority of molecules lies within the  $x$ - $z$  plane [see Fig. 12.7 (d)]. However, the range of corresponding lattice constants is smaller here. Rather we observe  $S$  to *rise* again already at  $a \approx 1.4$  nm. This suggests that the molecule-substrate potential, which favours planar uniaxial order, now starts to “out-win” the impact of the intermolecular interactions. Finally, the system enters a state of nearly perfect planar uniaxial order, as illustrated by the angular probability distributions plotted in Figs. 12.7 (b) and (c). The only difference to the non-interacting system studied before appears when we consider the function  $P(\alpha)$ : In the system with electrostatic substrate field, the peaks occur at  $\alpha \approx 24^\circ$  and  $\alpha \approx 156^\circ = 180^\circ - 24^\circ$ , thus they are shifted relative to the corresponding peaks in the non-interacting case, see Fig. 12.6 (e). We interpret this shift as a competition between the quadrupolar molecule-molecule interactions, which favour in-plane, T-like configuration of the moments  $\mathbf{q}_i$ , and the electrostatic molecule-substrate interaction. The latter favours the fictitious quadrupoles  $\mathbf{q}'_i$  to lie parallel to  $y$ -axis, and thus counteracts the molecular quadrupole interactions.

## 12.2 Growth

During growth the particle density changes so rapidly that particle orientations cannot always fully equilibrate. Correspondingly, we expect the collective orientation to not only depend on the temperature and particle density discussed in Sec. 12.1, but also the adsorption rate defined in Eq. (10.25). To study the influence of particle adsorption, we first observe the particle density as a function of time, and gain insight into orientational ordering in Sec. 12.2.1. Next, we focus on orientational ordering for different adsorption rates in Sec. 12.2.2, before testing

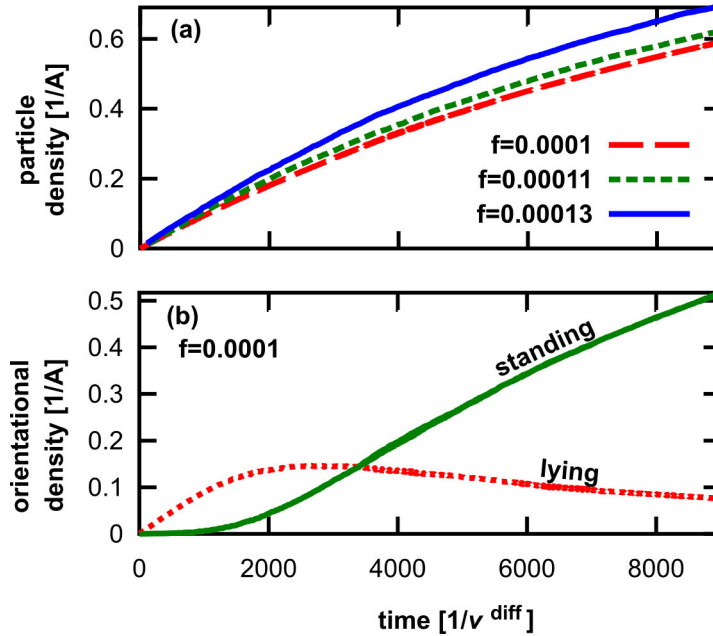


FIGURE 12.8: Growth morphology as a function of the coverage for different adsorption rates  $f$ . Part (a) depicts the surface coverage expressed in terms of the unit cell surface  $A = a \cdot b = 0.17 \text{ nm}^2$  as a function of time, while part (b) shows the fraction of particles that are standing (i.e., that have  $|\vartheta_i| \leq 0.25\pi$ ).

the robustness of the results in Sec. 12.2.3 and finally gaining first insight into the clustering of particles in Sec. 12.2.4.

### 12.2.1 Surface coverage

As discussed in Sec. 11.2.1, there are different ways to approach the coverage. First, we study the particle density in Fig. 12.8 (a). The particle density is pre-determined by the adsorption rate (see Sec. 11.2). For higher adsorption rates  $f$  the particle density increases more rapidly. Following Eq. (11.4), the particle density saturates with time.

In equilibrium, we find that molecules lie along the substrate charge lines for low densities and stand for high densities, as discussed in Sec. 12.1.1. For low enough adsorption rates, we find a similar behaviour when studying the absolute orientational particle density (see Fig. 12.8 (b)). The first molecules that adsorb on the substrate lie until  $t \approx 2000$ . Afterwards molecules stand up as the particle density increases with time until at  $t \approx 10000$  the large majority of molecules stand.

This behaviour closely resembles the results found experimentally for the growth of self-assembled monolayers [129]. In the experiment, orientationally sensitive scattering measurements are used to determine the particle density for given orientations. The scattering signal shows that the first particles adsorbed on the substrate lie down nearly immediately, forming a lying phase. However, as the particle density increases, the molecules stand up, forming a well ordered standing phase (see Ref. [128, 129, 304]). During this standing growth phase newly adsorbing particles stand immediately in experiment, as we also observe in our simulations.

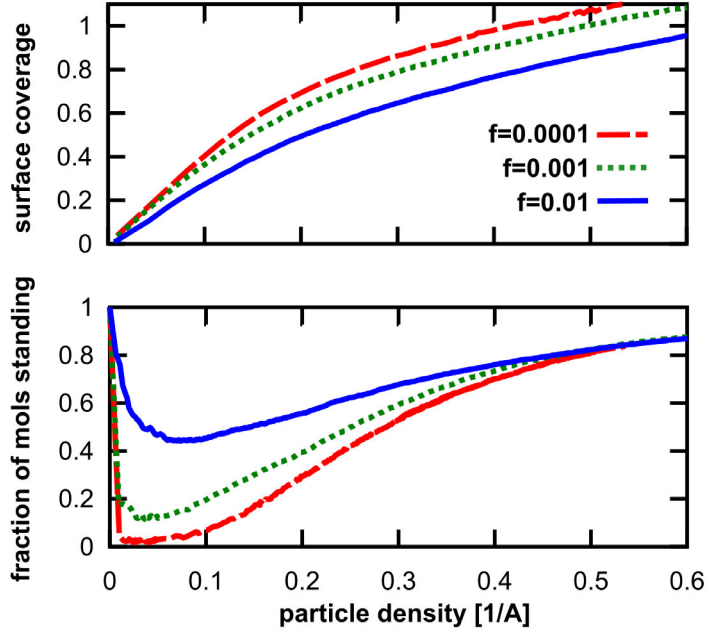


FIGURE 12.9: Growth for different adsorption rates  $f$  characterised through the surface coverage and the fraction of standing molecules as a function of the particle density. Part (a) depicts the surface coverage defined in Eq. (11.7), while part (b) shows the relative fraction of particles that are standing (i.e., that have  $|\varphi_i| \leq 0.25\pi$ ).

Considering that the majority of COMs initially lies flat on the surface due to van-der-Waals attraction and many form standing crystallites for the right substrate and growth conditions [14, 73, 107, 128, 304], this behaviour appears to be generic for a wide class of material combinations. Note that COMs tend to stay in a lying configuration and grow in multilayers of lying molecules for very attractive substrates [304].

In order to clearly see the influence of the adsorption rate on the collective ordering, we express all units from now on in terms of the particle density instead of time from now on.

First, we study the influence of the adsorption rate on the collective ordering by examining the surface fraction and the relative orientational particle density as a function of the particle density in Fig. 12.9. Both observables show that initially particles prefer an in-plane alignment, while particles prefer a standing orientation for higher particle densities. The decreasing gradient of the surface fraction in Fig. 12.9 (a) indicates that initially every new molecule adsorbed on the surface has a large contribution to the surface fraction, while molecules that adsorb later contribute less. This supports that the first molecules prefer a lying orientation while later molecules stand, as observed in Fig. 12.8 (b) and Fig. 12.9 (b).

As the adsorption rate increases, the initial fraction of lying molecules decreases. Consequently, the surface fraction moves closer to a linear dependency on the particle density. For  $f = 0.0001$ , up to approx. 98% of the molecules lie in the lying phase, while, for  $f = 0.01$ , this fraction goes down to approx. 58% (see Fig. 12.8 (b)). The adsorption-rate dependency reflects the kinetic competition that arises during growth: The adsorption rate competes with the rotational (and translational) diffusion. For high adsorption rates, particles have little time to lie down before the particle density forces them to stand upright again. Hence, the collective orientation depends strongly on the adsorption rate. The initially high fraction of standing molecules

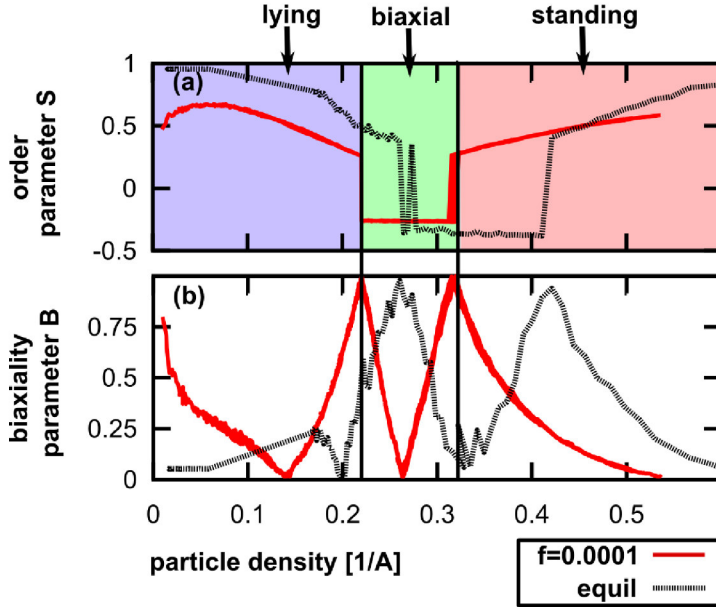


FIGURE 12.10: Characterisation during growth in terms of order parameters. The graphs depict the nematic order parameter in part (a) and the biaxiality parameter in part (b) as a function of the particle density for equilibrium (denoted as ‘equil’) as well as the relatively low adsorption rates  $f = 0.0001$ . The legend of the graph is located in the box on the bottom right of the image. The underlying colour-blocks in part (a) mark the different forms of ordering that arise. The vertical lines associate the transitions between forms of ordering with the corresponding features of the biaxiality parameter depicted in part (b).

reflects the vertical adsorption configuration of the molecules. The influence of the adsorption configuration on the orientational ordering will be discussed in more detail in Sec. 12.2.3.

### 12.2.2 Orientational ordering

To study the adsorption-rate dependency of the orientational ordering in more detail, we determine the nematic and biaxial order parameters defined in Sec. 11.1.1 for equilibrium as well as for different adsorption rates (see Figs. 12.10 and 12.11). The equilibrium results for the nematic order parameter are discussed in Sec. 12.1.3. Note that the equilibrium results are scaled to the unit cell size  $A$  to compare them to growth results on a fixed lattice with unit cell size  $A$ .

In equilibrium, there are two transitions that can clearly be identified in the nematic order parameter (see Fig. 12.10): the transition from a nematic lying regime to a planar confined order in the  $(x-z)$ -plane (called ‘biaxial’ here) at a particle density of approx.  $0.26 \text{ } A^{-1}$ , and a transition from the planar-confined to a nematic standing order at a particle density of approx.  $0.41 \text{ } A^{-1}$ . The increase of the biaxial order parameter near these transitions indicates that the transitions are well-ordered, while the minimum of the biaxial order at a particle density of approx.  $0.32 \text{ } A^{-1}$  together with the corresponding nematic order parameter  $S \approx -0.4$  indicate a high biaxial ordering between the transitions.

For a low adsorption rate the transitions shift to lower particle densities. This reflects the competition of time scales previously discussed for Fig. 12.9 (b): The lower the adsorption rate, the more time particles have to find their ordered minimal-energy configuration. For

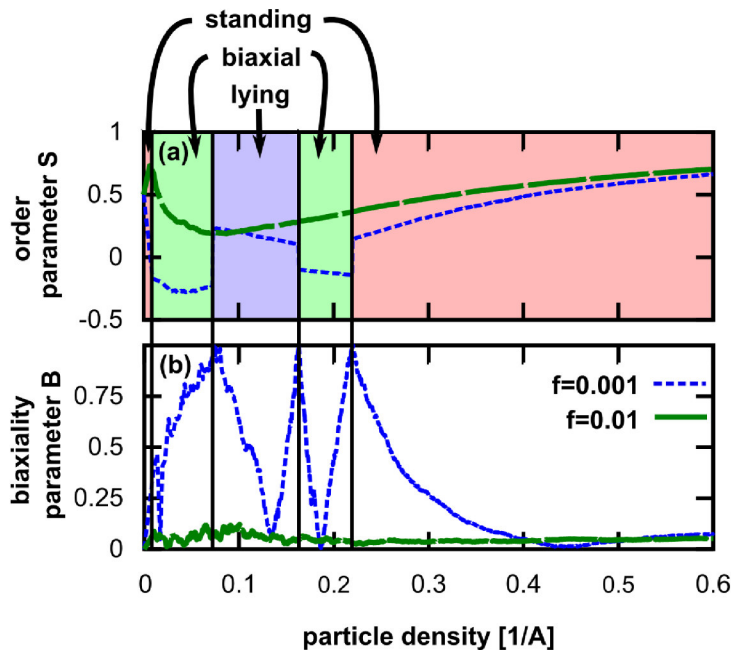


FIGURE 12.11: Molecular ordering during growth, characterised in terms of the same order parameters as depicted in Fig. 12.10. The sub-figures show the same order parameters, however the data depicted in this image is taken from simulations performed at high (i.e.  $f = 0.01$ ) and intermediate (i.e.  $f = 0.001$ ) adsorption rates.

infinitesimally small adsorption rates, i.e. very near to equilibrium, particles have more time to form a nematical lying order than for a finite adsorption rate. Correspondingly, the transition from lying to biaxial moves to lower particle densities close to  $0.22 \text{ \AA}^{-1}$ . Similarly, for infinitesimally small adsorption rates, particles have most time to stay lying during a biaxially ordered regime, moving the second transition to lower particle densities near  $0.32 \text{ \AA}^{-1}$  for finite adsorption rates.

A further difference between equilibrium and low adsorption rates occurs in the biaxiality parameter  $B$ . For very low particle densities in equilibrium  $B$  is negligible, however for finite adsorption rates it assumes a high value at very low particle densities. This difference reflects the influence of the adsorption orientation, where the newly adsorbed particles still stand while the other particles already have aligned with the substrate field.

For very high adsorption rates (e.g.  $f = 0.01$ ), the standing order through particle adsorption dominates the entire orientational ordering throughout the growth process, as depicted in Fig. 12.11. Here, the nematic order parameter  $S$  for the high adsorption rate of  $f = 0.01$  never assumes negative values and the biaxiality parameter never is significantly larger than zero. This positive  $S$  indicates a standing nematic growth throughout the particle adsorption. The highest disorder that occurs for this growth rates is visible through the minimal value of  $S \approx 0.2$  at a particle density of approx.  $0.075 \text{ \AA}^{-1}$ . For larger adsorption densities, the adsorption configuration no longer is the dominating influence and the particle density is still small, giving molecules large rotational freedom.

Intermediate adsorption rates (e.g.  $f = 0.001$ ) display a strong competition between the kinetic considerations that concern high adsorption rates and the equilibrium collective ordering that dominate growth at low adsorption rates (see Fig. 12.11). The resulting growth displays

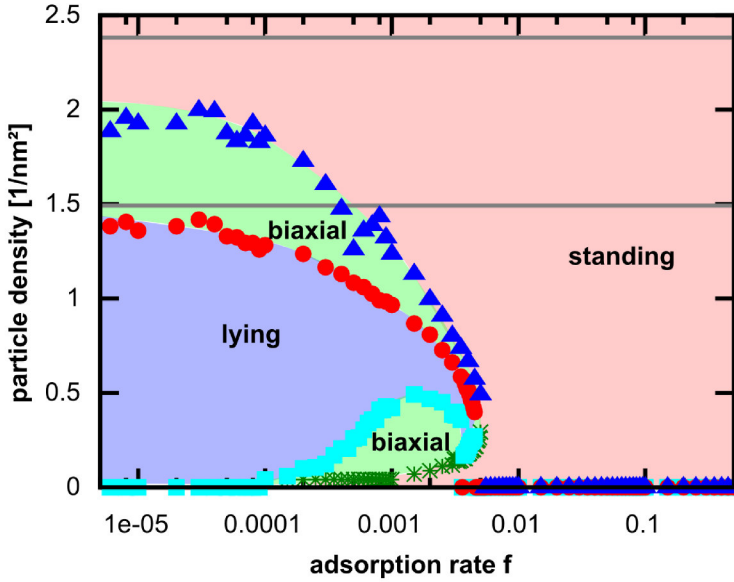


FIGURE 12.12: All transitions as a function of adsorption rates for vertically adsorbed particles. The green stars mark a transition from standing to biaxial order, the turquoise boxes from biaxial to lying, the red dots from lying to biaxial and the blue triangles from biaxial to standing. The grey horizontal lines mark the transitions expected in equilibrium (see Sec. 12.1.3). Each simulation considers at least 2500 and up to  $10^6$  lattice sites.

a series of transitions in which various contributions become more influential as growth progresses. Initially, the nematic standing orientation of the adsorbing molecules is dominant, as was previously discussed for  $f = 0.01$ . Then the first particles have enough time to lie down and align with the substrate field. Correspondingly, the system transitions to a biaxial ordering at a particle density of approx.  $0.02 \text{ \AA}^{-1}$  and to a lying nematic order at a particle density of approx.  $0.078 \text{ \AA}^{-1}$ . As the particle density increases more slowly with time as growth progresses (confer Fig. 12.8 (a)), the equilibrium collective ordering becomes more significant with increasing particle density. Correspondingly, the transition from lying to biaxial order, as well as the transition from biaxial to standing order resemble the transitions seen at lower adsorption rates in Fig. 12.10, except that they are shifted to even lower particle densities. We call this phenomenon ‘re-entrant’ growth, because the same orientational ordering reoccurs during different stages of growth.

Motivated by the differences in ordering transitions that occur between high, intermediate and low adsorption rates in Figs. 12.10 and 12.11, we study the ordering transitions for a range of adsorption rates in Fig. 12.12.

For rates higher than a critical adsorption rate  $f \approx 0.005$ , standing nematic growth through particle adsorption transitions into the high density standing nematic phase without clear transition (as seen for  $f = 0.01$  in Fig. 12.11). On the other hand, for very low rates, the transitions converge towards the equilibrium transition points (as seen in Fig. 12.10). However, for adsorption rates in the range of  $0.0001 < f < 0.005$ , the new transitions previously discussed in Fig. 12.11 appear.

This biaxial phase arises for  $f \leq 0.005$ , while the lying nematic phase arises for  $f \leq 0.0045$ . Additionally, the transition from biaxial to lying (marked as turquoise squares in Fig. 12.12

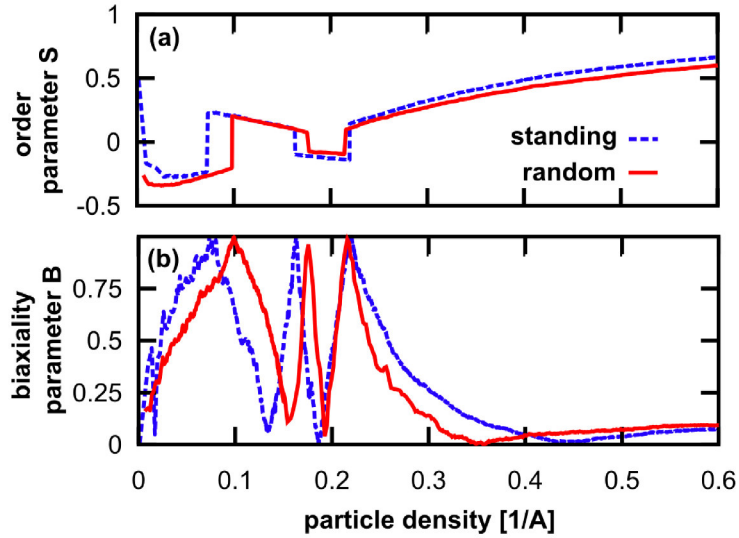


FIGURE 12.13: Comparison of the molecular order during growth for different molecular orientations during growth. The dashed line denoted as ‘standing’ represents data, where the molecules arrive on the substrate in a standing configuration, i.e.  $\vartheta_i = 0$  upon arrival. We compare molecules adsorbing with a standing configuration with molecules that arrive with a random configuration (red line, denoted as ‘random’). The data for standing adsorption is also depicted in Fig. 12.11. Both data sets correspond to  $f = 0.001$ .

is non-monotonous as a function of the adsorption rate<sup>1</sup>. Correspondingly, the orientational ordering for a density of  $0.25 \text{ nm}^{-2}$  follows a sequence from low to high adsorption rates: lying, biaxial, lying, biaxial and finally standing order. We interpret this non-monotonous ordering as a result of three competing effects: the standing orientation of the adsorbing molecules, the stable nematic lying orientation for low densities and the stable nematic standing orientation for the high densities. There are two mechanisms that drive the shift of transitions between orientationally ordered regions:

- For higher adsorption rates the molecules have less time to lie down, so the transitions leading from a lying to a standing orientation shift to lower densities (marked through blue triangles and red dots in Fig. 12.12).
- For higher adsorption rates, the adsorption configuration is preserved to higher densities, shifting the transitions from standing orientation to lying orientation to higher densities (marked through green stars and turquoise boxes in Fig. 12.12).

These lead to the re-entrant ordering in our system.

Non-monotonous orientational ordering as a function of adsorption rate through the competition of two phases that are stable at different densities was previously found in other systems [123, 305]. However, very few studies take non-monotonous behaviour into consideration.

<sup>1</sup>This observation is verified by multiple runs on lattices with  $10^6$  sites for  $0.005 \leq f \leq 0.0005$ .

### 12.2.3 Robustness to adsorption configuration

In experiments the orientation of the particles during adsorption remains uncertain. Therefore, different orientations are considered in literature. In DMC simulations so far, particles are adsorbed with a standing orientation [123, 306], with a random orientation [73, 74, 124], or confined to the substrate plane [125]. Our previous simulations were performed for a standing particle adsorption configuration, which was chosen to reduce possible particle overlap to a minimum. To test the robustness of our results and to gauge the influence of the adsorption orientation on our results, we compare the orientational ordering for particles adsorbed with a random orientation with the previously studied standing adsorption configuration in Fig. 12.13.

Qualitatively, the results are the same and even quantitatively the differences are fairly small. However, one specific feature is not apparent in the image: For random adsorption orientation, the first biaxial region with particle densities smaller than  $0.1 \text{ \AA}^{-2}$  corresponds to a  $(x-y)$ -biaxiality. For standing adsorption orientation, the first biaxial region for particle densities smaller than  $0.08 \text{ \AA}^{-2}$  corresponds to  $(x-z)$ -biaxiality.

The  $(x-z)$ -biaxiality for the adsorption of standing molecules is the result of the standing particle configuration. The energetically most favourable molecular orientation on the substrate is parallel to  $x$ . For random adsorption configuration no directional bias originates from the molecular orientation at adsorption. It is rather a different effect dominating the orientation: the symmetry breaking in molecule-substrate interaction. While the non-electrostatic molecule-substrate attraction decays with  $z^{-3}$  and prefers molecular orientations within the  $(x-y)$ -plane, the electrostatic molecular-substrate interaction decays exponentially and restricts the in-plane orientation to alignment with  $x$  (see Sec. 10.4). As the non-electrostatic interaction is longer-ranged and stronger (in our parametrisation, see Sec. 10.4 and 10.4.3), it dominates the molecular orientation more strongly than the electrostatic interaction, leading to an  $(x-y)$ -biaxiality.

Comparing the full, adsorption-rate dependent orientational ordering for random adsorption orientation (in Fig. 12.14) to the corresponding diagram for standing adsorption (in Fig. 12.12), we find small differences for adsorption rates  $f < 0.001$ . However, for larger adsorption rates, the diagrams differ. Most significantly, there is a non-negligible isotropically disordered region, where the adsorption conditions dominate or the orientational ordering before and after transitions is not as well-ordered (which leads to isotropic disorder ‘during’ the transition). We define isotropic disorder by  $|S| < 0.015$ , ensuring that (isotropically deposited) particles *without* rotational diffusion on our lattice sizes have a nematic order parameter that fluctuates below this value. However, the order parameter for standing particle deposition stays above  $|S| = 0.015$  (examples are depicted in Figs. 12.10 and 12.11).

The random deposition orientation shifts the abrupt onset of lying order to  $f = 0.0095$ . However, the general phenomenon of a ‘critical adsorption rate’ is preserved, whereas the previously discussed non-monotonous orientational ordering is not preserved. This indicates that all three factors are required: the stability of the two different orientational phases at different densities and the vertical particle adsorption. Instead, there may be some level of non-monotonous behaviour concerning the existence of an isotropic phase at particle densities close to  $0.75 \text{ nm}^{-2}$ . In general, the non-monotonous behaviour will need to be the focus of further

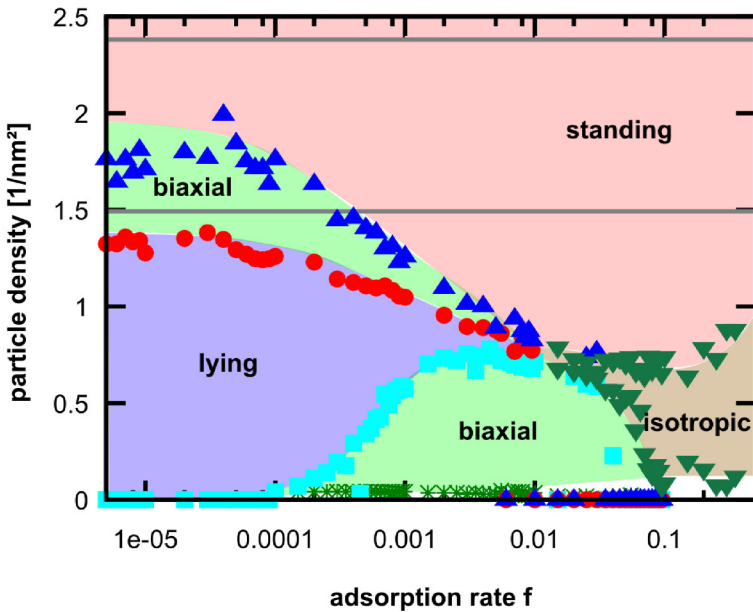


FIGURE 12.14: Orientational ordering as a function of the adsorption rates for molecules that adsorb with a random orientation. This graph follows the concept of Fig. 12.12, however it tests the robustness of our results with respect to the adsorption configuration by adsorbing molecules with random orientation. Again, the green stars mark a transition from standing to biaxial order, the turquoise boxes from biaxial to lying, the red dots from lying to biaxial and the blue triangles from biaxial to standing. The additional transitions in and out of isotropic disorder are marked through reverse dark green triangles, where an isotropic distribution is defined through  $|S| < 0.015$ . The area without a background colour at the bottom right is an area where the statistics are not sufficient to make a clear statement on the orientational ordering, however we expect the particles to be isotropic on average.

studies, as many different factors may contribute to possible non-monotonous behaviour (see App. G).

#### 12.2.4 Particle clustering during growth

Finally, we will study the island density in Fig. 12.15, which is determined using a cluster algorithm introduced in Sec. 11.2.3. This island density corresponds to the experimentally and theoretically studied island densities of isotropic particles (see Sec. 7.1), except that the expanded definition accounts for the anisotropy and the continuous 3D rotational degrees of freedom of our 6P molecules. Qualitatively, we find the same sequence of events: initially islands nucleate, then the island density saturates as the islands grow laterally and finally the island density drops as islands merge. Furthermore, Fig. 12.15 (a) also displays the adsorption rate dependency previously found for isotropic particles (discussed in Sec. 7.1.3), where a higher adsorption rate leads to a higher maximal island density.

Furthermore, we can now study the sequence through which particles stand up from the lying configuration in more detail, by distinguishing clusters through their average orientation, as depicted in Fig. 12.15 (b). We find that islands are already merging when clusters start to stand up, as the overall island density is already decreasing when the density of standing clusters starts to increase (around a particle density of approx.  $0.1 \text{ \AA}^{-1}$ ).

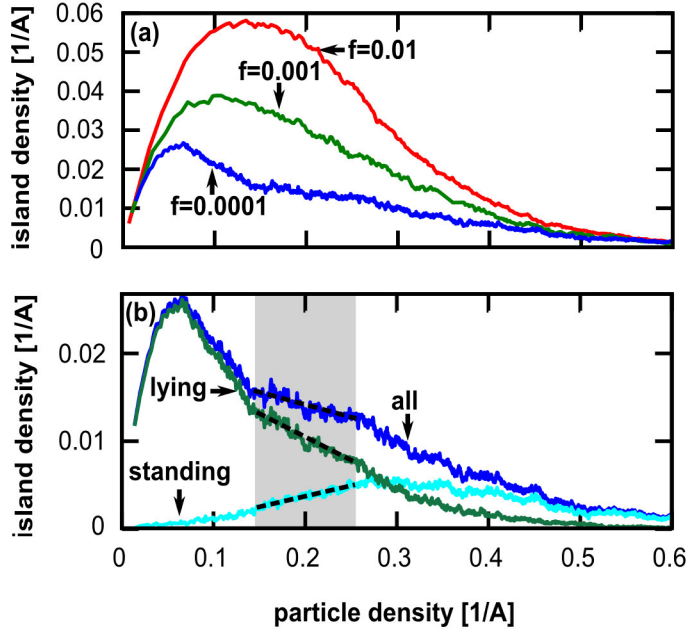


FIGURE 12.15: Island density during sub-monolayer growth. Part (a) displays the island size distribution for different adsorption rates, while part (b) resolves the island density for  $f = 0.0001$  in more detail by distinguishing between standing and lying clusters. Here, standing clusters have an average tilt angle  $|\vartheta_{\text{cluster}}| \leq 0.25\pi$ , while lying islands contribute the difference between the standing island density and the overall island density. Individual molecules without neighbours are here considered as clusters. The grey box in part (b) indicates a region in which the density of standing clusters increases rapidly, while the overall density decreases slowly and the lying density decreases rapidly. The dashed lines serve as a guide for the eye indicating the approximate gradients in these regions.

The overall particle density has a region of slower decrease, which is indicated through a grey background in Fig. 12.15 (b). This region of slower decrease between particle densities of  $0.14 \text{ \AA}^{-1}$  and  $0.26 \text{ \AA}^{-1}$  coincides with the strongest increase of standing islands. This may be indicative of transition where clusters stand up because the newly adsorbed particles allows the number of particles per cluster cross a critical value over which the clusters prefer a standing orientation. Within the transition range, i.e. for particle densities of  $0.14 \text{ \AA}^{-1}$  and  $0.26 \text{ \AA}^{-1}$  [see Fig. 12.15 (b)], we find an average cluster sizes between 9 and 21 molecules. Averaging over our data set within that range, we find a first approximate estimate for the cluster size associated with the transition between lying and standing clusters. This rough estimate gives an average cluster size of approx. 15 molecules for this transition, which resembles the transition cluster size of 14 found using energetic considerations for 6P on mica remarkably well [107].

However, note that Fig. 12.15 does not necessarily contain quantitatively correct data, because the exact parametrisation of the translational and rotational diffusion rates are so far not fully adapted to the specific material system (discussed in Secs. 10.6 and 14.2). A full quantitative study of observables such as the island density is beyond the scope of this thesis. However, it constitutes an interesting direction for further research that applies to many experimental questions, some of which are listed in Sec. 14.2. Hence, it provides a glimpse of questions and methods for future studies.

## Chapter 13

# Conclusion for the collective ordering of anisotropic molecules

In this part of the thesis we have proposed a classical, coarse-grained model for the representative material system of 6P molecules at the electrostatically patterned ZnO (10-10) surface and used it to study the collective ordering in equilibrium and during sub-monolayer growth. Within our model, the molecules are represented by rigid ellipsoids with point multipole moments motivated by the charge distribution of true 6P molecules. Likewise, the surface is considered to be an external perturbation giving rise to a static electric field.

Thus, our model lacks of atomistic degrees of freedom and, thus, the ability to respond to the adsorption process by conformational changes. However, it does take into account electrostatic contributions to both molecule-molecule and molecule-substrate interactions.

Based on our coarse-grained Hamiltonian, we have first performed MC simulations of a many-particle system focusing on the orientational ordering as function of density and lattice type. In the absence of the surface pattern, the model predicts, in addition to (3D) disordered states, standing and lying uniaxial configurations which have also been observed in experiments [28, 267]. Within these ordered phases, the quadrupole-quadrupole interactions play a decisive role for the nearest-neighbour configurations; in particular, we observe a structure resembling that in a herringbone lattice characteristic of bulk 6P systems [104, 267]. The electrostatic substrate field then causes pronounced alignment of the molecules along the charge lines of the ZnO(10-10) surface for a wide range of densities. Only at the highest density considered, the system with full molecule-molecule and molecule-substrate interactions still displays an upright uniaxial phase.

These equilibrium calculations provide the basic understanding for our growth simulations using DMC approaches. For slow adsorption rates, we find systems that show a transition between the low-density substrate alignment and the high-density standing alignment that corresponds to the previously discussed equilibrium ordering. However, for high adsorption rates (i.e. rates larger than  $f = 0.0095$ ) we find that molecules no longer have the time to form the low-density lying configuration. Instead, their order is dominated by the adsorption configuration and the high-density standing nematic order.

For adsorption rates only a little lower than the transition adsorption rates, re-entrant phases and non-monotonous ordering as a function of adsorption rate occur. Their origin lies in the competition between the two stable phases (lying nematic and standing nematic) with each other and the molecular configuration at adsorption. Here, the time scales of different processes drive the orientational ordering, leading to a plethora of new phenomena and enhancing the importance of growth studies for anisotropic molecules. Non-monotonous orientational ordering as a function of growth rate has also been observed for the study of self-assembled monolayers [123, 305]. However, not all non-monotonous behaviour arises through the same causes (discussed e.g. in App. G), which implies that growth is driven by fundamental principles that are not yet well understood.

Clearly, our model neglects various potentially important features, in particular the molecular flexibility. If a molecule bends the molecule's charge distribution (and that of the surface!) changes , yielding a change of strength (and even nature) of the resulting multipole moments. For example, it has been suggested [100] that the interaction of the ZnO substrate with a 6P molecule induces a molecular dipole moment, which is absent when considering the same molecule in vacuum. Nevertheless, the fact that in our rigid model we observe similar phases as in experiments suggests that we have captured key ingredients of this complex hybrid inorganic-organic system.

Moreover, one main advantage of our model is that we can easily include additional features such as an additional (permanent) dipole, which would arise when one considered 6P derivatives [307, 308]. Even with such additions, the model is still sufficiently simple to allow large-scale simulations inaccessible in full all-atom MD simulations. We thus consider our model to be a useful starting point for more elaborate coarse-grained simulations. Note that while the simulations performed here use the model representing 6P on ZnO(10-10), we expect the majority of the phenomena to be generic for the growth of COMs on electrostatically structured substrates.

As the field of coarse-grained growth simulations is not very well studied yet, many open questions remain. These include the influence of molecular order on multilayer growth [79], the factors that influence non-monotonous orientation as a function of adsorption rate [305] and kinetically arrested configurations that cannot be explained using equilibrium studies alone [28]. Further aspects that influence growth but are not well understood include anisotropic particle diffusion [106] and complex behaviour that may occur during step-edge crossing for anisotropic molecules [102, 277]. From the theoretical point of view, challenges that influence the future steps include the kinetic modelling and parametrisation of rotational diffusion (see Sec. 10.6), as well as the description of multilayer growth for highly anisotropic molecules and the influence of internal degrees of freedom [108].

While we have contributed significantly towards understanding the sub-monolayer growth of anisotropic molecules on structured substrates, the field is young and many questions remain.

## **Part IV**

# **General conclusion and Outlook**



# Chapter 14

## Overall conclusion and further directions of research

### 14.1 Overall conclusion

In this thesis we have developed new understanding of the growth and self-assembly of complex molecules on structured substrates. During our studies we have focused on two specific material systems, C<sub>60</sub> on C<sub>60</sub> (to be precise, a surface corresponds to the (111) facet of a C<sub>60</sub> crystal) and 6P on ZnO(10-10), which represent two categories of COM growth. These representative systems give us insight into fundamental aspects of COM growth, such as the similarities and differences to atomic and colloidal systems, as well as the principles behind the transition from lying to standing configurations during the growth of self-assembled monolayers. However, we were also able to make quantitative predictions of C<sub>60</sub> growth and develop new coarse-graining and simulation strategies that will be required for further progress when studying the growth of anisotropic molecules.

To this end, in part I, Chap. 1 we initially introduced the material systems of interest (COMs grown on both organic and inorganic substrates), along with their applicational interest, the challenges in application design and growth and the current status of theoretical studies. Here we identified that fundamental work is still necessary, especially in the field of anisotropic COMs, in order to understand and predict their growth. Two aspects that have been mostly neglected in the literature so far are the influence of the interaction range of COMs on growth (which differs from the interaction range of atoms and molecules), as well as understanding and predicting orientational ordering of anisotropic COMs.

We face these challenges using DMC methods, because these are the only simulation approaches that give access to the necessary time- and length-scales without losing the details of information at the level of individual molecules. We introduce and discuss the fundamental concepts behind DMC simulations as well as several algorithms in Chap. 2. Specifically, we show that the different algorithms are a procedural reordering of each other and the chosen algorithm does not influence the simulation result, only the efficiency. In DMC simulations, the exact details of molecular motion are neglected, and the surface evolution is treated in terms of transition rates between different states. The rates used in such simulations are

Arrhenius-type rates, that can be derived both from the Fokker-Planck equation and from Transition-State-Theory. We give an overview of the derivation, as well as other coarse-graining and fundamental theoretical aspects in Chap. 3. The coarse-graining includes the concepts of time-scale-separation, coarse-graining of the potential landscape and the description of a system evolution through a Markov-chain where particles perform a random walk on a lattice. These concepts are quintessential for DMC simulations of large systems, as the systems that we consider.

The first material system that we consider is the isotropic molecule C<sub>60</sub>, which we study in part II. Besides applicational interest, C<sub>60</sub> is a unique model system because its spherical symmetry allows direct comparison to atomic and colloidal systems (see Chap. 4). While some theoretical and experimental studies exist, prior to this work no studies existed that simulated the full multilayer growth of C<sub>60</sub>. We used simulations based closely on existing simulations for atomic systems to create a minimalistic multilayer growth model for C<sub>60</sub>. This model has only three degrees of freedom, which we fitted to the results of time-resolved X-ray scattering measurements of C<sub>60</sub> multilayer growth. The model and the experiment are described in Chap. 5, while the observables that we used to fit our model are discussed in Chap. 6. Prior to our collaboration, time resolved in- and out-of-plane X-ray scattering of molecular growth had never been combined with DMC simulations, so part of the challenge of the collaboration was to identify observables that are accessible in both simulations and measurements, and to interpret the results correctly.

In this collaboration, we were able to quantitatively understand and predict the multilayer growth of the spherical molecule C<sub>60</sub>. Furthermore, C<sub>60</sub> gives us new insight into the similarities and differences between colloidal systems, molecules and atomic systems. The differences between the systems originate in their different interaction ranges, so we have studied the influence of the different interaction ranges on the energy parameters that determine growth behaviour both on the particle-resolved level and on the level of the overall surface morphology as it evolves. To this end, we used the parameter set fitted to the experiment, and compared the parameter sets to typical atomic and colloidal systems. The result reflects the intermediate nature of C<sub>60</sub>: C<sub>60</sub> displays atom-like step-edge barriers, which differ from colloidal step-edge barriers. However, the ratio of free diffusion and neighbour binding energies of C<sub>60</sub> also differs substantially from the corresponding ratio for atomic systems. This has implications for growth, because the higher relative neighbour binding energy of atomic systems leads to far stronger fractal growth and much shorter free diffusion distances than occur for C<sub>60</sub> growth (see Chap. 7 and 8).

Expanding from the spherical C<sub>60</sub> molecule to anisotropic molecules, we chose the representative material system 6P on ZnO(10-10) to develop a coarse-grained model and study the collective ordering both in equilibrium and during growth (in part III, first introduced in Chap. 9). Again, this specific material system is promising for applications in hybrid organic-inorganic opto-electronics devices. However, more fundamentally, 6P has features that are common to many COMs: an anisotropic form and a quadrupole moment that arises from its delocalised orbitals. On the other hand, ZnO(10-10) displays features that are common to mixed-terminated metal-oxide surfaces: a surface charge pattern that forms lines caused by the differences in electron affinity of the metal and oxygen. Hence, while 6P on ZnO(10-10) is a specific material system, the fundamental processes observed are more generic.

For this anisotropic material, continuous rotational degrees of freedom in all three dimensions need to be modelled to reflect the complex rotational ordering known from experiment. No suitably coarse-grained model of 6P on ZnO(10-10) existed in literature prior to this work. Hence we introduced an empirical coarse-graining strategy in Chap. 10. We created a coarse-grained Hamiltonian that contains both electrostatic and non-electrostatic interactions between molecules as well as between each molecule and the substrate. The molecules are represented by rigid ellipsoids with point multipole moments motivated by the charge distribution of true 6P molecules. Likewise, the surface is modelled by van-der-Waals attraction and Pauli repulsion with an additional static electric field reflecting the alternating zinc and oxygen rows at the ZnO(10-10) surface. The resulting Hamiltonian is parametrised from DFT calculations and experiments.

Very few DMC simulations of anisotropic molecules exist to date — and other simulation approaches do not come close to the length and time scales required to understand the collective ordering of molecules during growth. As no DMC simulations studying the collective ordering of molecules with continuous 3D rotational degrees of freedom existed, we developed a DMC approach that includes full rotational freedom in a quasi-equilibrium approximation, while modelling translational diffusion through a lattice based on the substrate lattice (see Chap. 10). This orientational ordering is subsequently studied using the nematic order parameter and other observables listed in Chap. 11.

Studying the collective orientational ordering of 6P on ZnO(10-10), we were able to reproduce ordered structures that are seen in experiments, and understand the transition between lying and standing configurations that are seen in experiments during the growth of COMs (see Chap. 12 and 13). For high adsorption rates, we observe growth that is dominated by the adsorption configuration and the high-density ordering, and for very low adsorption rates we find growth that converges to the equilibrium ordering. However, for intermediate adsorption rates we find re-entrant growth and non-monotonous behaviour as a function of adsorption rate, which indicates complex behaviour. Here we trace the re-entrant and non-monotonous behaviour back to competition between the adsorption configuration, the lying molecular ordering that is stable for low particle densities and the standing nematic ordering that is stable for high particle densities.

## 14.2 Further directions of research

As discussed in part II of this thesis, despite their differences in interaction range, the spherical symmetry of C<sub>60</sub> allows us to model it in a rather similar fashion to modelling atomic growth. Hence, a natural expansion to the studies presented here involves transferring concepts from atomic growth to C<sub>60</sub> growth and studying the impact of the differences of interaction range more closely. Here, first studies have considered combining different materials and studying the dewetting of C<sub>60</sub> on CaF<sub>2</sub> [118], as we have also discussed for C<sub>60</sub> on mica (see Sec. 5.1). Determining the energy barriers using ab initio calculations (as used e.g. in Ref. [113, 309]) could give further detailed insight into the influence of interaction range on the molecule-substrate interactions for different substrates.

Including a substrate of a different material in general creates strain. While, for the mica substrate, we have shown that strain is not significant for growth, studies of atomic growth have shown the significance of strain during growth [310] and some preliminary work in our group has shown that strain directly influences the surface morphology and island shape during C<sub>60</sub> growth [311]. However, while reasonably efficient algorithms to include strain in DMC simulations exist [312], systematic studies of the influence of strain on COM growth are still lacking. For isotropic COMs, strain calculations are possible, though computationally quite expensive [311]. The strain in systems of anisotropic COMs is harder to implement, because no simulation approaches are established for COMs. Even though COMs are softer [304], strain may be a driving force e.g. at the boundaries between domains of different internal ordering. Such domains are experimentally observed to co-exist during the growth of 6P on ZnO [28], and their merging is not well understood. Their study has the potential to give insight into defect formation and collective ordering in structures of COMs at interfaces.

In part II, we have studied C<sub>60</sub> as a material system from a fundamental theoretical point of view, where effects known from both atomic and colloidal materials influence the growth characteristics. A further expansion of this thought concerns the entropy. In a colloidal system, the entropy is known to be a significant contribution to the free energy, and it thus can dominate the structures formed, especially when strain is included [313]. On the other hand, in the study of atomic systems the entropy is commonly negligible compared to the potential energy, as is reflected through the common use of an entropy-independent attempt frequency  $\nu_0 = 2kT/h \approx 10^{13}$  Hz [138, 139, 211] (see derivation of the diffusion rate in Sec. 3.1.3 for details). We briefly discussed the influence of entropy in our system in Sec. 3.1.3 and concluded that we can treat the entropy as a constant contribution for our materials and parameter ranges. However, entropy changes in COMs can be quite large [165], and especially internal vibrational degrees of freedom are expected to have a significant influence on the structure formation [304].

From an applicational point of view, the study of relaxation of pre-structured configurations is significant for device optimisation. Specifically, C<sub>60</sub> and its derivatives are frequently used as donor molecules in the bulk hetero-structures of OPVs (see Sec. 1.1 and Ref. [35]). Here, nano-structures are often not grown on a bare substrate, but printed, scratched or grown using a mask [138, 314, 315]. In order to obtain the ideal comb-like configuration of a bulk hetero-junction (see Sec. 1.1 and Fig. 1.4), a thick layer of the one material is created, then the comb is imprinted and finally the second material is added [314]. In this situation, it becomes relevant how the imprinted configuration relaxes with and without the impact of the second material and possible solvent liquids. Studies of pre-structured GaAs have shown some interesting phenomena including the development of facets [138], indicating that the study of pre-structured C<sub>60</sub> may be relevant for the creation of bulk hetero-structures for OPVs.

Bulk hetero-structures also open another field of interesting questions: what happens if two different materials are combined during growth? Here, different procedures exist. The different materials can be grown successively [316] or at the same time [317]. Experimental studies [316, 317] as well as MD simulations [256, 318] indicate that different mixing and demixing can occur, while MC studies of colloidal mixtures indicate that the alignment of one material can influence the alignment of the other, creating an order that the individual components do not create on their own [319, 320]. The level of mixing, as well as the alignment of COMs within the mixed or demixed areas, are of both fundamental and applicational interest [321].

While for atoms the mixing of species in crystals is well understood and colloidal mixtures are currently being investigated [319, 320, 322–324], only little insight is gained into mixtures of COMs and there are only very few publications of DMC simulations that consider growth of a mixture of anisotropic COMs [74]. Here, a vast field of questions concerning the fundamental principles and the material specifics is still nearly untouched. However, first theoretical results for mixtures of COMs show that the modelling assumptions need to be chosen with care [256].

One reason why the growth of mixed COMs remains mostly unexplored is that the growth of a single species of COMs is still not well understood. In part III of this thesis, we have studied the orientational ordering during growth for a coarse-grained model of 6P with full rotational degrees of freedom. This study required the development of a suitable coarse-grained model, as well as the development of a suitable DMC simulation regime. Here, our developments may shed light on a wide range of experimental observations for the collective ordering of COMs during growth, which are so far barely understood. These observations include:

- The increase of lying clusters of COMs at higher temperatures [28],
- the co-existence of two slightly different crystal structures of 6P during growth [79],
- the increasing tilt angle of fluorinated 6P with every additional grown layer [79],
- the different tilt vector assumed by each island nucleus during nucleation of the COM Diindenoperylene (DIP), which is propagated through the layers giving rise to rapid roughening [259],
- and the temperature-dependent collective rearrangement for DIP, where all previously adsorbed molecules simultaneously change their tilt angle when a certain coverage is reached [82].

These are examples of experimentally observed complex collective ordering phenomena that are little understood and that were previously not accessible using DMC simulations. While some of these questions can be approached using our simulation (with a different model for DIP), some of these questions require further expansion of the existing methodology. For example, in order to study the tilt changes during multilayer growth, the simulation needs to be expanded in a physical fashion to include multiple layers without losing the full rotational degrees of freedom. Similarly, in order to obtain quantitative information, our coarse-grained model will have to undergo some refinement and a systematic approach to deriving attempt frequencies will be necessary.

Finally, some interesting questions arise from theoretical predictions for the behaviour of individual COMs. For example, 6P is known to have anisotropic diffusion constants along the different lattice directions of the ZnO(10-10) substrate [106]. We also know that the diffusion rate of COMs additionally depends on the direction of diffusion with respect to the orientation of the COM [126]. The influence of these two different anisotropic diffusion phenomena on island shapes, island size distributions and other macroscopic observables is so far not known. Additionally, the re-entrant and non-monotonous behaviour observed in Sec. 12.2 of the thesis and in Ref. [305] is interesting on a fundamental level and requires a systematic study of the requirements that a system has to fulfil in order for this behaviour to arise.

Both theory and experiment pose a wide range of questions on both a fundamental and an applicational level that are intimately linked to the work presented in this thesis. Simulating the growth of COMs is a challenging but promising field, where a lot of work is being done on the experimental side, but only few groups are currently working on the theoretical side. While the work presented in this thesis contributes to the understanding of COM growth in several important points, further work is still required on the theoretical side to obtain a complete and thorough understanding of the principles behind the observed ordering phenomena and to be able to quantitatively predict structure formation for a range of material systems.

# Appendices



## Appendix A

# Full equivalence of RSM and KMC time scales

In this appendix, we show that the two DMC algorithms used in this thesis, KMC and RSM, statistically perform the same time evolution. The algorithms are introduced and discussed in Chap. 2, along with brief summary of the calculations discussed in this appendix. In the full considerations presented in this appendix, we slowly progress from a system in which one process is possible and we determine the average time for this process to take place and go through all the steps until we show the time each of these systems requires to perform *a* processes, if *n* processes are possible.

### A.1 One process occurs and one is possible

Assuming that just one single process is possible and it has a process rate  $r_1$ , what is the average time that the algorithms take for this process to take place?

**KMC:** In KMC simulations, a time step is drawn from the distribution

$$\Delta\tau = -\frac{1}{r^{\text{tot}}} \ln R, \quad (\text{A.1})$$

as was introduced in Eq. (2.6) in Sec. 2.5. Here,  $r^{\text{tot}} = r_1$ , as only one process is possible. The average time it takes for this process to take place is equal to the average time step length with which the system progresses when this process takes place.

$$\begin{aligned} \langle\tau\rangle_1 &= \langle\Delta\tau\rangle_1 \\ &= \left\langle -\frac{1}{r_1} \ln R \right\rangle = \frac{1}{r_1}. \end{aligned} \quad (\text{A.2})$$

**RSM:** In every iteration this only possible process is chosen and accepted with the probability

$$p_1 = r_1 \Delta t, \quad (\text{A.3})$$

as introduced in algorithm in Sec. 2.4. As there is only one process type the system time progresses by  $t = t + \Delta t/1$  every time the process is attempted, i.e., in every iteration. In every iteration, the process occurs with a probability  $p_1$  and the probability of it not occurring is  $1 - p_1$ . Thus, the probability of a process occurring within  $N$  time step is

$$P(\leq N)_1 = \sum_{i=0}^{N-1} (1 - p_1)^i \cdot p_1^1. \quad (\text{A.4})$$

Therefore the average time required for this process to occur is

$$\begin{aligned} \langle t \rangle_1 &= \sum_{n=0}^{\infty} N \Delta t P(N)_1 \\ &= \sum_{N=0}^{\infty} N \Delta t (P(\leq N)_1 - P(\leq (N-1))) \\ &= \sum_{N=0}^{\infty} N \Delta t (1 - p_1)^{N-1} p_1 \\ &= \frac{\Delta t p_1}{1 - p_1} \sum_{N=0}^{\infty} N (1 - p_1)^N \\ &= \frac{\Delta t p_1}{1 - p_1} \frac{(1 - p_1)}{(p_1)^2} = \frac{\Delta t}{p_1} = \frac{1}{r_1} \end{aligned} \quad (\text{A.5})$$

$$(A.6)$$

So a single possible process takes on average the same time in either simulation approach.

## A.2 One process takes place, two are possible

How long does the system evolve before one process takes place, if two processes with rates different rates and different probabilities  $p_1 = r_1 \Delta t$  and  $p_2 = r_2 \Delta t$  are possible?

**KMC:** Corresponding to Eq. (A.2), we find

$$\langle \tau \rangle_1 = \frac{1}{r^{\text{tot}}} = \frac{1}{r_1 + r_2}. \quad (\text{A.7})$$

**RSM:** The probability  $P$  of exactly one process of the two possible processes occurring after exactly  $N - 1$  process-less time steps is described by:

$$\begin{aligned} P_1(N) &= \left(\frac{1}{2}\right)^N \sum_{l=0}^{N-1} (1 - p_1)^l (1 - p_2)^{N-1-l} \binom{N-1}{l} (p_1 + p_2) \\ &= \left(\frac{1}{2}\right)^{N+1} (2 - p_1 - p_2)^{N-1} (p_1 + p_2) \end{aligned} \quad (\text{A.8})$$

As there are two possible processes, the system time now progresses as  $t = t + \Delta t/2$  in every iteration (see Sec. 2.4 for details). This defines the average time the system takes before this process takes place to be

$$\begin{aligned}
\langle t \rangle_1 &= \sum_{N=1}^{\infty} \frac{\Delta t}{2} N P_1(N) \\
&= \sum_{N=1}^{\infty} \frac{\Delta t}{2} N \left(\frac{1}{2}\right)^{N+1} (2 - p_1 - p_2)^{N-1} (p_1 + p_2) \\
&= \frac{\Delta t}{2} \frac{p_1 + p_2}{2 - p_1 - p_2} \sum_{N=1}^{\infty} \frac{\Delta t}{2} N \left(\frac{2 - p_1 - p_2}{2}\right)^n \\
&= \frac{\Delta t}{2} \frac{p_1 + p_2}{2 - p_1 - p_2} \frac{2 \cdot (2 - p_1 - p_2)}{(p_1 + p_2)^2} \\
&= \frac{1}{r_1 + r_2},
\end{aligned} \tag{A.9}$$

### A.3 Two processes take place, two are possible

What is the average time for two successive processes take place, if initially two processes with rates different rates  $r_{1,0}$  and  $r_{2,0}$  are possible, however these change to different rates  $r_{1,1}$  and  $r_{2,1}$  after a process (of any sort) has taken place? Note that in the actual simulation usually not all rates change, however some rates change, some processes may become possible and others may become impossible. Without lack of generality, we can assume here that all processes that can ever become possible are included as possible processes. Then, processes that are actually impossible simply have a probability  $p^{\text{impossible}} = 0$ .

We can here also assume without loss of generality that all rates change after one process takes place. Any rates that actually do not change are simply assigned the same value as they previously held, i.e.  $r_{i,j-1} = r_{i,j}$ .

**KMC:** Following Eq. (2.6) in Sec. 2.5, each successive time step is drawn using a random number. Here, we use the two uncorrelated random numbers  $R_0 \in [0, 1]$  and  $R_1 \in [0, 1]$  to draw the length of the first and second time step. For a simulation of two successive processes, the time steps are simply added. The average time for two processes to take place is therefore

$$\begin{aligned}
\langle \tau \rangle_2 &= \left\langle -\frac{1}{\sum_{i=1}^2 r_{i,0}} \ln R_0 - \frac{1}{\sum_{i=1}^2 r_{i,1}} \ln R_1 \right\rangle \\
&= \left\langle -\frac{1}{\sum_{i=1}^2 r_{i,0}} \ln R_0 \right\rangle + \left\langle -\frac{1}{\sum_{i=1}^2 r_{i,1}} \ln R_1 \right\rangle \\
&= \frac{1}{\sum_{i=1}^2 r_{i,0}} + \frac{1}{\sum_{i=1}^2 r_{i,1}} \\
&= \frac{1}{r_0^{\text{tot}}} + \frac{1}{r_1^{\text{tot}}},
\end{aligned} \tag{A.10}$$

where we refer to  $r_j^{\text{tot}} = \sum_{i=1}^n r_{i,j}$  and  $p_j^{\text{tot}} = \sum_{i=1}^n p_{i,j}$  as the total escape rate and total escape probability of the system at the configuration after  $j$  processes.

**RSM:** Determine the probability that two processes occur in  $N$  time steps, whereby the second process takes place in the last time step. There are  $l \in [0, N - 2]$  not-processes that take place before the first process takes place, and  $N - 2 - l$  not-processes take place afterwards. As the rates change with the process these two time blocks cannot be exchanged, so no binomial coefficient is needed for the summation over  $l$ . The using equation A.8 the probability can be found to be

$$P_2(N) = \left(\frac{1}{2}\right)^N \sum_{l=0}^{N-2} (2 - p_{1,0} - p_{2,0})^l (p_{1,0} + p_{2,0})(2 - p_{1,1} - p_{2,1})^{N-2-l} (p_{1,1} + p_{2,1}) \quad (\text{A.11})$$

$$= \left(\frac{1}{2}\right)^N \sum_{l=0}^{N-2} (2 - p_0^{\text{tot}})^l p_0^{\text{tot}} (2 - p_1^{\text{tot}})^{N-2-l} p_1^{\text{tot}} \quad (\text{A.12})$$

$$= \left(\frac{1}{2}\right)^N \frac{(2 - p_1^{\text{tot}})^{n-1} - (2 - p_0^{\text{tot}})^{n-1}}{p_0^{\text{tot}} - p_1^{\text{tot}}} p_0^{\text{tot}} p_1^{\text{tot}}. \quad (\text{A.13})$$

This expression gives us an average time

$$\begin{aligned} \langle t \rangle_2 &= \sum_{N=2}^{\infty} \frac{\Delta t}{2} N P_2(N) \\ &= \sum_{N=2}^{\infty} \frac{\Delta t}{2} N \left(\frac{1}{2}\right)^n p_0^{\text{tot}} p_1^{\text{tot}} \frac{(2 - p_1^{\text{tot}})^{N-1} - (2 - p_0^{\text{tot}})^{N-1}}{p_0^{\text{tot}} - p_1^{\text{tot}}} \\ &= \frac{\Delta t}{2} \frac{p_0^{\text{tot}} p_1^{\text{tot}}}{p_0^{\text{tot}} - p_1^{\text{tot}}} \frac{(2 - p_1^{\text{tot}})(2 + p_1^{\text{tot}}) (p_0^{\text{tot}})^2 - (2 - p_0^{\text{tot}})(2 + p_0^{\text{tot}}) (p_1^{\text{tot}})^2}{(p_0^{\text{tot}})^2 (p_1^{\text{tot}})^2 2} \\ &= 2 \frac{\Delta t}{2} \left( \frac{1}{p_0^{\text{tot}}} + \frac{1}{p_1^{\text{tot}}} \right) \\ &= \frac{1}{\sum_{i=1}^2 r_{i,0}} + \frac{1}{\sum_{i=1}^2 r_{i,1}}. \end{aligned} \quad (\text{A.14})$$

$$(\text{A.15})$$

## A.4 Two processes take place, $n$ are possible

Considering multiple process types with rates  $r_{i,j}$ , whereby  $i \in 1, \dots, n$  and  $j$  determines the number of processes that have already occurred. Here we try to expand out to the complete system as simulated, allowing each rate to change after each process.

**KMC:** The kinetic Monte Carlo simulation can be treated in a quite straightforward manner. The average time it takes the system is the sum of the average times sequential processes take, as determined above. Therefore, the average time a  $n$ -process system takes for two processes can be determined corresponding to Eq. (A.10).

$$\langle \tau \rangle_2 = \sum_{j=0}^1 \frac{1}{\sum_{i=1}^n r_{i,j}} \quad (\text{A.16})$$

**RSM:** Based on equation A.13, we can determine a rate for a  $n$ -process-type system by using the total system escape probabilities  $p_0^{\text{tot}} = \sum_{i=0}^N p_{i,0} = \delta \sum_{i=0}^N r_{i,0}$  and  $p_1^{\text{tot}} = \sum_{i=0}^N p_{i,1}$ . Then, the probability of no process taking place in one time-step before any process has taken place is  $n - p_0^{\text{tot}}$ , which includes all possible not-processes that can occur (not  $p_{0,0}$ , not  $p_{1,0}$  ... not  $p_{n,0}$ ). The probability of two processes taking place in  $N$  time steps (with the second process in the last time step) is

$$\begin{aligned} P_2(N) &= \left(\frac{1}{n}\right)^N \sum_{l=0}^{N-2} (n - p_0^{\text{tot}})^l p_0^{\text{tot}} (n - p_1^{\text{tot}})^{N-2-l} p_1^{\text{tot}} \\ &= \left(\frac{1}{n}\right)^N \frac{(n - p_1^{\text{tot}})^{N-1} - (n - p_0^{\text{tot}})^{N-1}}{p_0^{\text{tot}} - p_1^{\text{tot}}} p_0^{\text{tot}} p_1^{\text{tot}}. \end{aligned} \quad (\text{A.17})$$

Accordingly, the average time can be determined as above. Note that the system time progresses as  $t = t + \Delta t/n$  in a system of  $n$  possible processes.

$$\begin{aligned} \langle t \rangle_2 &= \sum_{N=2}^{\infty} \frac{\Delta t}{n} N \left(\frac{1}{n}\right)^N p_0^{\text{tot}} p_1^{\text{tot}} \frac{(n - p_1^{\text{tot}})^{N-1} - (n - p_0^{\text{tot}})^{N-1}}{p_0^{\text{tot}} - p_1^{\text{tot}}} \\ &= \frac{\Delta t}{n} \frac{p_0^{\text{tot}} p_1^{\text{tot}}}{(p_0^{\text{tot}} - p_1^{\text{tot}})} \frac{(n - p_1^{\text{tot}})(n + p_1^{\text{tot}})(p_0^{\text{tot}})^2 - (n - p_0^{\text{tot}})(n + p_0^{\text{tot}})(p_1^{\text{tot}})^2}{(p_0^{\text{tot}})^2 (p_1^{\text{tot}})^2 n} \\ &= n \frac{\Delta t}{n} \left( \frac{1}{p_0^{\text{tot}}} + \frac{1}{p_1^{\text{tot}}} \right) \\ &= \sum_{j=0}^1 \frac{1}{\sum_{i=1}^n r_{i,j}}. \end{aligned} \quad (\text{A.18})$$

(A.19)

## A.5 Mathematical induction for $a$ processes taking place for $n$ possible processes

Determining the average time that  $a$  processes take in a KMC simulation is easily determined following the steps taken for  $a = 2$  processes above. However, for RSM simulations the derivation is not as straightforward. Therefore, we use mathematical induction to show the equivalence of time scales. We use the derivations for  $a = 1$  and  $a = 2$  as the beginning for the induction. For the step from  $a$  processes to  $a + 1$  processes, the expected change in average time can be derived from KMC:

$$\langle \tau \rangle_{a+1} = \langle \tau \rangle_a + \frac{1}{r_a^{\text{tot}}}. \quad (\text{A.20})$$

Accordingly, we use the following induction step

$$\langle t \rangle_{a+1} = \langle t \rangle_a + \frac{1}{r_a^{\text{tot}}}. \quad (\text{A.21})$$

The  $a$  processes split the  $N$  time steps into  $a$  time blocks of not-processes, where each has the length  $t_0, t_1, \dots, t_{a-1} \leq N - a$ . Here, the condition  $\sum_{l=0}^{a-1} t_l = N - a$  determines the length of one time step,  $t_k = N - a - \sum_{l=0}^{k-1} t_l - \sum_{l=k+1}^{a-1} t_l$ . The probability of finding  $a$  processes in  $N$  time steps then is defined through the sum of all possible time block configurations

$$P_a(N) = \left( \frac{1}{n} \right)^N \left( \prod_{l=0}^{a-1} p_l^{\text{tot}} \right) \cdot \sum_{t_0=0}^{N-a} \left( \sum_{t_1=0}^{N-a-t_0} \left( \dots \sum_{t_{a-2}=0}^{N-a-\sum_{k=0}^{a-3} t_k} \left( \left( \prod_{l=0}^{a-2} (n - p_l^{\text{tot}})^{t_l} \right) \cdot (n - p_{a-1}^{\text{tot}})^{N-a-\sum_{k=0}^{a-2} t_k} \right) \dots \right) \right). \quad (\text{A.22})$$

Note that the sums this can be written recursively as

$$P_a(N) = \left( \frac{1}{n} \right)^N \prod_{l=0}^{a-1} p_l^{\text{tot}} \cdot S_0; \quad S_0 = \sum_{t_0=0}^{N-a} S_1; \quad S_l = \sum_{t_l=0}^{N-a-\sum_{k=0}^{l-1} t_k} S_{l+1}; \quad S_{a-2} = \left( \prod_{l=0}^{a-2} (n - p_l^{\text{tot}})^{t_l} \right) (n - p_{a-1}^{\text{tot}})^{N-a-\sum_{k=0}^{a-2} t_k}.$$

Though this description is shorter it is not useful for our calculations, this mention is for completeness. The average time  $a$  and  $a + 1$  processes take are determined by

$$\langle t \rangle_a = \sum_{N=a}^{\infty} N \frac{\Delta t}{n} \left( \frac{1}{n} \right)^N \left( \prod_{l=0}^{a-1} p_l^{\text{tot}} \right) \cdot \sum_{t_0=0}^{N-a} \left( \sum_{t_1=0}^{N-a-t_0} \left( \dots \sum_{t_{a-1}=0}^{N-a-\sum_{k=0}^{a-3} t_k} \left( \left( \prod_{l=0}^{a-2} (n - p_l^{\text{tot}})^{t_l} \right) \cdot (n - p_{a-1}^{\text{tot}})^{N-a-\sum_{k=0}^{a-2} t_k} \right) \dots \right) \right) \text{ and} \quad (\text{A.23})$$

$$\langle t \rangle_{a+1} = \sum_{N=a+1}^{\infty} N \frac{\Delta t}{n} \left( \frac{1}{n} \right)^N \left( \prod_{l=0}^a p_l^{\text{tot}} \right) \cdot \sum_{t_0=0}^{N-a-1} \left( \sum_{t_1=0}^{N-a-1-t_0} \left( \dots \sum_{t_{a-1}=0}^{N-a-1-\sum_{k=0}^{a-2} t_k} \left( \left( \prod_{l=0}^{a-1} (n - p_l^{\text{tot}})^{t_l} \right) \cdot (n - p_a^{\text{tot}})^{N-a-1-\sum_{k=0}^{a-1} t_k} \right) \dots \right) \right). \quad (\text{A.24})$$

The aim of the complete induction method is to manipulate Eq. (A.24) to reproduce Eq. (A.21). This involves lengthy rephrasing of equations, but for completeness sake I will include all of the steps at this point. At some point summation indices or product indices are neglected for sake of readability, but they should be determinable from previous lines of calculation. In order to rewrite the average time  $\langle t \rangle_{a+1}$ , we use Eq. (A.24) along with the following two relations:

$$t_a = N - a - 1 - \sum_{k=0}^{a-1} t_k \leftrightarrow t_{a-1} = N - a - 1 - \sum_{k=0}^{a-2} t_k - t_a, \quad \text{and} \quad N' := N - 1. \quad (\text{A.25})$$

Then, we get

$$\begin{aligned} \langle \Delta t \rangle_{a+1} &= \sum_{N'=a}^{\infty} (N'+1) \frac{\Delta t}{n} \left( \frac{1}{n} \right)^{(N'+1)} \left( p_a^{\text{tot}} \prod_{l=0}^{a-1} p_l^{\text{tot}} \right) \cdot \\ &\quad \sum_{t_0=0}^{N'-a} \left( \sum_{t_1=0}^{N'-a-t_0} \left( \dots \sum_{t_{a-1}=0}^{N'-a-\sum t_k} \left( \left( \prod_{l=0}^{a-2} (n - p_l^{\text{tot}})^{t_l} \right) \cdot (n - p_a^{\text{tot}})^{t_a} (n - p_{a-1}^{\text{tot}})^{N'-a-\sum_{k=0}^{a-2} t_k - t_a} \right) \dots \right) \right) \\ &= \sum_{N'=a}^{\infty} (N'+1) \frac{\Delta t}{n} \left( \frac{1}{n} \right)^{(N'+1)} \left( p_a^{\text{tot}} \prod_{l=0}^{a-1} p_l^{\text{tot}} \right) \cdot \\ &\quad \sum_{t_a=0}^{N'-a} \left( (n - p_a^{\text{tot}})^{t_a} \sum_{t_0=0}^{N'-a-t_a} \left( \dots \sum_{t_{a-2}=0}^{N'-a-\sum t_k - t_a} \left( \left( \prod_{l=0}^{a-2} (n - p_l^{\text{tot}})^{t_l} \right) \cdot (n - p_{a-1}^{\text{tot}})^{N'-a-\sum t_k - t_a} \right) \dots \right) \right) \end{aligned} \quad (\text{A.26})$$

Assuming convergence this sum can be split up into three individual infinite sums.  $A$  is for  $t_a = 0$ , whereby the factor  $(N^+ + 1)$  is split up into sum with  $N^+$  in part  $A$ , and sum with 1 contributes to  $C$ .  $B$  and the other part of  $C$  are the according sums for  $t_a > 0$ .

$$\begin{aligned}
\langle t \rangle_{a+1} &= \sum_{N^+=a}^{\infty} N^+ \frac{\Delta t}{n} p_a^{\text{tot}} \left( \frac{1}{n} \right)^{(N^++1)} \prod_{l=0}^{a-1} p_l^{\text{tot}} \cdot \sum_{t_0=0}^{N^+-a} \left( \dots \sum_{t_{a-2}=0}^{N^+-a-\sum t_k} \left( \left( \prod_{l=0}^{a-2} (n - p_l^{\text{tot}})^{t_l} \right) \cdot (n - p_{a-1}^{\text{tot}})^{N^+-a-\sum t_k} \right) \dots \right) \\
&\quad + \sum_{N^+=a+1}^{\infty} N^+ \frac{\Delta t}{n} p_a^{\text{tot}} \left( \frac{1}{n} \right)^{(N^++1)} \prod_{l=0}^{a-1} p_l^{\text{tot}} \cdot \\
&\quad \quad \sum_{t_a=1}^{N^+-a} \left( (n - p_a^{\text{tot}})^{t_a} \sum_{t_0=0}^{N^+-a-t_a} \left( \dots \sum_{t_{a-2}=0}^{N^+-a-\sum t_k-t_a} \left( \left( \prod_{l=0}^{a-2} (n - p_l^{\text{tot}})^{t_l} \right) \cdot (n - p_{a-1}^{\text{tot}})^{N^+-a-\sum t_k-t_a} \right) \dots \right) \right) \\
&\quad + \sum_{N^+=a}^{\infty} 1 \frac{\Delta t}{n} p_a^{\text{tot}} \left( \frac{1}{n} \right)^{(N^++1)} \prod_{l=0}^{a-1} p_l^{\text{tot}} \cdot \\
&\quad \quad \sum_{t_a=0}^{N^+-a} \left( (n - p_a^{\text{tot}})^{t_a} \sum_{t_0=0}^{N^+-a-t_a} \left( \dots \sum_{t_{a-2}=0}^{N^+-a-\sum t_k-t_a} \left( \left( \prod_{l=0}^{a-2} (n - p_l^{\text{tot}})^{t_l} \right) \cdot (n - p_{a-1}^{\text{tot}})^{N^+-a-\sum t_k-t_a} \right) \dots \right) \right) \\
&= A + B + C
\end{aligned} \tag{A.27}$$

The three constituting sums  $A$ ,  $B$ , and  $C$  can be treated individually. Comparing  $A$  to Eq. (A.23), we find that  $A$  contains the expression for the expectation value  $\langle t \rangle_a$ ,

$$A = \frac{p_a^{\text{tot}}}{n} \langle t \rangle_a. \tag{A.28}$$

In order to treat part  $B$ , we introduce  $t'_a := t_a - 1$ . Then, some clever index shifting shows that  $B$  contains the expression for  $\langle t \rangle_a$  defined in Eq. (A.24)

$$\begin{aligned} B &= \sum_{N=a}^{\infty} N, \frac{\Delta t}{n} \left( \frac{1}{n} \right)^{(N+1)} \prod_{l=0}^a p_l^{\text{tot}}. \\ &\quad \sum_{t'_a=0}^{N-a-1} \left( (n - p_a^{\text{tot}})^{t'_a+1} \sum_{t_0=0}^{N-a-t'_a-1} \left( \dots \sum_{t_{a-2}=0}^{N-a-\sum t_k-t'_a-1} \left( \left( \prod_{l=0}^{a-2} (n - p_l^{\text{tot}})^{t_l} \right) \cdot (n - p_{a-1}^{\text{tot}})^{N-a-\sum t_k-t'_a-1} \right) \dots \right) \right) \\ &= \frac{(n - p_a^{\text{tot}})}{n} \sum_{N=a}^{\infty} N, \frac{\Delta t}{n} \left( \frac{1}{n} \right)^{(N)} \prod_{l=0}^a p_l. \\ &\quad \sum_{t'_a=0}^{N-a-1} \left( \sum_{t_0=0}^{N-a-1-t'_a} \left( \dots \sum_{t_{a-2}=0}^{N-a-1-\sum t_k-t'_a} \left( \left( \prod_{l=0}^{a-2} (n - p_l^{\text{tot}})^{t_l} \right) (n - p_a^{\text{tot}})^{t'_a} \cdot (n - p_{a-1}^{\text{tot}})^{N-a-1-\sum t_k-t'_a} \right) \dots \right) \right) \\ &= \frac{(n - p_a^{\text{tot}})}{n} \langle t \rangle_{a+1}. \end{aligned} \tag{A.29}$$

(A.30)

Finally, the time component  $\Delta t/n$  can be extracted out of the expression for  $C$ , leaving a fairly straightforward expression

$$\begin{aligned} C &= \sum_{N=a}^{\infty} \frac{\Delta t}{n} \left( \frac{1}{n} \right)^{(N+1)} \prod_{l=0}^a p_l^{\text{tot}} \cdot \sum_{t_0=0}^{N-a} \left( \dots \sum_{t_{a-1}=0}^{N-a-\sum t_k} \left( \left( \prod_{l=0}^{a-1} (n - p_l^{\text{tot}})^{t_l} \right) \cdot (n - p_a^{\text{tot}})^{N-a-1-\sum_{k=0}^{a-1} t_k} \right) \dots \right) \\ &= \sum_{N=a+1}^{\infty} \frac{\Delta t}{n} \left( \frac{1}{n} \right)^{(N)} \prod_{l=0}^a p_l^{\text{tot}} \cdot \sum_{t_0=0}^{N-a-1} \left( \dots \sum_{t_{a-1}=0}^{N-a-1-\sum t_k} \left( \left( \prod_{l=0}^{a-1} (n - p_l^{\text{tot}})^{t_l} \right) \cdot (n - p_a^{\text{tot}})^{N-a-1-\sum_{k=0}^a t_k} \right) \dots \right) \\ &= \sum_{N=a+1}^{\infty} \frac{\Delta t}{n} P_{a+1}(N) = \frac{\Delta t}{n}. \end{aligned} \tag{A.31}$$

This last step arises because the probability of the process  $a + 1$  occurring some time between the  $(a + 1)^{\text{rst}}$  time step and infinity is exactly 1 by

definition.

Thus adding up all elements of the sum gives us the transition from the mean time the system takes for  $a$  processes to the mean time the system takes for  $a + 1$  processes as

$$\begin{aligned}\langle t \rangle_{a+1} &= \frac{p_a^{\text{tot}}}{n} \langle t \rangle_a + \frac{(n - p_a^{\text{tot}})}{n} \langle t \rangle_{a+1} + \frac{\Delta t}{n} \\ \langle t \rangle_{a+1} \left(1 - \frac{n - p_a^{\text{tot}}}{n}\right) &= \langle t \rangle_{a+1} \left(\frac{p_a^{\text{tot}}}{n}\right) = \frac{p_a^{\text{tot}}}{n} \langle t \rangle_a + \Delta t \\ \rightarrow \langle t \rangle_{a+1} &= \langle t \rangle_a + \frac{\Delta t}{p_a^{\text{tot}}}\end{aligned}$$

This is the propagation of the system time that we proposed in Eq. (A.21). Thus, this section shows that the average time evolution of the two algorithms is identical,

$$\langle \tau \rangle_{a,KMC} = \sum_{l=0}^{a-1} \frac{1}{\sum_{i=0}^n r_{i,l}} \quad (\text{A.32})$$

$$\langle t \rangle_{a,RSM} = \sum_{l=0}^{a-1} \frac{1}{\sum_{i=0}^n r_{i,l}}. \quad (\text{A.33})$$

## Appendix B

# Algorithm details for C60 growth

In this appendix we discuss specifics of the algorithm used in the simulation for C60 multilayer growth. This is an extension of the list included in Sec. 5.3 and goes into more detail. Note, however, that I do not discuss all points listed in Sec. 5.3 in more detail here, as some are self-explanatory in the short illustration given. Instead, I will also mention some data structures and finer points on the implementation.

### B.1 Particle relaxation on a hexagonal lattice

On a hexagonal lattice, each site has 3 support sites, but in the (2+1)-dimensional model the particle is represented by an increase in height of one specific site  $s_1$  (see Sec. 5.2 for a brief discussion of (2+1)-dimensionality and the details of system requirements in order to implement (2+1)-dimensionality). A relaxation process can be introduced to avoid this relic asymmetry gained through the (2+1)-dimensionality of the modelling. In this relaxation process, each particle is required to have three filled support sites. If a particle does not fulfil this requirement, it is moved until all three support sites are filled. The particle chooses a site randomly according to the following approach: The particle relaxes in any of the possible 6 directions with a probability proportional to the rate of the corresponding diffusion process.

Figure B.1 depicts a sample process in which adsorbed particles relax.

### B.2 Periodic boundary conditions

A common assumption on the lattice are toroidal boundary conditions. This means that leaving the lattice at  $(x_{\max}, y)$  is equivalent to reentering at  $(0, y)$  and similar conditions hold for leaving at  $y_{\max}$ . As we consider surfaces, it does not make sense to implement periodic boundary conditions in  $z$ -direction for our simulation.

Assume each lattice points  $(x_1, y_1)$  is described by one integer number  $i = y_1 + x_1 \cdot y_{\max}$ . Then moving from point  $(x_1, y_1)$  by  $(\Delta x, \Delta y)$  can be achieved through

$$i_{\text{new}} = (i + \Delta y) \% y_{\max} + ((i / y_{\max} + \Delta x) \% x_{\max}) \cdot y_{\max}, \quad (\text{B.1})$$

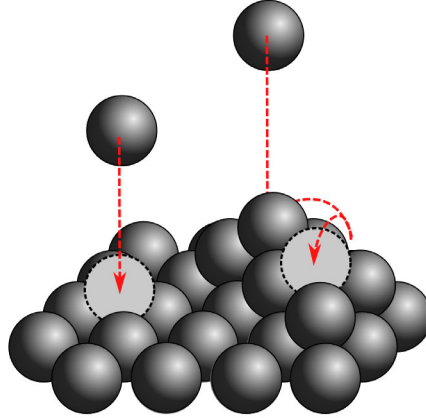


FIGURE B.1: Schematic of a relaxation process on a hexagonal lattice: the particle on the left adsorbs to a fully supported lattice site, while the particle on the right adsorbs to a not fully supported site and relaxes until it reaches a fully supported site.

where  $\%$  denotes a modulo operation and  $i/y_{\max}$  is rounded to the next smallest integer value, i.e.  $i/y_{\max} = \lfloor i/y_{\max} \rfloor$ .

Periodic boundary conditions can lead to self-interaction, therefore their influence has to be observed carefully.

### Cubic lattice

A cubic lattice is the easiest lattice to treat, as the data structures of the computer are cubic. Using  $i = y + x \cdot y_{\max}$  the neighbours of any site on the lattice can be determined using

$$n_{1,3} = (y \pm 1) \% y_{\max} + x \cdot y_{\max} \quad \text{and} \quad (\text{B.2})$$

$$n_{2,4} = y + (x \pm 1) \cdot y_{\max} \% (x_{\max} \cdot y_{\max}). \quad (\text{B.3})$$

$$(\text{B.4})$$

The cubic lattice is ideal for the application of a solid-on-solid model, but few crystal structures can be approximated to be cubic.

### Hexagonal lattice

The easiest way to simulate a hexagonal lattice is to project it onto a cubic lattice (see Fig. B.2 to see a projection schematic). This can be achieved by distorting the rhombic unit cell to be square. As a site on the hexagonal lattice has 6 rather than 4 in-plane neighbour sites, these have to be considered in the calculation.

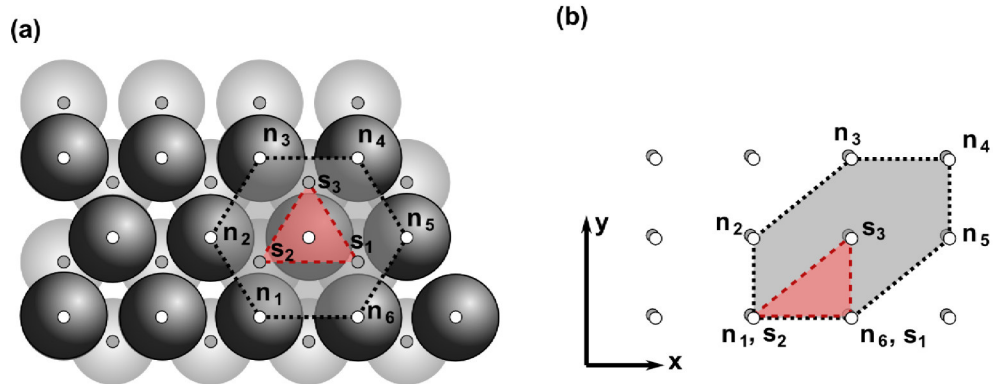


FIGURE B.2: Schematic of the projection of a hexagonal lattice onto a quadratic lattice. Part (a) depicts the real hexagonal surface in top view, while part (b) depicts the projection onto a quadratic lattice. The white dots represent the centres of the particles in the upper plane, the grey dots are particles in the support plane. In part (b), the projection of the white dots is depicted through black arrows, the projection of the grey dots through red arrows. The grey panel in parts (a) and (b) represent the local neighbourhood of the central particle in the respective representation, while the red triangle represents the three supporting sites.

$$n_{1,3} = (y \mp 1)\%y_{\max} + (x \mp 1) \cdot y_{\max} \% (x_{\max} \cdot y_{\max}), \quad (B.5)$$

$$n_{2,4} = y + (x \mp 1) \cdot y_{\max} \% (x_{\max} \cdot y_{\max}) \quad \text{and} \quad (B.6)$$

$$n_{3,6} = (y \pm 1) \% y_{\max} + x \cdot y_{\max}. \quad (B.7)$$

When simulating a solid-on-solid model on a hexagonal lattice it is especially important to consider the sites a particle sits on. On a hexagonal lattice each particle has 3 support sites, as depicted in Fig. B.2. Their coordinates can be determined as

$$s_1 = (y - 1) + x \cdot y_{\max}, \quad (B.8)$$

$$s_2 = (y - 1) \% y_{\max} + (x - 1) \cdot y_{\max} \% (x_{\max} \cdot y_{\max}) \quad \text{and} \quad (B.9)$$

$$s_3 = y + x \cdot y_{\max}, \quad (B.10)$$

### B.3 Binary tree data structures

We are using Ref. [325] as a basis for the data structure.

(Binary) Trees are data structures that can be used to reduce the cost of a simulation. They are usually binary, as a decision structure is intrinsically binary (yes/no). A binary tree structure contains a finite number of elements sorted into a branching structure such that each element can be found through a sequence of questions that have two distinct answers (e.g. ‘Is the element larger than x?’). Each of these questions needs to split the elements into two distinct subsets such that the sequence of answers leading to one specific element is unique and defines the element. Thus for a well-balanced tree the number of steps necessary is maximally equal to the number of bits needed to represent the cardinality of elements of the tree, i.e.  $\lceil \log_2 n \rceil$ , whereas badly constructed trees can need more steps.

The goal of this structure is to enable the algorithm to find elements in the tree without having to scan through all elements sequentially. Optimally, a tree structure allows a particular element in a system of size  $n$  to be found in  $\log_2 n$  steps (splitting the number of possible elements into two equal amounts of half the size with every step) rather than the  $\mathcal{O}(n)$  complexity that sequential scanning would have.

The binary tree structure that we use is an augmented version of a ‘order statistic tree’ (example shown in Fig. B.3, an algorithm for the normal order statistic tree can be found in Ref. [325]). This augmented order statistic tree is ideal as the KMC algorithm needs to be able to target one specific element quickly (see Sec. 2.5), but also requires the total number of processes of one process type at any time. One tree is implemented per process type. Then each leaf corresponds to a lattice site, and the information stored in each leaf is an integer-valued number of processes at that site. At non-leaf nodes, the value is the sum of its child nodes, until finally the root of the tree contains the overall number of processes of this type that are possible in the system. This structure makes the overall number of processes of a given type very easy to access. Finding the site that corresponds to a given process requires a  $\log_2 n$  step decision process through the tree: going from the root to the leaves, every branching point corresponds to the question ‘is my current value larger than the left path?’. If the answer is ‘yes’, then you subtract the value of the left path and ask the same question for the value that corresponds to the right path. If the answer is ‘no’, then you ask the same question for the value that corresponds to the left path. This process is repeated until you reach a leaf. Finally, updating the process tree simply corresponds to updating a leaf and then all sums on the path between leaf and root.

Here, it is worth noting that my specific algorithm does not navigate through the tree using pointers. Instead, the entire tree is written in one large array, where the root occupies the index 1. Then, the two children of a node at index  $n$  are given as  $(2n)$  and  $2n + 1$ . Correspondingly, instead of following pointers, moving one level closer to the root corresponds to dividing your current index by 2. This kind of structure resembles a variation of the ‘heap’ structure that is commonly used for priority queues [325].

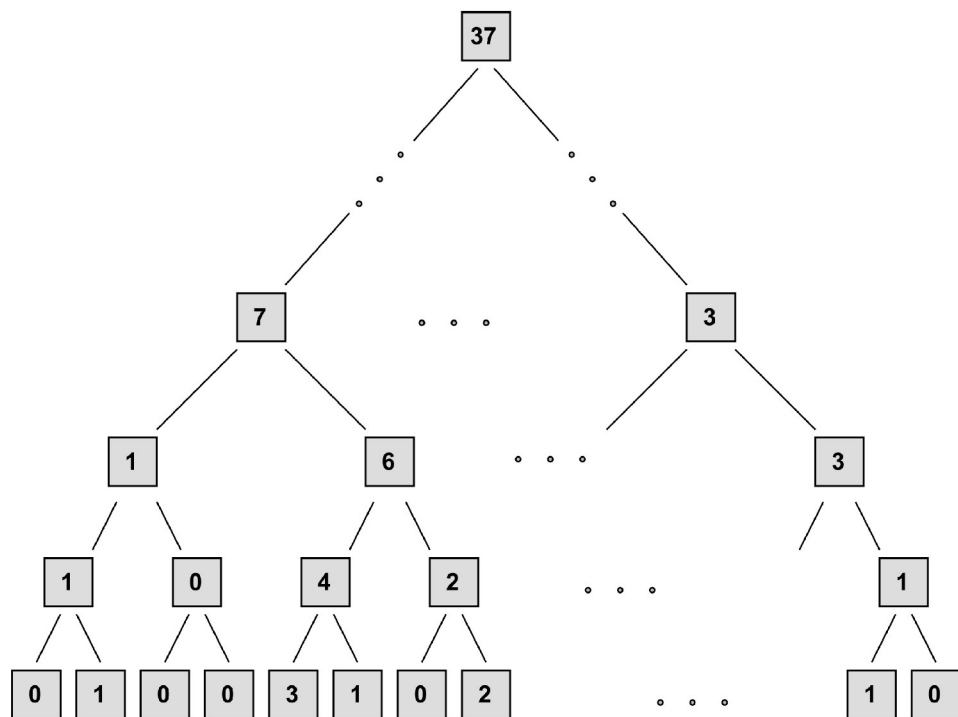


FIGURE B.3: Example for the augmented order statistic tree used in this lattice-based KMC simulation. The value of each node is the sum of its two children. This binary tree structure exploits the fact that the sum of all leaves is easily accessible and that the number of leaves is known at all times.

## Appendix C

# The Hoshen-Kopelman cluster algorithm

The Hoshen-Kopelman algorithm [220] is an efficient algorithm to find and determine clusters, where the user can define the conditions that particles have to fulfil to count as the same cluster. The algorithm is most easily expressed on a lattice, where most studies use the occupation of adjacent lattice sites as a condition for particles to belong to the same cluster. Particles that are further away, e.g. on sites diagonal to each other, may or may not be considered part of the same cluster, depending on the physical problem (see e.g. Ref. [326]). This task essentially resembles problems such as finding connected components in a graph. Note that the Hoshen-Kopelman algorithm can also be defined without a lattice, where clusters are then defined via particle-particle distance (see, e.g. Ref. [327]).

In order to introduce the basic principle of the algorithm, we illustrate the easiest case: a quadratic lattice, where two particles are part of the same cluster if they occupy adjacent sites. Figure C.1 (a) depicts our sample setup, where white squares mark particles and black squares mark the lack of particles. Starting at the top left corner (square a1), the algorithm iterates through each row from left to right, sequentially. Every occupied site is given an ID, or ‘coloured in’. If none of the neighbouring lattice sites has an ID assigned, then a new ID is created for the current site and a new element is added to the reference vector, containing this ID. However, if a neighbouring lattice site already has an ID, then the current site will take that ID. If more than one neighbouring site already has an ID, as depicted Fig. C.1 (b) for site d3, then the current site will take the smallest neighbour-ID. Furthermore, the reference vector will be altered, so all conflicting IDs point to the same, smallest ID, as illustrated through  $3 \rightarrow 1$  in the reference vector in Fig. C.1 (b).

After this first labelling iteration, every site has an ID and every ID is contained in the reference vector, illustrated in Fig. C.1 (c). Note that the algorithm takes the periodic boundary conditions into consideration, linking IDs 7 and 6 in the reference vector. A further feature that is implemented in this first iteration involves following references down to the root, as is illustrated for ID  $5 \rightarrow 3 \rightarrow 1$ . This makes relabelling in the second iteration faster. If desired, a rewriting of the reference vector after the first pass can be used to assign minimal IDs to the clusters, i.e. the IDs 1, 2, 3, and 4 in this example. Figure C.1 does not include this step.

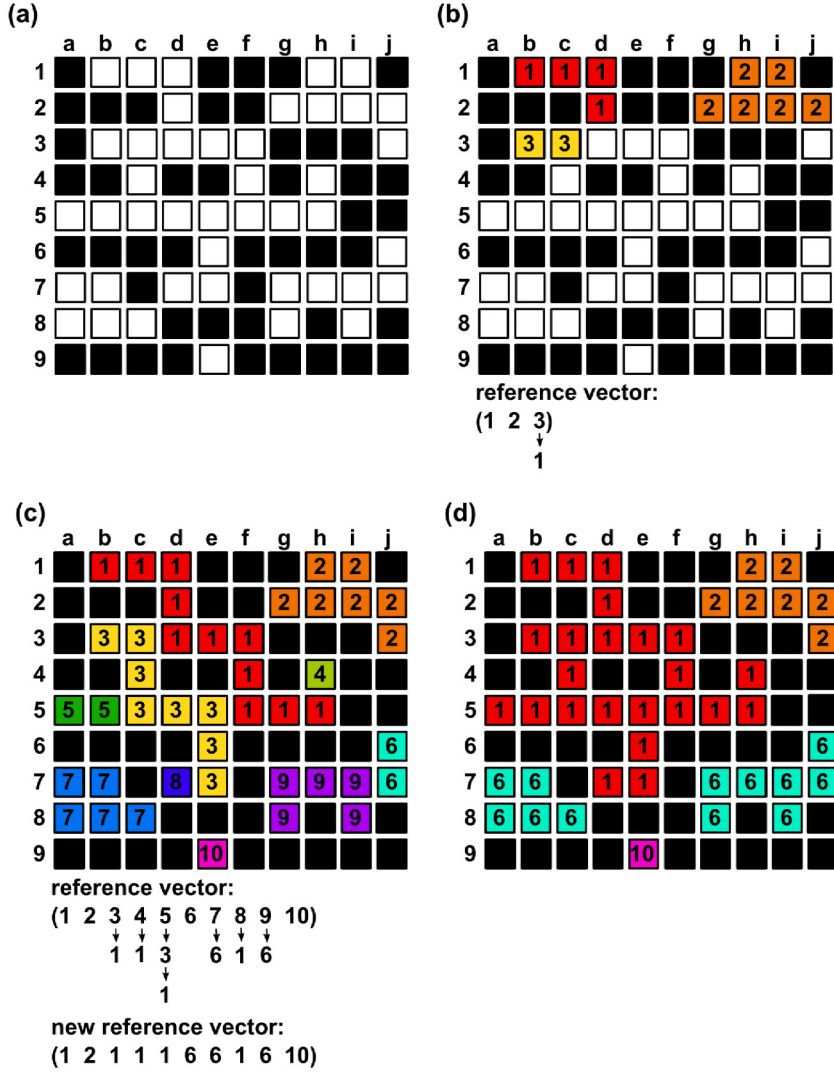


FIGURE C.1: Visualisation of steps of the Hoshen-Kopelman cluster algorithm on a square lattice with periodic boundary conditions. Part (a) depicts the current configuration, where white squares represent occupied sites. The cluster algorithm iterates through the system twice, once establishing labels and a reference vector (visualised through parts (b) and (c)), and once to follow the reference vector to assign the correct labels, visualised in part (d).

The result of the second iteration is depicted in Fig. C.1 (d): all sites are relabelled according to the list of linked IDs created in the reference list. In this final configuration, every site with the same ID is considered part of the same cluster, different IDs identify different clusters.

## Appendix D

# Multipole expansion up to the hexadecapole moment

In this appendix, we consider the multipole expansion of a general charge distribution in Cartesian coordinates. The derivation is textbook physics [283] (though most textbooks do not include the hexadecapole moment). We derive the multipoles here for completeness of the thesis and consistency in the definitions used (especially concerning constant pre-factors).

### D.1 Continuous charge distribution

To gain traceless expressions for the multipoles we expand the potential that a charge distribution  $\rho(r')$  causes at distance  $r$  for  $r' \ll r$

$$\Phi(r) = \frac{1}{4\pi\epsilon_0} \int \frac{\rho(r')}{|r - r'|} d^3r', \quad (\text{D.1})$$

by expanding  $\frac{1}{|r - r'|}$  for small  $r'$ :

$$\begin{aligned} \frac{1}{|r - r'|} &= \frac{1}{r} + \sum_{\alpha} \frac{\partial}{\partial r_{\alpha}} \frac{1}{|r - r'|} \Big|_{r' = 0} (-r_{\alpha}') \\ &\quad + \frac{1}{2} \sum_{\alpha\beta} \frac{\partial^2}{\partial r_{\alpha}' \partial r_{\beta}'} \frac{1}{|r - r'|} \Big|_{r' = 0} (r_{\alpha}' r_{\beta}') \\ &\quad + \frac{1}{6} \sum_{\alpha\beta\gamma} \frac{\partial^3}{\partial r_{\alpha}' \partial r_{\beta}' \partial r_{\gamma}'} \frac{1}{|r - r'|} \Big|_{r' = 0} (-r_{\alpha}' r_{\beta}' r_{\gamma}') \\ &\quad + \frac{1}{24} \sum_{\alpha\beta\gamma\eta} \frac{\partial^4}{\partial r_{\alpha}' \partial r_{\beta}' \partial r_{\gamma}' \partial r_{\eta}'} \frac{1}{|r - r'|} \Big|_{r' = 0} (-r_{\alpha}' r_{\beta}' r_{\gamma}' r_{\eta}') \\ &\quad + \dots \end{aligned} \tag{D.2}$$

$$\begin{aligned} &= \frac{1}{r} + \sum_{\alpha} \frac{r_{\alpha}}{|r|^3} (r_{\alpha}') \\ &\quad + \frac{1}{2} \sum_{\alpha\beta} \frac{3r_{\alpha}r_{\beta} - \delta_{\alpha\beta}r^2}{|r|^5} (r_{\alpha}' r_{\beta}') \\ &\quad + \frac{1}{2} \sum_{\alpha\beta\gamma} \frac{5r_{\alpha}r_{\beta}r_{\gamma} - r^2(r_{\alpha}\delta_{\beta\gamma} + r_{\beta}\delta_{\alpha\gamma} + r_{\gamma}\delta_{\alpha\beta})}{|r|^7} (r_{\alpha}' r_{\beta}' r_{\gamma}') \\ &\quad + \frac{1}{8} \sum_{\alpha\beta\gamma\eta} \left[ \frac{35r_{\alpha}r_{\beta}r_{\gamma}r_{\eta}}{|r|^9} \right. \\ &\quad \left. - \frac{5r^2(r_{\alpha}r_{\beta}\delta_{\gamma\eta} + r_{\alpha}r_{\gamma}\delta_{\beta\eta} + r_{\alpha}r_{\eta}\delta_{\beta\gamma} + r_{\beta}r_{\gamma}\delta_{\alpha\eta} + r_{\beta}r_{\eta}\delta_{\alpha\gamma} + r_{\gamma}r_{\eta}\delta_{\alpha\beta})}{|r|^9} \right. \\ &\quad \left. + \frac{r^4(\delta_{\alpha\beta}\delta_{\gamma\eta} + \delta_{\alpha\gamma}\delta_{\beta\eta} + \delta_{\alpha\eta}\delta_{\beta\gamma})}{|r|^9} \right] (r_{\alpha}' r_{\beta}' r_{\gamma}' r_{\eta}') \\ &\quad + \dots \end{aligned} \tag{D.3}$$

With this expansion we can rephrase the potential in terms of the traceless moments of the charge distribution, using

$$\sum_{\alpha\beta} \frac{3r_{\alpha}r_{\beta} - \delta_{\alpha\beta}r^2}{|r|^5} (r_{\alpha}' r_{\beta}') = \sum_{\alpha\beta} \frac{3r_{\alpha}r_{\beta}r_{\alpha}'r_{\beta}'}{|r|^5} - \frac{r^2r'^2}{|r|^5} = \sum_{\alpha\beta} (r_{\alpha}r_{\beta}) \frac{3r_{\alpha}'r_{\beta}' - \delta_{\alpha\beta}r'^2}{|r|^5}. \tag{D.4}$$

The potential then takes the form

$$\begin{aligned} \Phi(r) &= \frac{1}{4\pi\epsilon_0} \left[ \frac{q}{r} + \sum_{\alpha} \frac{p_{\alpha}r_{\alpha}}{r^3} + \sum_{\alpha\beta} \frac{r_{\alpha}r_{\beta}}{r^5} Q_{\alpha\beta} + \sum_{\alpha\beta\gamma} \frac{r_{\alpha}r_{\beta}r_{\gamma}}{r^7} O_{\alpha\beta\gamma} \right. \\ &\quad \left. + \sum_{\alpha\beta\gamma\eta} \frac{r_{\alpha}r_{\beta}r_{\gamma}r_{\eta}}{r^9} H_{\alpha\beta\gamma\eta} + \dots \right], \end{aligned} \tag{D.5}$$

with following definitions of the normalised traceless multipole moments

$$q = \int \rho(r) d^3r \quad (\text{D.6})$$

$$p_\alpha = \int \rho(r) r_\alpha d^3r \quad (\text{D.7})$$

$$Q_{\alpha\beta} = \frac{1}{2} \int \rho(r) \left[ 3r_\alpha r_\beta - \delta_{\alpha\beta} r^2 \right] d^3r \quad (\text{D.8})$$

$$O_{\alpha\beta\gamma} = \frac{1}{2} \int \rho(r) \left[ 5r_\alpha r_\beta r_\gamma - r^2 (r_\alpha \delta_{\beta\gamma} + r_\beta \delta_{\alpha\gamma} + r_\gamma \delta_{\alpha\beta}) \right] d^3r \quad (\text{D.9})$$

$$\begin{aligned} H_{\alpha\beta\gamma\eta} = & \frac{1}{8} \int \rho(r) \left[ 35r_\alpha r_\beta r_\gamma r_\eta \right. \\ & - 5r^2 (r_\alpha r_\beta \delta_{\gamma\eta} + r_\alpha r_\gamma \delta_{\beta\eta} + r_\alpha r_\eta \delta_{\beta\gamma} + r_\beta r_\gamma \delta_{\alpha\eta} + r_\beta r_\eta \delta_{\alpha\gamma} + r_\gamma r_\eta \delta_{\alpha\beta}) \\ & \left. + r^4 (\delta_{\alpha\beta} \delta_{\gamma\eta} + \delta_{\alpha\gamma} \delta_{\beta\eta} + \delta_{\alpha\eta} \delta_{\beta\gamma}) \right] d^3r. \end{aligned} \quad (\text{D.10})$$

I have chosen to include all pre-factors of the expansion into the definition of the moments, other authors may define these differently.

Considering a charge distribution the next question of interest concerns the interaction of this charge distribution with an arbitrary external field. In other words we are interested in the energy of a charge distribution in an external field if this charge distribution is phrased in terms of its multipole moments.

The energy of a charge distribution  $\rho(r)$  at position  $r$  in the external potential  $\Phi^{ext}(r)$  is determined as

$$U = \int \rho(r) \Phi^{ext}(r) d^3r. \quad (\text{D.11})$$

Expanding the external potential around the origin  $r = 0$  gives us an expression of the energy which contains multipole moments  $M$ ,  $M_\alpha$ ,  $M_{\alpha\beta}$ ,  $M_{\alpha\beta\gamma}$  and  $M_{\alpha\beta\gamma\eta}$ , which are the unnormalised and traced:

$$\begin{aligned} U = & \int \rho(r) \Phi^{ext}(0) d^3r + \sum_\alpha \int \rho(r) \left( \frac{\partial}{\partial r_\alpha} \Phi^{ext}(r) \Big|_{r=0} \right) r_\alpha d^3r \\ & + \frac{1}{2} \sum_{\alpha\beta} \int \rho(r) \left( \frac{\partial^2}{\partial r_\alpha \partial r_\beta} \Phi^{ext}(r) \Big|_{r=0} \right) r_\alpha r_\beta d^3r \\ & + \frac{1}{6} \sum_{\alpha\beta\gamma} \int \rho(r) \left( \frac{\partial^3}{\partial r_\alpha \partial r_\beta \partial r_\gamma} \Phi^{ext}(r) \Big|_{r=0} \right) r_\alpha r_\beta r_\gamma d^3r \\ & + \frac{1}{24} \sum_{\alpha\beta\gamma\eta} \int \rho(r) \left( \frac{\partial^4}{\partial r_\alpha \partial r_\beta \partial r_\gamma \partial r_\eta} \Phi^{ext}(r) \Big|_{r=0} \right) r_\alpha r_\beta r_\gamma r_\eta d^3r + \dots \end{aligned} \quad (\text{D.12})$$

$$\begin{aligned} = & M \Phi^{ext} + M_\alpha \frac{\partial}{\partial r_\alpha} \Phi^{ext} + \frac{1}{2} M_{\alpha\beta} \frac{\partial^2}{\partial r_\alpha \partial r_\beta} \Phi^{ext} + \frac{1}{6} M_{\alpha\beta\gamma} \frac{\partial^3}{\partial r_\alpha \partial r_\beta \partial r_\gamma} \Phi^{ext} \\ & + \frac{1}{24} M_{\alpha\beta\gamma\eta} \frac{\partial^4}{\partial r_\alpha \partial r_\beta \partial r_\gamma \partial r_\eta} \Phi^{ext} + \dots \end{aligned} \quad (\text{D.13})$$

This energy may depend on the choice of origin, conventionally the origin is chosen at the position of the centre of the charge distribution.

The traced unnormalised multipoles can be expressed in terms of the normalised traceless multipole by exploiting the Laplace equation

$$\frac{\partial^2}{\partial r_\alpha \partial r_\alpha} \Phi^{ext} = -\frac{\partial}{\partial r_\alpha} \tilde{E}_\alpha = 0 \quad (\text{D.14})$$

and the fact that derivatives are interchangeable, e.g.

$$\frac{\partial^3}{\partial r_\alpha \partial r_\beta \partial r_\alpha} \Phi^{ext} = \frac{\partial^3}{\partial r_\beta \partial r_\alpha \partial r_\alpha} \Phi^{ext} = \frac{\partial}{\partial r_\beta} \left( \frac{\partial^2}{\partial r_\alpha \partial r_\alpha} \Phi^{ext} \right) = 0. \quad (\text{D.15})$$

Then we gain the following correlations

$$q\Phi^{ext} = M\Phi^{ext} \quad (\text{D.16})$$

$$p_\alpha \frac{\partial}{\partial r_\alpha} \Phi^{ext} = M_\alpha \frac{\partial}{\partial r_\alpha} \Phi^{ext} \quad (\text{D.17})$$

$$Q_{\alpha\beta} \frac{\partial^2}{\partial r_\alpha \partial r_\beta} \Phi^{ext} = \frac{3}{2} M_{\alpha\beta} \frac{\partial^2}{\partial r_\alpha \partial r_\beta} \Phi^{ext} \quad (\text{D.18})$$

$$O_{\alpha\beta\gamma} \frac{\partial^3}{\partial r_\alpha \partial r_\beta \partial r_\gamma} \Phi^{ext} = \frac{5}{2} M_{\alpha\beta\gamma} \frac{\partial^3}{\partial r_\alpha \partial r_\beta \partial r_\gamma} \Phi^{ext} \quad (\text{D.19})$$

$$H_{\alpha\beta\gamma\eta} \frac{\partial^4}{\partial r_\alpha \partial r_\beta \partial r_\gamma \partial r_\eta} \Phi^{ext} = \frac{35}{8} M_{\alpha\beta\gamma\eta} \frac{\partial^4}{\partial r_\alpha \partial r_\beta \partial r_\gamma \partial r_\eta} \Phi^{ext}, \quad (\text{D.20})$$

which in turn let us express the energy of a charge distribution in an external potential as

$$\begin{aligned} U = & q\Phi^{ext} + p_\alpha \frac{\partial}{\partial r_\alpha} \Phi^{ext} + \frac{1}{3} Q_{\alpha\beta} \frac{\partial^2}{\partial r_\alpha \partial r_\beta} \Phi^{ext} + \frac{1}{15} O_{\alpha\beta\gamma} \frac{\partial^3}{\partial r_\alpha \partial r_\beta \partial r_\gamma} \Phi^{ext} \\ & + \frac{1}{105} H_{\alpha\beta\gamma\eta} \frac{\partial^4}{\partial r_\alpha \partial r_\beta \partial r_\gamma \partial r_\eta} \Phi^{ext} + \dots \end{aligned} \quad (\text{D.21})$$

Note that, while the interaction of two charge distributions scales strongly with their distance to each other, the interaction of a single charge distribution with an external potential only depends on the behaviour of the potential at the position of the charge. Thus the multipole expansion of two interacting charge distributions can be truncated after very few expansion terms, as the energy contribution of higher order terms decreases increasingly strongly with the distance. However, when considering the interaction of a charge distribution with an external potential, the higher order terms are likely to constitute significant contributions to the the energy sum and cannot be neglected.

The individual contributions from the multipole moments are

$$U_p(\mathbf{r}) = - \sum_{\alpha} p_{\alpha} \tilde{E}_{\alpha}(\mathbf{r}), \quad (\text{D.22})$$

$$U_Q(\mathbf{r}) = - \frac{1}{3} \sum_{\alpha, \beta} Q_{\alpha\beta} \frac{\partial \tilde{E}_{\alpha}}{\partial x_{\beta}}(\mathbf{r}), \quad (\text{D.23})$$

$$U_O(\mathbf{r}) = - \frac{1}{15} \sum_{\alpha, \beta, \gamma} O_{\alpha\beta\gamma} \frac{\partial^2 \tilde{E}_{\alpha}}{\partial x_{\beta} \partial x_{\gamma}}(\mathbf{r}), \quad (\text{D.24})$$

$$U_H(\mathbf{r}) = - \frac{1}{105} \sum_{\alpha, \beta, \gamma, \eta} H_{\alpha\beta\gamma\eta} \frac{\partial^3 \tilde{E}_{\alpha}}{\partial x_{\beta} \partial x_{\gamma} \partial x_{\eta}}(\mathbf{r}), \quad (\text{D.25})$$

where  $\tilde{E}_{\alpha} = -\frac{\partial}{\partial r_{\alpha}} \Phi^{ext}$  is the electric field generated by the external potential  $\Phi^{ext}$ .

## D.2 Discrete charge distribution

In molecules, the atoms can be associated with point partial charges. Then the multipole moments require a sum over partial charges  $q_l$  instead of an integral over charge distributions. Then the multipole moments take the form

$$q = \sum_{l=1}^M q_l, \quad (\text{D.26})$$

$$p_{\alpha} = \sum_l q_l r_{l\alpha}, \quad (\text{D.27})$$

$$Q_{\alpha\beta} = \sum_l \frac{1}{2} q_l (3r_{l\alpha} r_{l\beta} - r_l^2 \delta_{\alpha\beta}), \quad (\text{D.28})$$

$$O_{\alpha\beta\gamma} = \sum_l \frac{1}{2} q_l (5r_{l\alpha} r_{l\beta} r_{l\gamma} - r_{l\alpha} r_l^2 \delta_{\beta\gamma} - r_{l\beta} r_l^2 \delta_{\alpha\gamma} - r_{l\gamma} r_l^2 \delta_{\alpha\beta}), \quad (\text{D.29})$$

$$\begin{aligned} H_{\alpha\beta\gamma\eta} = & \sum_l \frac{1}{8} q_l (35r_{l\alpha} r_{l\beta} r_{l\gamma} r_{l\eta} - 5r_{l\alpha} r_{l\beta} r_l^2 \delta_{\gamma\eta} \\ & - 5r_{l\beta} r_{l\gamma} r_l^2 \delta_{\alpha\eta} - 5r_{l\gamma} r_{l\alpha} r_l^2 \delta_{\beta\eta} \\ & - 5r_{l\alpha} r_{l\eta} r_l^2 \delta_{\beta\gamma} - 5r_{l\beta} r_{l\eta} r_l^2 \delta_{\alpha\gamma} \\ & - 5r_{l\gamma} r_{l\eta} r_l^2 \delta_{\alpha\beta} + \delta_{\alpha\beta} \delta_{\gamma\eta} + \delta_{\alpha\gamma} \delta_{\beta\eta} + \delta_{\alpha\eta} \delta_{\beta\gamma}). \end{aligned} \quad (\text{D.30})$$

In Eqs. (D.26)–(D.30) the sums run over all partial charges  $l = 1, \dots, M$  in the molecule. The indices  $\alpha, \beta, \gamma, \eta \in \{x, y, z\}$  denote the elements in Cartesian coordinates, i.e.  $r_{l\alpha}$  denotes component  $\alpha$  of the vector  $\mathbf{r}_l$ , which has the length  $r_l = |\mathbf{r}_l|$ .

## Appendix E

### Multipole moments of 6P

In this appendix we provide numerical values for the multipole moments defined in Eqs. (D.26)–(D.30), see Table E.1.

	planar	twisted	della Sala <i>et al.</i>
$q$ [e]	0.004	0	-
$p_x, p_y, p_z$ [e nm]	0.003, 0, 0	-0.0002, 0, 0	-
$Q_{xx}, Q_{yy}, Q_{zz}$ [e nm <sup>2</sup> ]	0.015, 0.011, -0.026	0.032, 0.039, -0.071	0.015, 0.013, -0.028
$O_{xxx}, O_{xxy}, O_{xxz}$ [e nm <sup>3</sup> ]	0.028, 0, 0	-0.0005, 0.0007, 0	-
$O_{yyx}, O_{yyy}, O_{yyz}$ [e nm <sup>3</sup> ]	0.007, 0, 0	0.0003, -0.0006, 0	-
$O_{zzx}, O_{zzy}, O_{zzz}$ [e nm <sup>3</sup> ]	-0.035, 0, 0	0.0002, -0.0001, 0	-
$H_{xxxx}, H_{yyyy}, H_{zzzz}$ [e nm <sup>4</sup> ]	0.432, -0.087, 0.024	1.119, -0.242, 0	-
$H_{xxyy}, H_{xxzz}, H_{yyzz}$ [e nm <sup>4</sup> ]	0.037, -0.060, -0.053	0.098, -0.171, -0.182	-
$H_{yyxx}, H_{zzxx}, H_{zzyy}$ [e nm <sup>4</sup> ]	0.069, 0, -0.015	0.186, 0, -0.045	-
$H_{xxxy}, H_{xxxz}, H_{yyyx}$ [e nm <sup>4</sup> ]	0, 0, 0	-0.061, 0, -0.053	-
$H_{yyyz}, H_{zzzx}, H_{zzzy}$ [e nm <sup>4</sup> ]	0, 0, 0	0, 0, 0	-

TABLE E.1: Multipole moments related to different atomistic configurations of a 6P molecule. Specifically, the table includes values for the monopole  $q$ , dipole  $p_\alpha$ , quadrupole  $Q_{\alpha\beta}$ , octupole  $O_{\alpha\beta\gamma}$  and hexadecapole moment  $H_{\alpha\beta\gamma\delta}$  for a planar and a twisted molecular configuration. Included are results from the DFT study of della Sala *et al.* [100]. The corresponding values  $Q_{\alpha\beta}$  follow from the values  $M_{\alpha\beta}$  given in [100] by using the relation [188]  $Q_{\alpha\beta} = (M_{\alpha\beta} - 1/3 \sum_\alpha M_{\alpha\alpha})/2$ . All multipole moments are listed in their eigensystem (which eliminates many elements). Also note the following symmetries:  $O_{\alpha\alpha\beta} = O_{\alpha\beta\alpha} = O_{\beta\alpha\alpha}$ ,  $H_{\alpha\alpha\beta\beta} = H_{\alpha\beta\alpha\beta} = H_{\beta\alpha\alpha\beta}$  and  $H_{\alpha\alpha\alpha\beta} = H_{\alpha\alpha\beta\alpha} = H_{\beta\alpha\alpha\alpha} = H_{\beta\alpha\alpha\alpha}$ .

## Appendix F

# Quadrupole-field interaction for 6P on ZnO(10-10)

In this appendix, we treat the interaction of a linear quadrupole with the electric substrate field of ZnO(10-10), given in Eq. (10.16) to gain some insight into the alignment of 6P molecules in the electric field. As the field has no  $x$ -dependency, the interaction energy does not depend on the  $x$ -coordinate of the quadrupole. In addition the  $z$ -dependency of the energy is given through the exponential prefactor  $\exp(-kz)$ , which results in a maximal energy for minimal  $z$  with the restraint that  $z \geq 0$ , since molecules can only occupy the space above the substrate. As additional factors determine the  $z$ -coordinate of the molecule, we determine it using a Lennard-Jones like molecule-substrate interaction that is discussed in detail in Sec. 10.4.1. Therefore, we the interaction energy as a function of three variables: the  $y$ -position, as well as the azimuth  $\Phi$  and the tilt  $\Theta$  of the quadrupole,

$$\tilde{E}(x, y, z, \Phi, \Theta)|_{z=0} = \tilde{E}(y, \Phi, \Theta)|_{z=0}. \quad (\text{F.1})$$

The new Euler angles  $\Phi$  and  $\Theta$  are introduced to aid intuition. In our simulation the direction of each quadrupole moment is determined through the three Euler angles  $\varphi$ ,  $\vartheta$  and  $\alpha$ , however two angles are easier to understand.

We here discuss the interaction of the fictitious quadrupole moment given in Eq. (10.20) with the field  $\tilde{E}(y, \Phi, \Theta)|_{z=0}$ . This quadrupole moment corresponds to two positive charges  $+q$  and a larger negative charge  $-2q$  aligned in an alternating fashion, i.e.  $+q, -2q, +q$  in a line. The angles  $\Phi$  and  $\Theta$  are chosen such, that the quadrupole lies aligned with the  $y$ -axis for  $\Phi = 0$  and  $\Theta = 0$ .

The interaction energy, which is determined corresponding to the definition given in Eq. (10.17), is expressed in terms of arbitrary units (a.u.), as we are here solely interested in the qualitative behaviour. The parametrisation of the interaction energy used in our simulations is discussed in Sec. 10.4.3.

First, we set  $\Theta = 0$  and vary  $\Phi$  and  $y$  in Fig. F.1 (a). Here, the energetic minimum arises for  $\Phi = 0$  and  $y = 3a/4 = 0.389$  nm, where  $a$  is the lattice constant in  $y$ -direction. This position corresponds to a quadrupole moment that lies within the ( $x$ - $y$ )-plane, perpendicular to the charge lines (i.e. along the  $y$ -direction) and directly above the positive charge line. Here, the

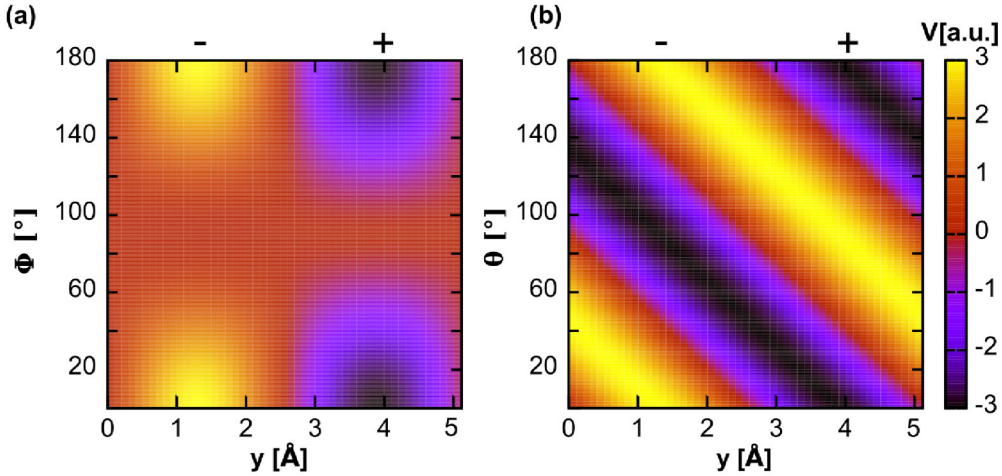


FIGURE F.1: The energy of a linear quadrupole on the surface charge field of ZnO, plotted in arbitrary units. Here  $\theta_r = 0$ , i.e. the molecule lies flat on the surface and is rotated around the z-axis by  $\phi_r$  as well as moved along the y-axis.

energy is maximised because the  $-2q$  charge lies directly above the positive charge line, while the  $+q$ -charges lie towards the negative charge lines of the substrate.

If  $\Phi = 90^\circ$ , the quadrupole is aligned with the  $x$ -direction, where the field is not structured and the attraction of the  $-2q$  charge exactly cancels out the repulsion of the two  $+q$  charges no matter where the quadrupole lies with respect to the charge lines. However, if the quadrupole lies aligned with the  $y$ -direction (i.e.  $\Phi = 0$ ) and lies above the negative charge lines (i.e.  $y = 1a/4 = 0.130\text{ nm}$ ), then the repulsion strongly out-wins each attraction.

The position above the negative charge lines only becomes attractive for a quadrupole aligned with the  $z$ -axis (i.e.  $\Theta = 90^\circ$ ), as can be seen in Fig. F.1 (b). Here, it becomes apparent that the intrinsic rotational symmetry of the field [see Eq. (10.16)] means that every  $y$ -position is equally attractive, if  $\Theta$  can be varied freely. However, for a molecule that sits above the positive charge lines (i.e.  $y = 3a/4 = 0.389\text{ nm}$ ), the quadrupole-field interaction clearly is maximised for a configuration in which the quadrupole is aligned with the  $y$ -direction (see Fig. F.2).

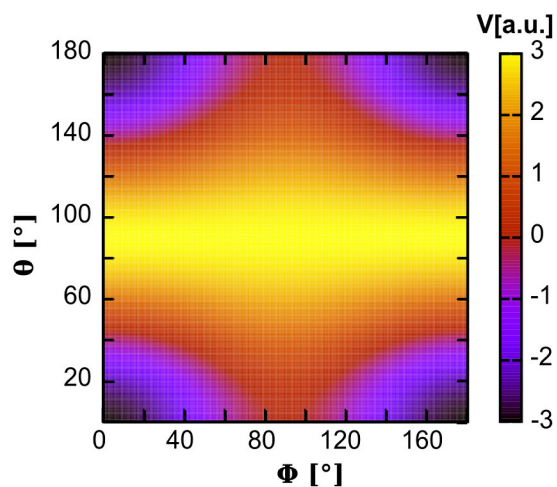


FIGURE F.2: The energy of a linear quadrupole on the surface charge field of ZnO, plotted in arbitrary units. Here  $y = 3a/4$ , i.e. the molecule lies directly above the positive surface charge of the system.

## Appendix G

# Non-monotonous growth behaviour

During growth, the limit for vanishingly low adsorption rates is expected to reproduce equilibrium results (see Secs. 2.1–2.3 for details on how DMC simulations are constructed in order to reproduce equilibrium results for vanishing adsorption rates). In general, systems are assumed to approach equilibrium in a monotonous fashion, i.e. in a fashion that results in every observable approaching equilibrium as a monotonous function of the adsorption rate. However, non-monotonous behaviour has been reported in literature [123, 305].

Based on our observation of non-monotonous orientational behaviour during 6P growth (see Secs. 12.2.2 and 12.2.3), the question of the minimal requirements for non-monotonous growth arises. Note that this appendix is not a complete study, but introduces notions and concepts for further discussion.

### G.1 Experimental indicators for non-monotonous behaviour

Experimentally, we find indicators for non-monotonous behaviour for C<sub>60</sub> molecules studied in part II of the thesis, though we don't directly observe the non-monotony. The C<sub>60</sub> molecules grow in a layer-by-layer fashion for the studied adsorption rates (see Chap. 7). During layer-by-layer growth, the roughness saturates and oscillates around its saturation point (see Fig. 7.9), while the roughness of a randomly deposited structure that would arise for extremely rapid deposition increases [111, 328]. However, this layer-by-layer structure is also smoother than the dewetted structure found after relaxation of the system (see Sec. 5.2). Correspondingly, the roughness of C<sub>60</sub> growth must have a minimum at some adsorption rate, yielding a roughness that is non-monotonous as a function of the adsorption rate.

The random deposition configuration is very unstable, as C<sub>60</sub> are quite mobile. The layer-by-layer configuration is obviously not stable, as the deposited films dewet for any film thinner than several tens of monolayers [119]. However, it appears that the layer-by-layer configuration is more stable than the random deposition configuration. Furthermore, the layer-by-layer configuration appears to be easier to reach through random deposition than a dewetted configuration. The layer-by-layer configuration is reasonably stable, so the deposition at a suitable rate keeps the system in layer-by-layer growth and does not allow the system to relax into the dewetted configuration. Hence, a layer-by-layer configuration may be associated with local

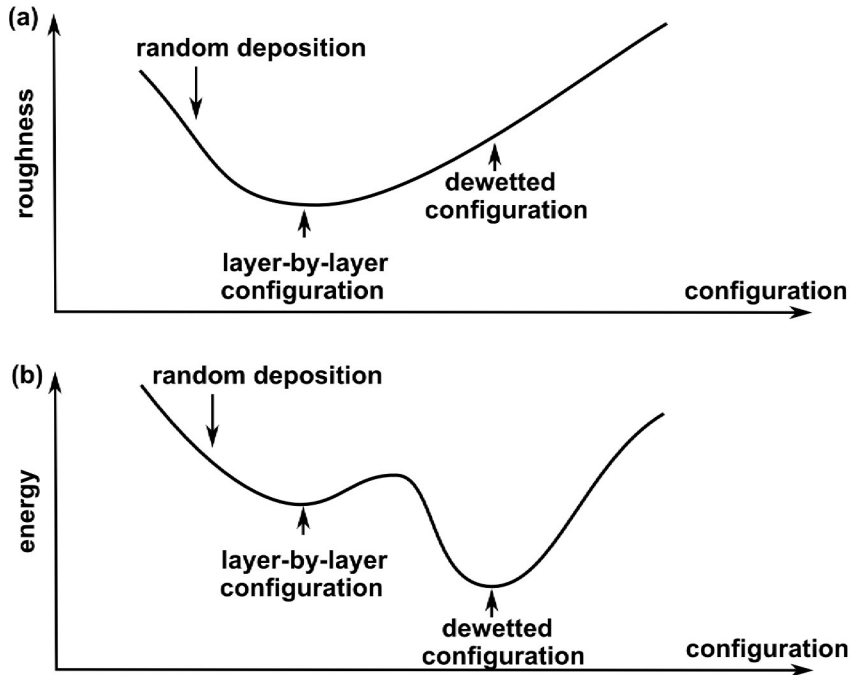


FIGURE G.1: Sketched proposal to explain the non-monotonous roughness expected for C<sub>60</sub> growth on mica. Part (a) depicts a sketch of the roughness for different configurations, while part (b) depicts a proposed energy landscape. The three configurations correspond to the experimental observations/expectations for different adsorption rates: for very high adsorption rates, a random deposition configuration is expected because molecules do not have the time to move. For intermediate adsorption rates, experiments find a layer-by-layer configuration with a low roughness (see Sec. 5.2) and finally, in a relaxed configuration that probably corresponds to equilibrium, the experiments find a rough dewetted configuration (also discussed in Sec. 5.2). We propose that the dewetted configuration corresponds to the global energetic minimum, while layer-by-layer configurations correspond to local energetic minima.

energetic minimum in the configurational potential landscape, as sketched in Fig. G.1 (b). If the random deposition occurs rapidly enough, the system is pushed far enough from the global energetic minimum that it keeps moving into the local energetic minimum instead of the global minimum.

Correspondingly, the features that make non-monotonous behaviour possible here are: adsorption conditions with a high roughness, a local energetic minimum with small roughness that needs to be traversed in order to go from the rough adsorption to the global energetic minimum, and finally a global energetic minimum with high roughness.

## G.2 Simulations indicating a non-monotonous island density

Following this notion of a semi-stable configuration that serves as a intermediate between the adsorption configuration and the global energetic minimum, we developed a minimal approach to simulate non-monotonous behaviour.

The observable chosen in this minimal model is the island density at a surface coverage of 10%, as presented in Fig. G.2. Note that the results presented here are preliminary results

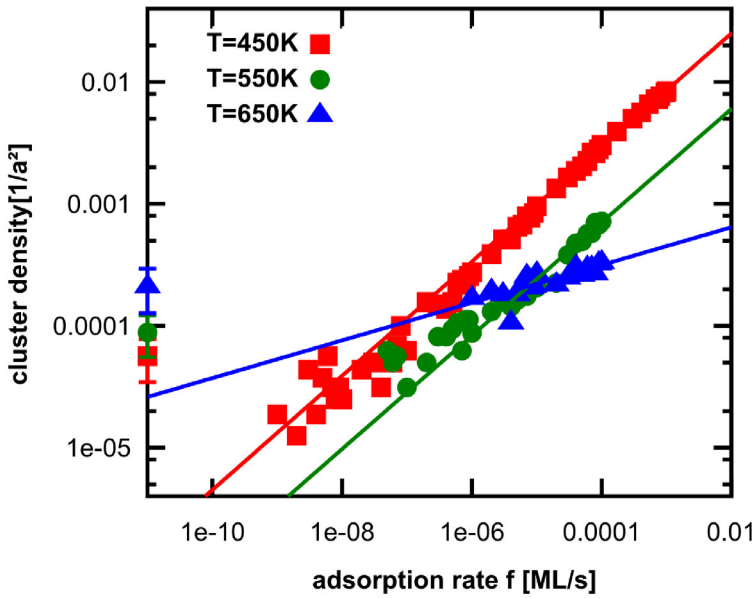


FIGURE G.2: Island densities as a function of coverage for GaAs (using  $E_D = 1.25$  eV,  $E_n = 0.35$  eV and  $E_S = -0.1$  eV). The data points with error bars on the y-axis indicate the equilibrium results, while the data in the graph was obtained during growth. The solid lines are guides for the eye, obtained by fitting a power-law dependency to the measured data points. Growth simulations were performed for 400x400 lattice sites, equilibrium simulations for 200x200 sites. The error bars for the equilibrium simulations are the standard deviation of the data obtained from 15 independent runs per data point. All data in this graph was obtained and evaluated in the scope of a project with the graduate students S. Dietrich, B. Hartung and M. Placke from the TU Berlin.

obtained in a short student project with the graduate students S. Dietrich, B. Hartung and M. Placke from the TU Berlin<sup>1</sup> under my guidance.

The island density is obtained from a DMC simulation on a simple-cubic, based on the GaAs simulations of Jones *et al.*[138]. Instead of using pre-structured GaAs, the growth simulations are performed on an initially blank substrate, where particles were adsorbed at a given rate until 10% coverage was reached. The equilibrium results are obtained from simulations initiated with 10% coverage in a variety of initial configurations (stripes, random distribution, delta-peaks, etc.) and equilibrated until the result no longer depended on the initial conditions. This equilibration was verified using auto-correlation functions. Each equilibrium data point was obtained by averaging over 15 independent runs, in order to completely exclude correlations.

A cluster algorithm (see App. C) was used to obtain the island density from both grown and equilibrium surface structured. Note that this work also considers individual ad-particles without neighbours as clusters. This remark is especially relevant for equilibrium where phase separation occurs and the majority of particles aggregate into one ‘solid phase’ cluster with surrounding ‘gas phase’ particles.

During growth, the island density increases with adsorption rate, because previously adsorbed particles can diffuse less far before they meet newly adsorbed particles and form islands (see Fig. G.2). However, the island density also increases with decreasing temperature, because

<sup>1</sup>Institut für Theoretische Physik, Technische Universität Berlin, Hardenbergstr. 36, 10623 Berlin, Germany.

particles can diffuse less far if the temperature is lower. As, Fig. G.2 clearly shows, this is not the entire truth, as islands can also dissolve again if they are given enough time. Island dissolution leads to observed crossover between the data for  $T = 550\text{ K}$  and  $T = 650\text{ K}$ . It is apparent that even in this very simple model there is a variety of effects that dominate growth.

The equilibrium results lie above the lowest data points for all three temperatures, indicating that there may be a non-monotonous effect. This non-monotonous behaviour can be interpreted in terms of the competing time scales: for very slow adsorption rates, more particles have time to desorb from clusters, which may lead to an increase of cluster density. However, it is worth noting that equilibrium results of this type notoriously are sensitive to finite size scaling [219]. So while this data indicates possible non-monotonous behaviour, this is not necessarily really the case here.



# Bibliography

- [1] “<http://news.thewindowsclub.com/flexible-display-windows-phone-shown CES-2013-59035/>,” 2015.
- [2] “<http://www.environmentteam.com/2010/02/24/electronic-bags-with-dssc-photovoltaic-panels/>,” 2015.
- [3] “<http://www.oled-info.com/daimlers-smart-forvision-car-concept-uses-transparent-white-oleds/>,” 2015.
- [4] “<http://www.peerplus.nl/default/index/smart-energy-glass/>,” 2015.
- [5] W. Walukiewicz, “Intrinsic limitations to the doping of wide-gap semiconductors,” *Phys. B: Condens. Matter*, vol. 302–303, p. 123, 2001.
- [6] S. B. Zhang, S.-H. Wei, and A. Zunger, “Microscopic origin of the phenomenological equilibrium ‘doping limit rule’ in *n*-type III-V semiconductors,” *Phys. Rev. Lett.*, vol. 84, p. 1232, 2000.
- [7] A. Janotti and C. G. Van de Walle, “Native point defects in ZnO,” *Phys. Rev. B*, vol. 76, p. 165202, 2007.
- [8] S. Lany and A. Zunger, “Assessment of correction methods for the band-gap problem and for finite-size effects in supercell defect calculations: Case studies for ZnO and GaAs,” *Phys. Rev. B*, vol. 78, p. 235104, 2008.
- [9] G. L. Drisko and C. Sanchez, “Hybridization in materials science — evolution, current state, and future aspirations,” *Eur. J. Inorg. Chem.*, vol. 2012, no. 32, p. 5097, 2012.
- [10] Lian Wang, Myung-Han Yoon, Gang Lu, Yu Yang, A. Facchetti, and T. Marks, “High-performance transparent inorganic-organic hybrid thin-film n-type transistors,” *Nat. Mater.*, vol. 5, p. 893, 2006.
- [11] J. H. Heo, S. H. Im, J. H. Noh, T. N. Mandal, C.-S. Lim, J. A. Chang, Y. H. Lee, H.-j. Kim, A. Sarkar, M. K. Nazeeruddin, M. Graetzel, and S. I. Seok, “Efficient inorganic-organic hybrid heterojunction solar cells containing perovskite compound and polymeric hole conductors,” *Nat. Photon.*, vol. 7, no. 6, p. 487, 2013.
- [12] M. Sessolo and H. J. Bolink, “Hybrid organic-inorganic light-emitting diodes,” *Adv. Mater.*, vol. 23, no. 16, p. 1829, 2011.
- [13] B. R. Saunders and M. L. Turner, “Nanoparticle-polymer photovoltaic cells,” *Adv. Colloid and Interface Science*, vol. 138, no. 1, p. 1, 2008.
- [14] G. Hlawacek and C. Teichert, “Nucleation and growth of thin films of rod-like conjugated molecules,” *J. Phys.: Condens. Matter*, vol. 25, no. 14, p. 143202, 2013.
- [15] R. B. Woodward, “Structure and the absorption spectra of  $\alpha,\beta$ -unsaturated ketones,” *J. Am. Chem. Soc.*, vol. 63, no. 4, p. 1123, 1941.
- [16] L. F. Fieser, M. Fieser, and S. Rajagopalan, “Adsorption spectroscopy and the structure of diosterols,” *J. Org. Chem.*, vol. 13, no. 6, p. 800, 1948.
- [17] Q. Chu and Y. Pang, “Vibronic structures in the electronic spectra of oligo(phenylene ethynylene): effect of m-phenylene to the optical properties of poly(m-phenylene ethynylene),” *Spectrochim. Acta Part A*, vol. 60, no. 7, p. 1459, 2004.
- [18] M. A. Loi, J. Gao, F. Cordella, P. Blondeau, E. Menna, B. Bártová, C. Hébert, S. Lazar, G. A. Bottom, M. Milko, and C. Ambrosch-Draxl, “Encapsulation of conjugated oligomers in single-walled carbon nanotubes: Towards nanohybrids for photonic devices,” *Adv. Mater.*, vol. 22, no. 14, p. 1635, 2010.
- [19] T. Yumura and H. Yamashita, “Modulating the electronic properties of multimeric thiophene oligomers by utilizing carbon nanotube confinement,” *J. Phys. Chem. C*, vol. 118, no. 10, p. 5510, 2014.
- [20] B. Galiana, M. Benedicto, L. Díez-Merino, S. Lorbek, G. Hlawacek, C. Teichert, and P. Tejedor, “Modified

- energetics and growth kinetics on H-terminated GaAs(110)," *J. Chem. Phys.*, vol. 139, no. 16, p. 164712, 2013.
- [21] U. Heinemeyer, K. Broch, A. Hinderhofer, M. Kytko, R. Scholz, A. Gerlach, and F. Schreiber, "Real-time changes in the optical spectrum of organic semiconducting films and their thickness regimes during growth," *Phys. Rev. Lett.*, vol. 104, p. 257401, 2010.
- [22] G. Koller, S. Berkebile, M. Oehzelt, P. Puschnig, C. Ambrosch-Draxl, F. P. Netzer, and M. G. Ramsey, "Intra- and intermolecular band dispersion in an organic crystal," *Science*, vol. 317, no. 5836, p. 351, 2007.
- [23] Y. Liang, D. Feng, Y. Wu, S.-T. Tsai, G. Li, C. Ray, and L. Yu, "Highly efficient solar cell polymers developed via fine-tuning of structural and electronic properties," *J. Am. Chem. Soc.*, vol. 131, no. 22, p. 7792, 2009.
- [24] V. Podzorov, E. Menard, A. Borissov, V. Kiryukhin, J. A. Rogers, and M. E. Gershenson, "Intrinsic charge transport on the surface of organic semiconductors," *Phys. Rev. Lett.*, vol. 93, p. 086602, 2004.
- [25] H. Proehl, R. Nitsche, T. Dienel, K. Leo, and T. Fritz, "In situ differential reflectance spectroscopy of thin crystalline films of ptcda on different substrates," *Phys. Rev. B*, vol. 71, p. 165207, 2005.
- [26] T. Sugaya, T. Amano, and K. Komori, "Improved optical properties of InAs quantum dots grown with an As<sub>2</sub> source using molecular beam epitaxy," *J. Appl. Phys.*, vol. 100, no. 6, p. 063107, 2006.
- [27] J. Geng, W. Zhou, P. Skelton, W. Yue, I. A. Kinloch, A. H. Windle, and B. F. G. Johnson, "Crystal structure and growth mechanism of unusually long fullerene (C<sub>60</sub>) nanowires," *J. Am. Chem. Soc.*, vol. 130, no. 8, p. 2527, 2008.
- [28] S. Blumstengel, H. Glowatzki, S. Sadofev, N. Koch, S. Kowarik, J. P. Rabe, and F. Henneberger, "Band-offset engineering in organic/inorganic semiconductor hybrid structures," *Phys. Chem. Chem. Phys.*, vol. 12, p. 11642, 2010.
- [29] B. Geffroy, P. le Roy, and C. Prat, "Organic light-emitting diode (OLED) technology: materials, devices and display technologies," *Polym. Int.*, vol. 55, no. 6, p. 572, 2006.
- [30] X. Du, Y. Huang, S. Tao, X. Yang, X. Ding, and X. Zhang, "Highly efficient white fluorescence/phosphorescence hybrid organic light emitting devices based on an efficient hole-transporting blue emitter," *Dyes and Pigments*, vol. 115, p. 149, 2015.
- [31] Y. Yang, P. Cohn, A. L. Dyer, S.-H. Eom, J. R. Reynolds, R. K. Castellano, and J. Xue, "Blue-violet electroluminescence from a highly fluorescent purine," *Chem. Mater.*, vol. 22, no. 12, p. 3580, 2010.
- [32] A. Sugimoto, H. Ochi, S. Fujimura, A. Yoshida, T. Miyadera, and M. Tsuchida, "Flexible OLED displays using plastic substrates," *IEEE J. Select. Top. Quant. Electr.*, vol. 10, no. 1, p. 107, 2004.
- [33] D. Yokoyama, "Molecular orientation in small-molecule organic light-emitting diodes," *J. Mater. Chem.*, vol. 21, p. 19187, 2011.
- [34] J.-S. Kim, P. K. H. Ho, N. C. Greenham, and R. H. Friend, "Electroluminescence emission pattern of organic light-emitting diodes: Implications for device efficiency calculations," *J. Appl. Phys.*, vol. 88, no. 2, 2000.
- [35] M. Scharber and N. Sariciftci, "Efficiency of bulk-heterojunction organic solar cells," *Prog. Polym. Sci.*, vol. 38, no. 12, p. 1929, 2013. Topical issue on Conductive Polymers.
- [36] C. J. Brabec, "Organic photovoltaics: technology and market," *Solar Energy Mater. and Solar Cells*, vol. 83, no. 2-3, p. 273, 2004. The development of organic and polymer photovoltaics.
- [37] J. A. Hauch, P. Schilinsky, S. A. Choulis, S. Rajoelson, and C. J. Brabec, "The impact of water vapor transmission rate on the lifetime of flexible polymer solar cells," *Appl. Phys. Lett.*, vol. 93, no. 10, p. 103306, 2008.
- [38] T. Sasaki, K. Tabata, K. Tsukagoshi, A. Beckel, A. Lorke, and Y. Yamamoto, "Control of molecular orientation and morphology in organic bilayer solar cells: Copper phthalocyanine on gold nanodots," *Thin Solid Films*, vol. 562, no. 0, p. 467, 2014.
- [39] P. K. Watkins, A. B. Walker, and G. L. B. Verschoor, "Dynamical Monte Carlo modelling of organic solar cells: The dependence of internal quantum efficiency on morphology," *Nano Lett.*, vol. 5, no. 9, p. 1814, 2005.

- [40] Y. Liu, J. Zhao, Z. Li, C. Mu, W. Ma, H. Hu, K. Jiang, H. Lin, H. Ade, and H. Yan, “Aggregation and morphology control enables multiple cases of high-efficiency polymer solar cells,” *Nat. Comm.*, vol. 5, 2014.
- [41] D. Chen, A. Nakahara, D. Wei, D. Nordlund, and T. P. Russell, “P3HT/PCBM bulk heterojunction organic photovoltaics: Correlating efficiency and morphology,” *Nano Lett.*, vol. 11, no. 2, p. 561, 2011.
- [42] L. Schmidt-Mende, A. Fechtenkötter, K. Müllen, E. Moons, R. H. Friend, and J. D. MacKenzie, “Self-organized discotic liquid crystals for high-efficiency organic photovoltaics,” *Science*, vol. 293, no. 5532, p. 1119, 2001.
- [43] M. Mantina, A. C. Chamberlin, R. Valero, C. J. Cramer, and D. G. Truhlar, “Consistent van der waals radii for the whole main group,” *J. Phys. Chem. A*, vol. 113, no. 19, p. 5806, 2009.
- [44] P. Pyykkö and M. Atsumi, “Molecular single-bond covalent radii for elements 1-118,” *Chem.: Europ. J.*, vol. 15, no. 1, p. 186, 2009.
- [45] P. A. Golubkov and P. Ren, “Generalized coarse-grained model based on point multipole and gay-berne potentials,” *J. Chem. Phys.*, vol. 125, no. 6, p. 064103, 2006.
- [46] B. Krause, R. Boldt, and P. Pötschke, “A method for determination of length distributions of multiwalled carbon nanotubes before and after melt processing,” *Carbon*, vol. 49, no. 4, p. 1243, 2011.
- [47] P. M. Cotts, T. M. Swager, and Q. Zhou, “Equilibrium flexibility of a rigid linear conjugated polymer,” *Macromol.*, vol. 29, no. 23, p. 7323, 1996.
- [48] H. Loewen, “Introduction to colloidal dispersions in external fields,” *Eur. Phys. J. Special Topics*, vol. 222, no. 11, p. 2727, 2013.
- [49] J. Stellbrink, J. Allgaier, M. Monkenbusch, D. Richter, A. Lang, C. N. Likos, M. Watzlawek, H. Löwen, G. Ehlers, and P. Schleger, “Neither gaussian chains nor hard spheres — star polymers seen as ultrasoft colloids,” *Prog. Polym. Sci.*, vol. 115, p. 88, 2000.
- [50] J. E. Jones, “On the determination of molecular fields. II. from the equation of state of a gas,” *Proc. R. Soc. London A*, vol. 106, no. 738, p. 463, 1924.
- [51] L. A. Girifalco, “Molecular properties of fullerene in the gas and solid phases,” *J. Phys. Chem.*, vol. 96, no. 2, p. 858, 1992.
- [52] S. Asakura and F. Oosawa, “On interaction between two bodies immersed in a solution of macromolecules,” *J. Chem. Phys.*, vol. 22, no. 7, 1954.
- [53] S. Asakura and F. Oosawa, “Interaction between particles suspended in solutions of macromolecules,” *J. Polym. Sci.*, vol. 33, no. 126, pp. 183–192, 1958.
- [54] S. P. Tewari, G. Dhingra, and P. Silotia, “Collective dynamics of a nano-fluid: Fullerene, C60,” *Internat. J. Mod. Phys. B*, vol. 24, no. 22, p. 4281, 2010.
- [55] L. N. Yakub, “Thermodynamic properties of solid fullerite-60,” *Fizika Nizkikh Temperatur*, vol. 19, no. 6, p. 726, 1993.
- [56] T. Shchelkacheva, “Continuum percolation and melting of C60,” *Phys. Lett. A*, vol. 214, no. 1-2, p. 95, 1996.
- [57] V. Zubov, N. Tretiakov, J. T. Rabelo, and J. S. Ortiz, “Calculations of the thermal expansion, cohesive energy and thermodynamic stability of a van der waals crystal - fullerene C60,” *Phys. Lett. A*, vol. 194, no. 3, p. 223, 1994.
- [58] P. Orea, “Phase diagrams of model C60 and c70 fullerenes from short-range attractive potentials,” *J. Chem. Phys.*, vol. 130, no. 10, p. 104703, 2009.
- [59] M. Magomedov, “Interfullerene interaction and properties of fullerites,” *High Temp.*, vol. 43, no. 3, p. 379, 2005.
- [60] H. N. W. Lekkerkerker and R. Tuinier, *Colloids and the Depletion Interaction – Lecture notes in Physics*, vol. 833. 69121 Heidelberg, Germany: Springer-Verlag Berlin, 2011.
- [61] J. K. G. Dhont, *An Introduction to Dynamics of Colloids*. Elsevier Science B.V., Springer, 1996.
- [62] S. H. L. Klapp, S. Grandner, Y. Zeng, and R. von Klitzing, “Charged silica suspensions as model materials for liquids in confined geometries,” *Soft Matt.*, vol. 6, p. 2330, 2010.

- [63] H. Schmidle, S. Jager, C. K. Hall, O. D. Velev, and S. H. L. Klapp, "Two-dimensional colloidal networks induced by a uni-axial external field," *Soft Matt.*, vol. 9, p. 2518, 2013.
- [64] W. C. K. Poon, "The physics of a model colloid-polymer mixture," *J. Phys.: Condens. Matter*, vol. 14, no. 33, p. R859, 2002.
- [65] M. H. J. Hagen, E. J. Meijer, G. C. A. M. Mooij, D. Frenkel, and H. N. W. Lekkerkerker, "Does C<sub>60</sub> Have A Liquid-Phase," *Nature*, vol. 365, no. 6445, p. 425, 1993.
- [66] L. J. Gallego, J. García-Rodeja, M. M. G. Alemany, and C. Rey, "Solidlike-to-liquidlike transition in small clusters of C<sub>60</sub> molecules or transition-metal atoms," *Phys. Rev. Lett.*, vol. 83, p. 5258, 1999.
- [67] C. P. Royall and S. R. Williams, "C<sub>60</sub>: The first one-component gel?," *J. Phys. Chem. B*, vol. 115, no. 22, p. 7288, 2011.
- [68] E. Zaccarelli and W. C. K. Poon, "Colloidal glasses and gels: The interplay of bonding and caging," *Proc. Nat. Ac. Sci.*, vol. 106, no. 36, p. 15203, 2009.
- [69] H. Liu, Z. Lin, L. V. Zhigilei, and P. Reinke, "Fractal structures in fullerene layers: Simulation of the growth process," *J. Phys. Chem. C*, vol. 112, no. 12, p. 4687, 2008.
- [70] V. J. Anderson and H. N. W. Lekkerkerker, "Insights into phase transition kinetics from colloid science," *Nature*, vol. 416, no. 6883, p. 811, 2002.
- [71] M. Feng, J. Zhao, and H. Petek, "Atomlike, hollow-core bound molecular orbitals of C<sub>60</sub>," *Science*, vol. 320, no. 5874, p. 359, 2008.
- [72] M. Hara, H. Sasabe, A. Yamada, and A. F. Garito, "Epitaxial growth of organic thin films by organic molecular beam epitaxy," *Jpn. J. Appl. Phys.*, vol. 28, no. 2A, p. L306, 1989.
- [73] D. Choudhary, P. Clancy, R. Shetty, and F. Escobedo, "A computational study of the sub-monolayer growth of pentacene," *Adv. Func. Mater.*, vol. 16, no. 13, pp. 1768–1775, 2006.
- [74] M. Haran, J. E. Goose, N. P. Clote, and P. Clancy, "Multiscale modeling of self-assembled monolayers of thiophenes on electronic material surfaces," *Langmuir*, vol. 23, no. 9, p. 4897, 2007.
- [75] S. Kowarik, A. Gerlach, S. Sellner, F. Schreiber, L. Cavalcanti, and O. Konovalov, "Real-time observation of structural and orientational transitions during growth of organic thin films," *Phys. Rev. Lett.*, vol. 96, p. 125504, 2006.
- [76] P. Cao, K. Xu, J. O. Varghese, and J. R. Heath, "Atomic force microscopy characterization of room-temperature adlayers of small organic molecules through graphene templating," *J. Am. Chem. Soc.*, vol. 133, no. 8, p. 2334, 2011.
- [77] O. Acton, M. Dubey, T. Weidner, K. M. O'Malley, T.-W. Kim, G. G. Ting, D. Hutchins, J. E. Baio, T. C. Lovejoy, A. H. Gage, D. G. Castner, H. Ma, and A. K.-Y. Jen, "Simultaneous modification of bottom-contact electrode and dielectric surfaces for organic thin-film transistors through single-component spin-cast monolayers," *Adv. Func. Mater.*, vol. 21, no. 8, p. 1476, 2011.
- [78] D. Placencia, W. Wang, R. C. Shallcross, K. W. Nebesny, M. Brumbach, and N. R. Armstrong, "Organic photovoltaic cells based on solvent-annealed, textured titanyl phthalocyanine/C<sub>60</sub> heterojunctions," *Adv. Func. Mater.*, vol. 19, no. 12, pp. 1913–1921, 2009.
- [79] M. Sparenberg, A. Zykov, P. Beyer, L. Pithan, C. Weber, Y. Garmshausen, F. Carla, S. Hecht, S. Blumstengel, F. Henneberger, and S. Kowarik, "Controlling the growth mode of para-sexiphenyl (6P) on ZnO by partial fluorination," *Phys. Chem. Chem. Phys.*, vol. 16, p. 26084, 2014.
- [80] M. Kunitake, N. Batina, and K. Itaya, "Self-organized porphyrin array on iodine-modified au(111) in electrolyte solutions: In situ scanning tunneling microscopy study," *Langmuir*, vol. 11, no. 7, p. 2337, 1995.
- [81] C. Chiutu, A. M. Sweetman, A. J. Lakin, A. Stannard, S. Jarvis, L. Kantorovich, J. L. Dunn, and P. Moriarty, "Precise orientation of a single C<sub>60</sub> molecule on the tip of a scanning probe microscope," *Phys. Rev. Lett.*, vol. 108, p. 268302, 2012.
- [82] C. Frank, J. Novák, R. Banerjee, A. Gerlach, F. Schreiber, A. Vorobiev, and S. Kowarik, "Island size evolution and molecular diffusion during growth of organic thin films followed by time-resolved specular and off-specular scattering," *Phys. Rev. B*, vol. 90, p. 045410, 2014.
- [83] A. Hinderhofer, A. Gerlach, S. Kowarik, F. Zontone, J. Krug, and F. Schreiber, "Smoothing and coherent structure formation in organic-organic heterostructure growth," *Eur. Phys. Lett.*, vol. 91, no. 5, p. 56002,

- 2010.
- [84] K. Youngkyoo, S. Cook, S. Tuladhar, S. Choulis, J. Nelson, J. Durrant, D. Bradley, M. Giles, I. McCulloch, Chang-sik Ha, and M. Ree, "A strong regioregularity effect in self-organizing conjugated polymer films and high-efficiency polythiophene:fullerene solar cells," *Nat. Mater.*, vol. 5, p. 197, 2006.
  - [85] F. S. Khokhar, G. Hlawacek, R. van Gastel, H. J. W. Zandvliet, C. Teichert, and B. Poelsema, "The influence of substrate temperature on growth of para-sexiphenyl thin films on Ir111 supported graphene studied by LEEM," *Surf. Sci.*, vol. 606, no. 3-4, p. 475, 2012.
  - [86] C. D. Dimitrakopoulos, A. R. Brown, and A. Pomp, "Molecular beam deposited thin films of pentacene for organic field effect transistor applications," *J. Appl. Phys.*, vol. 80, no. 4, 1996.
  - [87] Y. Wu, K. Liu, D. Li, Y. Guo, and S. Pan, "In situ AFM and raman spectroscopy study of the crystallization behavior of Ge<sub>2</sub>Sb<sub>2</sub>Te<sub>5</sub> films at different temperature," *Appl. Surf. Sci.*, vol. 258, no. 4, p. 1619, 2011.
  - [88] L. Croin, E. Vittone, and G. Amato, "In situ control of dewetting of cu thin films in graphene chemical vapor deposition," *Thin Solid Films*, vol. 573, p. 122, 2014.
  - [89] S. Kowarik, A. Gerlach, S. Sellner, L. Cavalcanti, and F. Schreiber, "Dewetting of an organic semiconductor thin film observed in real-time," *Adv. Engin. Mater.*, vol. 11, no. 4, p. 291, 2009.
  - [90] J. Zhu, Z. Liang, Y. Li, Y. Zhang, and X. Wei, "Epitaxial growth of BaTiO<sub>3</sub> thin films at a low temperature under 300°C with temperature-controlled BaTiO<sub>3</sub> buffer layer," *J. Cryst. Growth*, vol. 294, no. 2, p. 236, 2006.
  - [91] K. Claytor, S. Khatua, J. M. Guerrero, A. Tcherniak, J. M. Tour, and S. Link, "Accurately determining single molecule trajectories of molecular motion on surfaces," *J. Chem. Phys.*, vol. 130, no. 16, p. 164710, 2009.
  - [92] R. V. Lapshin, "Automatic drift elimination in probe microscope images based on techniques of counter-scanning and topography feature recognition," *Measurement Sci. Technol.*, vol. 18, no. 3, p. 907, 2007.
  - [93] G. Schitter and M. J. Rost, "Scanning probe microscopy at video-rate," *Mater. Today*, vol. 11, Supplement, p. 40, 2008.
  - [94] R. Ganapathy, M. R. Buckley, S. J. Gerbode, and I. Cohen, "Direct measurements of island growth and step-edge barriers in colloidal epitaxy," *Science*, vol. 327, no. 5964, p. 445, 2010.
  - [95] T. Kumagai, M. Kaizu, S. Hatta, H. Okuyama, T. Aruga, I. Hamada, and Y. Morikawa, "Direct observation of hydrogen-bond exchange within a single water dimer," *Phys. Rev. Lett.*, vol. 100, p. 166101, 2008.
  - [96] B. S. Swartzentruber, "Direct measurement of surface diffusion using atom-tracking scanning tunneling microscopy," *Phys. Rev. Lett.*, vol. 76, p. 459, 1996.
  - [97] L. X. Chen, X. Zhang, E. C. Wasinger, J. V. Lockard, A. B. Stickrath, M. W. Mara, K. Attenkofer, G. Jennings, G. Smolentsev, and A. Soldatov, "X-ray snapshots for metalloporphyrin axial ligation," *Chem. Sci.*, vol. 1, p. 642, 2010.
  - [98] L. Campbell, S. Tanaka, and S. Mukamel, "Ligand effects on the X-ray absorption of a nickel porphyrin complex: a simulation study," *Chem. Phys.*, vol. 299, no. 2-3, p. 225, 2004.
  - [99] P. Kratzer, *Multiscale Simulation Methods in Molecular Sciences – Lecture Notes*. NIC, 2009.
  - [100] F. Della Sala, S. Blumstengel, and F. Henneberger, "Electrostatic-field-driven alignment of organic oligomers on ZnO surfaces," *Phys. Rev. Lett.*, vol. 107, p. 146401, 2011.
  - [101] P. Puschnig, S. Berkebile, A. J. Fleming, G. Koller, K. Emtsev, T. Seyller, J. D. Riley, C. Ambrosch-Draxl, F. P. Netzer, and M. G. Ramsey, "Reconstruction of molecular orbital densities from photoemission data," *Science*, vol. 326, no. 5953, p. 702, 2009.
  - [102] J. E. Goose, E. L. First, and P. Clancy, "Nature of step-edge barriers for small organic molecules," *Phys. Rev. B*, vol. 81, p. 205310, 2010.
  - [103] S. M. Falke, C. A. Rozzi, D. Brida, M. Maiuri, M. Amato, E. Sommer, A. De Sio, A. Rubio, G. Cerullo, E. Molinari, and C. Lienau, "Coherent ultrafast charge transfer in an organic photovoltaic blend," *Science*, vol. 344, no. 6187, p. 1001, 2014.

- [104] E. P. Soccia, B. L. Farmer, and W. W. Adams, "Molecular dynamics simulations of a poly(p-phenylene) oligomer," *J. Polym. Sci. B*, vol. 31, no. 13, p. 1975, 1993.
- [105] K. Palczynski, G. Heimel, J. Heyda, and J. Dzubiella, "Growth and characterization of molecular crystals of para-sexiphenyl by all-atom computer simulations," *Cryst. Growth & Design*, vol. 14, no. 8, p. 3791, 2014.
- [106] K. Palczynski and J. Dzubiella, "Anisotropic electrostatic friction of para-sexiphenyl on the ZnO (10 $\overline{1}$ 0) surface," *J. Phys. Chem. C*, vol. 118, no. 45, p. 26368, 2014.
- [107] T. Potocar, S. Lorbek, D. Nabok, Q. Shen, L. Tumbek, G. Hlawacek, P. Puschnig, C. Ambrosch-Draxl, C. Teichert, and A. Winkler, "Initial stages of a *para*-hexaphenyl film growth on amorphous mica," *Phys. Rev. B*, vol. 83, p. 075423, 2011.
- [108] T. Heinemann, K. Palczynski, J. Dzubiella, and S. H. L. Klapp, "Angle-resolved effective potentials for disk-shaped molecules," *J. Chem. Phys.*, vol. 141, no. 21, 2014.
- [109] D. M. Huang, A. J. Moule, and R. Faller, "Characterization of polymer-fullerene mixtures for organic photovoltaics by systematically coarse-grained molecular simulations," *Fluid Phase Equilibria*, vol. 302, no. 1-2, p. 21, 2011.
- [110] K. Binder and A. Milchev, "Off-lattice Monte Carlo methods for coarse-grained models of polymeric materials and selected applications," *J. Comp.-Aided Mater. Design*, vol. 9, no. 1, p. 33, 2002.
- [111] J. W. Evans, P. A. Thiel, and M. C. Bartelt, "Morphological evolution during epitaxial thin film growth: Formation of 2d islands and 3d mounds," *Surf. Sci. Rep.*, vol. 61, no. 1-2, p. 1, 2006.
- [112] K. Fu, Y. Fu, P. Han, Y. Zhang, and R. Zhang, "Kinetic Monte Carlo study of metal organic chemical vapor deposition growth dynamics of GaN thin film at microscopic level," *J. Appl. Phys.*, vol. 103, no. 10, p. 103524, 2008.
- [113] K. Reuter and M. Scheffler, "First-principles kinetic Monte Carlo simulations for heterogeneous catalysis: Application to the CO oxidation at RuO<sub>2</sub>(110)," *Phys. Rev. B*, vol. 73, p. 045433, 2006.
- [114] A. F. Voter, *Radiation Effects in Solids*. Nato Science Series II, Springer, 2007 ed., 2005.
- [115] U. Kürpick and T. S. Rahman, "Diffusion processes relevant to homoepitaxial growth on Ag(100)," *Phys. Rev. B*, vol. 57, p. 2482, 1998.
- [116] A. Karim, A. N. Al-Rawi, A. Kara, T. S. Rahman, O. Trushin, and T. Ala-Nissila, "Diffusion of small two-dimensional Cu islands on Cu(111) studied with a kinetic Monte Carlo method," *Phys. Rev. B*, vol. 73, p. 165411, 2006.
- [117] S. I. Shah, G. Nandipati, A. Kara, and T. S. Rahman, "Self-diffusion of small Ni clusters on the Ni(111) surface: A self-learning kinetic Monte Carlo study," *Phys. Rev. B*, vol. 88, p. 035414, 2013.
- [118] M. Körner, F. Loske, M. Einax, A. Kühnle, M. Reichling, and P. Maass, "Second-layer induced island morphologies in thin-film growth of fullerenes," *Phys. Rev. Lett.*, vol. 107, p. 016101, 2011.
- [119] S. Bommel, N. Kleppmann, C. Weber, H. Spranger, P. Schaefer, J. Novak, S. V. Roth, F. Schreiber, S. H. L. Klapp, and S. Kowarik, "Unravelling the multilayer growth of the fullerene C<sub>60</sub> in real time," *Nat. Comm.*, vol. 5, p. 5388, 2014.
- [120] N. Kleppmann and S. H. L. Klapp, "Particle-resolved dynamics during multilayer growth of C<sub>60</sub>," *Phys. Rev. B*, vol. 91, p. 045436, 2015.
- [121] L. Tumbek, C. Gleichweit, K. Zojer, and A. Winkler, "Origin of the bimodal island size distribution in ultrathin films of *para*-hexaphenyl on mica," *Phys. Rev. B*, vol. 86, p. 085402, 2012.
- [122] W. C. Wang, D. Y. Zhong, J. Zhu, F. Kalischewski, R. F. Dou, K. Wedeking, Y. Wang, A. Heuer, H. Fuchs, G. Erker, and L. F. Chi, "Patterned nucleation control in vacuum deposition of organic molecules," *Phys. Rev. Lett.*, vol. 98, p. 225504, 2007.
- [123] P. K. Jana and A. Heuer, "Deposition of model chains on surfaces: Anomalous relation between flux and stability," *J. Chem. Phys.*, vol. 138, no. 12, p. 124708, 2013.
- [124] F. L. Forgerini and W. Figueiredo, "Thin-film growth by random deposition of rod-like particles on a square lattice," *Phys. Stat. Sol. C*, vol. 8, no. 11-12, p. 3119, 2011.
- [125] S. F. Hopp and A. Heuer, "Anisotropic behavior of organic molecules on prepatterned surfaces," *J. Chem. Phys.*, vol. 136, no. 15, p. 154106, 2012.

- [126] J. S. Raut and K. A. Fichthorn, "Molecular diffusion on solid surfaces: A lattice-model study," *J. Chem. Phys.*, vol. 110, no. 1, 1999.
- [127] N. Kleppmann and S. H. L. Klapp, "A scale-bridging modeling approach for anisotropic organic molecules at patterned semiconductor surfaces," *The Journal of Chemical Physics*, vol. 142, no. 6, p. 064701, 2015.
- [128] F. Schreiber, "Structure and growth of self-assembling monolayers," *Progress in Surface Science*, vol. 65, no. 5-8, pp. 151 – 257, 2000.
- [129] F. Schreiber, A. Eberhardt, T. Y. B. Leung, P. Schwartz, S. M. Wetterer, D. J. Lavrich, L. Berman, P. Fenter, P. Eisenberger, and G. Scoles, "Adsorption mechanisms, structures, and growth regimes of an archetypal self-assembling system: Decanethiol on au(111)," *Phys. Rev. B*, vol. 57, pp. 12476–12481, 1998.
- [130] N. Metropolis, A. W. Rosenbluth, M. N. Rosenbluth, A. H. Teller, and E. Teller, "Equation of state calculations by fast computing machines," *J. Chem. Phys.*, vol. 21, no. 6, 1953.
- [131] A. Chatterjee and D. G. Vlachos, "An overview of spatial microscopic and accelerated kinetic Monte Carlo methods," *J. Comp.-Aided Mater. Des.*, vol. 14, no. 2, p. 253, 2007.
- [132] C. C. Battaile and D. J. Srolovitz, "Kinetic Monte Carlo simulation of chemical vapor deposition," *Ann. Rev. Mater. Res.*, vol. 32, no. 1, p. 297, 2002.
- [133] K. A. Fichthorn and W. H. Weinberg, "Theoretical foundations of dynamical Monte Carlo simulations," *J. Chem. Phys.*, vol. 95, no. 2, pp. 1090–1096, 1991.
- [134] M. Biehl, "Lattice gas models and Kinetic Monte Carlo simulations of epitaxial growth," in *Multiscale Modeling in Epitaxial Growth* (A. Voigt, ed.), vol. 149 of *ISNM International Series of Numerical Mathematics*, p. 3, Birkhäuser Basel, 2005.
- [135] A. Gorban, "Detailed balance in micro- and macrokinetics and micro-distinguishability of macro-processes," *Results in Physics*, vol. 4, p. 142, 2014.
- [136] E. Gelenbe, "G-networks with triggered costumer movement," *J. Appl. Probability*, vol. 30, no. 3, p. 742, 1993.
- [137] F. Kelly, *Reversibility and stochastic networks*. Wiley series in probability and mathematical statistics: Tracts on probability and statistics, J. Wiley, 1979.
- [138] A. K. Jones, A. Ballestad, T. Li, M. Whitwick, J. Rottler, and T. Tiedje, "Faceting at the step flow threshold in epitaxial growth on patterned surfaces," *Phys. Rev. B*, vol. 79, p. 205419, 2009.
- [139] I. K. Marmorkos and S. Das Sarma, "Atomistic numerical study of molecular-beam-epitaxial growth kinetics," *Phys. Rev. B*, vol. 45, p. 11262, 1992.
- [140] P. Šmilauer and D. D. Vvedensky, "Coarsening and slope evolution during unstable spitaxial growth," *Phys. Rev. B*, vol. 52, pp. 14263–14272, 1995.
- [141] M. Müller, K. Albe, C. Busse, A. Thoma, and T. Michely, "Island shapes, island densities, and stacking-fault formation on Ir(111): Kinetic Monte Carlo simulations and experiments," *Phys. Rev. B*, vol. 71, p. 075407, 2005.
- [142] D. T. Gillespie, "A general method for numerically simulating the stochastic time evolution of coupled chemical reactions," *J. Comp. Phys.*, vol. 22, no. 4, p. 403, 1976.
- [143] S. Plimpton, C. Battaile, M. Ch, L. Holm, A. Thompson, V. Tikare, G. Wagner, X. Zhou, C. G. Cardona, and A. Slepoy, "Crossing the mesoscale no-man's land via parallel kinetic monte carlo," 2009.
- [144] Y. Cao, H. Li, and L. Petzold, "Efficient formulation of the stochastic simulation algorithm for chemically reacting systems," *J. Chem. Phys.*, vol. 121, no. 9, 2004.
- [145] J. Goswami, G. Ananthakrishna, and S. Shivashankar, "Monte carlo simulation of nucleation and growth of thin films," *Bull. Mater. Sci.*, vol. 20, no. 6, p. 823, 1997.
- [146] S. Jabbari-Farouji and E. Trizac, "Dynamic Monte Carlo simulations of anisotropic colloids," *J. Chem. Phys.*, vol. 137, no. 5, p. 054107, 2012.
- [147] D. T. Gillespie, "Exact stochastic simulation of coupled chemical reactions," *J. Phys. Chem.*, no. 25, p. 2340, 1977.
- [148] A. B. Bortz, M. H. Kalos, and J. L. Lebowitz, "A new algorithm for Monte Carlo simulations of Ising spin systems," *J. Comp. Phys.*, vol. 17, p. 10, 1975.

- [149] V. R. Barlett, J. Bigeón, M. Hoyuelos, and H. Martín, “Differences between fixed time step and kinetic Monte Carlo methods for biased diffusion,” *J. Comput. Phys.*, vol. 228, no. 16, p. 5740, 2009.
- [150] J. P. K. Doye and D. Frenkel, “Kinetic Monte Carlo simulations of the growth of polymer crystals,” *J. Chem. Phys.*, vol. 110, no. 5, p. 2692, 1999.
- [151] G. Henkelman and H. Jónsson, “Long time scale kinetic Monte Carlo simulations without lattice approximation and predefined event table,” *J. Chem. Phys.*, vol. 115, p. 9657, 2001.
- [152] E. Heinsalu, M. Patriarca, I. Goychuk, and P. Hägggi, “Fractional diffusion in periodic potentials,” *J. Phys.: Condens. Matter*, vol. 19, no. 6, p. 065114, 2007.
- [153] E. Pollak, “Theory of activated rate processes: A new derivation of Kramers’ expression,” *J. Chem. Phys.*, vol. 85, no. 2, p. 865, 1986.
- [154] H. Risken, *The Fokker-Planck Equation: Methods of Solutions and Applications*. Springer Series in Synergetics, Springer, 2nd ed. 1989. 3rd printing ed., 1996.
- [155] G. H. Vineyard, “Frequency factors and isotope effects in solid state rate processes,” *J. Phys. Chem. Sol.*, vol. 3, no. 1-2, p. 121, 1957.
- [156] M. J. Gillan, “Quantum-classical crossover of the transition rate in the damped double well,” *J. Phys. C*, vol. 20, no. 24, p. 3621, 1987.
- [157] M. J. Murphy, G. A. Voth, and A. L. R. Bug, “Classical and quantum transition state theory for the diffusion of helium in silica sodalite,” *J. Phys. Chem. B*, vol. 101, no. 4, p. 491, 1997.
- [158] P. Hägggi, P. Talkner, and M. Borkovec, “Reaction-rate theory: fifty years after Kramers,” *Rev. Mod. Phys.*, vol. 62, p. 2511, 1990.
- [159] K. F. Herzfeld, “Zur Theorie der Reaktionsgeschwindigkeiten in Gasen,” *Z. Electrochem. Angew. Phys. Chem.*, vol. 25, no. 17-18, p. 301, 1919.
- [160] H. Eyring and M. Polanyi, “Über einfache Gasreaktionen,” *Z. Phys. Chem. Abt. B*, vol. 12, p. 279, 1931.
- [161] H. Eyring, “The activated complex in chemical reactions,” *J. Chem. Phys.*, vol. 3, no. 2, 1935.
- [162] R. Littlejohn and K. Mitchell, “Gauge theory of small vibrations in polyatomic molecules,” in *Geometry, Mechanics, and Dynamics* (P. Newton, P. Holmes, and A. Weinstein, eds.), p. 407, Springer New York, 2002.
- [163] C. Lanczos, *The Variational Principles of Mechanics*. Dover books on physics and chemistry, Dover Publications, 1970.
- [164] M. Borkovec and B. J. Berne, “Energy and angular momentum diffusion theory of dissociation rate constants,” *J. Chem. Phys.*, vol. 84, no. 8, 1986.
- [165] P. Frank, N. Koch, M. Koini, R. Rieger, K. Müllen, R. Resel, and A. Winkler, “Layer growth and desorption kinetics of a discoid molecular acceptor on Au(111),” *Chem. Phys. Lett.*, vol. 473, no. 4-6, p. 321, 2009.
- [166] B. Joshi, “A detailed balanced reaction network is sufficient but not necessary for its markov chain to be detailed balanced,” *Discrete and Continuous Dynamical Systems – Series B*, vol. 20, no. 4, p. 1077, 2015.
- [167] R. Metzler and J. Klafter, “The random walk’s guide to anomalous diffusion: a fractional dynamics approach,” *Phys. Rep.*, vol. 339, no. 1, p. 1, 2000.
- [168] H.-G. Busmann, R. Hiss, H. Gaber, and I. V. Hertel, “Growth mechanisms of C<sub>60</sub>-molecular beam epitaxy on mica,” *Surf. Sci.*, vol. 289, no. 3, p. 381, 1993.
- [169] “<http://web.archive.org/web/20150109011908/http://www.nanotube.msu.edu/fullerene/fullerene-isomers.html>,” 2015.
- [170] H. W. Kroto, J. R. Heath, S. C. O’Brien, R. F. Curl, and R. E. Smalley, “C<sub>60</sub>: Buckminsterfullerene,” *Nat.*, vol. 318, pp. 162–163, 1985.
- [171] D. Schmicker, S. Schmidt, J. G. Skofronick, J. P. Toennies, and R. Vollmer, “Epitaxial growth of single-crystal C<sub>60</sub> on mica by helium-atom scattering,” *Phys. Rev. B*, vol. 44, p. 10995, 1991.
- [172] A. Hirsch, Z. Chen, and H. Jiao, “Sphärische Aromatizität in Ih-symmetrischen Fullerenen: die 2(N+1)2-Regel,” *Angew. Chem.*, vol. 112, no. 21, p. 4079, 2000.

- [173] P. R. Buseck, S. J. Tsipursky, and R. Hettich, "Fullerenes from the geological environment," *Science*, vol. 257, no. 5067, p. 215, 1992.
- [174] P. W. Dunk, N. K. Kaiser, C. L. Hendrickson, J. P. Quinn, C. P. Ewels, Y. Nakanishi, Y. Sasaki, H. Shinohara, A. G. Marshall, and H. W. Kroto, "Closed network growth of fullerenes," *Nat. Comm.*, vol. 3, 2012.
- [175] J. Cami, J. Bernard-Salas, E. Peeters, and S. E. Malek, "Detection of C<sub>60</sub> and C<sub>70</sub> in a young planetary nebula," *Science*, vol. 329, no. 5996, p. 1180, 2010.
- [176] W. Krätschmer, L. D. Lamb, K. Fostiropoulos, and D. R. Huffman, "Solid C<sub>60</sub>: a new form of carbon," *Nature*, vol. 347, 1990.
- [177] M. B. Xing and R. X. Wang, "Dispersion of fullerene C<sub>60</sub> in mineral based refrigeration oils," in *Remote Sensing, Environment and Transportation Engineering (RSETE), 2012 2nd International Conference on*, p. 1, 2012.
- [178] T. Haisch, E. J. Mittemeijer, and J. W. Schultze, "On the influence of microstructure and carbide content of steels on the electrochemical dissolution process in aqueous NaCl-electrolytes," *Mater. Corrosion*, vol. 53, no. 10, p. 740, 2002.
- [179] T. Baati, F. Bourasset, N. Gharbi, L. Njim, M. Abderrabba, A. Kerkeni, H. Szwarc, and F. Moussa, "The prolongation of the lifespan of rats by repeated oral administration of [60]fullerene," *Biomater.*, vol. 33, no. 19, p. 4936, 2012.
- [180] S. Palanisamy, B. Thirumalraj, S.-M. Chen, M. Ali, and F. M. Al-Hemaid, "Palladium nanoparticles decorated on activated fullerene modified screen printed carbon electrode for enhanced electrochemical sensing of dopamine," *J. Colloid and Interface Science*, vol. 448, p. 251, 2015.
- [181] P. Zhu, P. Wang, L. Kan, G. Sun, Y. Zhang, and J. Yu, "An enhanced photoelectrochemical immunosensing platform: Supramolecular donor-acceptor arrays by assembly of porphyrin and c<sub>60</sub>," *Biosensors and Bioelectronics*, vol. 68, p. 604, 2015.
- [182] M. Campoy-Quiles, T. Ferenczi, T. Agostinelli, P. G. Etchegoin, Y. Kim, T. D. Anthopoulos, P. N. Stavrinou, D. D. C. Bradley, and J. Nelson, "Morphology evolution via self-organization and lateral and vertical diffusion in polymer: fullerene solar cell blends," *Nat. Mater.*, vol. 7, no. 2, p. 158, 2008.
- [183] Z. Li, H. C. Wong, Z. Huang, H. Zhong, C. H. Tan, W. C. Tsui, J. S. Kim, J. R. Durrant, and J. T. Cabral, "Performance enhancement of fullerene-based solar cells by light processing," *Nat. Comm.*, vol. 4, 2013.
- [184] K. Hutchison, J. Gao, G. Schick, Y. Rubin, and F. Wudl, "Bucky light bulbs: White light electroluminescence from a fluorescent C-60 adduct-single layer organic LED," *J. Am. Chem. Soc.*, vol. 121, no. 23, p. 5611, 1999.
- [185] T. Liu and A. Troisi, "What makes fullerene acceptors special as electron acceptors in organic solar cells and how to replace them," *Adv. Mater.*, vol. 25, no. 7, p. 1038, 2013.
- [186] Y. He and Y. Li, "Fullerene derivative acceptors for high performance polymer solar cells," *Phys. Chem. Chem. Phys.*, vol. 13, p. 1970, 2011.
- [187] F. J. M. Z. Heringdorf, M. C. Reuter, and R. M. Tromp, "Growth dynamics of pentacene thin films," *Nature*, vol. 412, no. 6846, p. 517, 2001.
- [188] Private communications with M. Sparenberg, S. Blumstengel and F. Henneberger.
- [189] A. A. Khosroabadi, D. L. Matz, P. Gangopadhyay, J. E. Pemberton, and R. A. Norwood, "Study of the C<sub>60</sub>/Ag interface of a large area nanoarchitected Ag substrate using surface-enhanced raman scattering," *J. Phys. Chem. C*, vol. 118, no. 31, p. 18027, 2014.
- [190] Z. Cao, *Thin Film Growth: Physics, Materials Science and Applications*. Woodhead Publishing Series in Electronic and Optical Materials, Elsevier Science, 2011.
- [191] G. Renaud, R. Lazzari, and F. Leroy, "Probing surface and interface morphology with grazing incidence small angle x-ray scattering," *Surf. Sci. Rep.*, vol. 64, no. 8, p. 255, 2009.
- [192] P. Müller-Buschbaum, "Grazing incidence small-angle X-ray scattering: an advanced scattering technique for the investigation of nanostructured polymer films," *Analyt. Bioanalyst. Chem.*, vol. 376, no. 1, p. 3, 2003.

- [193] V. Holý and T. Baumbach, "Nonspecular x-ray reflection from rough multilayers," *Phys. Rev. B*, vol. 49, p. 10668, 1994.
- [194] C. Lorch, R. Banerjee, C. Frank, J. Dieterle, A. Hinderhofer, A. Gerlach, and F. Schreiber, "Growth of competing crystal phases of  $\alpha$ -sexithiophene studied by real-time *in situ* X-ray scattering," *J. Phys. Chem. C*, vol. 119, no. 1, p. 819, 2015.
- [195] L. Pithan, C. Cocchi, H. Zschiesche, C. Weber, A. Zykov, S. Bommel, S. J. Leake, P. Schäfer, C. Draxl, and S. Kowarik, "Light controls polymorphism in thin films of sexithiophene," *Cryst. Growth & Design*, vol. 15, no. 3, p. 1319, 2015.
- [196] S. Kowarik, A. Gerlach, M. W. A. Skoda, S. Sellner, and F. Schreiber, "Real-time studies of thin film growth: Measurement and analysis of X-ray growth oscillations beyond the anti-Bragg point," *Eur. Phys. J. Special Topics*, vol. 167, p. 11, 2009.
- [197] S. Bommel, *Unravelling nanoscale molecular processes in organic thin films*. PhD thesis, Humboldt University Berlin, 2015.
- [198] P. A. Gravil, M. Devel, P. Lambin, X. Bouju, C. Girard, and A. A. Lucas, "Adsorption of  $C_{60}$  molecules," *Phys. Rev. B*, vol. 53, p. 1622, 1996.
- [199] R. Cantrell and P. Clancy, "A computational study of surface diffusion of  $c_{60}$  on pentacene," *Surf. Sci.*, vol. 602, no. 22, p. 3499, 2008.
- [200] B. Drake, C. Prater, A. Weisenhorn, S. Gould, T. Albrecht, C. Quate, D. Cannell, H. Hansma, and P. Hansma, "Imaging crystals, polymers, and processes in water with the atomic force microscope," *Science*, vol. 243, no. 4898, p. 1586, 1989.
- [201] F. C. Frank and J. H. van der Merwe, "One-dimensional dislocations. I. static theory," *Proc. Roy. Soc. London A*, vol. 198, no. 1053, p. 205, 1949.
- [202] F. C. Frank and J. H. van der Merwe, "One-dimensional dislocations. II. misfitting monolayers and oriented overgrowth," *Proc. Roy. Soc. London A*, vol. 198, no. 1053, pp. 216–225, 1949.
- [203] F. C. Frank and J. H. van der Merwe, "One-dimensional dislocations. III. influence of the second harmonic term in the potential representation, on the properties of the model," *Proc. Roy. Soc. London A*, vol. 200, no. 1060, pp. 125–134, 1949.
- [204] C. Weber, C. Frank, S. Bommel, T. Rukat, W. Leitenberger, P. Schäfer, F. Schreiber, and S. Kowarik, "Chain-length dependent growth dynamics of n-alkanes on silica investigated by energy-dispersive x-ray reflectivity *in situ* and in real-time," *J. Chem. Phys.*, vol. 136, no. 20, p. 204709, 2012.
- [205] V. I. Trofimov and V. G. Mokerov, "Rate equations model for layer epitaxial growth kinetics," *Thin Solid Films*, vol. 428, no. 1-2, p. 66, 2003. Proceedings of Symposium J on Growth and Evolution of Ultrathin Films: Surface and Interface Geometric and Electronic Structure, of the E-MRS Spring Conference.
- [206] V. I. Trofimov, V. G. Mokerov, and A. G. Shumyankov, "Kinetic model for molecular beam epitaxial growth on a singular surface," *Thin Solid Films*, vol. 306, no. 1, p. 105, 1997.
- [207] P. I. Cohen, G. S. Petrich, P. R. Pukite, G. J. Whaley, and A. S. Arrott, "Birth-death models of epitaxy: I. diffraction oscillations from low index surfaces," *Surf. Sci.*, vol. 216, no. 1-2, p. 222, 1989.
- [208] A. R. Woll, T. V. Desai, and J. R. Engstrom, "Quantitative modeling of *in situ* x-ray reflectivity during organic molecule thin film growth," *Phys. Rev. B*, vol. 84, p. 075479, 2011.
- [209] G. Renaud, R. Lazzari, C. Revenant, A. Barbier, M. Noblet, O. Ulrich, F. Leroy, J. Jupille, Y. Borensztein, C. R. Henry, J.-P. Deville, F. Scheurer, J. Mane-Mane, and O. Fruchart, "Real-time monitoring of growing nanoparticles," *Science*, vol. 300, no. 5624, p. 1416, 2003.
- [210] M. Schwartzkopf, A. Buffet, V. Koerstgens, E. Metwalli, K. Schlage, G. Benecke, J. Perlich, M. Rawolle, A. Rothkirch, B. Heidmann, G. Herzog, P. Mueller-Buschbaum, R. Roehlsberger, R. Gehrke, N. Stribeck, and S. V. Roth, "From atoms to layers: *in situ* gold cluster growth kinetics during sputter deposition," *Nanoscale*, vol. 5, no. 11, p. 5053, 2013.
- [211] M. F. Gyure, J. J. Zinck, C. Ratsch, and D. D. Vvedensky, "Unstable growth on rough surfaces," *Phys. Rev. Lett.*, vol. 81, p. 4931, 1998.
- [212] S. Rols, J. Cambedouzou, M. Chorro, H. Schober, V. Agafonov, P. Launois, V. Davydov, A. V. Rakhmanina, H. Kataura, and J.-L. Sauvajol, "How confinement affects the dynamics of  $C_{60}$  in carbon nanopeapods," *Phys. Rev. Lett.*, vol. 101, p. 065507, 2008.

- [213] P. A. Heiney, J. E. Fischer, A. R. McGhie, W. J. Romanow, A. M. Denenstein, J. P. McCauley Jr., A. B. Smith, and D. E. Cox, “Orientational ordering transition in solid C<sub>60</sub>,” *Phys. Rev. Lett.*, vol. 66, pp. 2911–2914, 1991.
- [214] E. A. Katz, “Fullerene thin films as photovoltaic materials,” in *Nanostructured Materials for Solar Energy Conversion* (T. Soga, ed.), ch. 13, p. 361, Elsevier Science, 2006.
- [215] S. Clarke and D. D. Vvedensky, “Growth kinetics and step density in reflection high-energy electron diffraction during molecular-beam epitaxy,” *J. Appl. Phys.*, vol. 63, no. 7, 1988.
- [216] T. J. Oliveira and F. D. A. Aarão Reis, “Scaling in reversible submonolayer deposition,” *Phys. Rev. B*, vol. 87, p. 235430, 2013.
- [217] G. Ehrlich and F. G. Hudha, “Atomic view of surface self-diffusion: Tungsten on tungsten,” *J. Chem. Phys.*, vol. 44, no. 3, 1966.
- [218] R. L. Schwoebel and E. J. Shipsey, “Step motion on crystal surfaces,” *J. Appl. Phys.*, vol. 37, no. 10, 1966.
- [219] J. Cardy, *Finite-Size Scaling*. Current Physics – Sources and Comments, Elsevier Science, 2012.
- [220] J. Hoshen and R. Kopelman, “Percolation and cluster distribution. I. cluster multiple labeling technique and critical concentration algorithm,” *Phys. Rev. B*, vol. 14, p. 3438, 1976.
- [221] P. Karmakar and D. Ghose, “Ion beam sputtering induced ripple formation in thin metal films,” *Surf. Sci.*, vol. 554, no. 2-3, p. L101, 2004.
- [222] J. Yu and J. G. Amar, “Scaling behavior of the surface in ballistic deposition,” *Phys. Rev. E*, vol. 65, p. 060601, 2002.
- [223] S. Das Sarma, C. J. Lanczycki, R. Kotlyar, and S. V. Ghaisas, “Scale invariance and dynamical correlations in growth models of molecular beam epitaxy,” *Phys. Rev. E*, vol. 53, p. 359, 1996.
- [224] D. W. Schaefer, J. E. Martin, P. Wiltzius, and D. S. Cannell, “Fractal geometry of colloidal aggregates,” *Phys. Rev. Lett.*, vol. 52, p. 2371, 1984.
- [225] R. Ruiz, B. Nickel, N. Koch, L. C. Feldman, R. F. Haglund, A. Kahn, F. Family, and G. Scoles, “Dynamic scaling, island size distribution, and morphology in the aggregation regime of submonolayer pentacene films,” *Phys. Rev. Lett.*, vol. 91, p. 136102, 2003.
- [226] T. Michely and J. Krug, *Islands, Mounds and Atoms*. Physics and astronomy online library, Springer Berlin Heidelberg, 2004.
- [227] T. Bohlein, J. Mikhael, and C. Bechinger, “Observation of kinks and antikinks in colloidal monolayers driven across ordered surfaces,” *Nat. Mater.*, vol. 11, no. 2, p. 126, 2012.
- [228] D. Frenkel and D. J. Wales, “Colloidal self-assembly — designed to yield,” *Nat. Mater.*, vol. 10, no. 6, p. 410, 2011.
- [229] J. D. Ferguson, G. Arıkan, D. S. Dale, A. R. Woll, and J. D. Brock, “Measurements of surface diffusivity and coarsening during pulsed laser deposition,” *Phys. Rev. Lett.*, vol. 103, p. 256103, 2009.
- [230] P. Reimann, G. J. Schmid, and P. Hänggi, “Universal equivalence of mean first-passage time and Kramers rate,” *Phys. Rev. E*, vol. 60, no. 1, p. R1, 1999.
- [231] G. Pólya, “Über eine Aufgabe der Wahrscheinlichkeitsrechnung betreffend die Irrfahrt im Straßennetz,” *Math. Ann.*, vol. 84, no. 1-2, p. 149, 1921.
- [232] G. Nandipati, Y. Shim, J. G. Amar, A. Karim, A. Kara, T. S. Rahman, and O. Trushin, “Parallel kinetic Monte Carlo simulations of Ag(111) island coarsening using a large database,” *J. Phys.: Condens. Matter*, vol. 21, no. 8, p. 084214, 2009.
- [233] M. Li, Y. Han, P. A. Thiel, and J. W. Evans, “Formation of complex wedding-cake morphologies during homoepitaxial film growth of Ag on Ag(111): atomistic, step-dynamics, and continuum modeling,” *J. Phys.: Condens. Matter*, vol. 21, no. 8, p. 084216, 2009.
- [234] H. Brune, K. Bromann, H. Röder, K. Kern, J. Jacobsen, P. Stoltze, K. Jacobsen, and J. Nørskov, “Effect of strain on surface diffusion and nucleation,” *Phys. Rev. B*, vol. 52, p. R14380, 1995.
- [235] A. Latz, L. Brendel, and D. E. Wolf, “A three-dimensional self-learning kinetic Monte Carlo model: application to Ag(111),” *J. Phys.: Condens. Matter*, vol. 24, no. 48, p. 485005, 2012.

- [236] W. Li-Li, H. Juan-Mei, and W. Feng-Min, “A study of surfactant-induced growth of Ag on Ag (111),” *Commun. Theoret. Phys.*, vol. 50, no. 6, p. 1439, 2008.
- [237] S. Blackwell, R. Smith, S. D. Kenny, and J. M. Walls, “Modeling evaporation, ion-beam assist, and magnetron sputtering of thin metal films over realistic time scales,” *Phys. Rev. B*, vol. 86, p. 035416, 2012.
- [238] M. Hohage, M. Bott, M. Morgenstern, Z. Zhang, T. Michely, and G. Comsa, “Atomic processes in low temperature Pt-dendrite growth on Pt(111),” *Phys. Rev. Lett.*, vol. 76, p. 2366, 1996.
- [239] P. J. Feibelman and T. Michely, “Pt-dimer dissociation on Pt(111),” *Surf. Sci.*, vol. 492, no. 1-2, p. L723, 2001.
- [240] C. Aubert and D. S. Cannell, “Restructuring of colloidal silica aggregates,” *Phys. Rev. Lett.*, vol. 56, p. 738, 1986.
- [241] J. Liu, W. Y. Shih, M. Sarikaya, and I. A. Aksay, “Fractal colloidal aggregates with finite interparticle interactions: Energy dependence of the fractal dimension,” *Phys. Rev. A*, vol. 41, p. 3206, 1990.
- [242] J. Krug, “Origins of scale invariance in growth processes,” *Adv. Phys.*, vol. 46, 1997.
- [243] F. Tong, K. Kim, D. Martinez, R. Thapa, A. Ahyi, J. Williams, D.-J. Kim, S. Lee, E. Lim, K. K. Lee, and M. Park, “Flexible organic/inorganic hybrid solar cells based on conjugated polymer and ZnO nanorod array,” *Semicond. Sci. Technol.*, vol. 27, no. 10, 2012.
- [244] Private communications with K. Palczynski and J. Dzubiella.
- [245] R. Koch, J. J. Finnerty, and T. Bruhn, “Theoretical study on the nonlinear optical properties of phenylenes and influencing factors,” *J. Phys. Org. Chem.*, vol. 21, no. 11, p. 954, 2008.
- [246] J. Roales, J. M. Pedrosa, P. Castillero, M. Cano, T. H. Richardson, A. Barranco, and A. R. Gonzalez-Elipe, “Selective detection of volatile organic compounds by spectral imaging of porphyrin derivatives bound to TiO<sub>2</sub> porous films,” *ACS Appl. Mater. Interfaces*, vol. 4, no. 10, p. 5147, 2012.
- [247] E. Zojer, N. Koch, P. Puschnig, F. Meghdadi, A. Niko, R. Resel, C. Ambrosch-Draxl, M. Knupfer, J. Fink, J. L. Brédas, and G. Leising, “Structure, morphology, and optical properties of highly ordered films of para -sexiphenyl,” *Phys. Rev. B*, vol. 61, p. 16538, 2000.
- [248] C. Simbrunner, “Epitaxial growth of sexi-thiophene and para-hexaphenyl and its implications for the fabrication of self-assembled lasing nano-fibres,” *Semicond. Sci. Technol.*, vol. 28, no. 5, p. 053001, 2013.
- [249] X. Shen, B. Sun, D. Liu, and S.-T. Lee, “Hybrid heterojunction solar cell based on organic-inorganic silicon nanowire array architecture,” *J. Am. Chem. Soc.*, vol. 133, no. 48, p. 19408, 2011.
- [250] D. Nazarova, L. Nedelchev, P. Sharlandjiev, and V. Dragostinova, “Anisotropic hybrid organic/inorganic (azopolymer/SiO<sub>2</sub> NP) materials with enhanced photoinduced birefringence,” *Appl. Opt.*, vol. 52, no. 22, p. E28, 2013.
- [251] A. L. Briseno and P. Yang, “Optoelectronics combining chemical worlds,” *Nat. Mater.*, vol. 8, no. 1, p. 7, 2009.
- [252] T. Wehlus, T. Körner, S. Nowy, J. Frischeisen, H. Karl, B. Stritzker, and W. Brüttling, “Hybrid organic-inorganic materials for integrated optoelectronic devices,” *Phys. Stat. Sol. A*, vol. 208, no. 2, p. 264, 2011.
- [253] C. Simbrunner, D. Nabok, G. Hernandez-Sosa, M. Oehzelt, T. Djuric, R. Resel, L. Romaner, P. Puschnig, C. Ambrosch-Draxl, I. Salzmann, G. Schwabegger, I. Watzinger, and H. Sitter, “Epitaxy of rodlike organic molecules on sheet silicates — growth model based on experiments and simulations,” *J. Am. Chem. Soc.*, vol. 133, no. 9, p. 3056, 2011.
- [254] K. Barnham and D. Vvedensky, *Low-Dimensional Semiconductor Structures: Fundamentals and Device Applications*. Cambridge University Press, 2008.
- [255] U. W. Pohl, *Epitaxy of Semiconductors*. Springer-Verlag Berlin Heidelberg, 2013.
- [256] P. Clancy, “Application of molecular simulation techniques to the study of factors affecting the thin-film morphology of small-molecule organic semiconductors,” *Chem. Mater.*, vol. 23, no. 3, p. 522, 2011.
- [257] J. S. Raut and K. A. Fichthorn, “Diffusion mechanisms of short-chain alkanes on metal substrates: Unique molecular features,” *J. Chem. Phys.*, vol. 108, no. 4, p. 1626, 1998.
- [258] R. Ruiz, D. Choudhary, B. Nickel, T. Toccoli, K.-C. Chang, A. C. Mayer, P. Clancy, J. M. Blakely, R. L.

- Headrick, S. Iannotta, and G. G. Malliaras, "Pentacene thin film growth," *Chem. Mater.*, vol. 16, no. 23, p. 4497, 2004.
- [259] A. C. Dürr, F. Schreiber, K. A. Ritley, V. Kruppa, J. Krug, H. Dosch, and B. Struth, "Rapid roughening in thin film growth of an organic semiconductor (diindenoperylene)," *Phys. Rev. Lett.*, vol. 90, p. 016104, 2003.
- [260] J. Kundu and R. Rajesh, "Phase transitions in a system of hard rectangles on the square lattice," *Phys. Rev. E*, vol. 89, p. 052124, 2014.
- [261] T. Fischer and R. L. C. Vink, "Restricted orientation "liquid crystal" in two dimensions: Isotropic-nematic transition or liquid-gas one(?)", *EPL*, vol. 85, no. 5, 2009.
- [262] R. Dickman, "Discontinuous phase transition in a dimer lattice gas," *J. Chem. Phys.*, vol. 136, no. 17, p. 174105, 2012.
- [263] X. Feng, H. W. J. Blöte, and B. Nienhuis, "Lattice gas with nearest- and next-to-nearest-neighbor exclusion," *Phys. Rev. E*, vol. 83, p. 061153, 2011.
- [264] R. Shekhar, J. K. Whitmer, R. Malshe, J. A. Moreno-Razo, T. F. Roberts, and J. J. de Pablo, "Isotropic-nematic phase transition in the Lebwohl-Lasher model from density of states simulations," *J. Chem. Phys.*, vol. 136, no. 23, p. 234503, 2012.
- [265] A. M. Luo, S. Wenk, and P. Ilg, "Temperature-dependent orientational ordering on a spherical surface modeled with a lattice spin model," *Phys. Rev. E*, vol. 90, p. 022502, 2014.
- [266] N. Ghoshal, K. Mukhopadhyay, and S. K. Roy, "Effect of an external magnetic field on the nematic-isotropic phase transition in mesogenic systems of uniaxial and biaxial molecules: A Monte Carlo study," *Phys. Rev. E*, vol. 89, p. 042505, 2014.
- [267] R. Resel, "Surface induced crystallographic order in sexiphenyl thin films," *J. Phys.: Condens. Matter*, vol. 20, no. 18, p. 184009, 2008.
- [268] S. Blumstengel, S. Sadofev, and F. Henneberger, "Electronic coupling of optical excitations in organic/i-norganic semiconductor hybrid structures," *New J. Phys.*, vol. 10, p. 065010, 2008.
- [269] I. Repins, M. A. Contreras, B. Egaas, C. DeHart, J. Scharf, C. L. Perkins, B. To, and R. Noufi, "199%-efficient ZnO/CdS/CuInGaSe<sub>2</sub> solar cell with 812% fill factor," *Prog. Photovolt.: Res. Appl.*, vol. 16, no. 3, p. 235, 2008.
- [270] Y. Sun, J. H. Seo, C. J. Takacs, J. Seifter, and A. J. Heeger, "Inverted polymer solar cells integrated with a low-temperature-annealed sol-gel-derived ZnO film as an electron transport layer," *Adv. Mater.*, vol. 23, no. 14, p. 1679, 2011.
- [271] A. Andreev, H. Sitter, N. Sariciftci, C. Brabec, G. Springholz, P. Hinterdorfer, H. Plank, R. Resel, A. Thierry, and B. Lotz, "Highly ordered anisotropic nano-needles in para-sexiphenyl films," *Thin Solid Films*, vol. 403-404, no. 0, p. 444, 2002.
- [272] A. Komolov, P. Müller, J. Mortensen, S. Komolov, and E. Lazneva, "Electronic properties of a zinc oxide surface modified by ultra-thin layers of conjugated organic molecules," *Surf. Sci.*, vol. 586, no. 1-3, p. 129, 2005.
- [273] C.-Y. Huang, C.-C. Yang, H.-C. Yu, and Y.-C. Chen, "Impact of preparation condition of ZnO electron transport layer on performance of hybrid organic-inorganic light-emitting diodes," *J. Appl. Phys.*, vol. 115, no. 8, p. 083109, 2014.
- [274] S. Berkebile, P. Puschnig, G. Koller, M. Oehzelt, F. P. Netzer, C. Ambrosch-Draxl, and M. G. Ramsey, "Electronic band structure of pentacene: An experimental and theoretical study," *Phys. Rev. B*, vol. 77, p. 115312, 2008.
- [275] P. Puschnig, E.-M. Reinisch, T. Ules, G. Koller, S. Soubatch, M. Ostler, L. Romaner, F. S. Tautz, C. Ambrosch-Draxl, and M. G. Ramsey, "Orbital tomography: Deconvoluting photoemission spectra of organic molecules," *Phys. Rev. B*, vol. 84, p. 235427, 2011.
- [276] K.-F. Braun and S.-W. Hla, "Probing the conformation of physisorbed molecules at the atomic scale using STM manipulation," *Nano Lett.*, vol. 5, no. 1, p. 73, 2005.
- [277] G. Hlawacek, P. Puschnig, P. Frank, A. Winkler, C. Ambrosch-Draxl, and C. Teichert, "Characterization of step-edge barriers in organic thin-film growth," *Science*, vol. 321, no. 5885, p. 108, 2008.

- [278] G. Koller, S. Berkebile, J. R. Krenn, F. P. Netzer, M. Oehzelt, T. Haber, R. Resel, and M. G. Ramsey, "Heteroepitaxy of organic-organic nanostructures," *Nano Lett.*, vol. 6, no. 6, p. 1207, 2006.
- [279] P. A. Golubkov and P. Ren, "Generalized coarse-grained model based on point multipole and gay-berne potentials," *J. Chem. Phys.*, vol. 125, no. 6, p. 064103, 2006.
- [280] J. G. Gay and B. J. Berne, "Modification of the overlap potential to mimic a linear site-site potential," *J. Chem. Phys.*, vol. 74, no. 6, pp. 3316–3319, 1981.
- [281] D. J. Cleaver, C. M. Care, M. P. Allen, and M. P. Neal, "Extension and generalization of the Gay-Berne potential," *Phys. Rev. E*, vol. 54, p. 559, 1996.
- [282] MarvinSketch by ChemAxon, Version 6.0, used via [www.reaxys.com](http://www.reaxys.com) on the 5th Feb. 2014.
- [283] C. Gray and K. Gubbins, *Theory of Molecular Fluids: I Fundamentals*. International Series of Monographs on Chemistry, OUP Oxford, 1984.
- [284] J. Stelzer, P. Galatola, G. Barbero, and L. Longa, "Molecular dynamics simulations of surface-induced ordering in a nematic liquid crystal," *Phys. Rev. E*, vol. 55, p. 477, 1997.
- [285] H. Steuer, S. Hess, and M. Schoen, "Phase behavior of liquid crystals confined by smooth walls," *Phys. Rev. E*, vol. 69, p. 031708, 2004.
- [286] D. Micheletti, L. Muccioli, R. Berardi, M. Ricci, and C. Zannoni, "Effect of nanoconfinement on liquid-crystal polymer chains," *J. Chem. Phys.*, vol. 123, no. 22, p. 224705, 2005.
- [287] F. Barmes and D. J. Cleaver, "Using particle shape to induce tilted and bistable liquid crystal anchoring," *Phys. Rev. E*, vol. 71, p. 021705, 2005.
- [288] T. Gruhn and M. Schoen, "Substrate-induced order in confined nematic liquid-crystal films," *J. Chem. Phys.*, vol. 108, no. 21, p. 9124, 1998.
- [289] J. Hansen and I. McDonald, *Theory of Simple Liquids: with Applications to Soft Matter*. Elsevier Science, 2006.
- [290] T. Parker, N. Condon, R. Lindsay, F. Leibsle, and G. Thornton, "Imaging the polar (000 $\bar{1}$ ) and non-polar (10 $\bar{1}0$ ) surfaces of ZnO with STM," *Surf. Sci.*, vol. 415, no. 3, p. L1046, 1998.
- [291] P. Allen and D. Tildesley, *Computer Simulation of Liquids*. Oxford Science Publ, Clarendon Press, 1989.
- [292] D. A. Strehober, H. Engel, and S. H. L. Klapp, "Oscillatory motion of sheared nanorods beyond the nematic phase," *Phys. Rev. E*, vol. 88, p. 012505, 2013.
- [293] P. K. Karahaliou, A. G. Vanakaras, and D. J. Photinos, "Symmetries and alignment of biaxial nematic liquid crystals," *J. Chem. Phys.*, vol. 131, no. 12, p. 124516, 2009.
- [294] R. J. Low, "Measuring order and biaxiality," *Eur. J. Phys.*, vol. 23, no. 2, p. 111, 2002.
- [295] T. Jankun-Kelly and K. Mehta, "Superellipsoid-based, real symmetric traceless tensor glyphs motivated by nematic liquid crystal alignment visualization," *Visualization and Computer Graphics, IEEE Transactions on*, vol. 12, no. 5, p. 1197, 2006.
- [296] S. D. Peroukidis, P. K. Karahaliou, A. G. Vanakaras, and D. J. Photinos, "Biaxial nematics: symmetries, order domains and field-induced phase transitions," *Liq. Cryst.*, vol. 36, no. 6–7, p. 727, 2009.
- [297] G. Rienäcker, M. Kröger, and S. Hess, "Chaotic and regular shear-induced orientational dynamics of nematic liquid crystals," *Physica A*, vol. 315, no. 3-4, p. 537, 2002.
- [298] D. Andrienko, M. P. Allen, G. Skačej, and S. Žumer, "Defect structures and torque on an elongated colloidal particle immersed in a liquid crystal host," *Phys. Rev. E*, vol. 65, p. 041702, 2002.
- [299] D. Andrienko, "Introduction to liquid crystals," 2006. International Max Planck Research School 'Modelling of soft matter' 11-15 September 2006, Bad Marienberg (Germany).
- [300] M. S. Park, B.-J. Yoon, J. O. Park, V. Prasad, S. Kumar, and M. Srinivasarao, "Raman scattering study of phase biaxiality in a thermotropic bent-core nematic liquid crystal," *Phys. Rev. Lett.*, vol. 105, p. 027801, 2010.
- [301] D. S. Wokes and P. L. Palmer, "Perspective projection of a spheroid onto an image plane," 2008. Lecture notes, Surrey Space Centre, Guildford, Surrey, GU2 7XH.
- [302] P. Bolhuis and D. Frenkel, "Tracing the phase boundaries of hard spherocylinders," *J. Chem. Phys.*, vol. 106, no. 2, p. 666, 1997.

- [303] K. Al-Shamery, H. Rubahn, and H. Sitter, *Organic Nanostructures for Next Generation Devices*. Springer Series in Materials Science, Springer, 2007.
- [304] W. Brütting, *Physics of Organic Semiconductors*. Wiley, 2006.
- [305] P. K. Jana, C. Wang, R. J. Jack, L. Chi, and A. Heuer, “Anomalous approach to thermodynamic equilibrium: structure formation of molecules after vapor deposition,” *submitted*, 2015.
- [306] M. D. Klopotek, “Kinetic Monte Carlo simulations of thin film growth with anisotropic particles,” Master’s thesis, Eberhard Karls University Tübingen, 2014.
- [307] Y. Garmshausen, J. Schwarz, J. Hildebrandt, B. Kobil, M. Pätzfel, and S. Hecht, “Making nonsymmetrical bricks: Synthesis of insoluble dipolar sexiphenyls,” *Org. Lett.*, vol. 16, no. 11, pp. 2838–2841, 2014.
- [308] I. Salzmann, S. Duhm, G. Heimel, J. P. Rabe, N. Koch, M. Oehzelt, Y. Sakamoto, and T. Suzuki, “Structural order in perfluoropentacene thin films and heterostructures with pentacene,” *Langmuir*, vol. 24, no. 14, p. 7294, 2008.
- [309] T. Wang, J. Jelic, D. Rosenthal, and K. Reuter, “Exploring pretreatment-morphology relationships: Ab-initio wulff construction for RuO<sub>2</sub> nanoparticles under oxidising conditions,” *Chem. Cat. Chem.*, vol. 5, no. 11, p. 3398, 2013.
- [310] D. Matsunaka and Y. Shibutani, “Effects of tensile strain on Ag(111) epitaxial growth by kinetic Monte Carlo simulations,” *J. Phys.: Condens. Matter*, vol. 23, no. 26, p. 265008, 2011.
- [311] C. Wächtler, “Heteroepitaxial growth of C<sub>60</sub> on substrates: a kinetic Monte Carlo study,” Master’s thesis, TU Berlin, 2014.
- [312] G. Subramanian, D. Perez, B. P. Uberuaga, C. N. Tomé, and A. F. Voter, “Method to account for arbitrary strains in kinetic Monte Carlo simulations,” *Phys. Rev. B*, vol. 87, p. 144107, 2013.
- [313] J. R. Savage, S. F. Hopp, R. Ganapathy, S. J. Gerbode, A. Heuer, and I. Cohen, “Entropy-driven crystal formation on highly strained substrates,” *Proc. Nat. Ac. Sci.*, vol. 110, no. 23, p. 9301, 2013.
- [314] X. He, F. Gao, G. Tu, D. Hasko, S. Hüttner, U. Steiner, N. C. Greenham, R. H. Friend, and W. T. S. Huck, “Formation of nanopatterned polymer blends in photovoltaic devices,” *Nano Lett.*, vol. 10, no. 4, p. 1302, 2010.
- [315] C. L. Stender, E. C. Greyson, Y. Babayan, and T. W. Odom, “Patterned MoS<sub>2</sub> nanostructures over centimeter-square areas,” *Adv. Mater.*, vol. 17, no. 23, p. 2837, 2005.
- [316] R. Banerjee, J. Novák, C. Frank, M. Girleanu, O. Ersen, M. Brinkmann, F. Anger, C. Lorch, J. Dieterle, A. Gerlach, J. Drnec, S. Yu, and F. Schreiber, “Structure and morphology of organic semiconductor-nanoparticle hybrids prepared by soft deposition,” *J. Phys. Chem. C*, vol. 119, no. 9, p. 5225, 2015.
- [317] K. Broch, A. Gerlach, C. Lorch, J. Dieterle, J. Novák, A. Hinderhofer, and F. Schreiber, “Structure formation in perfluoropentacene:diindenoperylene blends and its impact on transient effects in the optical properties studied in real-time during growth,” *J. Chem. Phys.*, vol. 139, no. 17, p. 174709, 2013.
- [318] Y. Zheng, S. K. Pregler, J. D. Myers, J. Ouyang, S. B. Sinnott, and J. Xue, “Computational and experimental studies of phase separation in pentacene:C<sub>60</sub> mixtures,” *J. Vac. Sci. & Technol. B*, vol. 27, no. 1, 2009.
- [319] S. D. Peroukidis and S. H. L. Klapp, “Spontaneous ordering of magnetic particles in liquid crystals: From chains to biaxial lamellae,” *submitted*, 2015.
- [320] S. D. Peroukidis, A. G. Vanakaras, and D. J. Photinos, “Liquid crystalline phases and demixing in binary mixtures of shape-anisometric colloids,” *J. Mater. Chem.*, vol. 20, p. 10495, 2010.
- [321] M. Gruber, M. Rawolle, J. Wagner, D. Magerl, U. Hörmann, J. Perlich, S. V. Roth, A. Opitz, F. Schreiber, P. Müller-Buschbaum, and W. Brütting, “Correlating structure and morphology to device performance of molecular organic donor-acceptor photovoltaic cells based on diindenoperylene (DIP) and C<sub>60</sub>,” *Adv. Energy Mater.*, vol. 3, no. 8, p. 1075, 2013.
- [322] A. V. A. Kumar, “Binary colloidal mixtures in a potential barrier: Demixing due to depletion,” *J. Chem. Phys.*, vol. 138, no. 15, p. 154903, 2013.
- [323] E. López-Sánchez, C. D. Estrada-Álvarez, G. Pérez-Ángel, J. M. Méndez-Alcaraz, P. González-Mozuelos, and R. Castañeda Priego, “Demixing transition, structure, and depletion forces in binary mixtures of hard-spheres: The role of bridge functions,” *J. Chem. Phys.*, vol. 139, no. 10, p. 104908, 2013.

- [324] K. Lichtner and S. H. L. Klapp, "Spinodal decomposition of a binary magnetic fluid confined to a surface," *Phys. Rev. E*, vol. 88, p. 032301, 2013.
- [325] T. H. Cormen, C. E. Leiserson, R. L. Rivest, and C. Stein, *Introduction to Algorithms, Third Edition*. The MIT Press, 3rd ed., 2009.
- [326] A. F. Voter, "Classically exact overlayer dynamics: Diffusion of rhodium clusters on Rh(100)," *Phys. Rev. B*, vol. 34, p. 6819, 1986.
- [327] D. Perez and L. J. Lewis, "Molecular-dynamics study of ablation of solids under femtosecond laser pulses," *Phys. Rev. B*, vol. 67, p. 184102, 2003.
- [328] S. Das Sarma, C. J. Lanczycki, R. Kotlyar, and S. V. Ghaisas, "Scale invariance and dynamical correlations in growth models of molecular beam epitaxy," *Phys. Rev. E*, vol. 53, p. 359, 1996.